

Processing and Thermo-Mechanical Considerations for Rare Earth Disilicates as Environmental Barrier Coatings

A

Dissertation

Presented to

the faculty of the School of Engineering and Applied Science

University of Virginia

In partial fulfillment

of the requirements for the degree

Doctor of Philosophy

by

Alejandro Salanova Giampaoli

March 26th, 2024

APPROVAL SHEET

This
Dissertation
is submitted in partial fulfillment of the requirements
for the degree of
Doctor of Philosophy

This Dissertation has been read and approved by the examining committee:

Advisor: Dr. Jon Ihlefeld

Committee Member: Dr. Elizabeth Opila

Committee Member: Dr. Prasanna Balachandran

Committee Member: Dr. Edward Gorzkowski

Committee Member: Dr. Ethan Scott

Accepted for the School of Engineering and Applied Science:



Jennifer L. West, School of Engineering and Applied Science

May 2024

Abstract

Silicon carbide based ceramic matrix composites (CMCs) are state of the art materials for shrouds in high temperature gas turbine engines. In this application, CMCs react in the presence of water vapor to produce a gaseous silicon hydroxide species. The CMCs require adequate protection through the use of a thermal/environmental barrier coating (EBC) to avoid premature degradation. The current technology at the forefront of EBCs are rare earth disilicates (REDS) due to a similar coefficient of thermal expansion (CTE) relative to CMCs, high melting temperatures, and low silicon activity relative to pure silica. This thesis involves several key studies to develop new knowledge on the properties of REDS: 1) the synthesis of single cation, multi-cation, and high-entropy REDSs through the sol-gel process; 2) the characterization of REDS through *in situ* hot stage diffraction to identify phase stability; and 3) the characterization of anisotropic CTE behavior of REDSs using X-ray and neutron diffraction and scattering.

The sol-gel synthesis was shown to be highly dependent on water as well as acid or base concentrations that served as a catalyst for the hydrolysis reaction necessary to produce silica from its precursor, tetraethyl orthosilicate. Additionally, multi- and high-entropy REDS sol-gels were successfully synthesized and stabilized into the monoclinic $C2/m$ phase following a rule of mixtures. *In situ* hot-stage diffraction was used to identify and determine phase stability from room temperature to temperatures up to 1200 °C. Synchrotron based diffraction and pair distribution function (PDF) analysis data was used to develop a tensor derived model for the anisotropic CTE behavior. The data showed that the directions of minimum and maximum CTE were temperature dependent for REDS containing lutetium, ytterbium, yttrium, and thulium. A series of experiments investigated the many possible properties that could be related to CTE anisotropy. electronic configuration of REDS through the band gap, calculating differences of up to 1 eV for different REDS presumably due to the rare earth cation. Despite the results, band gap did not seem to be directly correlated to CTE anisotropy. Next, the optical phonon behavior was investigated through Raman spectroscopy and FTIR. The optical phonon behavior showed no correlation to CTE anisotropy as all REDS have near identical spectra from room temperature to 1200 °C. The acoustic phonons were investigated, and phonon dispersion were provided through computational work performed by collaborators. Differences in the phonon dispersion curves of REDS did show distinctions that may be related to CTE anisotropy but require a deeper look and more experiments to prove or disprove. The differences in CTE behavior are attributed to the expansion and rotation of the rare earth-oxygen octahedron induced by local distortions. This thesis outlines the mechanisms through which REDSs can be further tailored to produce single phase homogeneous powders, stabilize rare earth cations in atypical but desired crystalline phases, and develop a model for anisotropic CTE that can inform the stresses that develop as a

function of heating for EBCs with specific attention on the short-range and long-range crystal symmetries and their evolution with temperature.

Acknowledgements

This work was supported by the U.S. National Science Foundation's (NSF) Designing Materials to Revolution and Engineer our Future (DMREF) program under award number 1921973. This work used resources of the Advanced Photon Source, a U.S. Department of Energy (DOE) Office of Science user facility operated by the Office of Science by Argonne National Laboratory under Contract No. DE-AC02-06CH11357. A portion of this research used resources at the Spallation Neutron Source, a DOE Office of Science User Facility operated by the Oak Ridge National Laboratory.

My academic journey ends after over two decades. Although my expertise is my own, it was gained through years of schooling, the help of my peers, mentorship, and tutelage from my advisors. While reflecting on the names and faces of the people that have helped me, I realized that no list I can make is too comprehensive. My family, Antonio, Cristina, Mandy, Coco, and Cruzy Salanova have been the constants in my life. From my first days in school, immigrating to the United States, becoming an older brother, and throughout the additions of beloved pets as part of the family, I can't thank you enough for all you have done for me. Mandy, thank you for growing up alongside me. I could not have wished for a better sister. To my family, I hope to have a fraction of the intelligence and kindness that you see in me. To my grandparents, I remain inspired by the examples you have left for me. Nonno and Avi, you were examples of what engineers should be and allowed me to be the man I am today. Nonna, you taught me about the joy of loving others and enjoying life. I miss the three of you dearly. Tata, you taught me how to hold my head high and how to stand up for myself. Without you four, I don't believe I would have made it as far as I am today.

I have been lucky to have friendships that started when I was much younger and last to this day. Krysten Diaz-Silveira and Carlos Casadevall have been the two friends that have helped me define who I am. I have known the both of you for over a decade and I can't wait for the years to come in which our friendship will continue flourishing. I also want to thank Marissa Salaya, David Palazzolo, Meech Henriquez, Lizzie Carsello, Dennis Tariche, Alec Dominguez, Tori Breeze, Eddie Angelbello, August Michaelideas, Henry Perillo, Jordan Mrha, Jed Rojas, Reese Dengler, Stephen Gainesburg, and Will Tang. There are countless more friends I am missing but thank you from the bottom of my heart. I cherish the memories we made together, and I am a better person because of them. Finally, Wes, I miss you and I hope you are proud.

I began my research journey at the University of Florida with Dr. Jennifer Andrew as my advisor. With her guidance as well as the indispensable help from Sara Mills and Amanda Uhl, I evolved as a researcher and material scientist. I then began my graduate school journey at the University of Virginia

with Dr. Jon Ihlefeld as my advisor. Jon had the confidence in me to not only hire me but to put me on a project that was outside of his typical area of expertise. He fostered my scientific thinking that allowed me to develop my own hypotheses and experimental procedures. His guidance has been pivotal in my success and will continue to be the case as I graduate. I benefitted from guidance and instruction from other researchers, including Dr. Michelle Dolgos and Dr. Matthew Tucker.

My research group at the University of Virginia has changed throughout the years. It started with Shelby Fields, Samantha Jaszewski, and Ian Brummel showing me the ropes of graduate school and being responsible for much of my success early on. They were responsible for the culture of the group that continues to this day, even though Shelby and Sam have graduated. I can't imagine better friends to have started with. Later on, more members were added to the group that have inspired and educated me, Dr. Takanori Mimura, Liron Shvilberg, Lauren Askew, Megan Lenox, Gabby Niculescu, Benjamin Aronson, Stephen O'Conner, Yong Kyu Choi, Kyle Lam, and Casey Zhang. Thank you all for your continued work and support.

I have been lucky to have met many people during my time in graduate school. I want to acknowledge one of the greatest sources of encouragement, my partner, Victoria Soto Estremera. She has believed in and supported me, and for that I will be eternally grateful. My friendships in graduate school have carried me past difficult times. From working on homework, spending time together after work, disappearing to some cabin in the woods, and talking about what the future holds, I have made connections with people here that I want to last a lifetime. I want to thank Sam Inman, Coleman Tolliver, Alex Jennion, Cameron Miller, Lee Kendall, and Gaby Abad for helping get to this point.

Table of Contents

Chapter 1	Introduction	19
1.1	Outcomes	19
1.2	Experimental Guide	20
Chapter 2	Literature Review	22
2.1	Environmental Barrier Coatings	22
2.1.1	Current Nickel Superalloy Technology	22
2.1.2	Ceramic Matrix Composites	23
2.1.3	Barrier Coating Considerations	24
2.1.4	Phase Diagrams	26
2.1.5	Thermal Expansion Tensor	30
2.2	High-Entropy Ceramics	31
2.2.1	Entropic Contribution to Free Energy	31
2.2.2	Improvements to Thermal Conductivity	32
2.3	Synthesis of Rare-Earth Disilicates	32
2.3.1	Sol-Gel Method	32
2.3.2	Phase Purity	34
2.4	Techniques	35
2.4.1	In-Lab X-Ray Diffraction	35
2.4.2	Synchrotron Experiments	35
2.4.3	Pair Distribution Function Analysis	36
2.4.4	Neutron Source Experiments	37
2.4.5	Rietveld Refinement	38
2.4.6	CTEAS	39
2.4.7	Raman Spectroscopy	40
2.4.8	UV-Vis Spectroscopy	41
Chapter 3	Initial Synthesis and Phase Purity of Rare-Earth Disilicates	42

3.1	Introduction	42
3.2	Modified Pechini Method.....	42
3.3	Single Component REDS	44
3.4	Multi-Component REDS	46
3.5	Summary.....	49
Chapter 4 Phase Stability and Tensorial Thermal Expansion Properties of Single to High-Entropy Rare-Earth Disilicates		50
4.1	Motivation	50
4.2	Abstract.....	50
4.3	Introduction	51
4.4	Experimental Methods.....	53
4.4.1	Powder Synthesis	53
4.4.2	Diffraction Experiments.....	53
4.4.3	Tensor Analysis.....	54
4.5	Results and Discussion	54
4.5.1	Phase Mixing.....	54
4.5.2	High Temperature XRD.....	57
4.5.3	CTE/Tensor Determination	61
4.6	Conclusions	72
4.7	Data Availability	73
4.8	Acknowledgement.....	73
Chapter 5 Cation Dependent Mechanisms of Anisotropic CTE in Rare-Earth Disilicates.....		74
5.1	Motivation	74
5.2	Cold Stage X-ray Diffraction	74
5.3	Raman Spectroscopy	76
5.4	UV-VIS Spectrophotometry	80
5.5	Synchrotron X-ray PDF Analysis.....	83

5.6	Neutron Diffraction and Scattering	86
5.7	Conclusions	97
5.8	Acknowledgments	98
Chapter 6 Phase Purity and Evolution in Sol-Gel Derived Single Component and Multi-Component Rare Earth Disilicates		99
6.1	Motivation	99
6.2	Abstract.....	99
6.3	Introduction	100
6.4	Experimental Methods.....	102
6.4.1	Sol-Gel Synthesis	102
6.4.2	Diffraction Experiments.....	103
6.4.3	Phase Identification.....	104
6.5	Results and Discussion	104
6.5.1	Effect of Water Content and pH on Phase Formation.....	104
6.5.2	Crystallization and Phase Evolution of Xerogel	112
6.6	Conclusion.....	118
6.7	Acknowledgements	119
Chapter 7 Conclusions		120
Chapter 8 Future Work.....		122
8.1	Recommendations on Future Research	122
8.1.1	Other REDS Compositions	122
8.1.2	Non-equimolar Rare-Earth Concentrations.....	122
8.1.3	Beamline Experiments above 1000 °C.....	122
8.1.4	Stress Calculations and Elastic Modulus	123
Chapter 9 Appendix		125
9.1	Supplemental Information	125
9.1.1	GSAS-II Sequential Rietveld Refinement of Hot Stage Data	125

9.1.2	Extra Thermal Expansion Ellipsoids.....	127
9.1.3	Negative Thermal Expansion.....	130
9.1.4	CTEAS Tensor Data	131
9.2	Abbreviations, Acronyms, etc.	155
Chapter 10	References	157

List of Figures

Figure 2.1: A flowchart illustrating the energy consumption of the United States of America in 2021. The "Transportation" box is applicable in the scope of this work given the difficulty in scaling aerospace to electric. The units are in Quads, which are equivalent to a quadrillion BTU. ³	22
Figure 2.2: A diagram created by Felsche illustrating the relationship between ionic radius of the rare-earth cations, temperature, and the resulting phase. The monoclinic Type C phase is the candidate for T/EBC applications due to close CTE match. ²⁷	25
Figure 2.3: An adapted diagram from Felsche that includes the ionic radii of all RE cations with a coordination number of 6. Not all RE cations have a 6-fold coordination for the other polymorphs. The RE cations that form the desired Type C phase are Er, Tm, Yb, Lu, Y, and Sc. ²⁷	26
Figure 2.4: An adapted phase diagram of ytterbium oxide and silica from Toropov and Bondar. The colored lines correspond to the mono- and disilicate line compounds. ²⁹	27
Figure 2.5: An adapted phase diagram of erbium oxide and silica from Toropov and Bondar. The colored lines correspond to the mono- and disilicate line compounds. ²⁹	27
Figure 2.6: An adapted phase diagram of neodymium oxide and silica from Toropov and Bondar. The colored lines correspond to the mono- and disilicate line compounds. ²⁹	28
Figure 2.7: An adapted phase diagram of dysprosium oxide and silica from Toropov and Bondar. The colored lines correspond to the mono- and disilicate line compounds. ²⁹	28
Figure 2.8: An adapted phase diagram of lutetium oxide and silica from Toropov and Bondar. The colored lines correspond to the mono- and disilicate line compounds. ³⁰	29
Figure 2.9: An adapted phase diagram of yttrium oxide and silica from Toropov and Bondar. The colored lines correspond to the mono- and disilicate line compounds. ³⁰	29
Figure 2.10: An adapted phase diagram of scandium oxide and silica from Toropov and Bondar. The colored lines correspond to the mono- and disilicate line compounds. ³⁰	30
Figure 2.11: A diagram depicting the experimental setup at Beamline 11-ID-C for performing in situ heating diffraction and scattering experiments.	36

Figure 2.12: PDF comparison of X-ray and neutrons for erbium disilicate. The differences in probabilities correspond to detection differences in the oxygen and silicon environments. Figure a) is a comparison of the two functions through the entire r range. Figure b) is zoomed in to lower r range that would correspond to the Si-O and RE-O atomic distances corresponding to the first and second peaks respectively. 38

Figure 3.1: A flowchart of the first proposed experimental plan using a modified Pechini method to mix RE nitrates and TEOS to produce a phase pure REDS. 43

Figure 3.2: XRD patterns of initial attempts to synthesize $\text{Yb}_2\text{Si}_2\text{O}_7$. The only phase identified is the Yb oxide phase, necessitating modifications to the procedure. 43

Figure 3.3: A flowchart of the refined sol-gel process that more consistently produced sol-gels of higher phase purity relative to previous iterations. 44

Figure 3.4: XRD pattern of the first successful Yb disilicate sol-gel process. The disilicate phase is indexed with green circles, and the secondary monosilicates phase is indexed with red squares.^{76,77} 45

Figure 3.5: XRD patterns of Er, Y, Dy, and Nd sol-gels. The predominant phases are shown below the plot as references. The black squares indicate a monosilicate peak, the black stars indicate the $P 2_1/n$ phase, and the purple circles indicate the $P 63/m$ apatite phase. 46

Figure 3.6: XRD patterns of REDS with two RE cations are shown. The predominant phase is referenced in the patterns below the plot, and the secondary apatite phase is indexed with purple circles. 47

Figure 3.7: XRD patterns of three-component REDS. Both phases are predominantly the monoclinic $C 2/m$ phase. The neodymium containing mixture produced a secondary apatite phase. 48

Figure 3.8: XRD patterns of four and five component REDS. Both are primarily triclinic as shown by the reference patterns below the plot, and both contain the apatite phase indexed by purple circles. 49

Figure 4.1: A rule of mixtures prediction of the stability of REDS in the $C 2/m$ phase. Average ionic radii below the heavy dashed line are predicted to result in a REDS in the monoclinic $C 2/m$ phase. Those on or above the dashed line would be the triclinic ($P 1$) phase. 55

Figure 4.2: XRD pattern of ytterbium disilicate ($\text{Yb}_2\text{Si}_2\text{O}_7$) showing the monoclinic $C 2/m$ phase as the primary phase with approximately 7% secondary phase presence of ytterbium monosilicate (Yb_2SiO_5).

The monosilicate phase is denoted by the green squares. The reference patterns for the disilicate and monosilicate are ICSD Collection Codes 16048 and 4446 respectively.^{76,77} 56

Figure 4.3: Room temperature XRD patterns of REDS with the labeled compositions and average RE ionic radii. Two samples contain dysprosium, both stable in the C 2/m phase. All patterns indicate stability in the C 2/m phase..... 57

Figure 4.4: Contour maps of the high temperature XRD measurements on a lab-scale diffractometer for (a) $\text{Er}_2\text{Si}_2\text{O}_7$ and (b) the four component $(\text{Yb,Er,Y,Dy})_2\text{Si}_2\text{O}_7$ disilicate. The $\text{Er}_2\text{Si}_2\text{O}_7$ reference pattern is from ICSD Collection Code 74779.⁸⁹ 58

Figure 4.5: Contour maps of high temperature XRD measurements on a lab-scale diffractometer for (a) (Yb,Er) disilicate, (b) (Yb, Er, Y) disilicate, and (c) (Lu, Yb, Er, Y, Dy) disilicate. There are no detectable phases that nucleated during heating of these materials, meaning that these solid solutions are stable from room temperature to 1200 °C. The erbium disilicate reference pattern is ICSD Collection Code 74779.⁸⁹ 58

Figure 4.6: Rietveld refinement of $\text{Yb}_2\text{Si}_2\text{O}_7$ with a residual weight of approximately 3.4%. The tick marks below the fit correspond to the disilicate and monosilicate reference files (ICSD Collection Codes 16048 and 4446 respectively).^{76,77} Full scan range is shown in (a), while the higher angle peaks are shown in (b). The wavelength of X-ray radiation was 0.1173 Å. 60

Figure 4.7: 3D representations of the CTE tensors for erbium and ytterbium disilicate at different temperatures. (a) $\text{Er}_2\text{Si}_2\text{O}_7$ at 25 °C. (b) $\text{Yb}_2\text{Si}_2\text{O}_7$ at 25 °C. (c) $\text{Er}_2\text{Si}_2\text{O}_7$ at 500 °C. (d) $\text{Yb}_2\text{Si}_2\text{O}_7$ at 500 °C. (e) $\text{Er}_2\text{Si}_2\text{O}_7$ at 1000 °C. (f) $\text{Yb}_2\text{Si}_2\text{O}_7$ at 1000 °C. 62

Figure 4.8: 2-D polar plots showing the change in the magnitude of CTE along crystallographic directions in the (010) plane from room temperature to 1000 °C. The color gradient represents the temperature, with blue being the lowest temperature and red being the highest. The ellipsoids represent the following REDS compositions: (a) Er,DS (b) Yb,DS (c) Yb,Er DS (d) Yb,Er,Y (e)Yb,Er,Y,Dy (f)Lu,Yb,Er,Y,Dy..... 64

Figure 4.9: The angle of the Eigenvectors relative to the c-axis, [001] direction, were calculated using CTEAS. The trends seen in the Eigenvectors match the shifts seen in the 2-D ellipsoids where the minimum and maximum CTE values changed as a function of temperature. The Eigenvectors and principal axes are equivalent..... 65

Figure 4.10: Plot of the angle of the eigenvectors relative to the c-axis versus temperature for several REDS compositions. The angles of the eigenvectors converge as temperature increases..... 66

Figure 4.11: Temperature-dependent lattice parameters normalized to room temperature for (a) Er disilicate and (b) Yb disilicate showing a difference in expansion regarding the c unit cell direction and β angle. The difference in β angles for (c) Er disilicate and (d) Yb disilicate are shown in more detail..... 67

Figure 4.12: Lattice parameters versus temperature normalized to the value of the parameters at room temperature (a-d). Beta angle versus temperature showing the U-shaped trend that coincides with any composition that exhibits a shift in principal axes (e-h). The compositions are as follows: (a) and (e) are (Yb,Er) disilicate, (b) and (f) are (Yb,Er,Y) disilicate, (c) and (g) are (Yb,Er,Y,Dy) disilicate, and (d) and (h) are (Lu,Yb,Er,Y,Dy) disilicate. Certain datasets (c, d, g, and h) were cut off below 1000 °C due to thermocouple issues and in others the data points coinciding with the heating element break were removed (a and e)..... 68

Figure 4.13: The data showing the discontinuities and errant data points mentioned in **Figure 4.12**. Lattice parameters versus temperature normalized to the value of the parameters at room temperature (a-d). Beta angle versus temperature showing the u-shaped trend that coincides with any composition that exhibits a shift in principal axes (e-h). The compositions are as follows: (a) and (e) are (Yb,Er) disilicate, (b) and (f) are (Yb,Er,Y) disilicate, (c) and (g) are (Yb,Er,Y,Dy) disilicate, and (d) and (h) are (Lu,Yb,Er,Y,Dy) disilicate..... 68

Figure 4.14: Shear component (α_{13}) and beta angle are plotted with respect to temperature for $\text{Yb}_2\text{Si}_2\text{O}_7$. A horizontal dashed line is given to represent when the shear component crosses over from positive to negative, and this intercept corresponds to similar temperatures at which the minimum of the beta curve occurs. 70

Figure 4.15: The shear components for all ytterbium containing samples compared to the beta angle trends with respect to temperature for a) $(\text{Yb,Er})_2\text{Si}_2\text{O}_7$, b) $(\text{Yb,Er,Y})_2\text{Si}_2\text{O}_7$, c) $(\text{Yb,Er,Y,Dy})_2\text{Si}_2\text{O}_7$, and d) $(\text{Lu,Yb,Er,Y,Dy})_2\text{Si}_2\text{O}_7$. The horizontal dashed line is to indicate the crossover point of the shear component from positive to negative. The x-intercept of the shear component lies at similar temperatures to the minimum of the beta angle curve. Erbium disilicate is not shown since the shear component is always negative and the beta angle shows a nearly constant increase with respect to temperature. 71

Figure 5.1: Monoclinic beta angles of ytterbium disilicate during cold stage X-ray diffraction..... 75

Figure 5.2: Monoclinic beta angles of erbium disilicate during cold stage X-ray diffraction. 75

Figure 5.3: Room temperature Raman spectra of $\text{Yb}_2\text{Si}_2\text{O}_7$, $\text{Er}_2\text{Si}_2\text{O}_7$, and $\text{Lu}_2\text{Si}_2\text{O}_7$.	77
Figure 5.4: Computational Raman spectra of $\text{Yb}_2\text{Si}_2\text{O}_7$, $\text{Er}_2\text{Si}_2\text{O}_7$, and $\text{Lu}_2\text{Si}_2\text{O}_7$.	77
Figure 5.5: Hot stage Raman spectra of $\text{Yb}_2\text{Si}_2\text{O}_7$ from room temperature to 1200 °C.	78
Figure 5.6: Hot stage Raman spectra of $\text{Er}_2\text{Si}_2\text{O}_7$ from room temperature to 1200 °C.	78
Figure 5.7: FTIR spectra of multiple REDS. These spectra do not have the resonance seen in Raman and are very similar across the range of rare earth cations.	80
Figure 5.8: UV-Vis data showing absorption versus energy for ytterbium and erbium disilicate as materials with direct and indirect band gaps. Additionally, reduced ranges for the direct and indirect plots are shown at the higher energies.	82
Figure 5.9: Direct and indirect band gap calculations and fit for ytterbium and erbium disilicate.	83
Figure 5.10: X-ray PDF of the small interatomic distances in ytterbium disilicate. The superscripts for the oxygen-oxygen distances are labeled to denote to which polyhedron they correspond.	85
Figure 5.11: X-ray PDF of the small interatomic distances in erbium disilicate. The superscripts for the oxygen-oxygen distances are labeled to denote to which polyhedron they correspond.	85
Figure 5.12: Neutron PDF of ytterbium disilicate from room temperature to 1000 °C before any resonance reduction.	87
Figure 5.13: Neutron PDF of ytterbium disilicate from room temperature to 1000 °C after the resonance reduction.	88
Figure 5.14: Neutron PDF of ytterbium and erbium disilicate at room temperature and at 1000 °C.	88
Figure 5.15: Monoclinic fit of room temperature neutron PDF data for ytterbium disilicate.	90
Figure 5.16: Triclinic fit of room temperature neutron PDF data for ytterbium disilicate.	91
Figure 5.17: Triclinic fits to neutron PDF data from room temperature to 1000 °C for ytterbium disilicate.	91

Figure 5.18: Monoclinic fits to neutron PDF data from room temperature to 1000 °C for erbium disilicate.	92
Figure 5.19: Comparison of neutron PDF data for ytterbium disilicate at different Q_{\max} values. Data has been offset for clarity.	92
Figure 5.20: Monoclinic fit of room temperature neutron PDF data for erbium disilicate.	93
Figure 5.21: Triclinic fit of room temperature neutron PDF data for erbium disilicate.	94
Figure 5.22: Rietveld refinements of ytterbium and erbium disilicate neutron diffraction patterns. The refinements confirm that the samples are monoclinic in the long range.	95
Figure 6.1: Experimental flowchart showing a synthesis procedure of a Yb disilicate sol-gel with the mass and volume for the nitrate and TEOS respectively.	103
Figure 6.2: XRD patterns of Yb silicate sol-gels made with varying water contents with a pH of 2. The dashed vertical lines correspond to the C 2/m $Yb_2Si_2O_7$ phase. The degree of phase purity increases as water content decreases, with 90% water content being predominantly the Yb_2SiO_5 phase.	106
Figure 6.3: XRD patterns of ytterbium disilicate sol-gels at with varying water concentrations. The pH was uncontrolled and is recorded.	106
Figure 6.4: XRD patterns of ytterbium disilicate sol-gels at pH of 10 with varying water concentrations.	107
Figure 6.5: XRD patterns of erbium disilicate sol-gels at pH of 10 with varying water concentrations.	109
Figure 6.6: XRD patterns of erbium disilicate sol-gels at pH of 2 with varying water concentrations. ...	109
Figure 6.7: XRD patterns of Sc, Lu, and Y silicate sol-gels made with 0% water added and a pH of 2. All three are predominantly the C 2/m phase but do have secondary phases indicated by black squares, stars, and circles for the monosilicates, silica, and oxide phases, respectively.	110
Figure 6.8: XRD pattern of a five component REDS. The C 2/m phase has been indexed via vertical dashed lines. The XRD pattern shows no secondary monosilicate phase and a silica peak at approximately 22° in 2-theta, marked by a star symbol.	111

Figure 6.9: Diffraction patterns of *in situ* hot-stage XRD for a Yb silicate sol-gel. A triclinic phase nucleates at 1000 °C and is eventually replaced by the *C 2/m* monosilicate phase. The triclinic phase is indexed above the 1050 °C pattern by black squares..... 113

Figure 6.10: Hot-stage XRD of Er silicate sol-gel. The vertical dashed lines correspond to the *C 2/m* phase that are seen *ex situ* and are absent in the given patterns. The predominant polymorph is the triclinic phase where the pattern for the triclinic *P 1* phase of Yb disilicate is given as a reference for general peak location in black below the plot and with black squares above the 1200 °C pattern. 114

Figure 6.11: Hot-stage XRD of a Y silicate sol-gel. The vertical dashed lines correspond to the *C 2/m* phase that is seen *ex situ* and is absent in the given patterns. The peaks corresponding to the triclinic phase have been indexed by black squares above the 1200 °C pattern. 115

Figure 6.12: Hot-stage XRD of a Sc silicate sol-gel. The vertical dashed lines correspond to the *C 2/m* phase seen *ex situ*. No triclinic or monosilicate was detected during crystallization. Instead, scandium oxide nucleates and decreases in weight fraction as temperature rises..... 115

Figure 6.13: Hot-stage XRD of a Lu silicate sol-gel. The vertical dashed lines correspond to the *C 2/m* phase that was seen in *ex situ* experiments. A monosilicate phase is visible and decreases in weight fraction as temperature increases. 116

Figure 6.14: *In situ* XRD of the multi-component REDS with the following composition: (Sc, Lu, Yb, Er, Y)₂Si₂O₇. Reference patterns for Yb disilicate polymorphs and Yb monosilicate are given below, and vertical dashed lines indicate the approximate location of *C 2/m* peaks. A star is used to mark an alumina sample holder peak..... 117

Figure 6.15: XRD patterns for Yb disilicate sol-gel derived powders heat treated at 1000 °C for 1, 3, 10, and 24 hours. The dashed vertical line indicate the peak positions of the monoclinic disilicate phase. The black squares indicates the triclinic peaks. 118

Figure 9.1: 2-D polar plots showing the change in the magnitude of CTE along crystallographic directions in the (010) plane from room temperature to 1000 °C for Lu disilicate. The color gradient represents the temperature, with blue being the lowest temperature and red being the highest. 128

Figure 9.2: 2-D polar plots showing the change in the magnitude of CTE along crystallographic directions in the (010) plane from room temperature to 1000 °C for Y disilicate. The color gradient represents the temperature, with blue being the lowest temperature and red being the highest. 129

Figure 9.3: 2-D polar plots showing the change in the magnitude of CTE along crystallographic directions in the (010) plane from room temperature to 1000 °C for Sc disilicate. The color gradient represents the temperature, with blue being the lowest temperature and red being the highest. 129

Figure 9.4: 2-D polar plots showing the change in the magnitude of CTE along crystallographic directions in the (010) plane from room temperature to 1000 °C for $(\text{Lu}_{0.5}\text{Er}_{0.5})_2\text{Si}_2\text{O}_7$. The color gradient represents the temperature, with blue being the lowest temperature and red being the highest. 130

Figure 9.5: 3D representations of the coefficient of thermal expansion (CTE) tensors for $(\text{Lu}_{0.5}\text{Er}_{0.5})_2\text{Si}_2\text{O}_7$ at different temperatures. The CTE along the y-axis becomes negative above 1000 °C. 131

Chapter 1 Introduction

1.1 Outcomes

The following is a summary of outcomes achieved in this work:

1. Rare-earth disilicates were successfully produced via sol-gel synthesis. The final phase purity of the materials was found to depend on pH and water content, and the hygroscopic nature of the rare-earth nitrate led to variance in phase purity depending on the rare-earth nitrate used.
2. The sol-gel process was scaled to include multiple rare-earth cations, and a correlation between the cations used and final phase composition was identified.
3. An average ionic radius affect was hypothesized and observed in multi-component rare-earth disilicates. The final phase of multicomponent disilicates tends to coincide with the single component rare-earth disilicate that has an ionic radius closest to the average of the mixture.
4. The temperature stability of single and multi-component rare-earth disilicates was studied using X-ray diffraction during *in situ* heating. Once crystallized, the rare earth disilicates studied were not seen to undergo phase transformations.
5. The thermal expansion 2nd rank tensors were calculated for rare-earth disilicates, illustrating anisotropic thermal expansion behavior.
6. A rare-earth cation dependent trend was observed in the thermal expansion where the directions of maximum and minimum thermal expansion changed with temperature depending on the cation in solid-solution.
7. Beamtime at Argonne National Laboratory's Advanced Photon source, beamline 11-ID-C, and Oak Ridge National Laboratory's, NOMAD, were acquired to study the mechanisms of the anisotropic CTE. Diffraction and Pair Distribution Function analysis were used to determine atomic positions and to subsequently identify polyhedral distortions and rotations.
8. Mechanisms for CTE anisotropy were identified through neutron PDF experiments. The PDF experiments found local distortions sub one unit cell dependent on RE cation. The ytterbium disilicate sample had triclinic distortions that allowed for greater degree of freedom when expanding, resulting in distinct CTE anisotropy relative to erbium disilicate.
9. A transient triclinic polymorph of ytterbium disilicate was observed to occur as the powder produced by sol-gel crystallizes. The phase crystallizes from the amorphous material and quickly converts to the expected monoclinic phase. The conversion from triclinic to monoclinic phase is irreversible and has only been reported in sol-gel derived ytterbium disilicate.

1.2 Experimental Guide

The works discussed in this dissertation are often times presented not in chronological order. Plans and experimental outlines do not take into account the constant pivots and redirections needed in research. As time progressed, to complete the work that would become my dissertation, I needed to learn new skills, change my procedures, and change my focus to overcome the setbacks and challenges throughout the process. This project began with the development of the sol-gel process for material synthesis. A procedure was needed to begin my work and begin producing samples for subsequent study. These initial failures and successes are described in **Chapter 3**, and concluded with the relatively consistent synthesis of rare-earth disilicate powders consisting primarily of the desired polymorph, with some secondary phase corresponding to a rare-earth monosilicate. These phase impure samples contained less than ten weight percent of the monosilicate secondary phases and were sufficient for the primary form of characterization, X-ray diffraction. The experiments outlined in **Chapter 4** were performed using these very same procedures where the coefficients of thermal expansion and anisotropic tensors were determined. A portion of the thermal expansion study was performed at a synchrotron facility capable of *in situ* diffraction and scattering. The scattering experiments attempted were for pair distribution function analysis, where exact knowledge of the composition is required, meaning that the phase impurity impeded further progress. The experiments discussed in **Chapters 5** and **6** were planned and commenced at roughly the same time, as the synthesis of phase pure rare-earth disilicates was important for the elucidation of the mechanisms of anisotropic thermal expansion discussed in **Chapter 5**. Commercially available powders from Praxair were used for the single rare-earth disilicate samples whenever possible in **Chapter 5**, but any multi-component samples were synthesized via sol-gel using the process outlined in **Chapter 6**. Additionally, thin films of the rare-earth disilicate were needed for UV-Vis spectroscopy experiments in order to determine the band gaps. The thin films were spin coated onto quartz slides, and the spin solution was adapted from the sol-gel process. An outline of the different sample preparation or acquisition techniques are given in **Table 1.1**.

Table 1.1: Summary of samples used in various experiments throughout this dissertation.

Chapter	Synthesis Method(s)	Details
Chapter 3	Sol-Gel	The sol-gels synthesized and discussed in Chapter 3 contained minor amounts of secondary phases.
Chapter 4	Sol-Gel	The samples used in Chapter 4 were made via sol-gel, as in Chapter 3. The quantity of secondary phase did not impede the acquisition of <i>in situ</i> X-ray diffraction in-lab and at a synchrotron facility. These samples were used to calculate the thermal expansion coefficients.
Chapter 5	Sol-Gel, Praxair powders purchased, and spin coating thin films	Chapter 5 required a number of synthesis techniques depending on the experiment. All single cation rare-earth disilicate samples were Praxair powders, while multi-component or high-entropy disilicates were synthesized via sol-gel. The only experiment that used neither of these were UV-Vis experiments that required spin coated thin films.
Chapter 6	Sol-Gel	Chapter 6 was devoted to the study of the sol-gel process and developing a procedure for consistent phase purity. Several of the experiments for Chapter 5 and 6 were performed during overlapping months, allowing for the phase pure sol-gel derived powders made in Chapter 6 to be used in the experiments discussed in Chapter 5.

Chapter 2 Literature Review

2.1 Environmental Barrier Coatings

2.1.1 Current Nickel Superalloy Technology

Gas-turbine engines are the staple in commercial and military aircraft propulsions, annually generating approximately US\$39 billion globally in aircraft orders, and several hundreds of thousands of new engines are projected to be sold through 2028 worth US\$1.07 trillion.^{1,2} Additionally, land-based gas-turbine engines generated ~20% of the world’s electricity in 2015.¹ While ubiquitous, the technology can still be improved and made more efficient as energy demands surge worldwide. As of 2021, the transportation industry in the United States of America consumed 26.9 quadrillion BTUs (approximately 28.4×10^{18} Joules). As shown in **Figure 2.1**, out of the 26.9 quadrillion BTUs, 21.2 quadrillion went to rejected energy, meaning that the majority of energy went to waste and that the process is only about 21% efficient.³

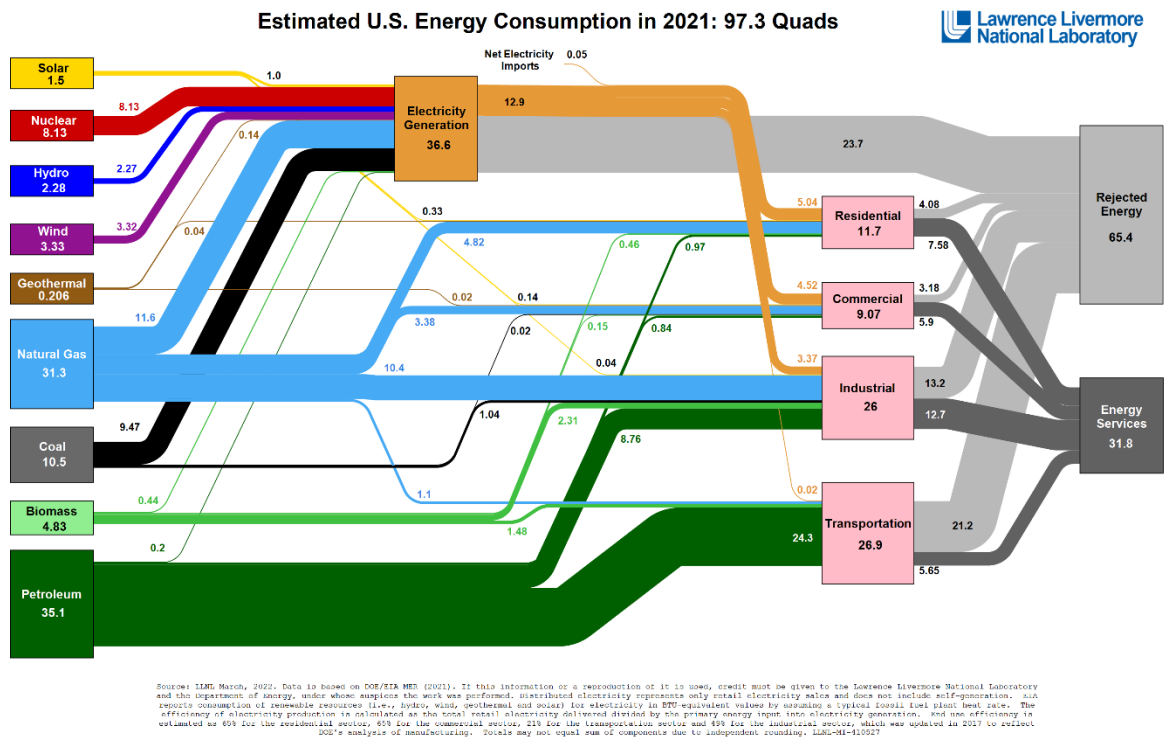


Figure 2.1: A flowchart illustrating the energy consumption of the United States of America in 2021. The "Transportation" box is applicable in the scope of this work given the difficulty in scaling aerospace to electric. The units are in Quads, which are equivalent to a quadrillion BTU.³

An ever-increasing demand for more efficient aircraft and spacecraft engines pushes the gas-turbine engine materials to greater extremes. An elevated operating temperature will improve the engine’s fuel

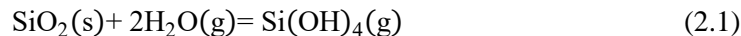
efficiency, as dictated by the Brayton cycle.⁴⁻⁶ The drive to increase operating temperatures of engines makes the environment more hostile, not only due to the elevated temperatures but also the faster operating speeds, higher stresses, and greater likelihood of deleterious reactions occurring.⁴ The current convention of nickel-base superalloys falls short due to lower temperature limit. This limit can be improved upon through the application of thermal and environmental barrier coatings (T/EBCs).⁴ Despite these improvements, the current uppermost limit for nickel-base superalloy technology in the field is a gas temperature at approximately 1500 °C, and the material suffers from potential spallation or erosion when subjected to the upper limits of its operation.^{4,5} Research into a replacement for the nickel-base superalloys has been ongoing for decades and one such viable replacement is ceramic matrix composites (CMCs).^{4,5,7-}

11

2.1.2 Ceramic Matrix Composites

The use of CMCs in commercial aircraft began in 2016 with the implementation of SiC/SiC turbine shrouds and blades.¹² Since then, the use of SiC CMCs has expanded in use cases to combustion liners, vanes, and flaps.¹³ Ceramic components can exhibit improved high temperature strength that are more resistant to high temperature oxidation and creep, as well as being lighter when compared to nickel-base superalloys.^{4,5,7,13} Typically, the SiC based CMCs are made of a SiC matrix reinforced with SiC fibers.⁴ The processing route of the CMC is as follows: the SiC fibers are coated with SiC via chemical vapor deposition (CVD), then the matrix is formed through a variety of different methods such as chemical vapor infiltration (CVI), particle slurry infiltration, repeated precursor infiltration and pyrolysis (PIP), and reactive melt infiltration (RMI).^{12,14} The RMI method is one of the most common methods of creating the SiC CMCs.

One issue with SiC based CMC technology is that SiC reacts in the presence of water vapor to form a silica scale that then can form a gaseous silicon hydroxide species.^{15,16} The reaction shown in **Equation 2.1** results in unacceptable recession rates that can lead to catastrophic failure of CMC components.



Protection is needed to maintain the integrity of the SiC components throughout their lifetime in these extreme conditions. A T/EBC can be used to mitigate environmental damage and improve performance.^{8,10,11,17-19} Currently, there are three generations of T/EBCs used in this application: mullite (Al₂O₃•SiO₂ mixture), BSAS (BaO•SrO•Al₂O₃•SiO₂ mixture), and rare-earth silicates (RE₂Si₂O₇ and RE₂SiO₅, where RE represents a rare-earth cation).⁸⁻¹⁰ Mullite was applied via plasma spray as an amorphous coating; subsequently suffering from shrinkage during crystallization as well as high amounts of SiO₂ loss. The shrinkage can lead to cracking and delamination of the coating necessitating a good match between the coefficients of thermal expansion (CTE) of the T/EBC and CMC.⁵ The issue of cracking was

improved upon in the subsequent generation that utilized BSAS. The cracking resistance increased when a Si bond coat was implemented that further enhanced T/EBC performance.¹⁷⁻¹⁹ The presence of a Si-based bond coat provides improved adhesion and durability, properties that have been continually engineered and enhanced in subsequent generations of T/EBCs through the addition of compounds like hafnia (HfO_2) to allow the system to have higher temperature capabilities.^{18,19} The second generation of T/EBCs saw use in gas-turbine engines, but experienced durability issues at elevated temperatures. These issues cut the lifetime of BSAS coatings, leading to the third generation of T/EBCs to be developed.⁸

The third and current generation of T/EBCs has transitioned to rare-earth silicates. The rare-earth silicates were identified as promising T/EBC candidates due to the following factors: some polymorphs have a low CTE mismatch with CMCs, they have high melting temperatures, and low silicon activity relative to pure silicon oxide.^{5,8,10,11,13} The scope of this work lies specifically in the rare-earth disilicates (REDS). REDSs have the chemical formula of $\text{RE}_2\text{Si}_2\text{O}_7$. The rare earths comprise the lanthanide series of elements (lanthanum through lutetium) as well as scandium and yttrium. Furthermore, REDSs can possess multiple rare-earth cations to eventually result in a multi-component or high entropy (HE) ceramic. HE REDS are discussed in detail in **Chapter 3**. REDSs in use are typically applied through a thermal plasma spray process onto the SiC CMC or a silicon bond coat.^{5,18,20} This technique utilizes a high temperature plasma jet that melts ceramic powder that was inserted through a powder feed. The molten ceramic is propelled towards the target where it then solidifies to produce a coating.²⁰

2.1.3 Barrier Coating Considerations

At the base level, an ideal T/EBC has high phase stability, low steam reactivity, low calcium-magnesium alumino-silicate (CMAS) reactivity, low bond coat oxidation, and low thermal stresses. These are not the only factors that go into designing a T/EBC; thermal conductivity and cost also contribute to design depending on application. Breaking down the criteria for T/EBCs further, phase stability means that the REDS does not undergo phase transitions upon heating or cooling through the lifetime of the coating. Steam and CMAS are two of the biggest sources of deleterious reactions that lead to failure of the coating.²¹⁻²³ CMAS will only be alluded to sparingly, this work was funded under the scope of looking predominantly at steam, but substantial interactions between REDS and CMAS are present in the literature.^{24,25} The goal of a T/EBC is also to mitigate the oxidation of the bond coat to continue allowing for the bond coat's contribution to durability of the components. Finally, thermal stresses are pivotal to not only T/EBCs but a large part of this work. Many of the T/EBCs are plasma sprayed deposited, producing an amorphous coating that then crystallizes upon heating. Once crystallized the CTE of the REDS must match the underlying bond coat and CMC or risk delamination due to stress. The CTE of CMCs is in the range of

$4.5\text{-}5.5 \times 10^{-6} \text{ } ^\circ\text{C}^{-1}$, meaning that any coating should have a CTE as close as possible compared to the value just given or risk spallation or other failure modes.^{5,8,26}

There are many polymorphs of REDS that each have varying CTE values. A polymorph that is a great candidate using the CTE criteria is the monoclinic $C 2/m$ phase (often referred to as the β or Type C phase). Work by Felsche in 1970 showed that the final phase is dependent on the rare-earth cation's ionic radius. **Figure 2.2** and **Figure 2.3** show the diagram directly from Felsche's work and an adapted diagram that includes more details regarding the ionic radii of the cations, respectively.^{27,28} Additionally, the Type C phase is appealing for T/EBC applications due to not having other polymorphs at lower or higher temperatures, meaning there is no phase instability upon heating or cooling, according to the diagram.

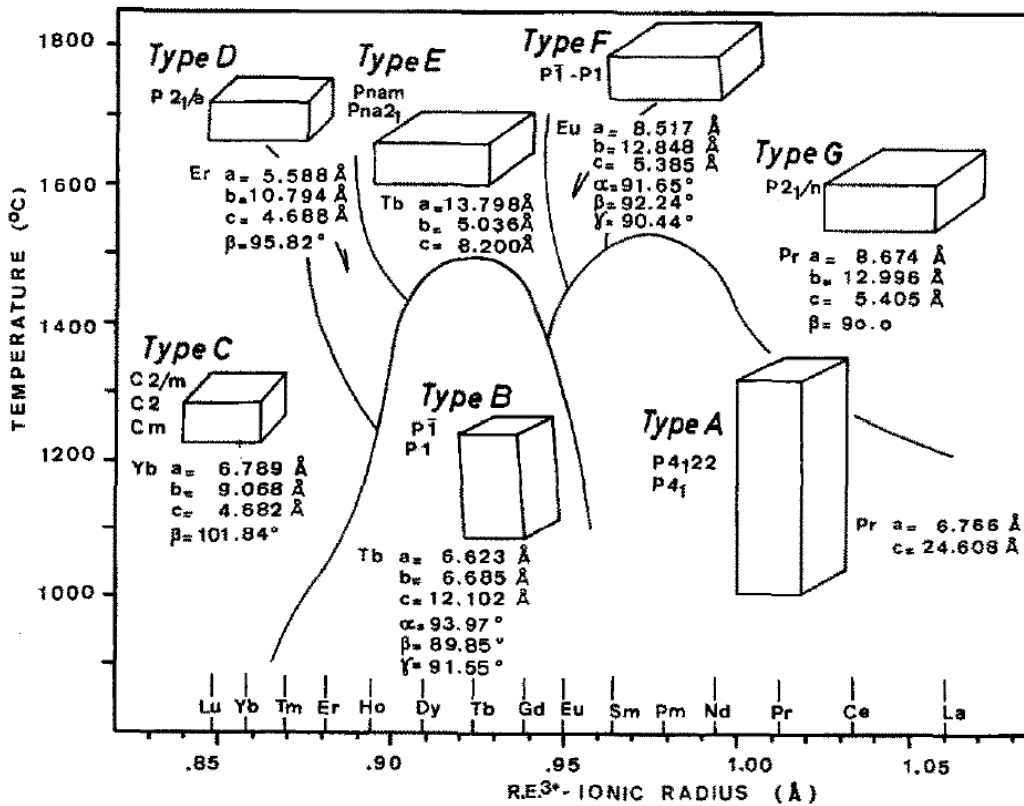


Figure 2.2: A diagram created by Felsche illustrating the relationship between ionic radius of the rare-earth cations, temperature, and the resulting phase. The monoclinic Type C phase is the candidate for T/EBC applications due to close CTE match.²⁷

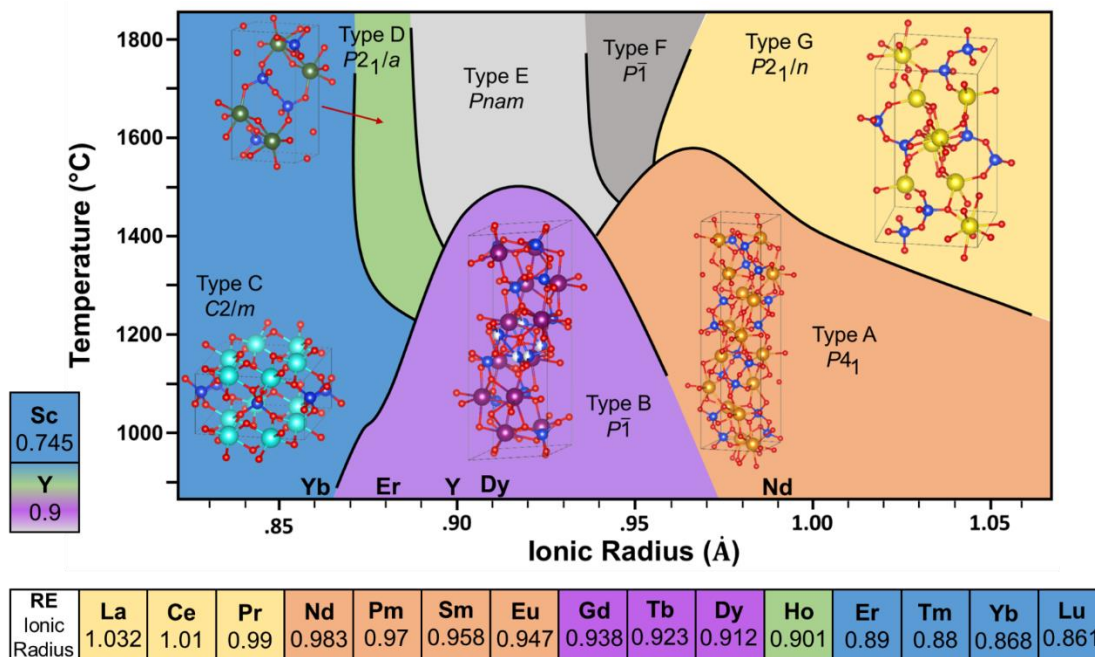


Figure 2.3: An adapted diagram from Felsche that includes the ionic radii of all RE cations with a coordination number of 6. Not all RE cations have a 6-fold coordination for the other polymorphs. The RE cations that form the desired Type C phase are Er, Tm, Yb, Lu, Y, and Sc.²⁷

2.1.4 Phase Diagrams

A phase diagram is a helpful tool for understanding and visualizing thermodynamic stability of equilibrium phases. Phase diagrams for the many different REDS give melting temperatures, stoichiometric ratios for the synthesis of line compounds, and phase transition temperatures. The phase diagrams available for the REDS pertinent to this work had the lowest temperature limited to around 1400 °C.²⁹⁻³¹ The only exception being the Nd₂O₃-SiO₂ phase diagram that provided data to approximately 850 °C. The issue with this is that in application, the phase transitions and stability of REDSs are pivotal to constant thermomechanical stability in a T/EBC. **Figures 2.4-2.10** all illustrate the adapted version of phase diagrams for REDSs containing different RE cations, and while the phase diagrams are quite similar, there are differences in melting temperatures and phases present for each diagram.

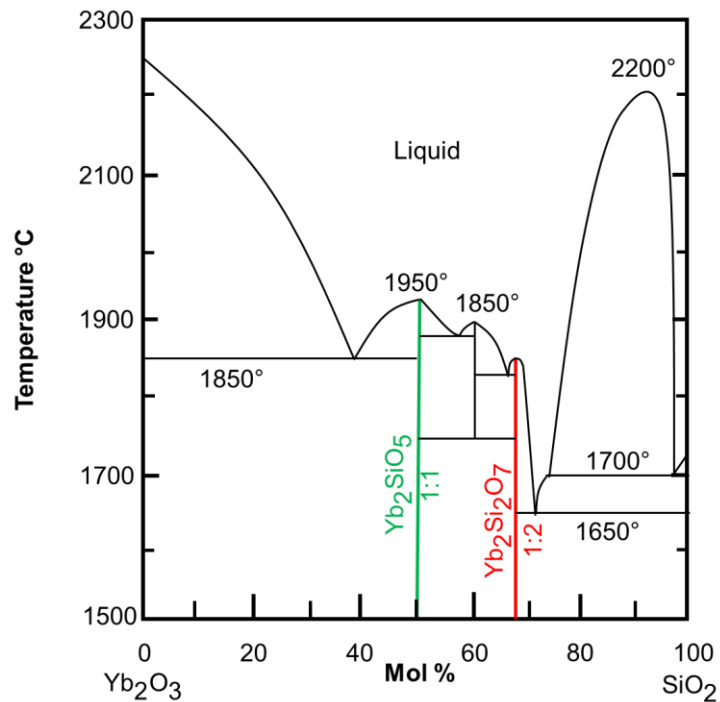


Figure 2.4: An adapted phase diagram of ytterbium oxide and silica from Toropov and Bondar. The colored lines correspond to the mono- and disilicate line compounds.²⁹

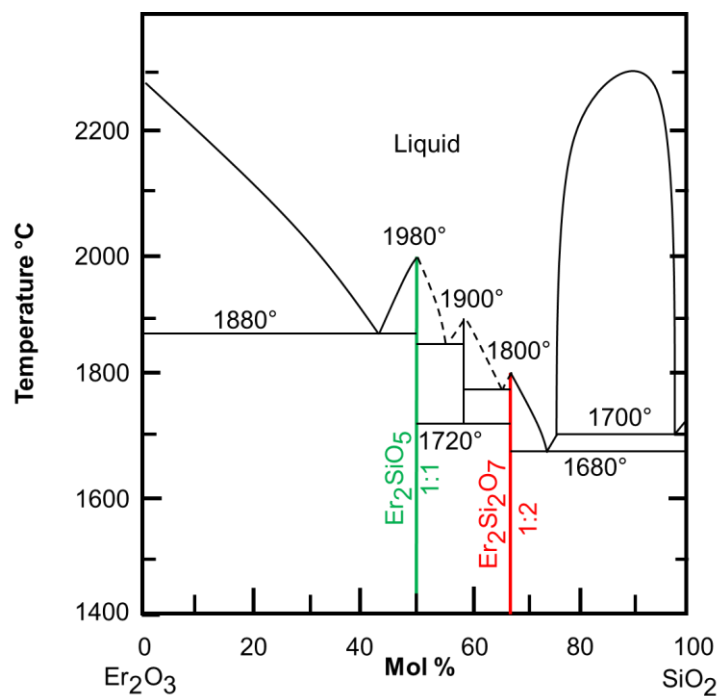


Figure 2.5: An adapted phase diagram of erbium oxide and silica from Toropov and Bondar. The colored lines correspond to the mono- and disilicate line compounds.²⁹

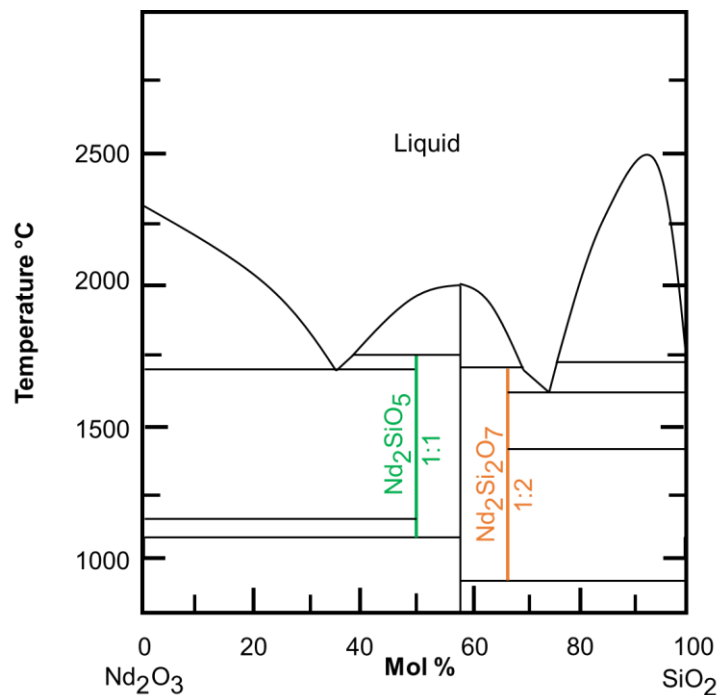


Figure 2.6: An adapted phase diagram of neodymium oxide and silica from Toropov and Bondar. The colored lines correspond to the mono- and disilicate line compounds.²⁹

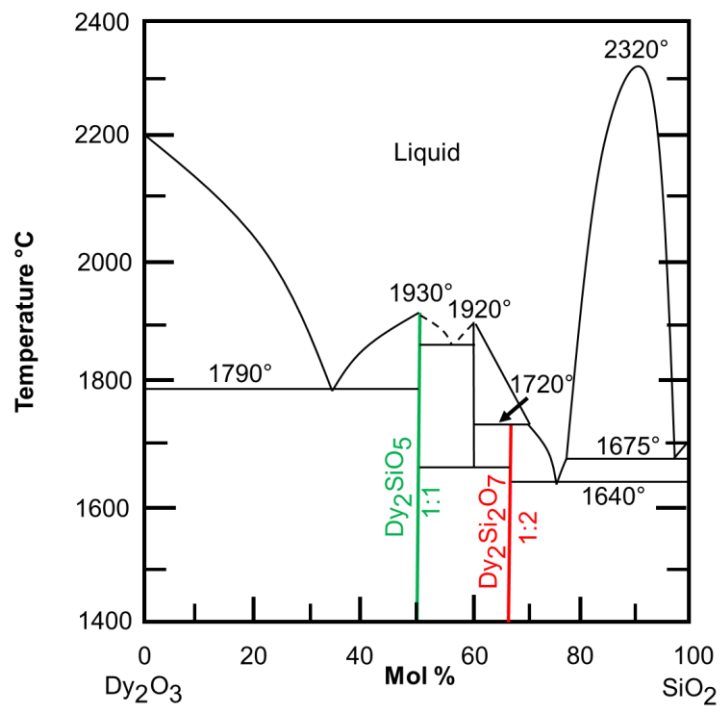


Figure 2.7: An adapted phase diagram of dysprosium oxide and silica from Toropov and Bondar. The colored lines correspond to the mono- and disilicate line compounds.²⁹

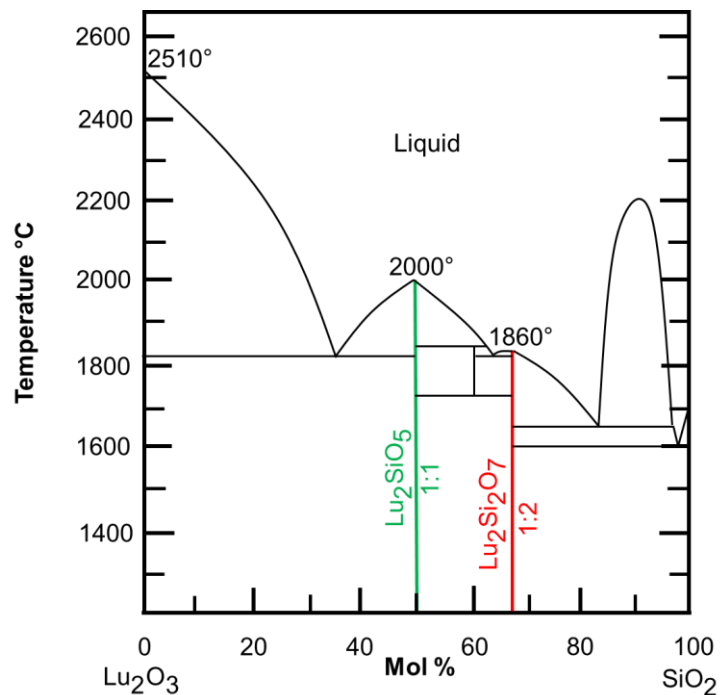


Figure 2.8: An adapted phase diagram of lutetium oxide and silica from Toropov and Bondar. The colored lines correspond to the mono- and disilicate line compounds.³⁰

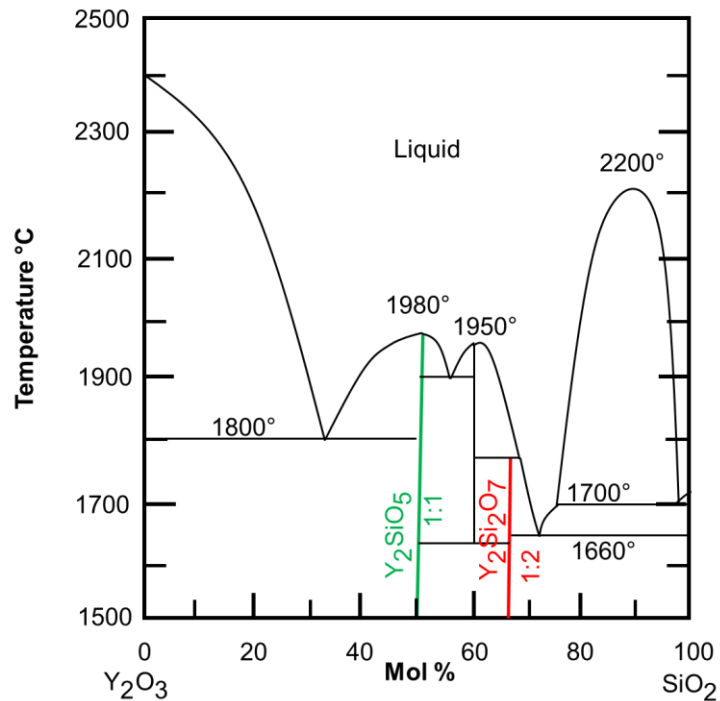


Figure 2.9: An adapted phase diagram of yttrium oxide and silica from Toropov and Bondar. The colored lines correspond to the mono- and disilicate line compounds.³⁰

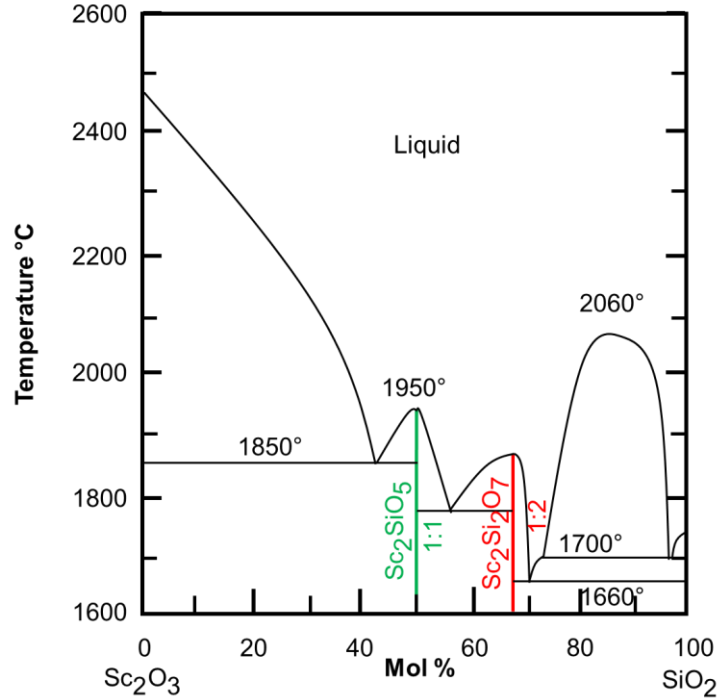


Figure 2.10: An adapted phase diagram of scandium oxide and silica from Toropov and Bondar. The colored lines correspond to the mono- and disilicate line compounds.³⁰

Work done by Zhao *et al.* has shown the presence of a lower temperature phase predicted by the curve seen in Felsche’s diagram, **Figure 2.2**.^{27,32} This lower temperature, transitional phase, is triclinic and corresponds with the Type B phase. Given this information, more work is required to model the phase behavior through the entire application range instead of just a high temperature window.

2.1.5 Thermal Expansion Tensor

The thermal expansion data typically presented for REDS comes in the form of linear CTE values. These values can be acquired through dilatometry or XRD experiments.^{33–35} While a single linear CTE value is useful when comparing or quickly describing thermal expansion, it is not an adequate representation of CTE in low symmetry crystals. As was mentioned before, the disilicate phase of interest in this work is monoclinic, and therefore requires a more complex descriptor of anisotropy than a single term to completely describe the thermal expansion. To accomplish this, a tensor can be used. Thermal expansion is a second-rank symmetric tensor with nine coefficients. The symmetry elements that make up the space group allow for a portion of the nine coefficients to be simplified into the tensor for a monoclinic crystal shown in **Equation 2.2**.

$$\begin{bmatrix} \alpha_{11} & 0 & \alpha_{13} \\ 0 & \alpha_{22} & 0 \\ \alpha_{13} & 0 & \alpha_{33} \end{bmatrix} \quad (2.2)$$

The two non-zero shear coefficient (α_{13} and α_{31}) terms are equivalent due to the mirror plane present in the $C2/m$ structure, while the normal components (α_{11} , α_{22} , and α_{33}) are all distinct by definition of a monoclinic crystal's lattice parameters being distinct from each other ($a \neq b \neq c$).³⁶ The normal tensor coefficients are orthogonal to each other and can be referred to as the principal axes only when the conditions in **Equation 2.3** are met.

$$S_1x_1^2 + S_2x_2^2 + S_3x_3^2 = 1 \quad (2.3)$$

In **Equation 2.3**, S and x correspond to the normal tensor coefficients and physical dimensions of the crystal, respectively. In the case of a monoclinic crystal, **Equation 2.3** is satisfied when S_2 is parallel to the y diad axis.³⁷ The use of these tensors is much less common than the linear CTE approach. While a tensor can be more abstract or complex than a single value, it has the power to enable 2D and 3D representations of properties and aid in understanding the thermal stresses that develop in real microstructures. The derivation of tensors via computer software is expanded in **Chapter 4**.

2.2 High-Entropy Ceramics

2.2.1 Entropic Contribution to Free Energy

Stability in extreme conditions is the fundamental problem these materials are attempting to solve. The thermomechanical stability is not just contingent on the CTE mismatch, but also the thermodynamic contributions to stability. Conventionally, thermodynamic stability is driven by negative enthalpy, but entropy plays a larger role as temperature increases. This relationship between temperature and entropy is shown in **Equation 2.4**, where stability is indicated by an increasingly negative Gibbs free energy, ΔG .

$$\Delta G = \Delta H - T\Delta S \quad (2.4)$$

Entropy can be calculated using **Equation 2.5**, Boltzmann's equation, where k_B is Boltzmann's constant equal to 1.38×10^{-23} J/K, and Ω is the number of microstates. In simplified terms, the configurational entropy can be increased through the addition of more and more distinct atoms.

$$S = k_B \ln \Omega \quad (2.5)$$

This concept is the motivation for high entropy alloys (HEA) and high entropy ceramics (HEC).³⁸⁻⁴⁰ Seminal work on HE materials started in the metallurgical spaces of materials science, reviewed by Miracle and Senkov, defining much of the fundamental criteria for what constitutes a HE material.³⁹ The space was further explored by Rost *et al.* by researching HE and entropy stabilized oxides, leading to the possibility of applying such techniques to the materials in this work.³⁸ REDS can achieve this by including additional rare earth cations. Once the equimolar solution reaches five distinct atoms, any additional atoms produce

negligible returns in reducing thermal conductivity or altering other properties, so a minimum of five constitutes an HEA.^{38,39}

Creating a high entropy REDS requires consideration of the effects of cation size on phase stability. As shown in **Figures 2.2** and **2.3**, REDS with larger cation ionic radii than erbium or ytterbium will form other polymorphs, such as the triclinic phase for dysprosium and gadolinium disilicate, or the tetragonal phase for neodymium disilicate. Work to make mixed component (2 or more cations, but less than five) and HE REDS typically follows a rule of mixtures to produce a final single phase.^{22,35,41,42} Following a rule of mixtures is hypothesized in this work to allow for the prediction of the final phase, and is covered in more detail in **Chapter 4**. The few cations that can form the $C 2/m$ phase as single cation REDSs are scandium, yttrium, lutetium, ytterbium, thulium, and erbium. Thulium will not be considered and not used in this work given its extreme rarity and prohibitive cost. The reason that HE REDS are not only made with the 5 previously mentioned lanthanides that readily form the $C 2/m$ phase is because REDS properties can change depending on the RE present. Therefore, there is value in stabilizing other cations into the $C 2/m$ phase be able to tailor material properties in REDS.^{22,22,35}

2.2.2 Improvements to Thermal Conductivity

The inclusion of multiple cations, like in an HEC, helps lower thermal conductivity, which is desired in T/EBCs. The addition of multiple cations will result in a distorted lattice and create local ion mass variations. This causes a reduction in phonon mean free path, which in turn leads to a lower thermal conductivity. This effect is described by Matthiessen's rule given in **Equation 2.6**, where the total resistivity, ρ , comprises other terms that represent electron scattering, thermal vibrations, impurities, and deformation-based effects.

$$\rho_{\text{total}} = \rho_{\text{thermal}} + \rho_{\text{impurity}} + \rho_{\text{deformation}} \quad (2.6)$$

2.3 Synthesis of Rare-Earth Disilicates

2.3.1 Sol-Gel Method

The sol-gel method is a long-existing technique used for processing inorganic materials. An advantage of the technique is high chemical homogeneity and the possibility to synthesize novel ceramic oxide compositions.⁴³⁻⁴⁶ The first sol-gels investigated were derived from tetraethyl orthosilicate (TEOS) to yield SiO_2 in the mid-1800s.^{47,48} A century later, Iler pioneered silica chemistry to produce colloidal silica powders.⁴⁹ Subsequently, Stober extended Iler's work to demonstrate the use of ammonia to control particle size and morphology by serving as a catalyst in the hydrolysis process.⁵⁰ The findings resulted in the so-

called Stober process that correlates the final size of silica powder to the concentration of water and ammonia, the type of silicon precursor, the alcohol used in the mixture, and reaction temperature.

An overview of the sol-gel process was provided by Hench and West⁴³, listing seven steps that are used for silica gels. The work by Brinker and Scherer⁵¹ provides additional detail as to the mechanisms that govern these steps. Pure SiO₂ sol-gel methods are the foundation for making REDS. Complexity is added by introducing rare earths, but many of the underlying processes are identical. Namely, the mixing and densification processes were the predominant focus of study to determine conditions that enable phase-pure REDS powders. The processing steps for the sol-gel process are as follows:

1. *Mixing*: Where the hydrolysis reactions occur, the silica tetrahedral bonds form, and the size of the sol particle can be controlled.
2. *Casting*: If desired, the sol can be cast into a mold due to the low viscosity of its current state.
3. *Gelation*: The colloidal particles and condensed species begin to link together, forming a three-dimensional network. Viscosity rises sharply with time and the sol can be pulled into fibers or used for spin coating as this step occurs.
4. *Aging*: This step is called syneresis. The thickness of interparticle necks increase and the porosity decreases, increasing the strength of the gel.
5. *Drying*: Liquid is removed from the interconnected pore network. If the gel is dried at ambient pressures, it is referred to as a xerogel or alcogel depending on if the gel is derived from a non-pure or pure alcohol solution, respectively. If the gel is hypercritically dried, an aerogel is produced.
6. *Dehydration*: Surface groups (such as silanol, Si-OH, bonds) are removed from the pore network, resulting in improved chemical stability of the xerogel. This typically occurs in the 500-800 °C range to desorb hydroxyl groups that are chemisorbed onto the surface of the pores.
7. *Densification*: Pores are eliminated and the density increases. The temperature at which this step occurs depends on the morphology of the network, but typically is greater than 1000 °C.

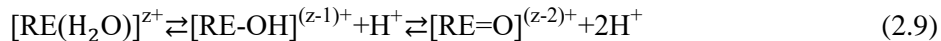
The production of silica via sol-gel is well documented, but the challenge lies in the addition of rare earths to produce single component, compositionally complex, or HE solid solutions desired. There are several examples of REDS being made via the sol-gel method, resulting in varying final products.^{35,52-58} Typically, a rare-earth nitrate and tetraethyl orthosilicate (TEOS) are used as a precursors and are dissolved in an alcohol-containing solution at different pH levels. The base of choice is typically ammonium hydroxide, while synthesis procedures that use acids have a variety of acids such as HCl and HNO₃.

Additionally, some procedures varied the ratio of RE:Si atoms by changing the concentration of TEOS. As illustrated by the phase diagrams shown previously in **Figures 2.4-2.10**, this can result in different phase mixtures. This was done to increase phase purity, as the samples with silica excess appeared phase pure in XRD. The issue with this change is that the presence of excess silica leads to a lower melting temperature eutectic that is deleterious for T/EBC properties. In short, the 1:1 ratio of silicon and rare-earth cations must be preserved. To accomplish this, the reaction of TEOS into silica must be understood in the presence of rare earth nitrates.

TEOS is a metal alkoxide, which typically reacts readily with water. This reaction is known as hydrolysis since a hydroxyl ion becomes attached to the metal atom.^{44,51} The reactions for partial and complete hydrolysis of TEOS are shown in **Equations 2.7** and **2.8** respectively.



In these reactions, *R* represents an ethyl group. Understanding the reactions that occur during the REDS sol-gel process can allow for tailoring weight fractions of the various phases of rare-earth silicates or producing a phase pure REDS. The rare earth nitrates are less well known in sol-gel, meaning the exact hydrolysis mechanics are not as readily available as they are for TEOS. The general equation for RE hydrolysis is given in **Equation 2.9**:



The hydrolysis reaction can be divided to produce three distinct ligands, an aquo (RE = H₂O), hydroxo (RE = OH), and an oxo (RE = O) ligand. In the case of REDSs, the oxo ligand is desired to produce a three-dimensional network of RE cation, oxygen, and silicon. The ligands formed in hydrolysis are dictated by the pH of the solution. Typically, higher pH values increase the formation of the oxoligands.^{44,51}

2.3.2 Phase Purity

The resulting powders vary in phase purity from a single-phase disilicate to a phase mixture containing the monosilicate phase (e.g. RE₂SiO₅) where the residual SiO₂ may be present as tertiary amorphous phase. Several prior works understated the presence of the secondary phase due to the extremely low intensity of peaks in X-ray diffraction analysis, while others attempted to remove the secondary phase by adding a surplus of TEOS to react out any silica-deficient monosilicate phase. The presence of excess silica is deleterious to the performance of a T/EBC, however, given that silica has a melting point several

hundred degrees lower than the REDS and a high reactivity with water vapor in combustion environments, requiring its removal before use.²⁹

2.4 Techniques

2.4.1 In-Lab X-Ray Diffraction

X-Ray diffraction (XRD) operates by generating X-rays that are incident on a sample where they diffract. The X-rays source or tube generates X-rays using an electron ejected from a tungsten filament to impact a metal target (typically copper), ejecting an electron off the metal, and generating a characteristic X-ray photon as electrons fall from high energy to low energy orbitals to fill the void. The characteristic X-rays are typically copper K_α and K_β X-rays, where the K_β is filtered out by a nickel K_β filter. The diffracted X-rays are then collected by a position-sensitive detector that is then translated to the data analyzed to determine information such as lattice parameters. Diffraction can be simplistically modeled by Bragg's law, given in **Equation 2.10**, where incident X-rays at an angle θ are diffracted by the atomic planes with a given d -spacing.^{59,60} The wavelength, λ , for copper K_α X-rays is approximately 1.54 Å, and n is an integer value (1, 2, 3...) representing the order of the reflection. A value of 1 is typically all that is needed in in-lab experiments. This results in a diffraction pattern with peaks at positions determined by the d -spacing of diffracted crystallographic planes.

$$2d\sin\theta=n\lambda \quad (2.10)$$

In-lab XRD was used to characterize phases in REDS powders. The in-lab XRD instrument predominantly used was the Panalytical Empyrean X-ray diffractometer (Cu K_α X-ray wavelength of 1.54 Å) and GaliPIX3D detector. The Empyrean can perform *in situ* heating and measurements using an Anton Parr HTK1200N hot stage. The hot stage was implemented for characterization of lattice parameters and thermal expansion. The second in-lab diffractometer used was a Panalytical X'pert X-ray diffractometer (Cu K_α X-ray wavelength of 1.54 Å) with an X'celerator detector.

2.4.2 Synchrotron Experiments

A synchrotron X-ray source is different from in-lab instruments for a variety of reasons. In a synchrotron, a hot cathode produces electrons and packs them into pulses. The electrons travel at relativistic speeds, >99.999999% of the speed of light, around a storage ring. Magnets in the storage ring change the electron travel direction, causing the electrons to follow the curved path. The acceleration of the electrons as they change directions emits X-rays tangential to the ring. These tangential beams of X-rays are typically then used by individual beamlines that possess optics and instrumentation that allow for unique measurements conditions for diffraction, scattering, spectroscopy, and microscopy techniques.

Hot-stage XRD experiments were conducted at beamline 11-ID-C at the Advanced Photon Source at Argonne National Laboratory. This beamline was selected for several reasons: sector 11 specializes in pair distribution functions, beamline 11-ID-C has very high throughput powder diffraction capabilities, and the beamline specializes in *in situ* work required for hot-stage experiments. Transmission XRD experiments were performed on REDS powders inside of a 1 mm diameter fused quartz capillary with an X-ray energy of 105.7 keV, which corresponds to a wavelength of 0.1173 Å. The sample holder set-up is shown in **Figure 2.11**. A 2-D detector was used to capture the Debye-Scherrer rings generated from the transmission experiment.

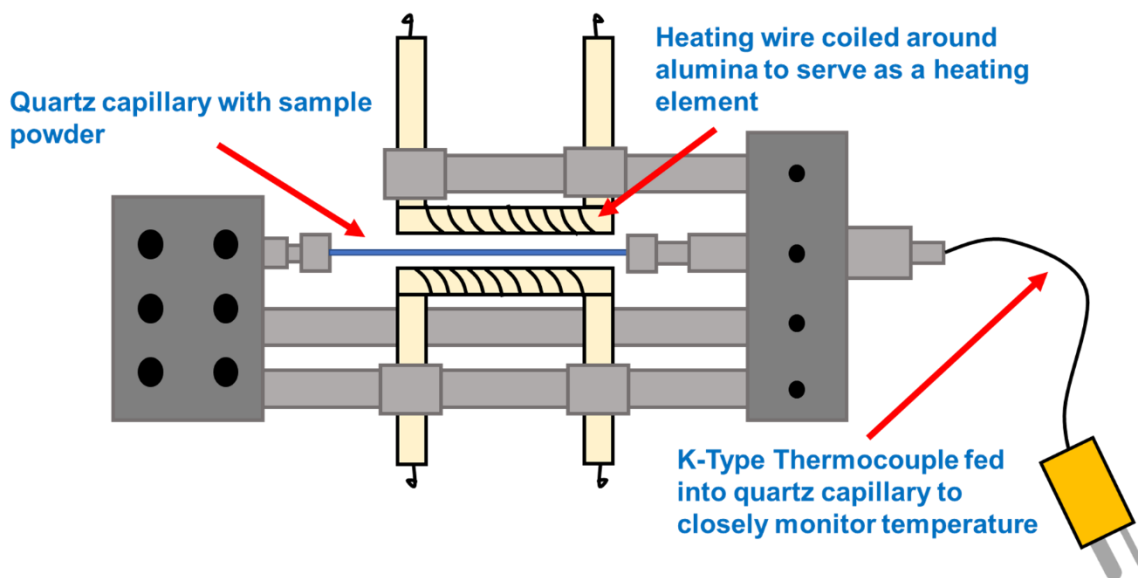


Figure 2.11: A diagram depicting the experimental setup at Beamline 11-ID-C for performing *in situ* heating diffraction and scattering experiments.

2.4.3 Pair Distribution Function Analysis

Pair distribution function (PDF) analysis operates by collecting scattering intensity as a function of Q , known as $I(Q)$ where Q is the 2-theta value normalized by the X-ray wavelength. Then a correction is applied to $I(Q)$ for the scattering power of atoms to acquire the total structure factor, known as $S(Q)$. Sample composition is needed to correctly apply the corrections. A Fourier transform is then applied to the total structure factor to determine the probability of finding an atom at a distance r . $G(r)$ is related to this probability and can give information regarding atomic distances, coordination number, disorder, and particle size. PDF analysis is typically presented in $G(r)$. Structural information is not limited to crystalline materials since the underlying principle in PDF is scattering, rather than constructive interference. This allows for PDF to be a powerful tool in investigating nanoscale, amorphous, and disordered materials. PDF can allow for resolving the structural behavior of REDS upon heating. More specifically PDF can lead to

insights regarding the evolution of bond lengths and polyhedral volumes as a function of temperature and rare earth cations.

In synchrotron X-ray experiments, PDF data collection was done separately from the powder diffraction measurements. The same sample configuration was used, except the detector distance was much shorter for the PDF measurements to capture higher angle Debye-Scherrer rings. The sample-to-detector distance for the diffraction experiments was 1700 mm, while the distance for the PDF experiments was 600 mm. In neutron scattering experiments, diffraction and PDF data were captured simultaneously.

2.4.4 Neutron Source Experiments

Experiments were performed at the Nanoscale-Ordered Materials Diffractometer (NOMAD) at the Spallation Neutron Source (SNS) at Oak Ridge National Laboratory. Neutrons are generated through spallation, which begins with an ion source that generates negative hydrogen (H^-) ions. The negative hydrogen ions are then accelerated to an energy of 2.5 million electron volts (MeV) and form a pulsed beam. The pulsed beam is then delivered to a large linear accelerator (linac). The linac accelerates the negative hydrogen further to 1000 MeV or 1 GeV. The linac contains conducting and superconducting radio-frequency cavities that accelerate the beam. The cavities are cooled with liquid helium, operating at a temperature of 2 K. The beam is then bunched and intensified in an accumulator ring. In the accumulator ring, the negative hydrogen has the electrons stripped by a diamond stripper foil, producing protons. The protons are then delivered to a steel target filled with 50 tons of swirling liquid mercury. The impact of the protons into the mercury atoms results in the spallation process and releases neutrons. The neutrons are slowed by passing them through cells filled with water or containers of liquid hydrogen at 20 K.

The diffraction patterns of neutrons and X-rays look remarkably similar, with the only differences being due to X-rays having greater interaction with heavy elements while neutrons interact more with lighter elements. This is due to X-ray interactions occurring with the electron clouds, so as there are more electrons, the more likely the X-rays are to scatter. Neutrons interact with the nucleus, and their scattering is based off the energy change pre and post scattering event. In the case of heavier atoms, the energy of the neutrons before and after scattering events are similar, unlike for lighter elements. **Figures 2.12** shows the differences between neutron and X-ray PDF for a REDS, where the higher intensity peaks for neutrons correspond to RE-O or Si-O distances. The higher intensity X-ray peaks belong to the RE-RE distances due to the high atomic number of RE cations scattering X-rays more than neutrons as mentioned earlier.

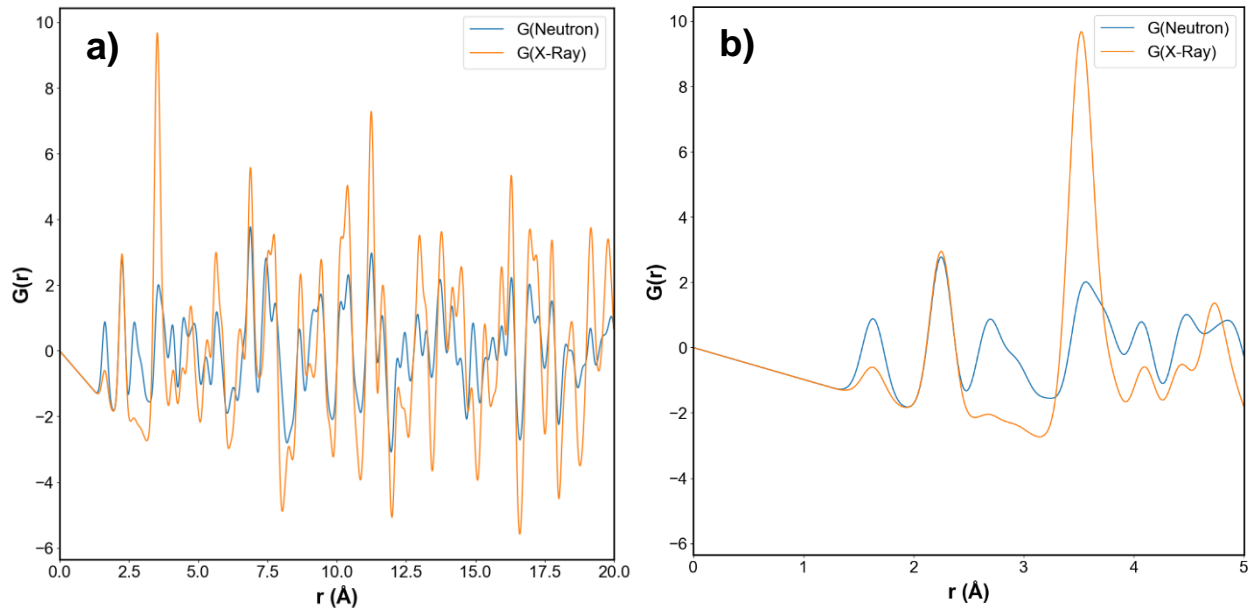


Figure 2.12: PDF comparison of X-ray and neutrons for erbium disilicate. The differences in probabilities correspond to detection differences in the oxygen and silicon environments. Figure a) is a comparison of the two functions through the entire r range. Figure b) is zoomed in to lower r range that would correspond to the Si-O and RE-O atomic distances corresponding to the first and second peaks respectively.

2.4.5 Rietveld Refinement

Rietveld refinement is a profile fitting method applied to X-ray and neutron diffraction patterns first proposed by H. M. Rietveld.⁶¹ This method fits peak shapes and is able to extract information such as lattice parameters, crystallite size, microstrain, weight fraction, and atomic positions. There are several different software packages capable of performing Rietveld refinement, the one used exclusively in this thesis is GSAS-II.⁶² GSAS-II was developed at Argonne National Laboratory. Lattice parameters were extracted from diffraction data using *.CIF files as standards that were found on the Inorganic Crystal Structures Database (ICSD). Standards such as LaB_6 and CeO_2 were used to determine instrument parameters to reduce error in final refined parameters. A general procedure is given in the appendix, **Chapter 9**.

A typical sign of a good fit is a low residual weight percent (Rw%). It is a standard that the closer to zero, the better the fit, but typically below 20% is good while 10% and lower is representative of publication quality. One of the most important ways to determine the quality of the fit is by visually inspecting the fit, especially at high angle peaks. Additionally, the final refined parameters should be within reasonable ranges, such as crystallite size not being above the expected grain or particle size of the material. Variable covariance is also an important factor to consider as changing or refining one may alter another

drastically. One such case of this is crystallite size and microstrain corresponding to peak broadening and shape.

2.4.6 CTEAS

Once lattice parameters were extracted in GSAS-II, the data was processed in a software app called CTEAS.⁶³ CTEAS is a graphical user interface that allows for the determination of thermal expansion tensors from XRD data. CTEAS allows for the creation and animation of three-dimensional thermal expansion quadrics, creation of two-dimensional sections of quadrics, and eigenvalue calculations. The data acquired from in-lab and synchrotron experiments was analyzed and represented using CTEAS, showing anisotropy.

CTEAS takes *hkl* listings, *d*-spacings, and lattice constants and uses them to calculate a conversion matrix between Cartesian and crystallographic coordinate systems, and thermal expansion tensor elements. The convention for the direction of the axes follows guidelines according to IEEE recommendations outlined by Newnham.^{63,64} Linear thermal expansion can be expressed by **Equation 2.11**:

$$\alpha = \frac{1}{l} \frac{\delta l}{\delta T} \quad (2.11)$$

In **Equation 8**, α is the linear thermal expansion coefficient, l is the length, and T is temperature. This is extended to a second rank tensor through the change in *d*-spacings for each *hkl*, that is then stored in memory, sorted, and arranged. Then a varying-order polynomial in powers of temperature is used to fit thermal expansion coefficients,⁶⁵ as shown in **Equation 2.12**:

$$\alpha_{hkl} = \frac{1}{d_{hkl}} \frac{\delta d_{hkl}}{\delta T} = A_{0,hkl} + A_{1,hkl}T + A_{2,hkl}T^2 + \dots \quad (2.12)$$

The values for the A coefficients are obtained by least-squares fitting and are subsequently used to calculate thermal expansion. CTEAS considers crystal symmetry when calculating the symmetrical second rank CTE tensor according to Neumann's principle, which states that "the symmetry elements of any physical property of a crystal must include all the symmetry elements of the point group of the crystal."³⁷ Visualizing the calculated thermal expansion coefficient is most commonly done via quadric, where the relationship between CTE of any crystallographic plane and the CTE tensor is given in **Equation 2.13**:⁶⁶

$$\alpha_{hkl} = \alpha_{11}X^2 + \alpha_{22}Y^2 + \alpha_{33}Z^2 + 2\alpha_{12}XY + 2\alpha_{23}YZ + 2\alpha_{13}XZ \quad (2.13)$$

In **Equation 2.13**, α_{ij} are six independent components of the CTE tensor, and X , Y , and Z are the direction cosines of the normal to the (*hkl*) plane in the cartesian coordinate system.

2.4.7 Raman Spectroscopy

Raman spectroscopy was used to investigate if the CTE anisotropy trends had phononic origins. A Renishaw InVia Confocal Raman microscope was used at the University of Virginia. The energy of a molecule can be simplistically separated into three components: rotation of the molecule, vibrations of constituent atoms, and electron motion in the molecule. The use of molecules to describe Raman is derived from literature, but the concepts and principles extend to crystals and are, therefore, valid for the crystalline materials studied in this work. These distinctions can be made due to stark differences in velocity between each of the classifications, and the list is given in order of slowest to fastest. Raman spectroscopy focuses on the vibrational aspect of energy in a molecule, which are typically observed in the range between 10^2cm^{-1} and 10^4cm^{-1} .⁶⁷ The vibrational spectra are what is seen in Raman spectroscopy, originating from the electronic polarization caused by ultraviolet or visible light. The principle of Raman spectroscopy operates by irradiating a molecule with monochromatic light with a frequency, ν . This induces an electronic polarization in the molecule which then emits light of frequency ν due to Raleigh scattering as well as light of frequency $\nu \pm \nu_i$ (Stoke and anti-Stokes lines) due to Raman scattering. The ν_i term represents a vibrational frequency, which means that vibrational frequencies are observed as Raman shifts from the incident frequency of light.⁶⁷ Stokes lines are typically closer to lower frequency while anti-Stokes are seen closer to higher frequencies.

Raman spectra can be more analytically described by the following classical theory. Consider a light wave with a frequency ν and with an electric field E . The electric field will fluctuate at frequency ν , and this can be described using **Equation 2.14**:

$$E = E_0 \cos 2\pi \nu t \quad (2.14)$$

E_0 is the amplitude and t is time in **Equation 2.14**. If the molecule irradiated is diatomic, then the dipole moment P can be represented by **Equation 2.15**:

$$P = \alpha E = \alpha E_0 \cos 2\pi \nu t \quad (2.15)$$

The α term is a proportionality constant and is referred to as polarizability. Furthermore, if the molecule vibrates at frequency ν_1 , the nuclear displacement q is given by **Equation 2.16**:

$$q = q_0 \cos 2\pi \nu_1 t \quad (2.16)$$

The q_0 is the vibrational amplitude in **Equation 2.16**. At small amplitudes, the polarizability is a function of the vibrational amplitude, leading to **Equation 2.17**:

$$\alpha = \alpha_0 + \left(\frac{\partial \alpha}{\partial q}\right)_0 q \quad (2.17)$$

Combining **Equations 2.15-2.17** results in **Equation 2.18**. **Equation 2.18** has two terms, the first describes Rayleigh scattering while the second term gives the Raman scattering frequencies. When the partial derivative portion of the second term is equal to zero, then the vibration is not Raman active.⁶⁷

$$P = \alpha_0 E_0 \cos 2\pi \nu t + \frac{1}{2} \left(\frac{\partial \alpha}{\partial q}\right)_0 q_0 E_0 [\cos \{2\pi(\nu + \nu_1)t\} + \cos \{2\pi(\nu - \nu_1)t\}] \quad (2.18)$$

2.4.8 UV-Vis Spectroscopy

Ultraviolet-visible (UV-Vis) spectroscopy was used to determine the band gaps of REDS. This technique allows for probing the electronic structure of REDS containing distinct rare earth cations. UV-Vis was used to collect reflectance and transmission spectra as it relates to wavelength. The reflectance data is then converted to an absorption spectrum through the Kubelka-Munk^{68,69} function given as **Equation 2.19**:

$$F(R_\infty) = K/S = (1 - R_\infty)^2 / 2R_\infty \quad (2.19),$$

where K is the absorption coefficient, S is the scattering coefficient, R_∞ is the reflectance of an infinitely thick specimen ($R_\infty = R_{\text{sample}}/R_{\text{standard}}$). **Equation 2.19** is inserted into **Equation 2.20**:

$$(F(R_\infty) \cdot h\nu)^{1/\gamma} = B(h\nu - E_g) \quad (2.20),$$

where h is Planck's constant, ν is the frequency of the photon, E_g is the band gap energy, B , is a constant, and γ is 0.5 or 2 depending on whether the band gap is direct or indirect respectively, to produce **Equation 2.21**:

$$(F(R_\infty) \cdot h\nu)^{1/\gamma} = B(h\nu - E_g) \quad (2.21)$$

Once the reflectance data is changed to absorption, the absorption can be plotted on the y-axis against energy on the x-axis. This plot is referred to as a Tauc plot. Transmission experiments are also possible, with the absorption being measured by shining through the sample with a blank standard in a parallel beam configuration. The Tauc plot can be used to extrapolate the band gap through a fit of a linear regime of the absorption data.⁶⁸⁻⁷⁰

Chapter 3 Initial Synthesis and Phase Purity of Rare-Earth Disilicates

3.1 Introduction

The production of REDSs via a solvent based method allows for modularity in adding or removing distinct RE cations. Additionally, the final product can be made in small controllable batches, lending to prolonged study and experimentation on the scale necessary in this work. A variety of synthesis methods appear in literature, with synthesis procedures varying drastically from pH, temperature, solvents, and ratios of precursors used. The most common method in literature to produce REDSs via sol-gel is to use TEOS and a RE-nitrate as precursors.^{43,44,52,53,56,57,71-74} The procedure for making a single phase REDS is not ubiquitous, and involves study of precursor reactions and solvent chemistry discussed in **Chapter 6**. Within this chapter, the initial synthesis procedures, results, and overall evolution of the process are documented.

3.2 Modified Pechini Method

A modified Pechini method was used as a starting point for the synthesis of REDS. The Pechini method is a sol-gel method typically used to synthesize mixed oxides, typically perovskites.⁷⁵ **Figure 3.1** illustrates the first proposed experimental procedure. The figure includes a final step that was meant for production of material for pulsed laser deposition (PLD), but this was not possible. The solvent was chosen due to both precursors readily dissolving in ethanol. Heating the solution and then adding polymeric agents is typical to help agglomeration of material. Once the gel formed, it is taken to a furnace for a heat treatment at 550 °C to produce a xerogel. The xerogel is turned into powder with a mortar and pestle and is then ready for characterization work, typically done with XRD. Initial attempts to synthesize Yb disilicate using the procedure outlined in **Figure 3.1** produced undesired phases, sometimes with little to no $C 2/m$ phase present. The first three attempts at a $\text{Yb}_2\text{Si}_2\text{O}_7$ sol-gel are shown in **Figure 3.2**. These attempts resulted in samples containing Yb oxide, and other unknown phases. Several iterations of the process were created, refining it more and more to produce an increasingly pure final product. Additives such as ammonium hydroxide and Ethylenediaminetetraacetic acid (EDTA) were used to replace citric acid and ethylene glycol for a time until work was found in the literature that produced relatively phase pure REDS without additives.⁵³ The difference between this method and prior work was the complete lack of water in the process. The procedure was once again reconstructed and is illustrated by the flowchart in **Figure 3.3**. This procedure was the experimental method used for all sol-gels produced in this work up until **Chapter 7**.

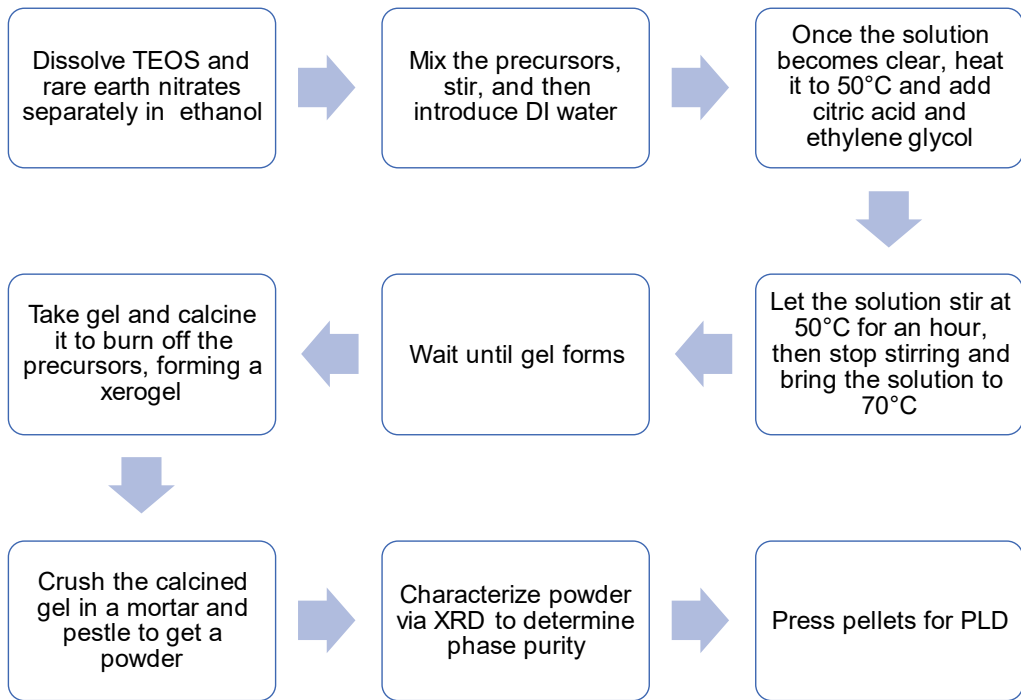


Figure 3.1: A flowchart of the first proposed experimental plan using a modified Pechini method to mix RE nitrates and TEOS to produce a phase pure REDS.

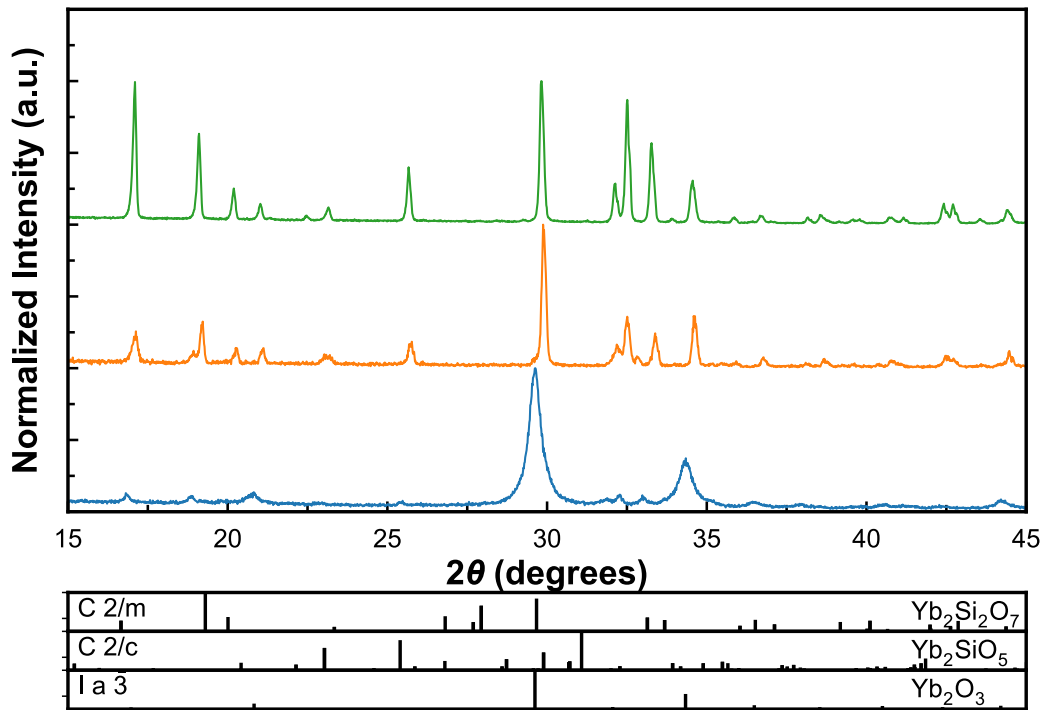


Figure 3.2: XRD patterns of initial attempts to synthesize Yb₂Si₂O₇. The only phase identified is the Yb oxide phase, necessitating modifications to the procedure.

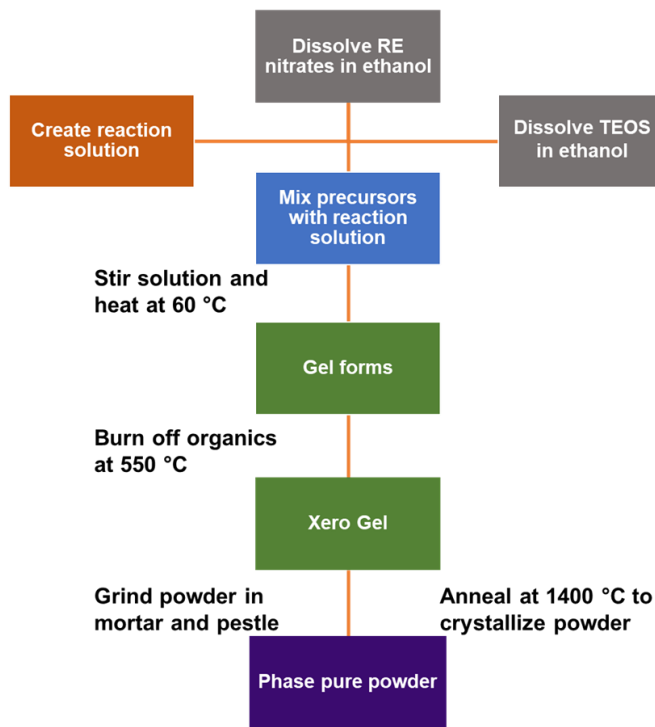


Figure 3.3: A flowchart of the refined sol-gel process that more consistently produced sol-gels of higher phase purity relative to previous iterations.

The experimental process outlined in **Figure 3.3** was used to produce the first successful ytterbium disilicate sample, where the reaction solution refers to the ethanol or potentially other solvents used for precursor dissolution. The sample contained a small amount of secondary monosilicate phase. The secondary phase presence would remain until further reaction investigations uncovered the causes in **Chapter 6**. The XRD pattern of the initial success is shown in **Figure 3.4**, where the secondary monosilicates phase is indexed with red squares, and the predominant disilicate phase is indexed with green circles. The reference patterns in **Figure 3.4** give the peak positions for the ytterbium disilicate, monosilicate, and oxide. These references were chosen based on the phase diagram for ytterbium disilicate in **Chapter 2**.

3.3 Single Component REDS

Once the disilicate phase was produced for Yb, the next steps were to determine if the process was possible with other RE cations. The procedure for the ytterbium disilicate sol-gel was repeated for erbium, yttrium, dysprosium, and neodymium. According to Felsche²⁷, erbium and yttrium should be the monoclinic $C2/m$ (Type C) phase. Dysprosium disilicate was predicted to be in the triclinic $P\bar{1}$ (Type B) phase. There were two possible phases for neodymium given the proximity of a phase transition temperature to the

temperature at which the sol-gel procedure crystallized the powders (1400 °C). The two expected phases were the lower temperature tetragonal $P 4_1$ (Type A) phase or the higher temperature monoclinic $P 2_1/n$ (Type G) phase. **Figure 3.5** shows the XRD pattern for all four of these REDSs, with the predominant phase given as a color-coded reference pattern below. The erbium and yttrium sol-gels produced the expected phase with the same monosilicate secondary phase as in ytterbium. The secondary phase is indexed with black squares in these two patterns. The dysprosium sol-gel did not produce the predicted phase, instead it formed into a hexagonal apatite phase. The reference pattern for this apatite phase is given in green in **Figure 3.5** instead of the predicted triclinic phase. The neodymium sol-gel produced a phase mixture composed of the higher temperature monoclinic $P 2_1/n$ phase and a hexagonal apatite phase. The monoclinic $P 2_1/n$ phase is indexed with black stars while the apatite phase is indexed with purple circles.

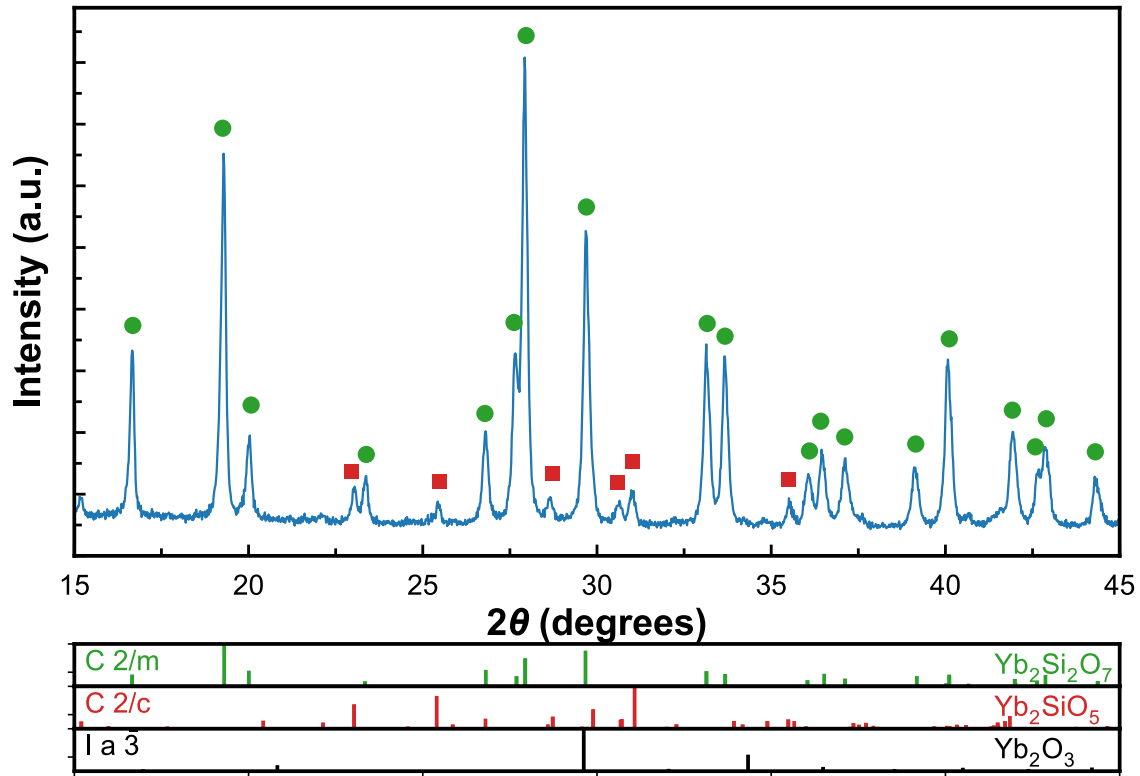


Figure 3.4: XRD pattern of the first successful Yb disilicate sol-gel process. The disilicate phase is indexed with green circles, and the secondary monosilicates phase is indexed with red squares.^{76,77}

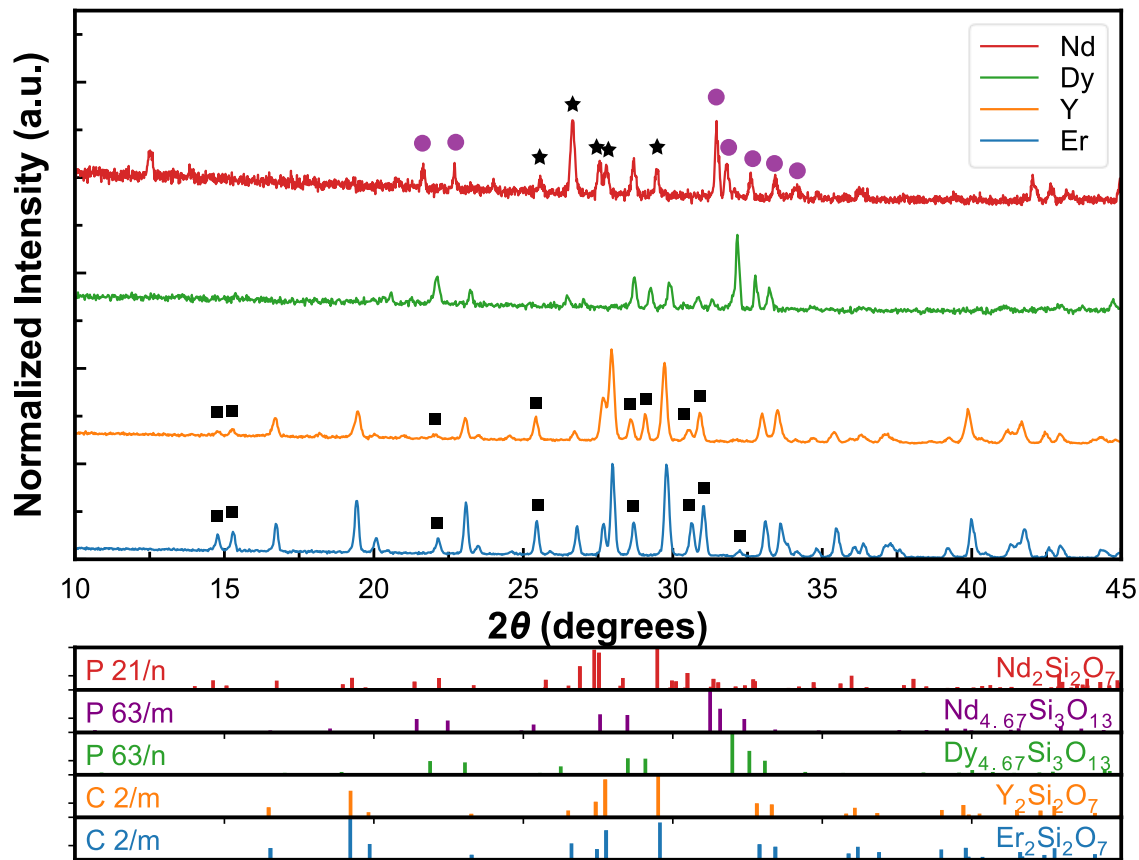


Figure 3.5: XRD patterns of Er, Y, Dy, and Nd sol-gels. The predominant phases are shown below the plot as references. The black squares indicate a monosilicate peak, the black stars indicate the $P 2_1/n$ phase, and the purple circles indicate the $P 63/m$ apatite phase.

3.4 Multi-Component REDS

Following the results of the single components REDS, multiple RE cations were simultaneously included in the experimental procedure. The inclusion of multiple cations allows for tailoring properties of the final REDS.^{21,41,78,79} Initial attempts at mixing distinct RE cations produced a variety of phases. XRD patterns of REDS with only two RE cations are given in **Figure 3.6**. The RE cations used in the two-component mixtures were Yb, Er, Y, and Nd. The REDSs containing Yb and Er or Y produced a nearly single phase ($C 2/m$) material. The Nd containing REDSs produced a two-phase mixture. The smaller cations (Yb and Y) stabilized in the triclinic phase, and the secondary phase is the hexagonal apatite phase that appeared in the XRD patterns shown in **Figure 3.5**. The differences in ionic radius between the cations was hypothesized to be causing the stabilization of multiple phases such as the triclinic phase, as well as secondary phases such as the apatite phase.

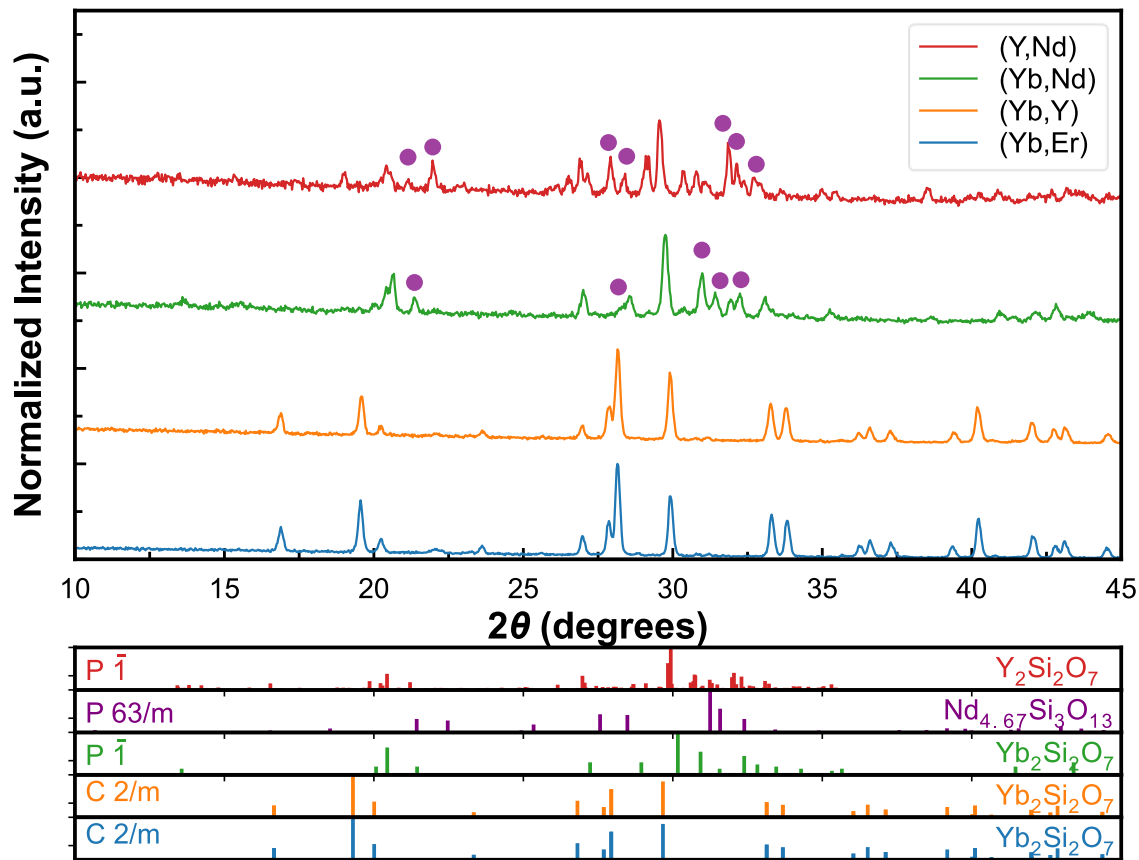


Figure 3.6: XRD patterns of REDS with two RE cations are shown. The predominant phase is referenced in the patterns below the plot, and the secondary apatite phase is indexed with purple circles.

The multi-component work continued by adding a third cation into the sol-gel procedure. Two mixtures were made to continue observing the effect of ionic radii on the final phase produced. **Figure 3.7** shows XRD patterns of sol gels, one with Yb, Er, and Y, and the other with Yb, Er, and Nd. The first composition was selected to see if the $C 2/m$ phase continues to be stable as more distinct cations are added. The second composition was selected to investigate if an averaging effect is occurring. By adding smaller ions (Yb and Er) relative to neodymium, the neodymium could be stabilized in a phase not reported by Felsche for the individual REDSs.²⁷ The (Yb, Er, Y) sol-gel produced a nearly phase pure ($C 2/m$) disilicate powder. The (Yb, Er, Nd) sol-gel produced a two phase mixture of $C 2/m$ disilicate and hexagonal neodymium apatite phase. These results differ from the two components (Yb, Nd) and (Y, Nd) mixtures that produced a triclinic phase instead of the monoclinic phase. Four (Yb, Er, Y, Nd) and five (Yb, Er, Y, Dy, Nd) component systems were then produced and the XRD patterns are illustrated in **Figure 3.8**. The trends seen for the four and five component systems are similar to the trends seen in the two component systems. Like in the two RE materials, the final phases were the triclinic phase and the

apatite phase. Additional rare-earth cation mixtures were tested and are included in **Chapter 6** as part of the investigation of the effect of ionic radii on final phase.

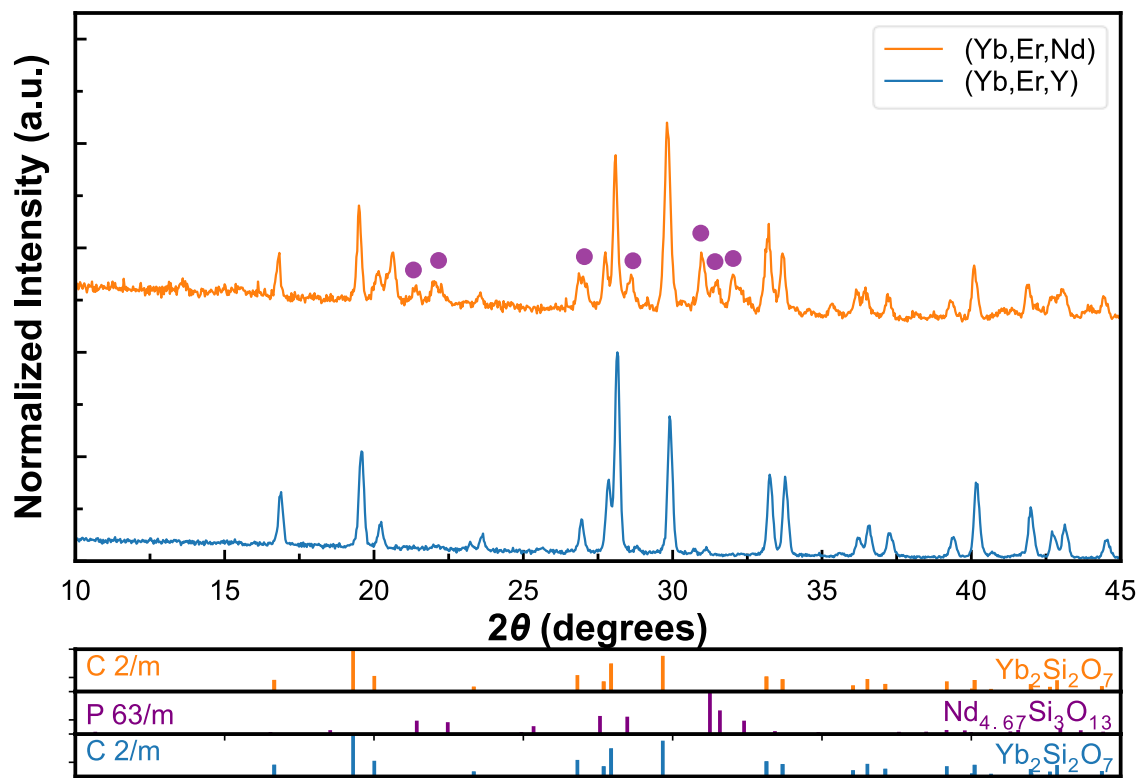


Figure 3.7: XRD patterns of three-component REDS. Both phases are predominantly the monoclinic $C 2/m$ phase. The neodymium containing mixture produced a secondary apatite phase.

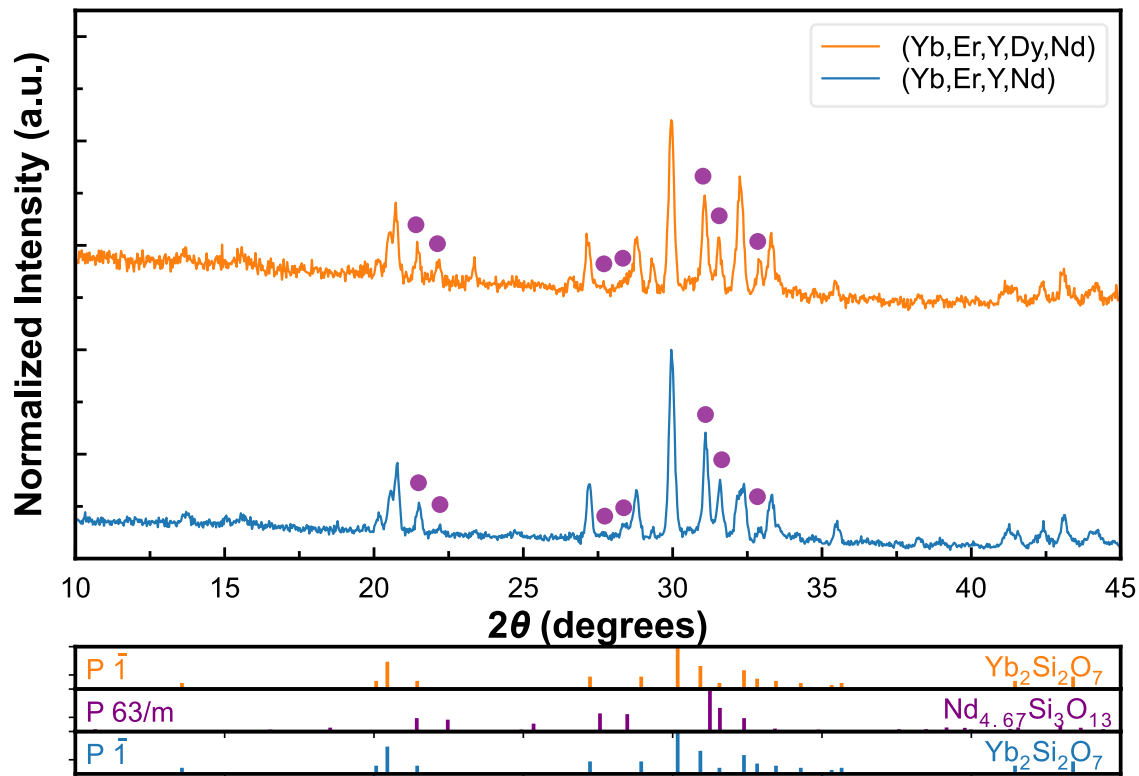


Figure 3.8: XRD patterns of four and five component REDS. Both are primarily triclinic as shown by the reference patterns below the plot, and both contain the apatite phase indexed by purple circles.

3.5 Summary

An adapted Pechini method (a sol-gel process) was used to produce Yb disilicate. The process was modified with subsequent synthesis attempts to reduce the monosilicate phase fraction and increase the disilicate phase fraction. Once a nearly phase pure disilicate was produced, the procedure was repeated on other RE cations, producing the monoclinic $C 2/m$ (Type C) phase for Er and yttrium, the triclinic $P \bar{1}$ (Type B) phase for Dy, and the monoclinic $P 2_1/n$ (Type G) as well as the $P 63/m$ apatite phases for Nd. In the multi-component mixtures, the $C 2/m$ phase was stabilized when Yb, Er, and Y were the only RE cations in the mixture. Any mixtures containing Nd produced two phase mixtures always containing some phase fraction of the apatite phase. The predominant phase in the multicomponent mixtures depended on the other RE cations in the mixture, producing either the $C 2/m$ or $P \bar{1}$ phase of the disilicate.

Chapter 4 Phase Stability and Tensorial Thermal Expansion Properties of Single to High-Entropy Rare-Earth Disilicates

The contents of this chapter are published in *Journal of the American Ceramic Society*, vol. 106, no. 5, pp. 3228–3238, 2023, doi: [10.1111/jace.18986](https://doi.org/10.1111/jace.18986), with the following authors:

Alejandro Salanova,¹ Ian A. Brummel,¹ Andrey A. Yakovenko,² Elizabeth J. Opila,¹ and Jon F. Ihlefeld^{1,3}

¹ Department of Materials Science and Engineering, University of Virginia, Charlottesville, VA 22904 USA

² Advanced Photon Source, Argonne National Laboratory, Lemont, IL 60439 USA

³ Charles L. Brown Department of Electrical and Computer Engineering, University of Virginia, Charlottesville, VA 22904 USA

The text has been adapted to include supplemental information and figures where appropriate.

4.1 Motivation

This chapter provides a continuation of REDS sol-gel synthesis and XRD characterization discussed in previous chapters. While the synthesis procedure is identical, the quantity of rare-earth cations is now increased to produce multi-component and HE REDS. Additionally, the use of hot stage XRD allowed for an investigation into the thermomechanical stability of the materials, leading to beamline experiments at Argonne National Laboratory (APS) and Oak Ridge National Laboratory (ORNL).

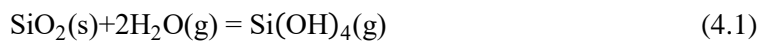
4.2 Abstract

Temperature limitations of nickel-base superalloys have resulted in the emergence of SiC-based ceramic matrix composites as a viable replacement for gas turbine components in aviation applications. Higher operating temperatures allow for reduced fuel consumption but present a materials design challenge related to environmental degradation. Rare-earth disilicates ($\text{RE}_2\text{Si}_2\text{O}_7$) have been identified as coatings that can function as environmental barriers and minimize hot component degradation. In this work, single- and multiple-component rare-earth disilicate powders were synthesized via a sol-gel method with compositions selected to exist in the monoclinic $C 2/m$ phase (β phase). Phase stability in multiple cation compositions was shown to follow a rule of mixtures and the $C 2/m$ phase could be realized for compositions that contained up to 25% dysprosium, which typically only exists in a triclinic, $P \bar{1}$, phase. All compositions

exhibited phase stability from room temperature to 1200 °C as assessed by X-ray diffraction. The thermal expansion tensors for each composition were determined from high-temperature synchrotron X-ray diffraction and accompanying Rietveld refinements. It was observed that ytterbium-containing compositions had larger changes in the α_{31} shear component with increasing temperature that led to a rotation of the principal axes. Principal axes rotation of up to 47° were observed for ytterbium disilicate. The results suggest that microstructure design and crystallographic texture may be essential future avenues of investigation to ensure thermo-mechanical robustness of rare-earth disilicate environmental barrier coatings.

4.3 Introduction

Nickel-base superalloys have reached the limit of their high temperature capabilities within gas turbine engines. Silicon carbide-based ceramic matrix composites (CMCs) provide a stronger, lighter, and more durable alternative to Ni-base turbine blades and vanes.^{4,5,7,13} In a combustion environment, however, SiC reacts with water vapor to form a gaseous silicon hydroxide species.¹⁵ This volatilization reaction is shown in **Equation 4.1** and can be minimized through the application of thermal/environmental barrier coatings (T/EBCs).^{5,8,10,11,17–19}



Rare earth disilicates (REDS) have been identified as promising T/EBC candidates due to their combination of a low coefficient of thermal expansion (CTE) mismatch with CMCs, high melting temperatures, and a low silicon activity relative to pure silicon oxide.²² In application, however, REDS still undergo reactions with water vapor and can transform into a rare-earth monosilicate or rare-earth oxide. One possible mechanism to increase the thermodynamic stability of REDS coatings is through the inclusion of multiple rare earth (RE) cations in equimolar ratios. With every cation addition, the configurational entropy increases and compositions containing five equimolar cations in solid solution are known as high-entropy (HE) ceramics.^{38,39} High entropy ceramics may have their free energy reduced compared to their individual components due to the negative $T\Delta S$ portion of Gibbs free energy and high configurational entropy and the addition of multiple REs can result in local ion mass variations and distortions within the lattice that serve to reduce phonon mean free paths. A reduction in phonon mean free path leads to a reduction in thermal conductivity,^{78,80} which makes the HE approach attractive for T/EBCs in ways single component REDS cannot.

Creating high entropy REDS requires consideration of cation size dependence of phase stability. When multiple cations are added into solid solution, the final phase is hypothesized to follow a rule of mixtures. Within the REDS system, there are several possible polymorphs. Between room temperature and

~1400 °C, single component REDS comprising ions of erbium and smaller (e.g. erbium to lutetium along with scandium and yttrium) stabilize into a monoclinic ($C 2/m$) phase, those comprising ions between dysprosium and gadolinium stabilize into a triclinic ($P \bar{1}$) phase, and those comprising europium and larger stabilize into the tetragonal ($P 4_1$) phase.^{27,34,41} There are additional phases that exist at elevated temperatures for many of these REDS. Only the $C 2/m$ phase, when comprising the smallest cations (i.e. Lu, Yb, and Sc), has effectively no polymorphic transformations upon heating. This, along with favorable thermal expansion properties with respect to SiC make the $C 2/m$ monoclinic phase (commonly denoted as the β phase or as type C as defined by Felsche²⁷) technologically attractive. Despite their great promise, to date, thermal expansion and phase stability data on mixed and HE REDS remain lacking.³³

Thermal expansion is a second-rank symmetric tensor with nine coefficients. Due to symmetry elements of the crystal, some of these coefficients are equivalent or are zero and the tensor for a monoclinic crystal with 4 distinct coefficients is shown below as **Equation 4.2**:

$$\begin{bmatrix} \alpha_{11} & 0 & \alpha_{31} \\ 0 & \alpha_{22} & 0 \\ \alpha_{31} & 0 & \alpha_{33} \end{bmatrix} \quad (4.2)$$

The shear coefficient (α_{13} and α_{31}) terms are equivalent due to the mirror plane present in the $C 2/m$ structure, while the normal coefficients (α_{11} , α_{22} , and α_{33}) are all distinct. The normal tensor coefficients are orthogonal to each other and can be referred to as the principal axes only when the conditions in **Equation 4.3** are met.

$$S_1 x_1^2 + S_2 x_2^2 + S_3 x_3^2 = 1 \quad (4.3)$$

In **Equation 4.3**, S and x correspond to normal tensor coefficients and physical dimensions, respectively. In a monoclinic crystal, this condition is satisfied when S_2 is parallel to the y diad axis.³⁷ Previous research on the CTE of REDS has reported a linear CTE derived from dilatometry or X-ray diffraction (XRD) experiments, but tensor representations of the CTE are significantly less common.^{33,34,81–87} The determination of the CTE tensor can more adequately describe anisotropy in materials than a single value in a linear CTE, or even CTE values of individual lattice parameters. With an improved representation of anisotropy, crystallographic information can be correlated to microstructural developments that impact the stress state and thermo-mechanical properties of T/EBCs. This study focuses on the phase stability of single-component, multi-component, and HE REDS and the temperature dependence of the anisotropic CTE.

4.4 Experimental Methods

4.4.1 Powder Synthesis

The REDS were synthesized via a modified sol-gel method as described in **Chapter 6**.^{42,53,57,58,71} Rare earth nitrates and tetraethyl orthosilicate (TEOS) served as the rare earth and silicon oxide precursors, respectively. For a REDS containing a single RE, 1.00 g of the chosen rare earth nitrate was dissolved in 30 mL of ethanol. The water content of the nitrate precursor was measured via thermogravimetric analysis (Netzsch STA-449 F1) and accounted for in the composition calculation and the mass of the rare earth nitrate was recorded to 0.001 g precision. The solution was stirred to aid in dissolution. Separately, TEOS was measured by volume and dissolved in 30 mL of ethanol. The volume of TEOS used corresponded to a 1:1 ratio of the moles of silicon and the moles of RE in the nitrate precursor. The dissolved precursors were then combined into a single beaker containing another 30 mL of ethanol. The reaction solution was stirred and heated at 60 °C and allowed to gel over 24-36 hours. The gel was then placed into a platinum crucible and dried in a box furnace at 550 °C for 24 hours in a static air ambient. The drying process converted the sol-gel into a xerogel that was brittle but maintained the networked structure of the sol-gel.⁷¹ The xerogel was subsequently ground into a powder with a Diamonite mortar and pestle. The powder was placed into a platinum crucible and exposed at 1400 °C for 18 hours in a box furnace and static air atmosphere to convert into the REDS. For a compositionally complex or high entropy REDS, the RE nitrates were dissolved together in the same solution. Equimolar quantities of each RE nitrate were batched (e.g. [Yb]=[Er]=[Y]=[Dy] for $\text{Yb}_{0.5}\text{Er}_{0.5}\text{Y}_{0.5}\text{Dy}_{0.5}\text{Si}_2\text{O}_7$). The appropriate volume of TEOS was used to keep the Si:RE ratio 1:1 with all the REs. All other synthesis steps were the same for samples containing multiple REs.

4.4.2 Diffraction Experiments

Preliminary XRD experiments were performed on a Panalytical Empyrean X-ray diffractometer (Cu $K\alpha$ X-ray wavelength of 1.54 Å) using an Anton Parr HTK1200 N hot stage with a ramp rate of 10 °C/min and temperatures from 25 °C to 1200 °C. Once the sample reached 50 °C, the temperature was held to collect the diffraction pattern. The hold and measure profiles were repeated at subsequent 50 °C intervals. Following preliminary analysis, experiments were conducted at beamline 11-ID-C at the Advanced Photon Source at Argonne National Laboratory. Transmission XRD experiments were performed on REDS powders inside of a 1 mm diameter fused quartz capillary with an X-ray energy of 105.7 keV, which corresponds to a wavelength of 0.1173 Å. A K-type thermocouple was fed in through one side of the capillary and contacted the powder to ensure that the temperature reading would report the temperature of the sample in the beam path. Diffraction patterns were collected using a Pilatus 300KW detector with a sample-to-detector distance to 1700 mm. Patterns were collected every thirty seconds as the

sample was heated at a rate of 10 °C/min from room temperature to 1000 °C. This corresponded to a diffraction measurement every 5 °C. Rietveld refinements were performed on the data using GSAS-II.^{61,62} National Institute for Standards and Technology instrument standards of LaB₆ (SRM-660c and SRM-660a for lab-scale and synchrotron, respectively) and CeO₂ (SRM-674b) were used for calibration.

4.4.3 Tensor Analysis

Once unit cell information was extracted from the refinements, *d*-spacings were calculated and input into Coefficient of Thermal Expansion Analysis Suite (CTEAS) software to visualize the CTE tensor, acquire tensor coefficients, and calculate thermal expansion as a function of temperature.⁶³ The temperature range was set from 25 to 1000 °C and the program fit the supplied data to a second order polynomial, and then calculated the thermal expansion and tensors through an algorithm outlined in appendix D of the CTEAS user manual.

4.5 Results and Discussion

4.5.1 Phase Mixing

The average ionic radius for the REs included in the disilicate in an 6-fold coordination were used to predict the final phase.⁸⁸ Through this model, it was hypothesized that REs could be stabilized into the *C 2/m* phase through a rule of mixtures as long as the average RE ionic radius was within the known range of stability as determined by Felsche.²⁷ For example, while Dy₂Si₂O₇ is not stable in the *C 2/m* phase, by using it as a fractional component of a REDS with other smaller radii RE ions, the average RE ionic radii is in range that is compatible with *C 2/m* formation. This is shown in **Figure 4.1** where dysprosium was included in compositionally complex and high entropy mixtures. Also shown is a composition including neodymium (Yb_{0.4}Er_{0.4}Y_{0.4}Dy_{0.4}Nd_{0.4}Si₂O₇). For this composition the average of the ionic radii is 0.911 Å and this is expected to be too large to be stable in the *β*-phase.

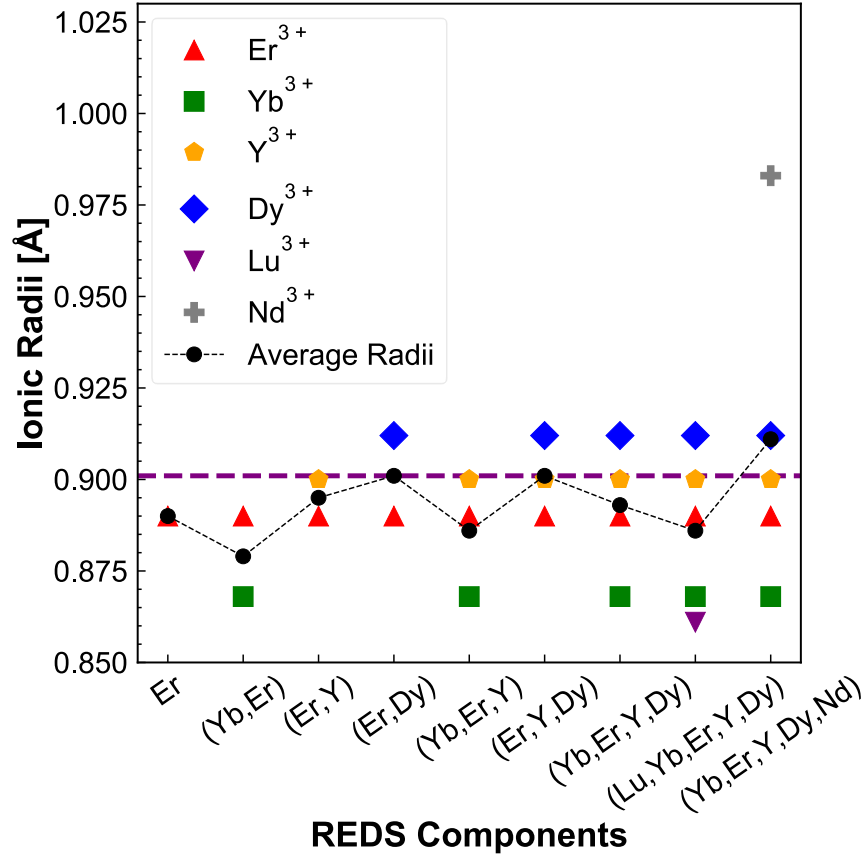


Figure 4.1: A rule of mixtures prediction of the stability of REDS in the $C 2/m$ phase. Average ionic radii below the heavy dashed line are predicted to result in a REDS in the monoclinic $C 2/m$ phase. Those on or above the dashed line would be the triclinic ($P \bar{1}$) phase.

The mixtures in **Figure 4.1** were synthesized using the methods described in the experimental methods. The powders were then characterized using XRD to confirm the phases present. **Figure 4.2** shows the XRD pattern of ytterbium disilicate produced via the method described. The powder contains majority phase peaks of monoclinic $C 2/m$ and secondary peaks belonging to the $C 2/c$ (X2 phase) rare-earth monosilicate line compound (i.e. Yb_2SiO_5). Analysis of peak intensities revealed that the monosilicate secondary phases were present in weight fractions of approximately 7%. This secondary monosilicate phase was present in all powders prepared in this study. Since the Si:RE was batched 1:1, the monosilicate secondary phase points towards the possible presence of an additional silica secondary phase that would not appear in XRD due to difficulty in crystallizing SiO_2 . The presence of the monosilicate secondary phase should not affect the composition of the primary disilicate phase since both are line compounds. **Figure 4.3** shows XRD patterns of REDS prepared in this study. Two of the compositions, $\text{Yb}_{0.5}\text{Er}_{0.5}\text{Y}_{0.5}\text{Dy}_{0.5}\text{Si}_2\text{O}_7$ and $\text{Lu}_{0.4}\text{Yb}_{0.4}\text{Er}_{0.4}\text{Y}_{0.4}\text{Dy}_{0.4}\text{Si}_2\text{O}_7$ experimentally validate that dysprosium-containing REDS can be stabilized into the $C 2/m$ phase through a rule of mixtures. No evidence of the triclinic phase could be

observed in the multi-component disilicate solid solutions comprising rare-earths with average radii below 0.900 Å. For the Nd-containing composition, however, a secondary triclinic phase was observed, demonstrating that too large of cation radii results in difficulty in stabilizing the β -phase. For the single phase compositions, variations in the β -phase peak positions are caused by differences in RE content and their distinct ionic radii leading to lattice expansion and provides an indication that solid-solutions containing each cation without phase separation or segregation of cations occurred.

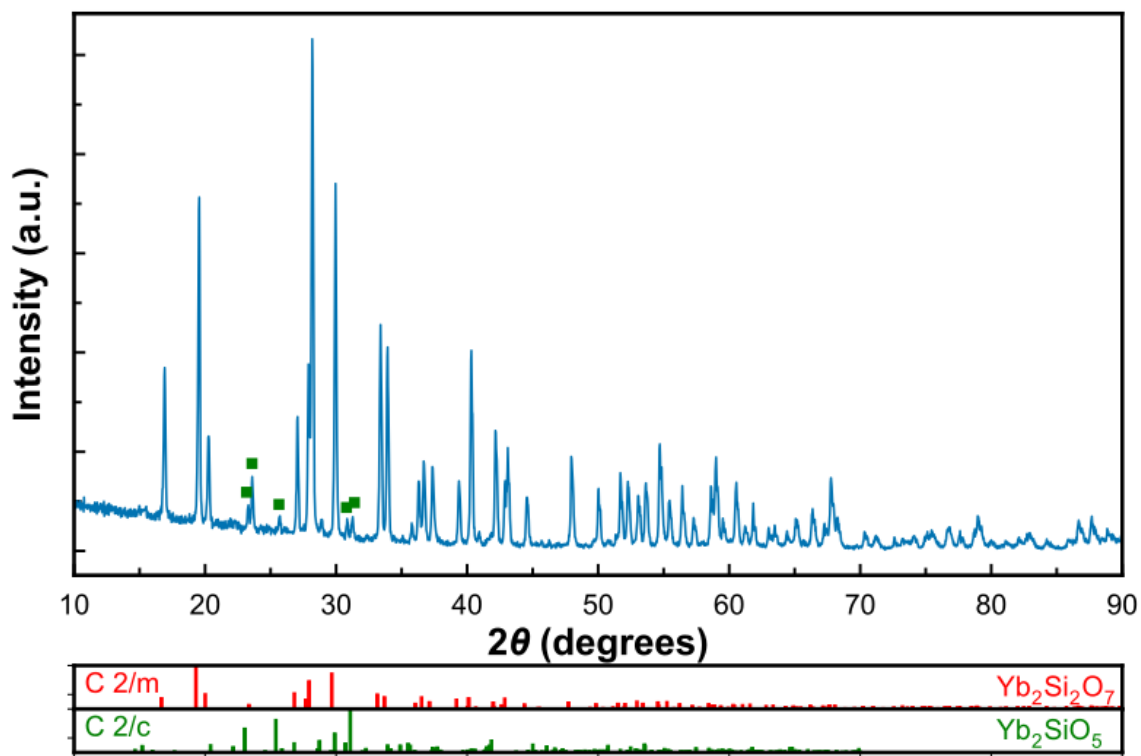


Figure 4.2: XRD pattern of ytterbium disilicate ($\text{Yb}_2\text{Si}_2\text{O}_7$) showing the monoclinic $C 2/m$ phase as the primary phase with approximately 7% secondary phase presence of ytterbium monosilicate (Yb_2SiO_5). The monosilicate phase is denoted by the green squares. The reference patterns for the disilicate and monosilicate are ICSD Collection Codes 16048 and 4446 respectively.^{76,77}

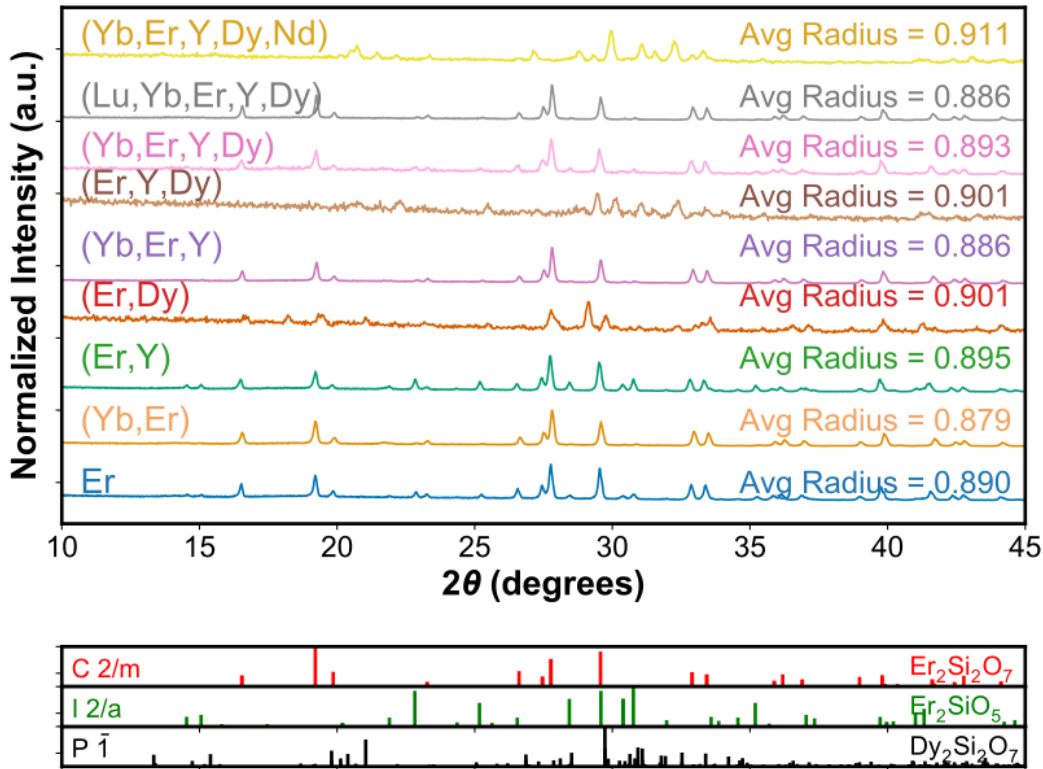


Figure 4.3: Room temperature XRD patterns of REDS with the labeled compositions and average RE ionic radii. Two samples contain dysprosium, both stable in the $C 2/m$ phase. All patterns indicate stability in the $C 2/m$ phase.

4.5.2 High Temperature XRD

To establish the stability of these phases at elevated temperatures, high temperature XRD experiments were conducted on REDS powders with lab-scale instrumentation in a Bragg-Brentano geometry and in a transmission geometry with synchrotron radiation. All samples that were primarily β -phase and shown in **Figure 4.3** were measured on the lab source, and compositions of $\text{Yb}_2\text{Si}_2\text{O}_7$, $\text{Er}_2\text{Si}_2\text{O}_7$, $(\text{Yb,Er})_2\text{Si}_2\text{O}_7$, $(\text{Yb,Er,Y})_2\text{Si}_2\text{O}_7$, $(\text{Yb,Er,Y,Dy})_2\text{Si}_2\text{O}_7$, and $(\text{Lu,Yb,Er,Y,Dy})_2\text{Si}_2\text{O}_7$ were measured at the synchrotron facility. The data taken at the beamline and with lab-scale instrumentation showed no indication of phase instability from 25 to 1000 °C (1200 °C for lab-scale measurements), including the REDS containing dysprosium. Contour maps of the lab-scale high temperature XRD are shown for $\text{Er}_2\text{Si}_2\text{O}_7$ and the four component $(\text{Yb,Er,Y,Dy})_2\text{Si}_2\text{O}_7$ in **Figure 4.4**. There are no new reflections that appear at higher temperatures, meaning that there are no new phases that nucleate upon heating to 1200 °C detectable by XRD. Contour map XRD patterns for all other compositions from this study are shown in **Figure 4.5**.

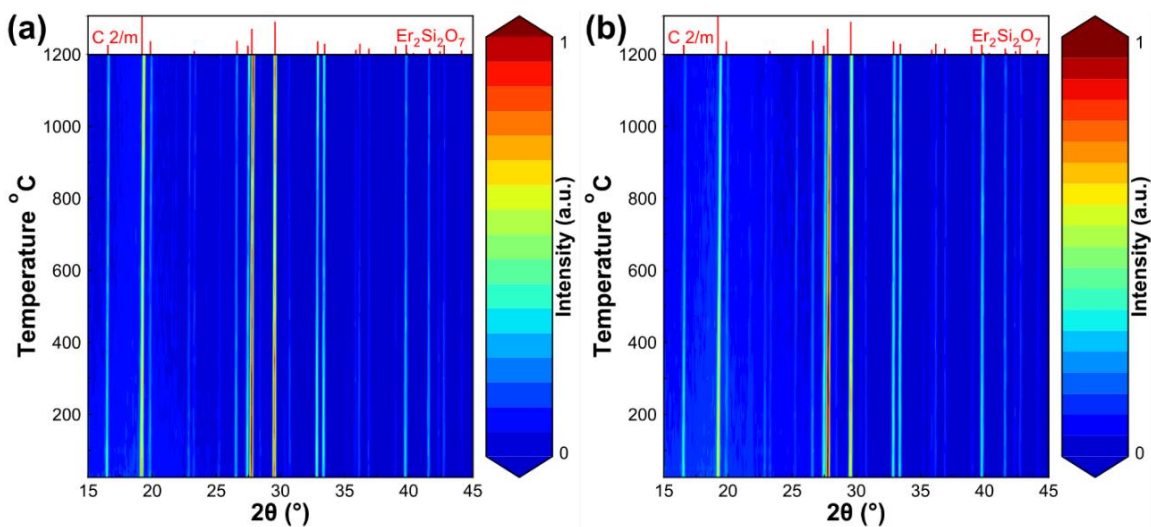


Figure 4.4: Contour maps of the high temperature XRD measurements on a lab-scale diffractometer for (a) $\text{Er}_2\text{Si}_2\text{O}_7$ and (b) the four component $(\text{Yb,Er,Y,Dy})_2\text{Si}_2\text{O}_7$ disilicate. The $\text{Er}_2\text{Si}_2\text{O}_7$ reference pattern is from ICSD Collection Code 74779.⁸⁹

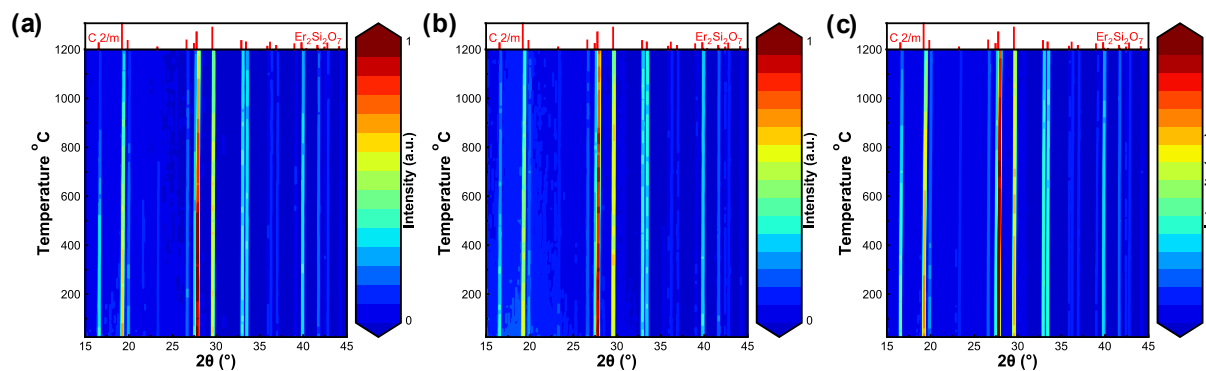


Figure 4.5: Contour maps of high temperature XRD measurements on a lab-scale diffractometer for (a) (Yb,Er) disilicate, (b) (Yb, Er, Y) disilicate, and (c) $(\text{Lu, Yb, Er, Y, Dy})$ disilicate. There are no detectable phases that nucleated during heating of these materials, meaning that these solid solutions are stable from room temperature to 1200 °C. The erbium disilicate reference pattern is ICSD Collection Code 74779.⁸⁹

Table 4.1: Lattice parameters from refined synchrotron X-ray diffraction data at 25, 500, and 1000 °C. The error is an order of magnitude lower than the significant figures presented and is therefore not reported. The raw values across the entire temperature range can be accessed through the University of Virginia Dataverse.⁹⁰ * The heating element failed during the temperature ramp and caused the heating to stop at approximately 970 °C instead of 1000 °C.

Composition	wR (%)	T= 25 °C	T= 500 °C	T= 1000 °C
		<i>a, b, c</i> (Å) beta (°)	<i>a, b, c</i> (Å) beta (°)	<i>a, b, c</i> (Å) beta (°)
Yb ₂ Si ₂ O ₇	3.313	6.80, 8.88, 4.71 101.98°	6.82, 8.89, 4.71 101.95°	6.83, 8.91, 4.72 101.98°
Er ₂ Si ₂ O ₇	4.710	6.85, 8.94, 4.72 101.77°	6.87, 8.96, 4.72 101.78°	6.89, 8.98, 4.73 101.80°
(Yb,Er) ₂ Si ₂ O ₇ *	3.371	6.83, 8.91, 4.71 101.87°	6.85, 8.93, 4.72 101.86°	6.86, 8.94, 4.72 101.88°
(Yb,Er,Y) ₂ Si ₂ O ₇	3.726	6.85, 8.94, 4.72 101.82°	6.86, 8.95, 4.72 101.82°	6.88, 8.97, 4.73 101.85°
(Yb,Er,Y,Dy) ₂ Si ₂ O ₇	3.700	6.86, 8.95, 4.72 101.80°	6.87, 8.96, 4.72 101.79°	6.89, 8.98, 4.73 101.82°
(Lu,Yb,Er,Y,Dy) ₂ Si ₂ O ₇ *	4.023	6.85, 8.94, 4.72 101.80	6.86, 8.95, 4.72 101.80	6.88, 8.97, 4.73 101.83

Temperature-dependent synchrotron XRD data was then refined to obtain lattice parameters, with the refinement of Yb₂Si₂O₇ shown in **Figure 4.6** as an example. All data were well fit, as indicated by low weighted residual percentage (wR) values. The lattice parameters, monoclinic beta angle, and wR values are shown in **Table 4.1**. The values are reported at room temperature, 500 °C, and 1000 °C. The full dataset for all measured temperatures is available at the University of Virginia Dataverse.⁹⁰

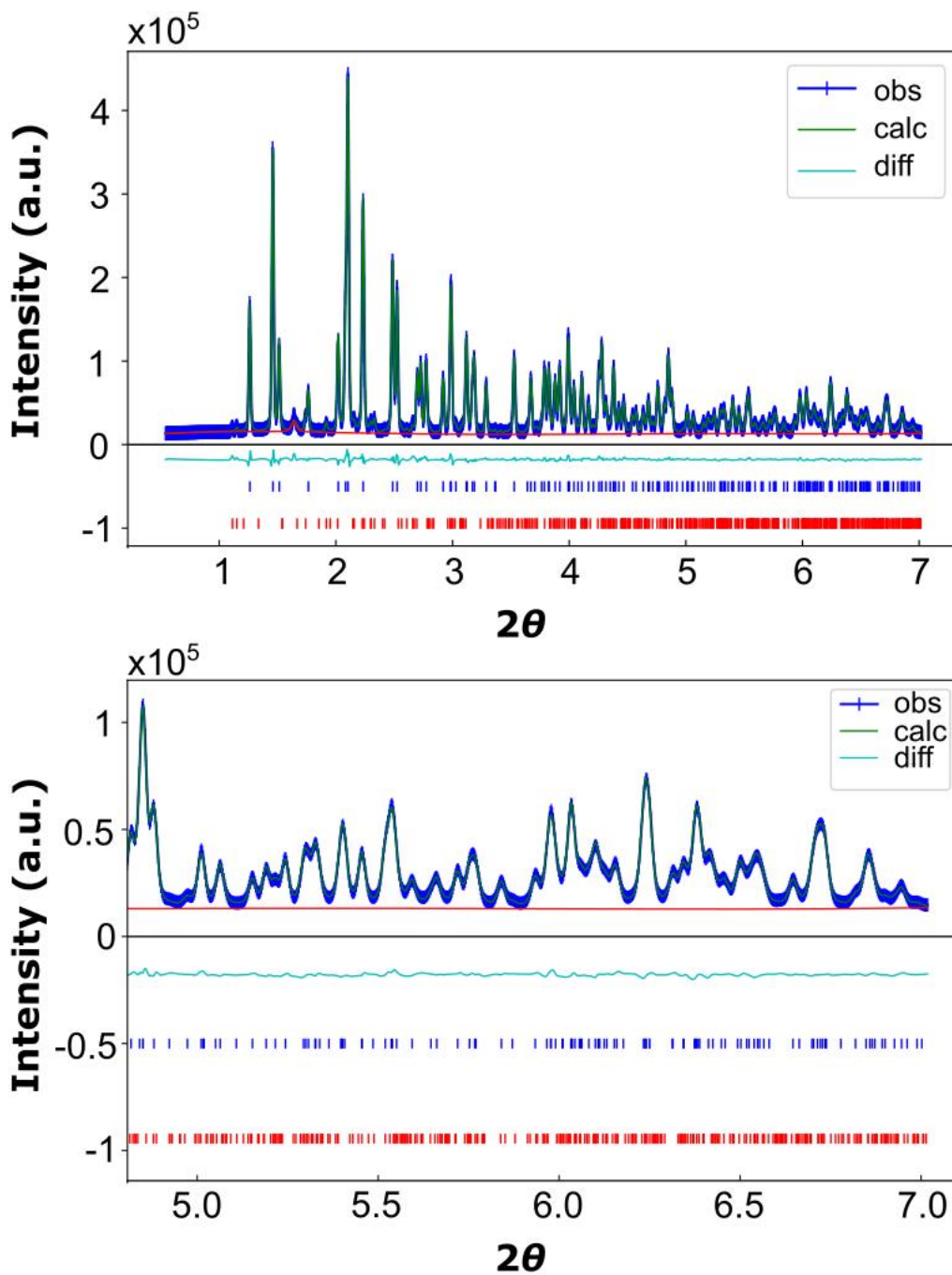


Figure 4.6: Rietveld refinement of Yb₂Si₂O₇ with a residual weight of approximately 3.4%. The tick marks below the fit correspond to the disilicate and monosilicate reference files (ICSD Collection Codes 16048 and 4446 respectively).^{76,77} Full scan range is shown in (a), while the higher angle peaks are shown in (b). The wavelength of X-ray radiation was 0.1173 Å.

4.5.3 CTE/Tensor Determination

Using the CTEAS software, tensors and graphical representations of the CTE were determined. The tensor components for different compositions are given in **Table 4.2** at 25, 500, and 1000 °C. The entire dataset is available through the University of Virginia Dataverse. The shear component, α_{31} , for erbium disilicate is the only coefficient that is negative at room temperature. In every other case, the shear components transition from positive to negative upon heating. The implication that this shear component has on the crystal structure will be discussed below. 3-D graphical representations of CTE are shown in **Figure 4.7** for $\text{Er}_2\text{Si}_2\text{O}_7$ and $\text{Yb}_2\text{Si}_2\text{O}_7$ between 25 and 1000 °C. The expansion along the Y -axis is approximate to that of the monoclinic b -axis unit vector direction, X is an arbitrary axis that is orthogonal to both Y and Z , where Z is approximate to the c -axis unit vector direction. Since the crystal is monoclinic, the angle (β) between the a and c unit vectors is not equal to 90°.

Table 4.2: Rietveld refinement of synchrotron XRD data and calculated tensor components from CTEAS software. Values for all collected temperatures are publicly available through the University of Virginia Dataverse.^{90*} The heating element failed during the temperature ramp and caused the heating to stop at approximately 970 °C instead of 1000 °C.

Composition	T= 25 °C	T= 500 °C	T= 1000 °C
	$\alpha_{11}, \alpha_{22}, \alpha_{33}, \alpha_{31}$ ($\times 10^{-6} \text{ } ^\circ\text{C}^{-1}$)	$\alpha_{11}, \alpha_{22}, \alpha_{33}, \alpha_{31}$ ($\times 10^{-6} \text{ } ^\circ\text{C}^{-1}$)	$\alpha_{11}, \alpha_{22}, \alpha_{33}, \alpha_{31}$ ($\times 10^{-6} \text{ } ^\circ\text{C}^{-1}$)
$\text{Yb}_2\text{Si}_2\text{O}_7$	3.64, 3.28, 2.43, 0.66	4.66, 3.76, 3.06, -0.17	5.74, 4.26, 3.72, -1.04
$\text{Er}_2\text{Si}_2\text{O}_7$	3.74, 3.68, 0.85, -0.29	4.73, 3.90, 1.59, -0.55	5.77, 4.12, 2.38, -0.83
$(\text{Yb},\text{Er})_2\text{Si}_2\text{O}_7$ *	3.41, 2.97, 1.86, 0.28	5.13, 4.04, 2.86, -0.45	6.49, 5.17, 3.93, -1.21
$(\text{Yb},\text{Er},\text{Y})_2\text{Si}_2\text{O}_7$	3.42, 2.78, 1.45, 0.27	5.35, 4.06, 2.16, -0.56	7.36, 5.41, 2.91, -1.44
$(\text{Yb},\text{Er},\text{Y},\text{Dy})_2\text{Si}_2\text{O}_7$	2.43, 2.32, 0.92, 0.34	4.85, 3.79, 2.01, -0.47	7.41, 5.34, 3.17, -1.31
$(\text{Lu},\text{Yb},\text{Er},\text{Y},\text{Dy})_2\text{Si}_2\text{O}_7$	3.09, 2.78, 1.17, 0.19	5.08, 4.00, 2.08, -0.56	7.18, 5.29, 3.04, -1.36

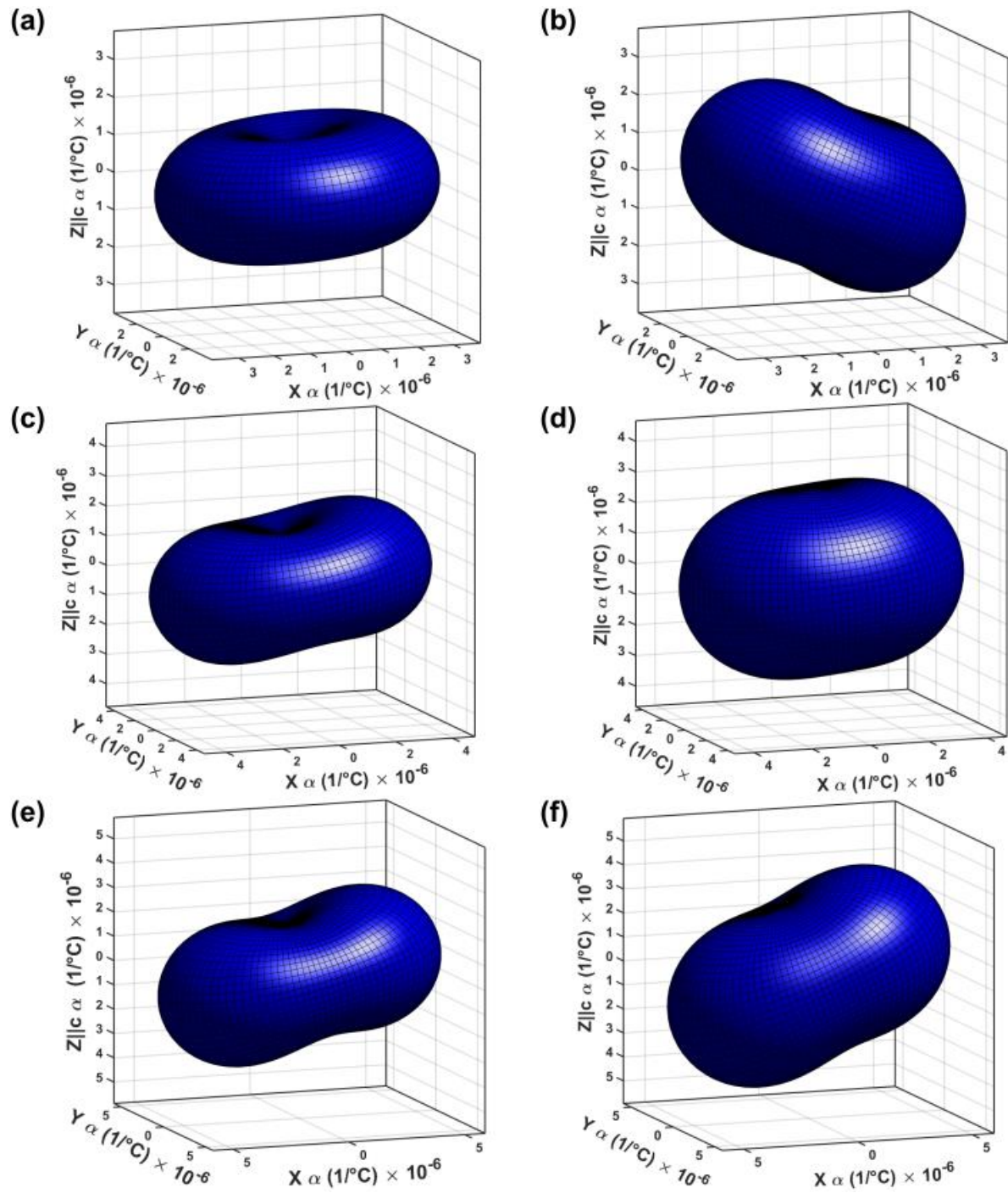


Figure 4.7: 3D representations of the CTE tensors for erbium and ytterbium disilicate at different temperatures. (a) $\text{Er}_2\text{Si}_2\text{O}_7$ at 25 °C. (b) $\text{Yb}_2\text{Si}_2\text{O}_7$ at 25 °C. (c) $\text{Er}_2\text{Si}_2\text{O}_7$ at 500 °C. (d) $\text{Yb}_2\text{Si}_2\text{O}_7$ at 500 °C. (e) $\text{Er}_2\text{Si}_2\text{O}_7$ at 1000 °C. (f) $\text{Yb}_2\text{Si}_2\text{O}_7$ at 1000 °C.

The distance from the origin to the 3-D surface corresponds to the magnitude of CTE in a specified crystallographic direction. From these expansion surface depictions, clear differences in the anisotropic

thermal expansion behavior between $\text{Er}_2\text{Si}_2\text{O}_7$ and $\text{Yb}_2\text{Si}_2\text{O}_7$ can be observed. Specifically, the rotation and variations normal to the Y axis in the 3D surface are temperature dependent. The shift in direction of maximum CTE is illustrated more clearly in a two-dimensional representation of CTE, which is a cross-section of the 3D depictions. **Figure 4.8** shows thermal expansion ellipsoids as polar plots in the (010) plane. Additional thermal expansion ellipsoids for lutetium, yttrium, and scandium are given in the appendix, **Chapter 9**. The a - and c -axis direction labels correspond to crystallographic directions in the (010) plane, while distance from origin is the magnitude of CTE. The blue portions of the ellipsoid represent cooler temperatures and red indicate elevated temperatures. The minimum and maximum temperatures shown are 25 °C and 1000 °C, respectively, and the intermediate steps shown are in 25 °C intervals. These data indicate that the principal axes are rotating upon heating. The direction of maximum CTE in $\text{Er}_2\text{Si}_2\text{O}_7$ shifts from approximately 85° to 77° relative to the c -axis across the range from room temperature to 1000 °C. In contrast, the direction of maximum CTE shifts from approximately 113° to 67° relative to the c -axis from room temperature to 1000 °C in $\text{Yb}_2\text{Si}_2\text{O}_7$. The angles of the eigenvectors relative to the c -axis were calculated via CTEAS and are shown in **Figure 4.9**. The ellipsoid shift represents a shift in principal axes without the principal axes having to lie exactly at the extremum. In fact, there is a difference of a few degrees between the angle of the eigenvectors and the CTE extremes relative to the c -axis. **Figure 4.9** shows the evolution of the eigenvectors (principal axes) with temperature for all compositions and illustrates that these thermal expansion extremum rotations are associated with nearly equivalent eigenvector changes. All REDS containing ytterbium exhibited a shift in direction of maximum CTE with temperature, including the high entropy sample, $(\text{Lu},\text{Yb},\text{Er},\text{Y},\text{Dy})_2\text{Si}_2\text{O}_7$. However, as the fraction of ytterbium in the composition decreased, the degree of rotation of the principal axes was reduced compared to pure $\text{Yb}_2\text{Si}_2\text{O}_7$. While certain REs, notably ytterbium, cause a rotation in principal axes, the driving mechanism is not clear. We speculate that this rotation is due to the ionic radii of the cations, specifically the smaller ytterbium and lutetium, filling more f-orbitals which may lead to variations in local bonding that manifests into anisotropic CTE.

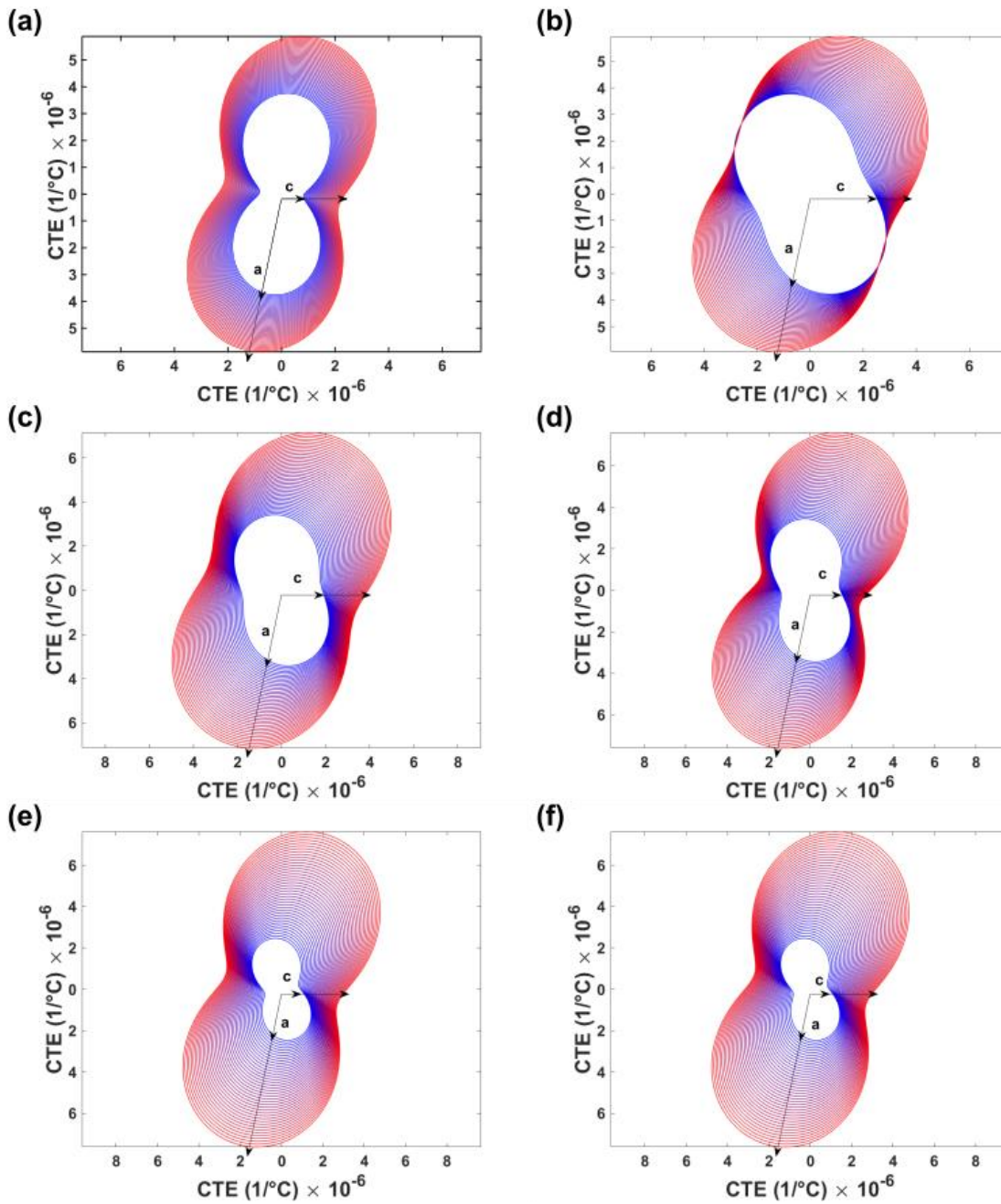


Figure 4.8: 2-D polar plots showing the change in the magnitude of CTE along crystallographic directions in the (010) plane from room temperature to 1000 °C. The color gradient represents the temperature, with blue being the lowest temperature and red being the highest. The ellipsoids represent the following REDS compositions: (a) Er,DS (b) Yb,DS (c) Yb,Er DS (d) Yb,Er,Y (e) Yb,Er,Y,Dy (f) Lu,Yb,Er,Y,Dy.

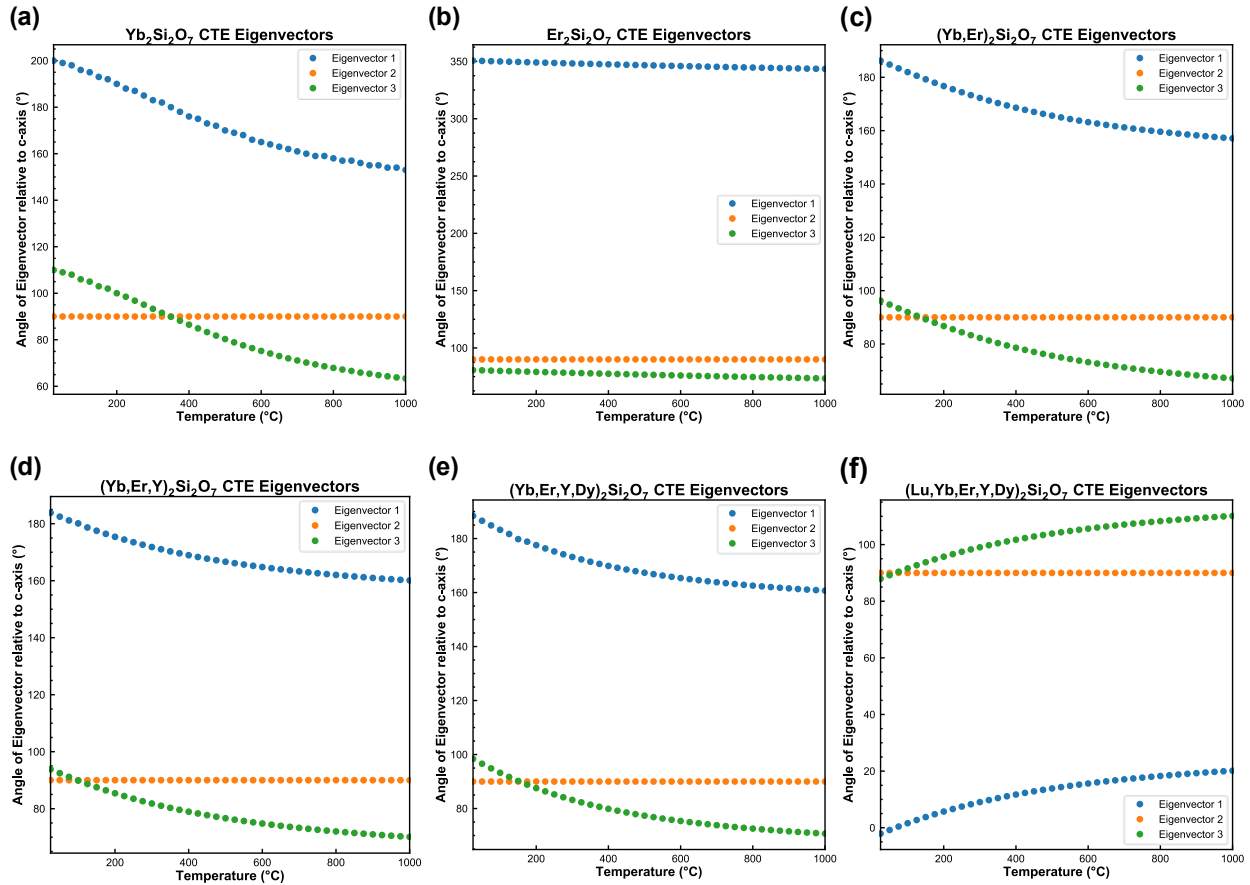


Figure 4.9: The angle of the Eigenvectors relative to the *c*-axis, [001] direction, were calculated using CTEAS. The trends seen in the Eigenvectors match the shifts seen in the 2-D ellipsoids where the minimum and maximum CTE values changed as a function of temperature. The Eigenvectors and principal axes are equivalent.

This variation in bonding is speculated to only affect CTE at lower temperatures before expansion can render the influence of the *f*-orbitals negligible, explaining why the final crystallographic direction of the maximum CTE converges to similar final angle for all samples regardless of composition, shown in **Figure 4.10**. The change in principal axes also manifests in the lattice parameters. **Figure 4.11** shows the normalized lattice parameters and beta angles of $\text{Er}_2\text{Si}_2\text{O}_7$ and $\text{Yb}_2\text{Si}_2\text{O}_7$. The distinction between the two compositions is seen through the magnitude of the expansion in the *c*-axis lattice parameter and shape of the beta angle trend across the temperature range. For compositions that undergo a shift in principal axes, the trend in beta angle with respect to temperature can be described as a U-shape. For $\text{Er}_2\text{Si}_2\text{O}_7$, the trend in beta angle is a near constant increase with temperature and no minimum can be observed. The normalized lattice parameters and beta angles versus temperature are included in **Figures 4.12** and **4.13** for all compositions. **Figure 4.14** shows how the a_{31} component is related to the beta angle for $\text{Yb}_2\text{Si}_2\text{O}_7$. The

temperature at which a_{31} transitions from negative to positive corresponds to the temperature of the beta angle minimum. The dependence of a_{31} and beta angle for all other Yb-containing compositions is shown in **Figure 4.15**.

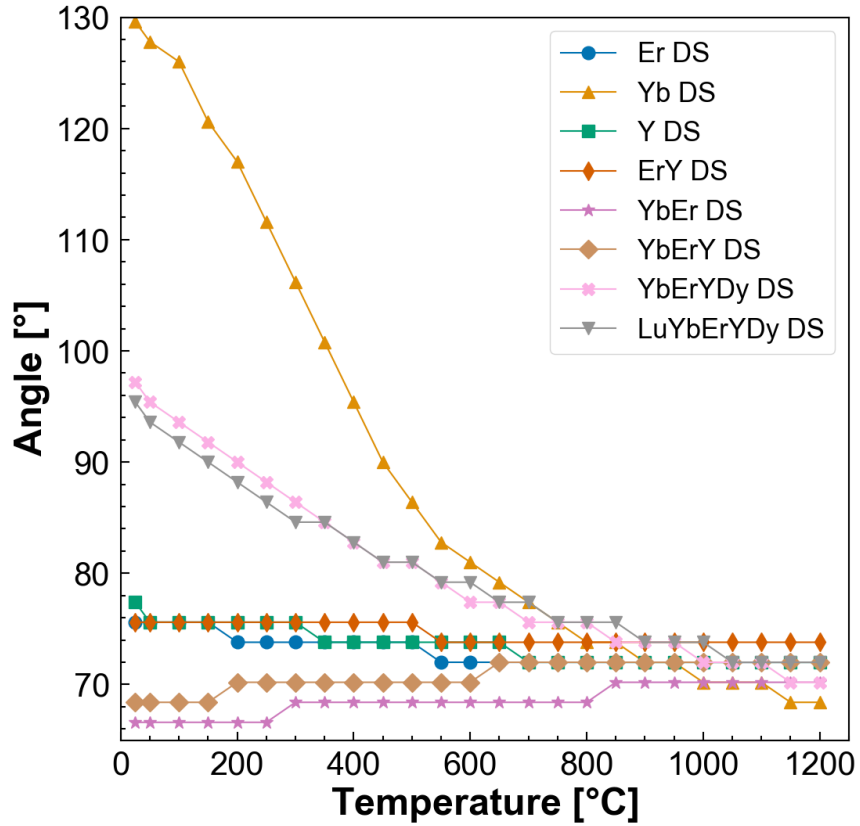


Figure 4.10: Plot of the angle of the eigenvectors relative to the c -axis versus temperature for several REDS compositions. The angles of the eigenvectors converge as temperature increases.

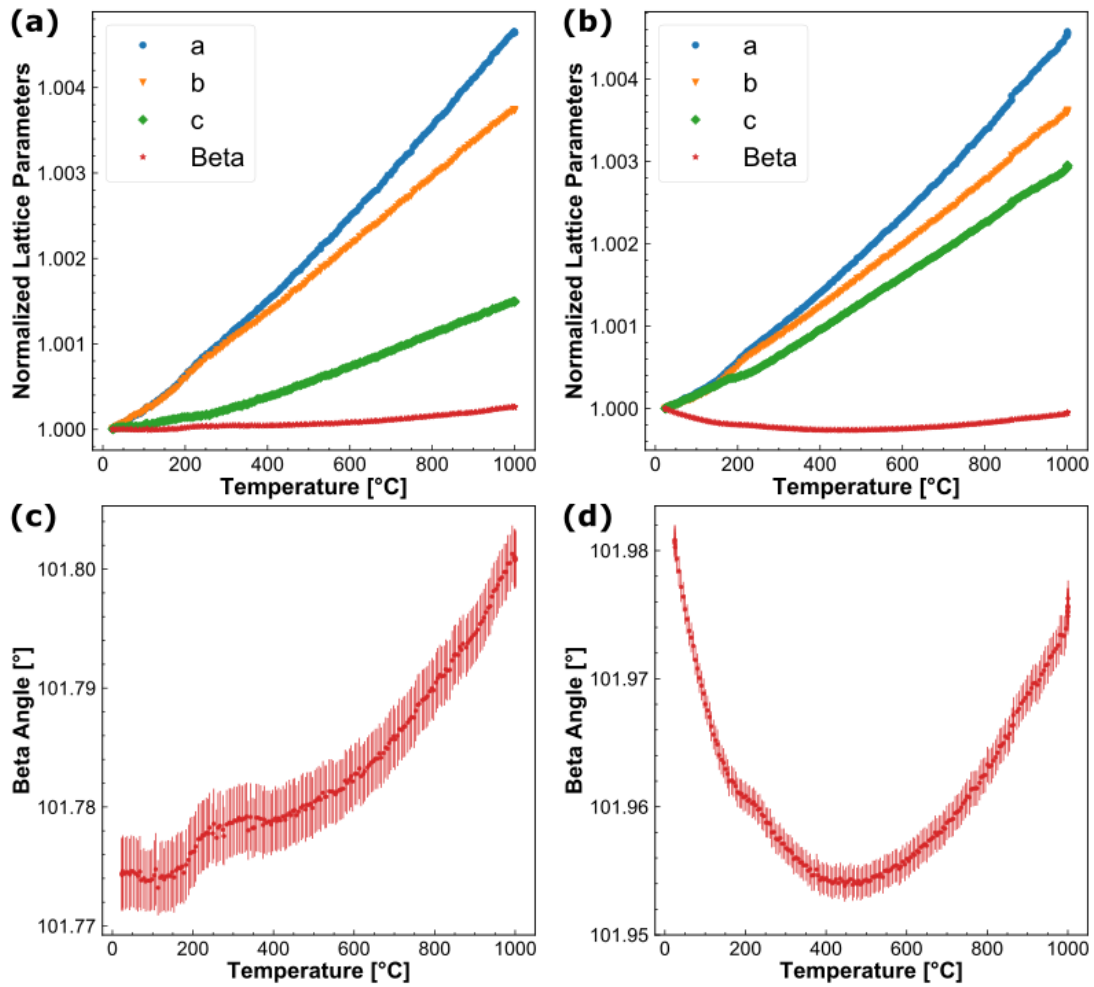


Figure 4.11: Temperature-dependent lattice parameters normalized to room temperature for (a) Er disilicate and (b) Yb disilicate showing a difference in expansion regarding the *c* unit cell direction and β angle. The difference in β angles for (c) Er disilicate and (d) Yb disilicate are shown in more detail.

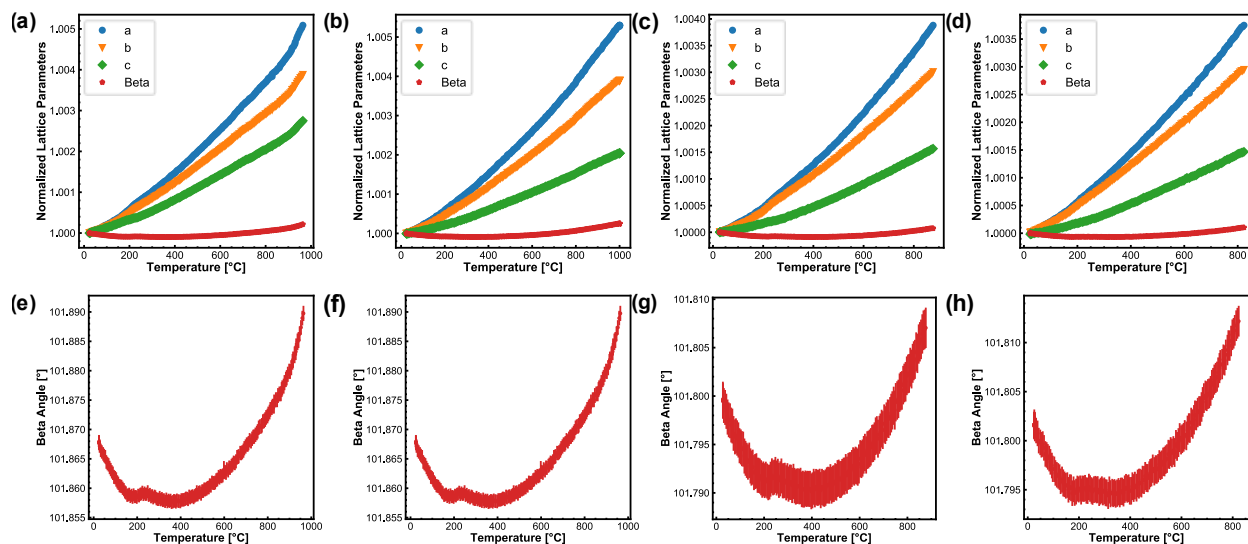


Figure 4.12: Lattice parameters versus temperature normalized to the value of the parameters at room temperature (a-d). Beta angle versus temperature showing the U-shaped trend that coincides with any composition that exhibits a shift in principal axes (e-h). The compositions are as follows: (a) and (e) are (Yb,Er) disilicate, (b) and (f) are (Yb,Er,Y) disilicate, (c) and (g) are (Yb,Er,Y,Dy) disilicate, and (d) and (h) are (Lu,Yb,Er,Y,Dy) disilicate. Certain datasets (c, d, g, and h) were cut off below 1000 °C due to thermocouple issues and in others the data points coinciding with the heating element break were removed (a and e).

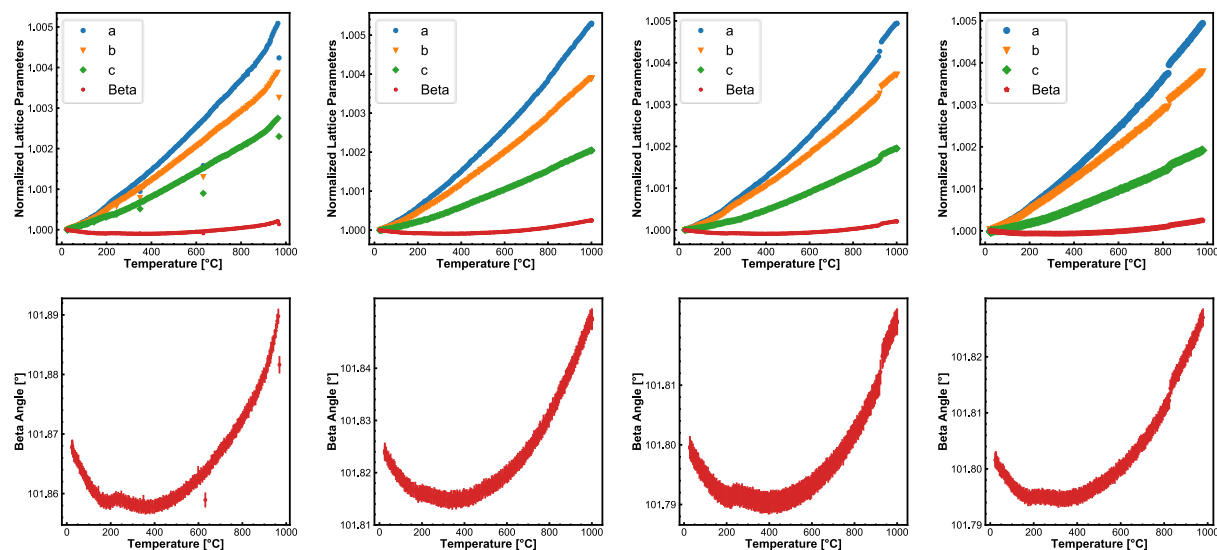


Figure 4.13: The data showing the discontinuities and errant data points mentioned in Figure 4.12. Lattice parameters versus temperature normalized to the value of the parameters at room temperature (a-d). Beta

angle versus temperature showing the u-shaped trend that coincides with any composition that exhibits a shift in principal axes (e-h). The compositions are as follows: (a) and (e) are (Yb,Er) disilicate, (b) and (f) are (Yb,Er,Y) disilicate, (c) and (g) are (Yb,Er,Y,Dy) disilicate, and (d) and (h) are (Lu,Yb,Er,Y,Dy) disilicate.

While the use of a linear CTE is commonplace, a single value does not describe an anisotropic crystal adequately. Additionally, the thermal expansion of a lattice can vary with temperature, meaning that temperature regimes of high and low expansion are lost within a singular linear CTE value. Linear CTE, however, is more commonly reported and is useful in comparing materials. With a tensor approach to CTE, the linear CTE can be calculated from the tensor components by averaging α_{11} , α_{22} , and α_{33} . Another method of calculating linear CTE, used by Fernández-Carrión *et al.*³³, provided similar linear CTE values without calculating tensor components. The aforementioned work by Fernández-Carrión *et al.* also reports similar linear CTE values for the REDS shown in this work.³³ The non-tensor method requires calculating $(\Delta V/3V_{RT})$, where ΔV is the change in unit cell volume relative to room temperature and V_{RT} is the unit cell volume at room temperature. Once the normalized change in unit cell volume is calculated, it is plotted versus temperature where a line of best fit is used. The slope of the line of best fit will be the estimated value of linear CTE. Both methods were assessed in this study and are shown to provide comparable values for linear CTE. The results are provided in **Table 4.3** for all compositions from the synchrotron diffraction experiment. Both methods of calculating the linear CTE produced values comparable to the values reported by Fernández-Carrión *et al.* for β -phase erbium and ytterbium disilicates.³³ **Table 4.4** gives the LCTE values from several sources in literature, where ranges are reported if multiple values were found.^{33,82,85,86} It is noted, however, that the tensor representation used in this work more clearly illustrates the rotation of direction of maximum thermal expansion via the change in principal axis vectors.

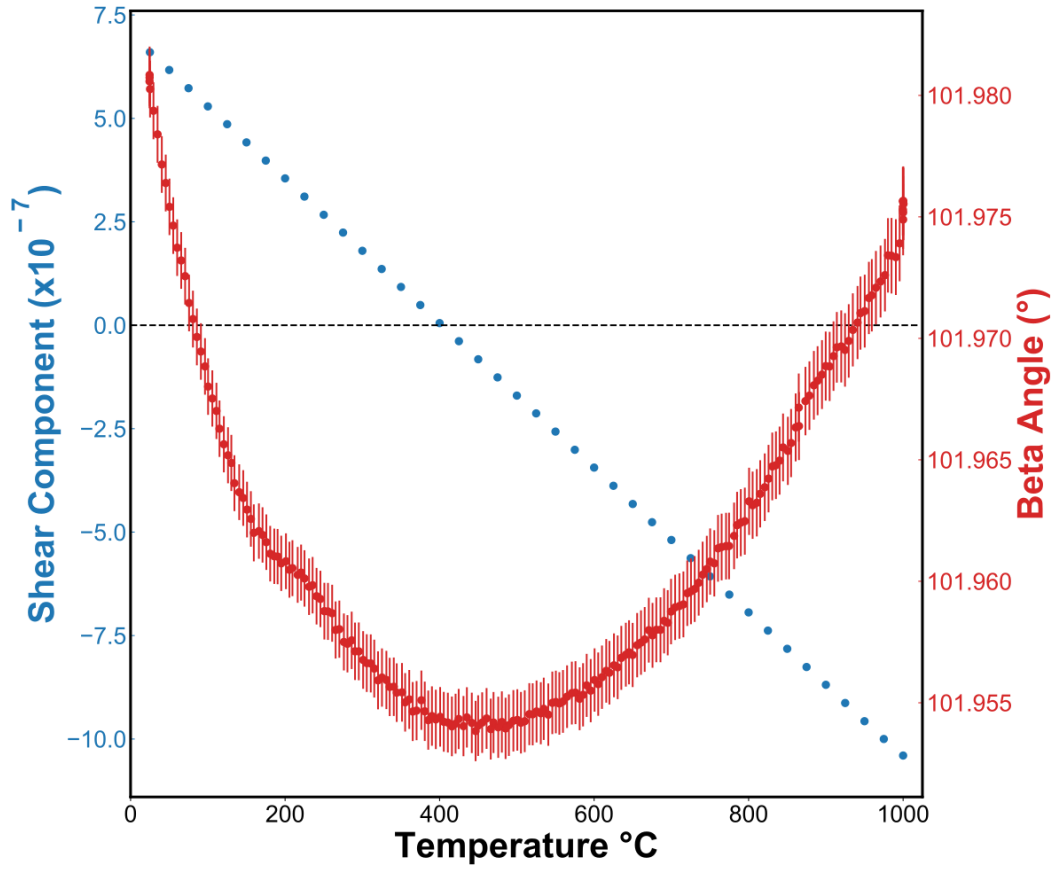


Figure 4.14: Shear component (α_{13}) and beta angle are plotted with respect to temperature for $\text{Yb}_2\text{Si}_2\text{O}_7$. A horizontal dashed line is given to represent when the shear component crosses over from positive to negative, and this intercept corresponds to similar temperatures at which the minimum of the beta curve occurs.

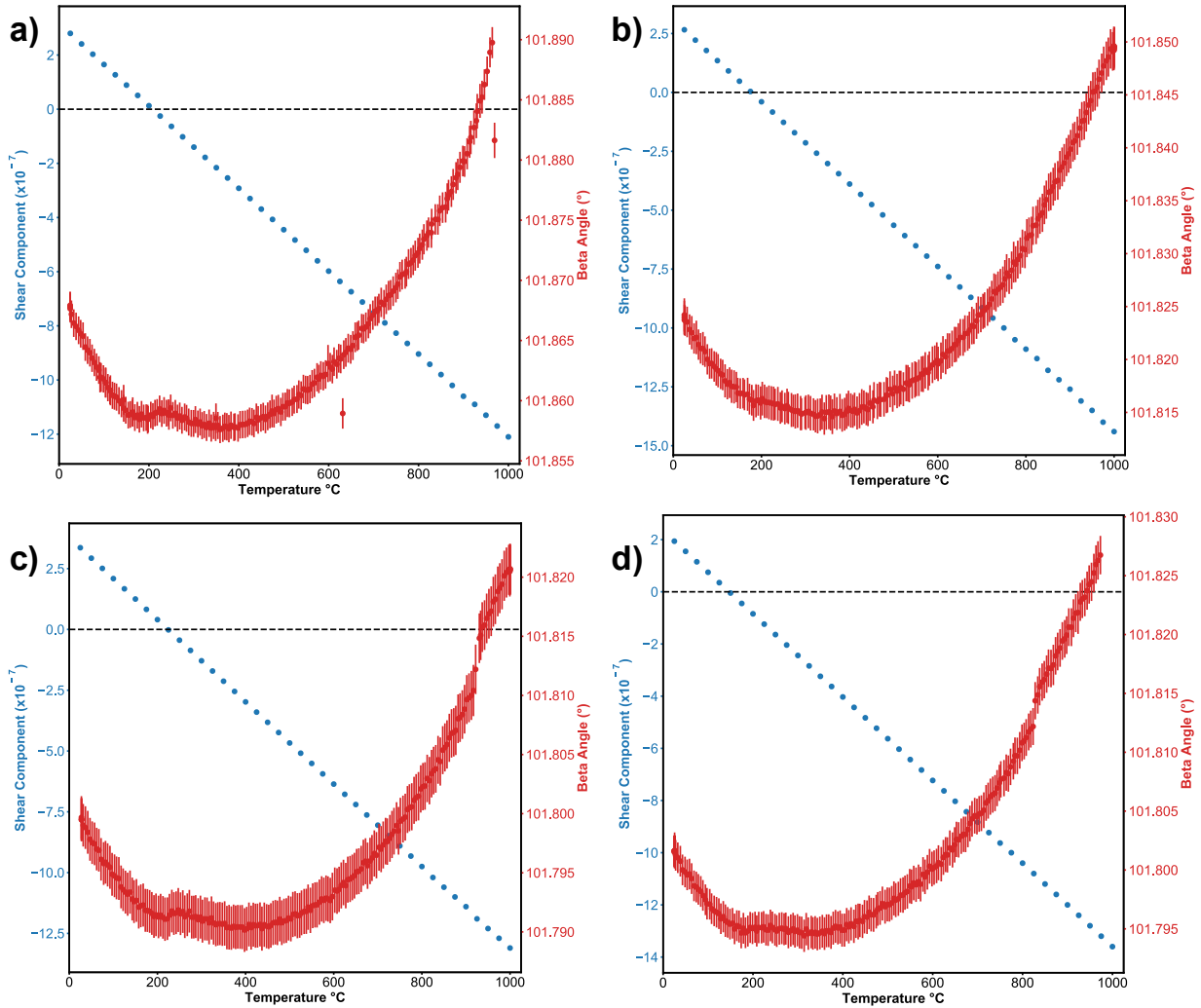


Figure 4.15: The shear components for all ytterbium containing samples compared to the beta angle trends with respect to temperature for a) (Yb,Er)₂Si₂O₇, b) (Yb,Er,Y)₂Si₂O₇, c) (Yb,Er,Y,Dy)₂Si₂O₇, and d) (Lu,Yb,Er,Y,Dy)₂Si₂O₇. The horizontal dashed line is to indicate the crossover point of the shear component from positive to negative. The x-intercept of the shear component lies at similar temperatures to the minimum of the beta angle curve. Erbium disilicate is not shown since the shear component is always negative and the beta angle shows a nearly constant increase with respect to temperature.

The temperature dependence of lattice parameters can allow for a deeper understanding of the thermo-mechanical considerations involved in engineering a T/EBC. The evolution of anisotropic CTE can impact the stress state of a polycrystalline material. It is clear from this work that ytterbium-containing compositions exhibit significant rotations in the principal axes and, therefore, complex local stresses may develop in the microstructure. Knowledge of the anisotropic CTE development, can be used to engineer T/EBCs through intentional crystallographic texturing to maximize compatibility with CMCs while

minimizing the intergranular stresses that may build up through the lifetime of the material, or may require alloying with non-ytterbium elements to reduce the degree of principal axis rotation.

Table 4.3: Comparison between two methods of calculating the average linear CTE from 25 °C to 1000 °C.

Composition	LCTE: Line of Best Fit (x10⁻⁶ 1/°C)	LCTE: Tensor Components (x10⁻⁶ 1/°C)
Yb ₂ Si ₂ O ₇	3.78	3.77
Er ₂ Si ₂ O ₇	3.48	3.49
(Yb,Er) ₂ Si ₂ O ₇	3.95	3.93
(Yb,Er,Y) ₂ Si ₂ O ₇	3.34	3.33
(Yb,Er,Y,Dy) ₂ Si ₂ O ₇	3.28	3.28
(Lu,Yb,Er,Y,Dy) ₂ Si ₂ O ₇	3.58	3.56

Table 4.4: Values for single component REDS from literature and the temperature ranges for the LCTE experiments. Due to differences in experimental methods, there are variations in values relative to the LCTEs derived from the samples shown in this work, and a range is shown for REDS with multiple LCTE values found. ^aRef. ³⁴, ^bRef. ³³, ^cRef. ⁸², ^dRef. ⁸⁵, and ^eRef ⁸⁶.

Sample	Literature LCTE (x10⁻⁶ °C⁻¹)	Temperature Ranges (°C)
Yb ₂ Si ₂ O ₇ ^{b,c,d,e}	3.62-4.5	25-1500
Y ₂ Si ₂ O ₇ ^a	4.1	25-1400
Er ₂ Si ₂ O ₇ ^b	3.9	30-1600

4.6 Conclusions

In summary, REDS powders were prepared using a sol-gel method. Additional cations were included to create single phase compositionally complex and high entropy ceramics. It was observed that the final phase of the REDS followed a rule of mixtures of cation radii that allowed for the stabilization of REs into atypical phases. The phase of the mixed and high entropy REDS studied remained stable from room

temperature to 1200 °C. High-temperature XRD data allowed for the determination of the second rank CTE tensors, enabling insight into anisotropy not possible with a single linear CTE value. The anisotropy of the REDS is contingent on the composition. The presence of ytterbium causes the direction of maximum CTE to shift with temperature, while $\text{Er}_2\text{Si}_2\text{O}_7$ has minimal shift in direction of maximum CTE. The influence of ytterbium in solid solution changed the principal axes and caused a distinct rotation behavior in the lattice throughout high temperature experiments. The cause for the shift in principal axes is currently unknown but is speculated to be due to the lanthanide contraction allowing for the f-orbitals of small rare-earth cations to indirectly impact bonding at lower temperature ranges. The effects of a rotating principal axis manifest through lattice parameters and CTE tensor shear components. Recognizing that these rotations exist and understanding their origins can help improve the thermo-mechanical considerations involved in creating T/EBCs for CMCs.

4.7 Data Availability

The data that support the findings of this study are available from the corresponding author upon reasonable request. The lattice parameters and tensor components for each composition in this study are openly available in the University of Virginia Dataverse at <https://doi.org/10.18130/V3/XI7QGF>.

4.8 Acknowledgement

The authors acknowledge Prof. Michelle Dolgos for instruction on Rietveld refinement procedures. Utilization of the Panalytical Empyrean and Anton Parr Hot-Stage instruments within UVA's Nanoscale Materials Characterization Facility (NMCF) was fundamental to this work. This work was supported by the U.S. National Science Foundation's (NSF) Designing Materials to Revolution and Engineer our Future (DMREF) program under award number 1921973. This research used resources of the Advanced Photon Source, a U.S. Department of Energy (DOE) Office of Science user facility operated by the Office of Science by Argonne National Laboratory under Contract No. DE-AC02-06CH11357.

Chapter 5 Cation Dependent Mechanisms of Anisotropic CTE in Rare-Earth Disilicates

5.1 Motivation

Chapter 4 introduced thermal expansion anisotropy and the dependence of eigenvector direction on rare earth cation. This chapter serves to elucidate the mechanisms by which the thermal expansion of the rare earth disilicates change as a function of temperature with only certain cations. Experiments were performed to study the interatomic distances, optical phonons, low temperature thermal expansion, and band gaps of ytterbium and erbium disilicates as these REDS showed contrasting CTE anisotropy behavior.

5.2 Cold Stage X-ray Diffraction

The hot stage X-ray diffraction data collected at the APS allowed for high resolution measurements of the change in lattice parameters. The monoclinic beta angle dependence on temperature was a major descriptor for the differences in CTE anisotropy between ytterbium and erbium disilicate, with ytterbium disilicate beta angle having a U-shaped trend while the beta angle in erbium disilicate had a near constant increase from room temperature to the maximum measurement temperature. From this data, a hypothesis arose that stipulated that the beta angle for erbium may also have a U-shape if the temperature range of the measurement is extended to lower temperatures, and the previously collected 25 °C to 1200 °C data is part of the half of the U-shape with a positive slope. To test this hypothesis, a single crystal X-ray diffractometer (Bruker D8 Venture) was used to collect the diffraction patterns of ytterbium and erbium disilicate at temperatures as low as 81 K (-192 °C). The diffraction patterns are shown in **Figures 5.1** and **5.2** for ytterbium and erbium disilicate respectively. While the slope of beta angle versus temperature for the ytterbium disilicate remained negative, the slope is flat for the erbium disilicate, revealing that there is no minimum between 81 K and room temperature. Thus, the hypothesis that a rotation of the thermal expansion principal axes of erbium disilicate does occur at low temperatures appears to be false.

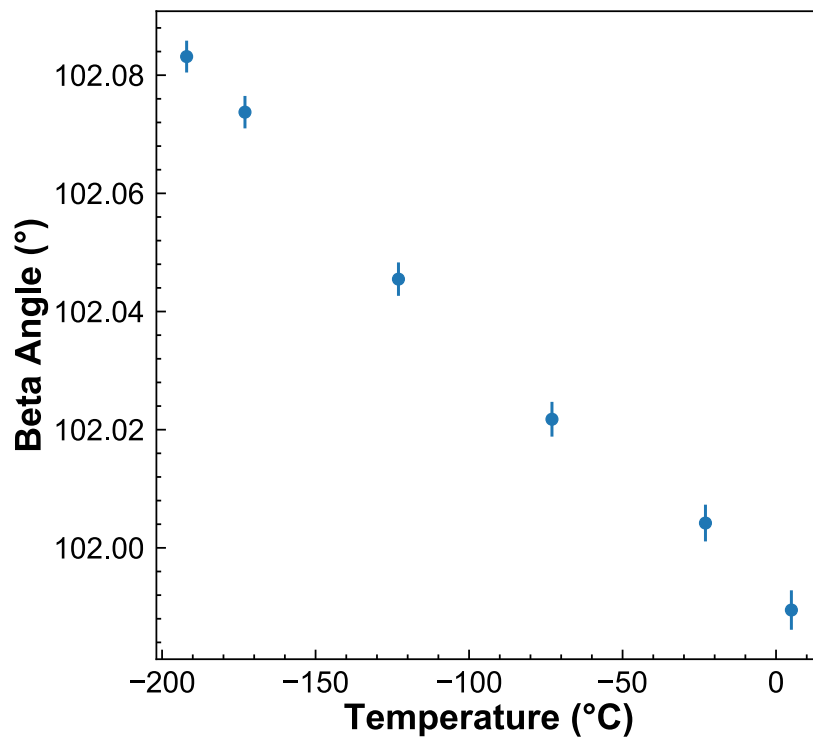


Figure 5.1: Monoclinic beta angles of ytterbium disilicate during cold stage X-ray diffraction.

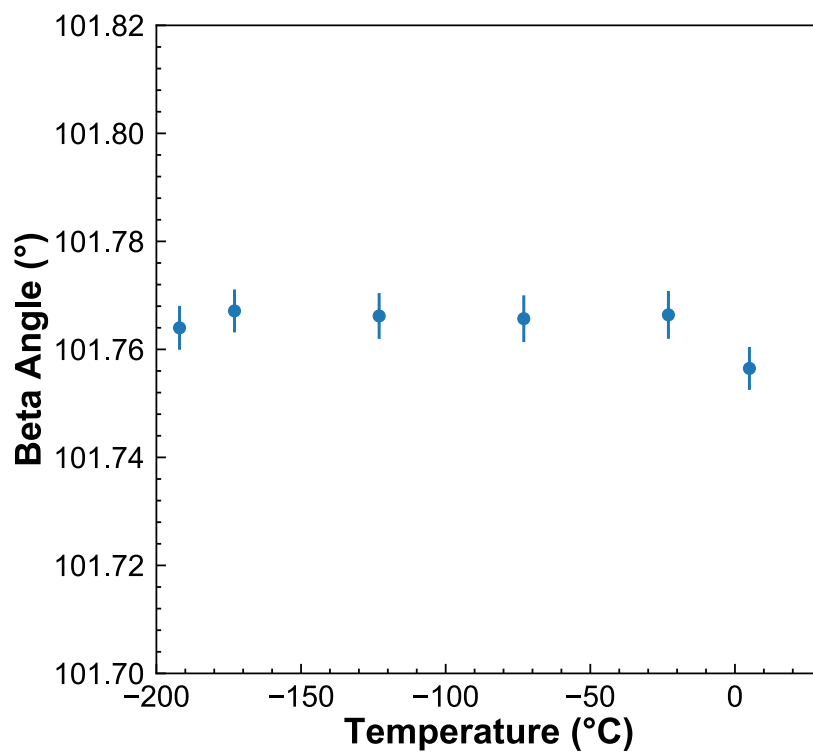


Figure 5.2: Monoclinic beta angles of erbium disilicate during cold stage X-ray diffraction.

5.3 Raman Spectroscopy

The bonding and structure of the REDS is a central point of investigation throughout this chapter. Raman spectroscopy was used to qualitatively compare the optical phonons of REDS and determine if there is a correlation with CTE anisotropy. Raman spectroscopy was the technique chosen since it was hypothesized that the Raman spectra, which corresponds to vibrational modes excited by the incident light, would indicate that the vibrational modes differ between the REDSs with distinct cations. Moreover, *in situ* Raman spectroscopy was used to compare the spectra across an identical temperature range to the *in situ* X-ray experiments. Ytterbium, erbium, and lutetium were the rare earth disilicates used to compare the CTE anisotropy behavior, with ytterbium and lutetium showing large eigenvector shifts and erbium exhibiting nearly no eigenvector shift.

The Raman experiments initially showed that the erbium disilicate powder was different from the other two, shown in **Figure 5.3**. These results contradicted computationally derived Raman spectra of the three given REDS, shown in **Figure 5.4**. Further discussion with collaborators helped identify that the only differences between the Raman spectra of the three REDS were the intense peaks above 1000 cm^{-1} . These peaks originate from resonance and are not representative of the structure or optical phonon behavior of the material. The resonant Raman added signal shown in the spectra in **Figure 5.3**, which is not accounted for in the computational model shown in **Figure 5.4**. Based off the computational Raman spectra, the three REDS would be nearly identical if the resonance was removed, and this proved to be the case experimentally. The experiments that followed were hot stage Raman measurements up to $1200\text{ }^{\circ}\text{C}$. The hot stage Raman data is shown in **Figures 5.5** and **5.6** for ytterbium and erbium disilicates, respectively. The resonance remains at higher temperatures but, like all signals, begins to decrease in intensity as the temperature increases due to a rising noise floor. All non-resonance peaks behave in near identical fashion for all three REDS, indicating that the trend seen in CTE anisotropy cannot be correlated with optical phonon behavior and other experiments are needed to continue exploring the origin of the anisotropy.

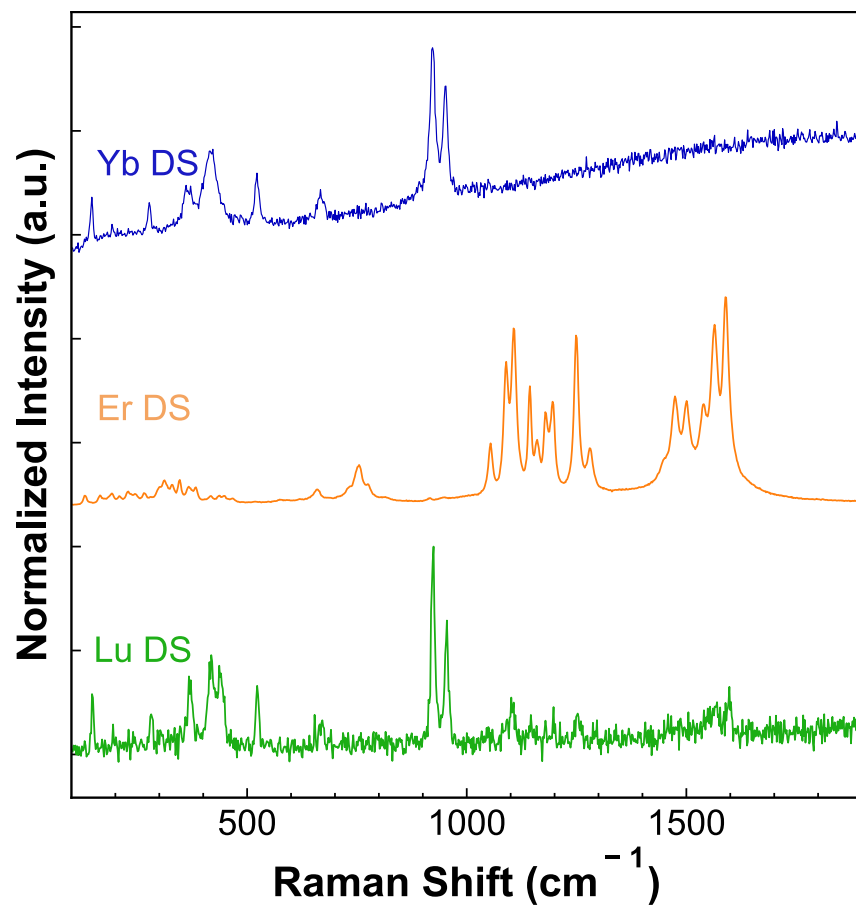


Figure 5.3: Room temperature Raman spectra of $\text{Yb}_2\text{Si}_2\text{O}_7$, $\text{Er}_2\text{Si}_2\text{O}_7$, and $\text{Lu}_2\text{Si}_2\text{O}_7$.

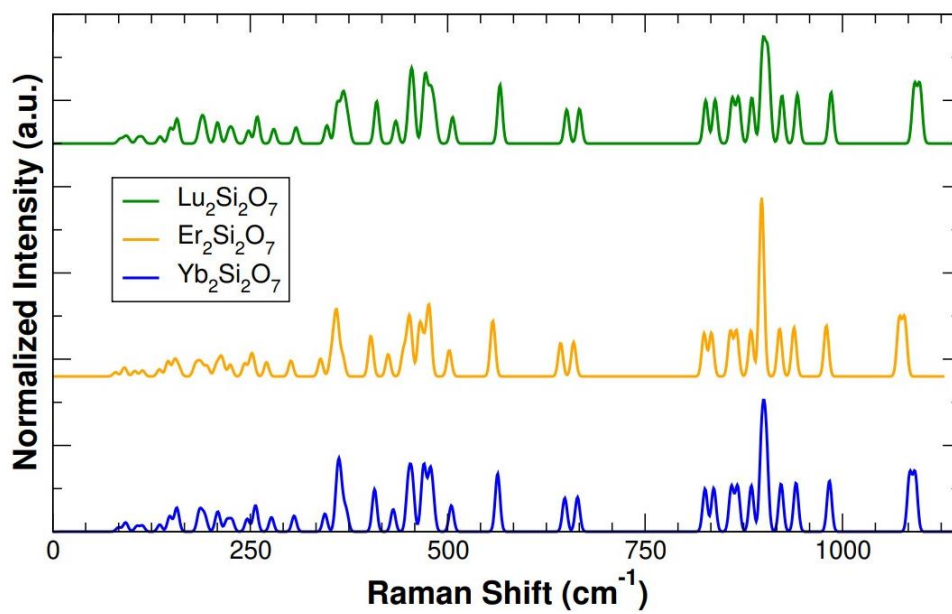


Figure 5.4: Computational Raman spectra of $\text{Yb}_2\text{Si}_2\text{O}_7$, $\text{Er}_2\text{Si}_2\text{O}_7$, and $\text{Lu}_2\text{Si}_2\text{O}_7$.

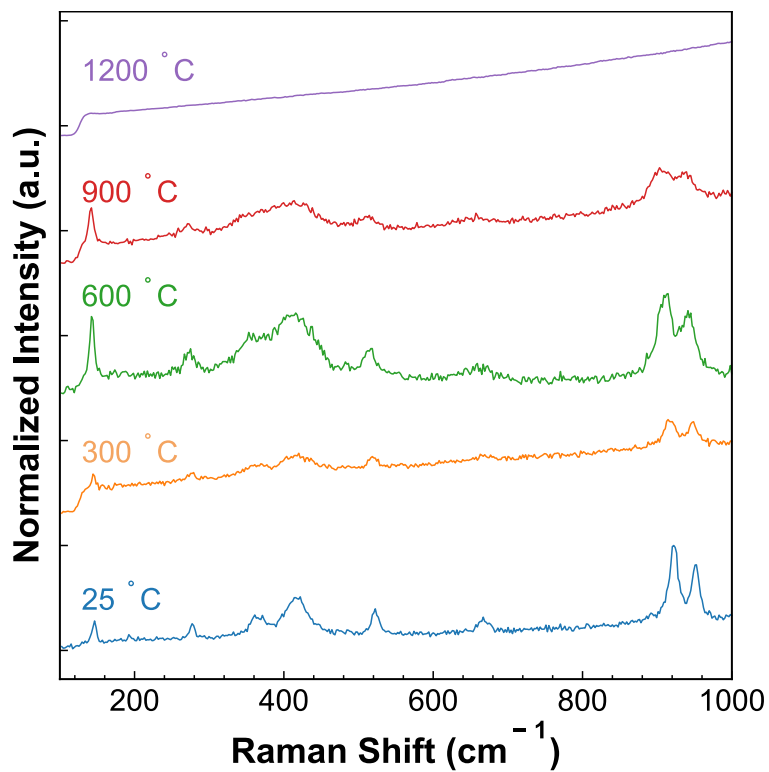


Figure 5.5: Hot stage Raman spectra of $\text{Yb}_2\text{Si}_2\text{O}_7$ from room temperature to 1200 °C.

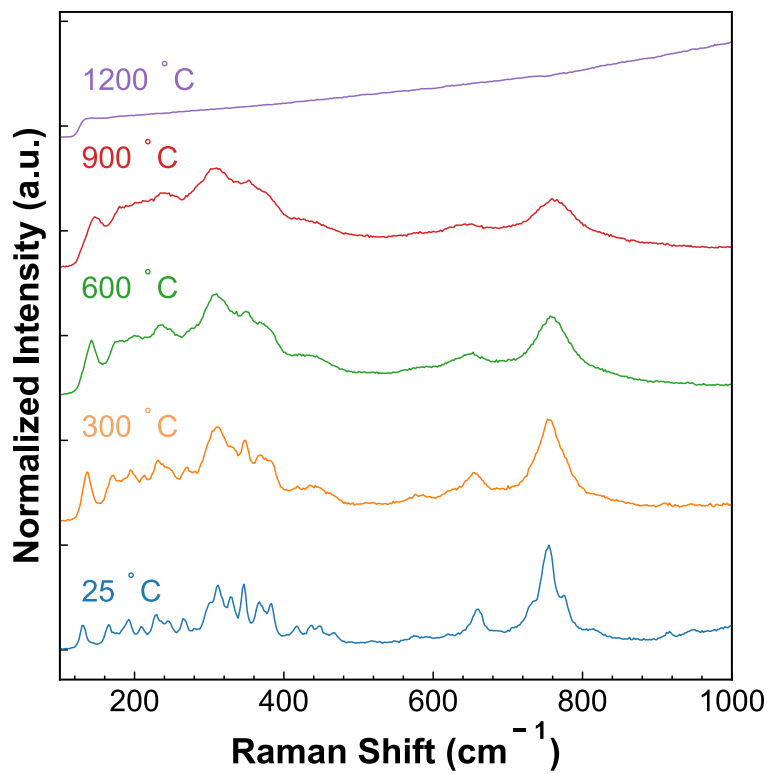


Figure 5.6: Hot stage Raman spectra of $\text{Er}_2\text{Si}_2\text{O}_7$ from room temperature to 1200 °C.

Due to the resonance, comparing the optical phonon behavior of the REDS was not possible through Raman spectroscopy. Instead, FTIR was used to probe optical phonons while avoiding any resonance. FTIR experiments were only done at room temperature since there was no method of performing hot stage measurements like in XRD and Raman. Additionally, more REDS were tested, including scandium and ytterbium disilicate. The FTIR spectra are shown in **Figure 5.7**, showing very little difference between the REDS. Some differences are to be expected with the FTIR spectra due to the size and mass difference in rare earth cations. Since the peaks correspond with atomic vibrations and are then correlated to the bonding, different ions will have distinct bond strength and therefore change peak position, intensity, and width. A distinction in the spectra is the pair of peaks at approximately 475 and 500 cm^{-1} . For scandium disilicate, this pair of peaks is missing, with only one peak at a slightly higher wavenumber. Without the resonance, it suggests that optical phonon behavior cannot be correlated to CTE anisotropy in this case. The acoustic phonons were then considered but, unfortunately, they are much more difficult to measure experimentally. Professor Prasanna Balachandran at UVA calculated the phonon dispersion curves that would show both optical and acoustic phonons. From these calculations it was noticed that the model predicted a difference in slope of an acoustic phonon where the difference was between the REDS that did and did not “rotate” in the anisotropic CTE models (erbium did not rotate while ytterbium and lutetium did). The difference in slope of a phonon curve corresponds to the speed of sound of a wave in that material along a specific crystallographic direction. This result once again indicated that there are anisotropies within REDS containing certain rare earth cations.

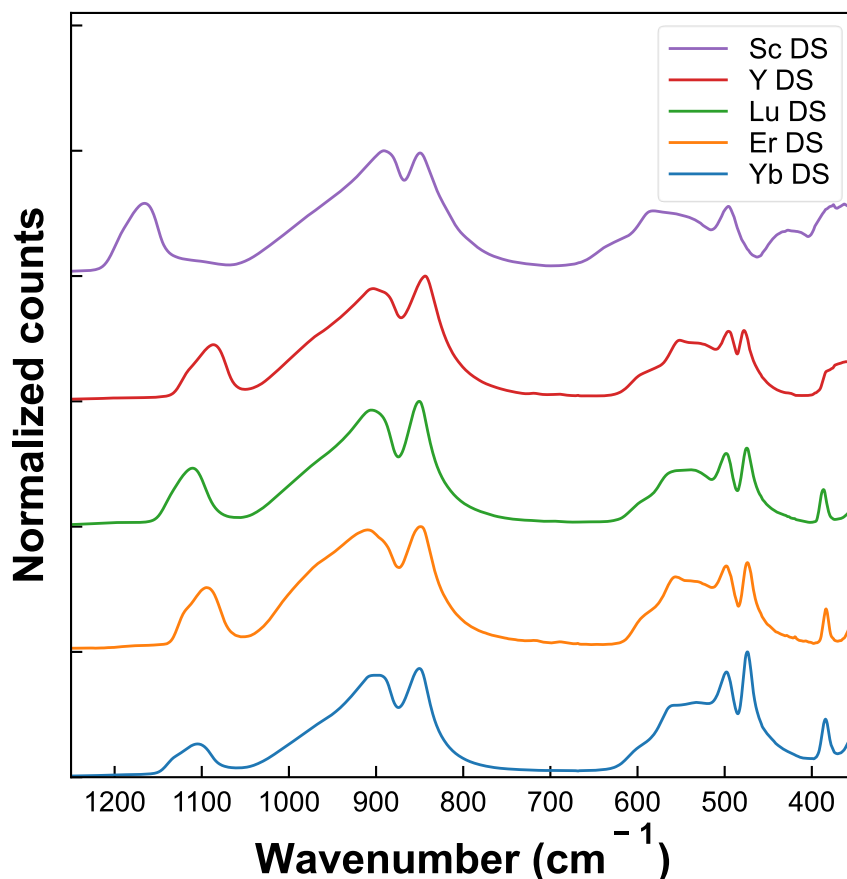


Figure 5.7: FTIR spectra of multiple REDS. These spectra do not have the resonance seen in Raman and are very similar across the range of rare earth cations.

5.4 UV-VIS Spectrophotometry

The next area of study following the optical phonon work with Raman spectroscopy and FTIR was measuring the band gaps of the REDS as a qualitative comparison tool for differences in electronic configuration. UV-Vis spectroscopy was used to collect transmission data as a function of wavelength, then this data was converted to absorption versus energy. The conversion to absorption will vary depending on if the band gap is direct or indirect, denoted by the power of 2 or $\frac{1}{2}$ respectively. Initially, REDS powder was mixed with potassium bromide powder in a 1:200 mg ratio of REDS and KBr to produce a transparent pellet for UV-Vis. These experiments were unsuccessful due to ambient humidity having a great effect on the opacity of the pellet. Instead of pellets, films of REDS were spin coated onto fused quartz. The spin coating process was adapted from the sol gel-procedures used in previous chapters and the specifics regarding the sol-gel process are discussed in much greater detail in **Chapter 6**. The steps for creating the solution and spinning the film are as follows:

1. Remove rare earth nitrate from glove box.
2. Weigh out nitrate precursor (less than a gram) and mix with 200 proof ethanol in a scintillation vial.
3. Weigh TEOS out for a 1:1 molar ratio between Si and rare earth and mix in the same vial as the rare earth nitrate precursor.
4. Add two drops of deionized water, a drop of HCl, and mix for two to three hours.
5. Once the solution is well mixed, it's time to begin the spin coating process.
6. Heat a hotplate next to the spin coater to 300 °C and wait for the hotplate to reach equilibrium.
7. Clean fused quartz substrate with isopropanol and compressed air.
8. Let the substrate dry on the hot plate for thirty seconds.
9. Place the substrate on a clean heat sink. A steel plate was used as a heat sink in these experiments.
10. Place the substrate into the spin coater and coat the substrate dropwise using a syringe until the quartz is completely covered.
11. The sample is spun for thirty seconds at 3000 rpm.
12. The sample is taken and placed onto the hotplate for minutes.
13. The sample is cooled again on the heat sink and steps 10-12 are repeated depending on the desired film thickness.

The transparent substrate and films produced via spin coating allowed for successful UV-Vis measurements. **Figures 5.8** shows the full energy range measured for ytterbium and erbium disilicate with absorption calculated for direct and indirect band gaps. The band gap values are extracted from the linear portion at the higher energies shown. At the highest energies, scattering occurs that results in the data being too noisy to extract useful band gap information. A reduced range of the direct and indirect band gap plots that compare ytterbium and erbium disilicate are shown in **Figure 5.8**. This figure shows the approximate ranges used for calculating band gaps and do not contain the same amount of high energy scatter. Qualitatively, these plots show a difference in band gaps due to distinct curves at high energies, meaning that the rare earth cation will change the band gap of the REDS. The difference in bandgap indicates that there is a difference in electronic structure between the REDS. Ytterbium has a full *s*- and *f*- orbital shell; additionally, Yb^{3+} loses both *s* electrons and a single *f* electron. Erbium has two electrons missing from the *f*-orbital, meaning that Er^{3+} has a total of three electrons missing from the *f* shell. The difference in electronic structure was hypothesized to be correlated to the CTE anisotropy since the differences in *f*-orbitals may result in crystal field splitting. The splitting would result in distinct *f*-orbital shapes between the different REDS and therefore result in anisotropic changes in bonding strength. The band gap measurements were

not a conclusive test of the hypothesis, but further literature indicated that while f -orbitals can in fact split, they typically do so for the actinides and not the lanthanides.^{91,92} Instead of orbital splitting, the f -orbitals may be contributing to bonding by screening of electric charge. By screening the bonding d -orbitals from the nucleus, the f -orbitals may be indirectly participating in bonding and subsequently affecting both band gap results of REDS as well as CTE anisotropy. The band gap fits and calculations are shown in **Figure 5.9** for both REDS as direct and indirect band gaps.

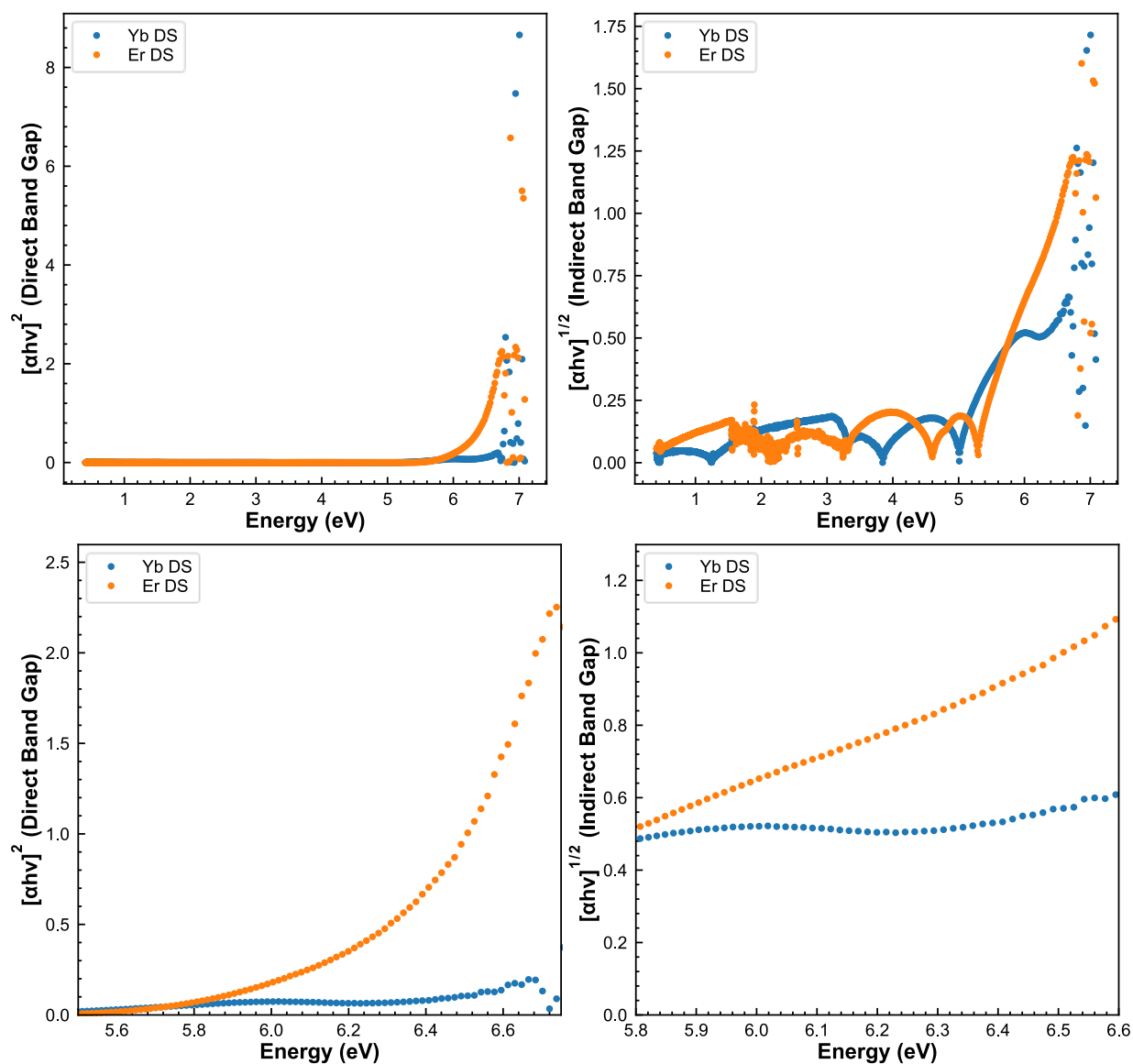


Figure 5.8: UV-Vis data showing absorption versus energy for ytterbium and erbium disilicate as materials with direct and indirect band gaps. Additionally, reduced ranges for the direct and indirect plots are shown at the higher energies.

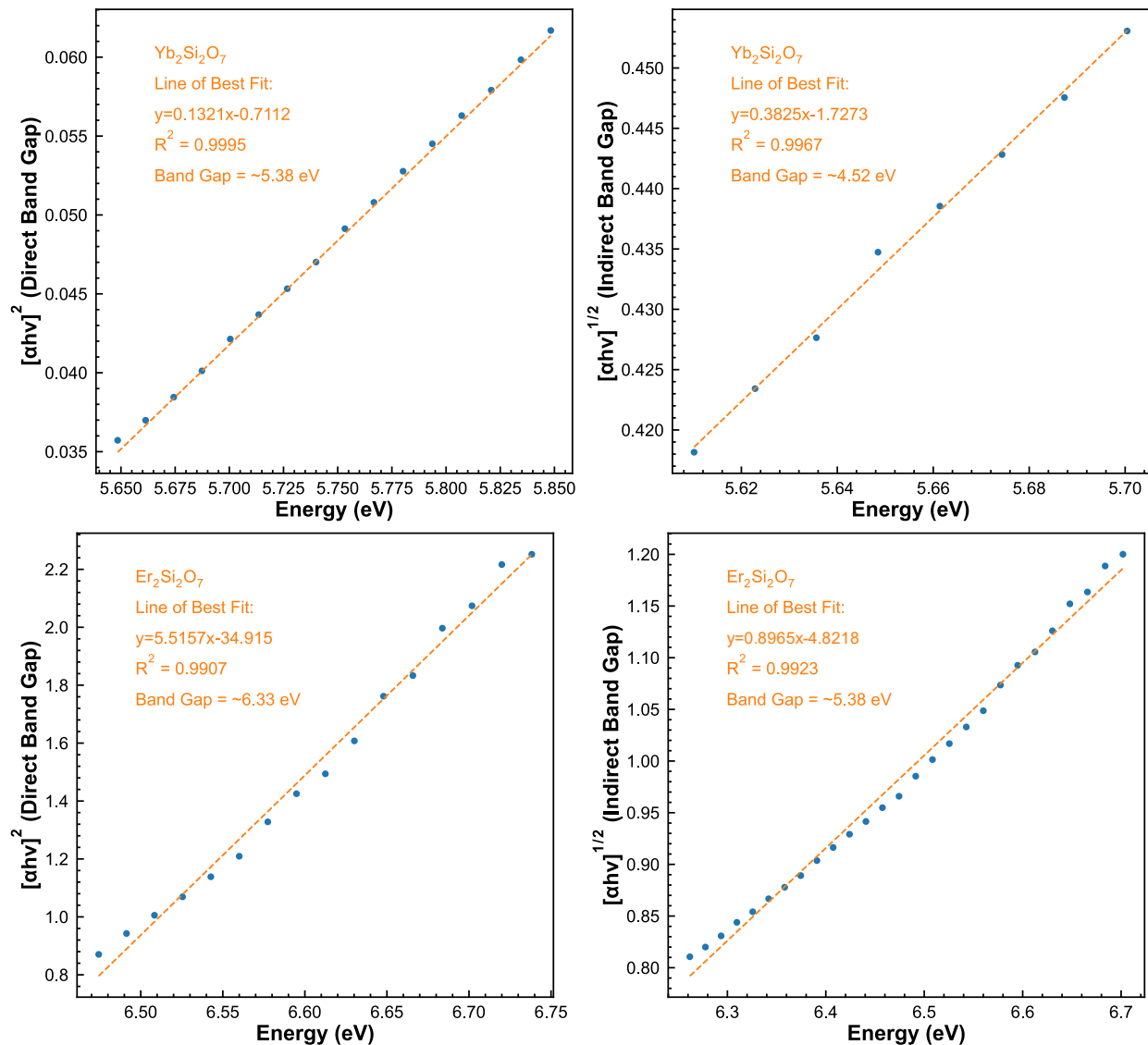


Figure 5.9: Direct and indirect band gap calculations and fit for ytterbium and erbium disilicate.

5.5 Synchrotron X-ray PDF Analysis

X-ray diffraction experiments performed at beamline 11-ID-C at the APS were mentioned in the previous chapter as a continuation of in-lab diffraction studies. Beamline 11-ID-C is also capable of *in situ* X-ray PDF measurements. The only change made to the experimental setup was reducing the sample to detector distance to 600 mm. The PDF measurements required longer collection times and would, therefore, only be possible for a larger temperature interval. A cerium oxide standard, provided by the beamline, was used to calibrate the instrument. PDF on the REDS were attempted twice, with the difference being the phase purity of the sample material. During the second trip to the APS, phase pure REDS procured from Praxair were brought to measure and produce PDFs more easily. The reason for why the phase purity was

necessary is because PDFs are generated by correcting for scattering factors, which requires inputting the composition of the sample material. In the first attempt, the phases were known but the exact chemical composition, including amorphous material, was unknown.

The PDF data for ytterbium and erbium disilicate powders are shown in **Figures 5.10** and **5.11**, where the data from 1-5 Å is shown with labeled peaks to indicate important distances such as the Si-O and Er-O distances. The O-O distances are labeled with a superscript to denote to which polyhedron the O-O belongs. The peak to the left of the Si-O labeled peak does not correspond to an interatomic distance and is most likely an artifact from the background or a resonance ripple. The PDFs were not of sufficient quality to determine if there are differences between the ytterbium and erbium disilicate that can be correlated to CTE anisotropy. A method of improving PDFs of the REDS is to perform the same *in situ* experiments but with neutron scattering instead of X-rays. The reason for this is because X-ray scattering intensity scales with atomic mass of elements because X-rays scatter off the electron cloud, meaning that higher Z elements are better X-ray scatterers. The lighter elements are difficult to detect using X-rays, and the very high energies used in the synchrotron studies at the APS were not sufficient to adequately resolve the Si-O or RE-O interatomic distance distributions. Alternatively, neutrons do not scatter off the electron cloud, instead neutrons scatter off the nucleus of atoms and there isn't an atomic number dependency with scattering cross-section. Neutron scattering is much more sensitive to lighter elements and can be used to properly capture the distances between the Si-O and RE-O atom pairs. These neutron experiments are outlined in **Section 5.6**.

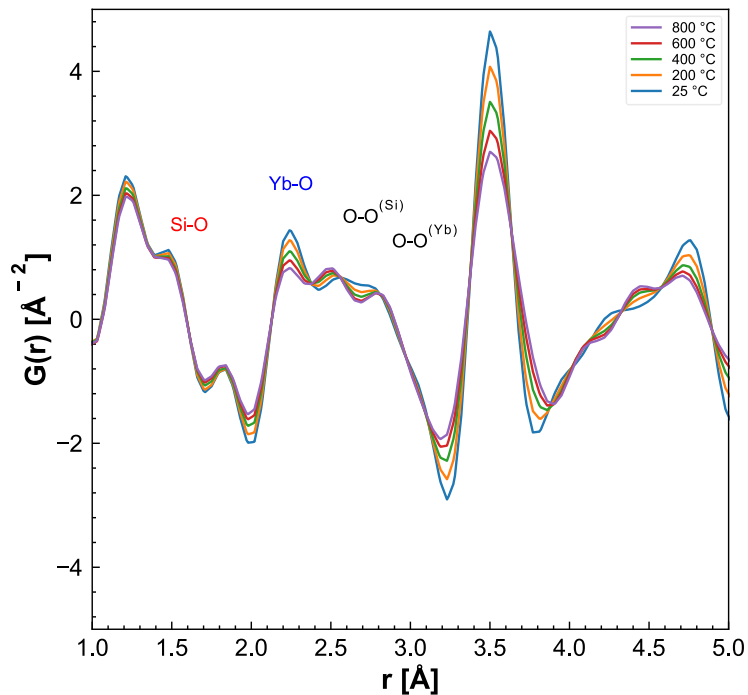


Figure 5.10: X-ray PDF of the small interatomic distances in ytterbium disilicate. The superscripts for the oxygen-oxygen distances are labeled to denote to which polyhedron they correspond.

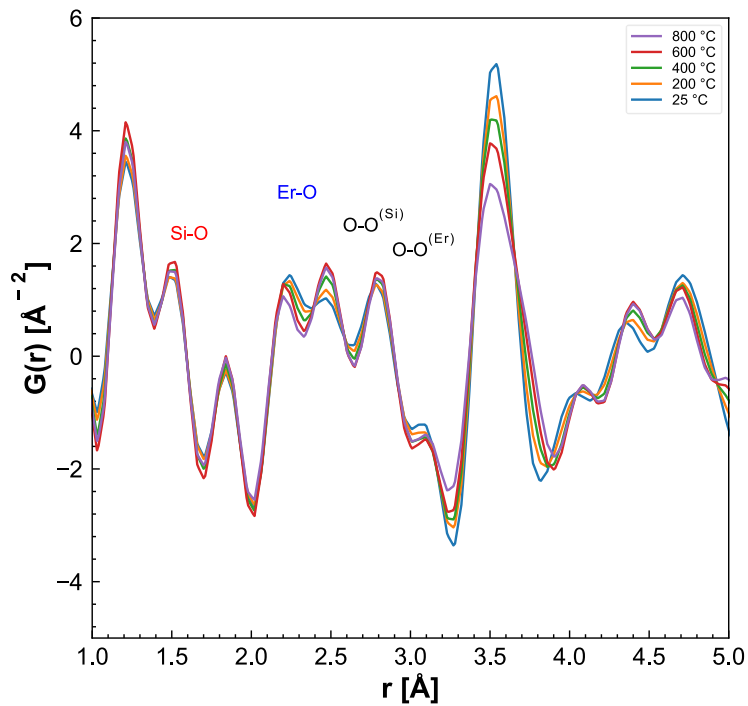


Figure 5.11: X-ray PDF of the small interatomic distances in erbium disilicate. The superscripts for the oxygen-oxygen distances are labeled to denote to which polyhedron they correspond.

5.6 Neutron Diffraction and Scattering

The PDF experiments at the APS served as a starting point for understanding how the interatomic distances change as a function of temperature for ytterbium and erbium disilicate. Due to the poor scattering of lighter elements, such as oxygen, for X-rays, the APS results were not sufficient to make conclusions regarding CTE. Neutron scattering was identified as an alternative to X-rays as neutrons will be able to detect oxygen in REDS. A general user proposal was written for time at the NOMAD beamline at Oak Ridge National Laboratory's Spallation Neutron Source (SNS). The difference between an X-ray and neutron PDF was shown in **Chapter 2**. The only peak with a greater intensity in X-ray scattering than neutron scattering would be the rare earth-rare earth distance, but the difference is not enough to affect the equality of the neutron PDF. Additionally, similar work has been conducted using neutron scattering to characterize the structural disorder and polyhedral movement as a function of temperature for silica tetrahedra.⁹³⁻⁹⁹ Given the comparison for REDS, neutrons are necessary for adequate PDF experiments and elucidating how interatomic distances change across the experimental temperature range.

While neutrons have an advantage over X-rays in this case, there are also challenges due to the resonance of ytterbium and even more so erbium with neutron scattering. The resonance affects the data by introducing additional peaks that may obscure the real crystallographic information. Resonance reduction was done by beamline scientists at Oak Ridge National Laboratory. The data before and after the resonance reduction are shown in **Figures 5.12** and **5.13** respectively. Certain peaks in these two figures are labeled to indicate important interatomic distances such as silicon and oxygen. Additionally, the oxygen-oxygen distances are followed by a superscript that denotes whether the oxygen pair is in a silicon or rare earth polyhedron. A consequence of the resonance reduction is that it results in data of lower resolution. The resonance in the erbium disilicate sample was more severe than in ytterbium, as erbium has greater neutron resonance absorption. Additionally, when creating the PDFs a challenge lies in selecting an appropriate Q_{\max} value. Q is the lattice vector defined by the following equation:

$$Q = 4\pi \sin(\theta) / \lambda \quad (5.1)$$

The Q value is of import due to PDFs being produced by applying a sine Fourier transform of the scattering factor, $S(Q)$, from $Q = 0 \text{ \AA}^{-1}$ to $Q = \infty \text{ \AA}^{-1}$. Experimentally, the zero to infinity range is not possible, so a Q_{\min} and Q_{\max} need to be defined. Selecting an appropriate Q_{\max} requires consideration, especially for the post resonance reduction data discussed in this work. Selecting a finite Q_{\max} results in ripples at low r that reduce in amplitude as r increases.¹⁰⁰ Selecting a Q_{\max} that is too low will make these ripples worse, and this trend continues as Q_{\max} decreases. These ripples can interfere with the investigation of short interatomic distances as is the case for this work. A Q_{\max} that is too high introduces noise into the PDF that may inhibit

proper analysis by overwhelming data with low counting statistics.¹⁰⁰ The “best” Q_{\max} for ytterbium and erbium disilicate samples were 24 \AA^{-1} and 17 \AA^{-1} respectively, with erbium having a lower Q_{\max} due to the greater degree of resonance absorption. The Q_{\max} was determined during the resonance reduction procedure by producing PDFs of varying Q_{\max} values and determining which PDF had the best balance between the tradeoffs of high and low Q_{\max} . A comparison between the room temperature and 1000 °C PDF data for ytterbium and erbium disilicate are shown in **Figure 5.14**. This figure illustrates the differences in peak intensity that decreased post resonance reduction. **Figure 5.14** can be used to qualitatively compare the local distortions in the lattices for ytterbium and erbium disilicate. The major differences visible between the two besides the difference in intensity is the peak shapes of the Si-O and O-O distances. These changes indicate that the polyhedron do not distort in the same manner in both samples, and due to the different rare earth cation there may be distortions in the silica tetrahedron as temperature increases.

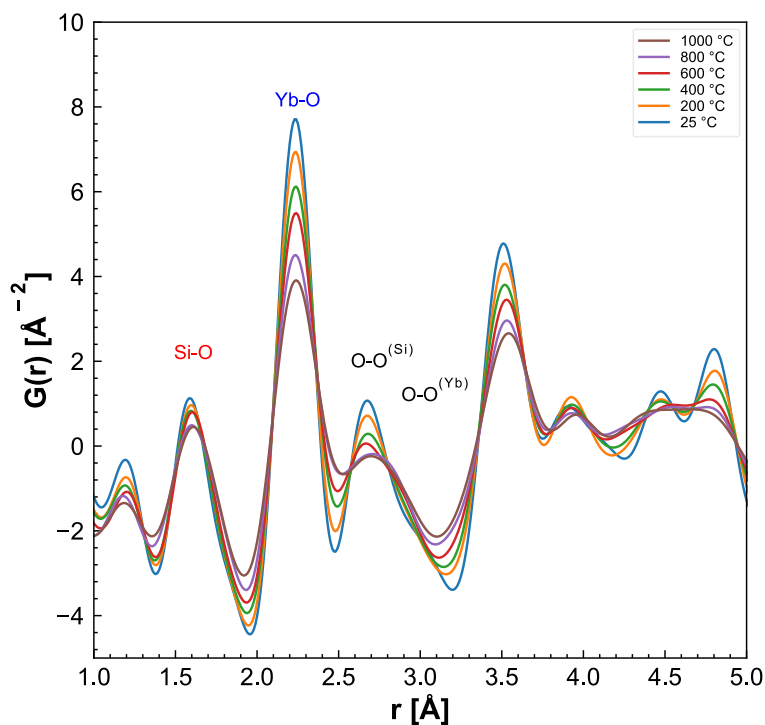


Figure 5.12: Neutron PDF of ytterbium disilicate from room temperature to 1000 °C before any resonance reduction.

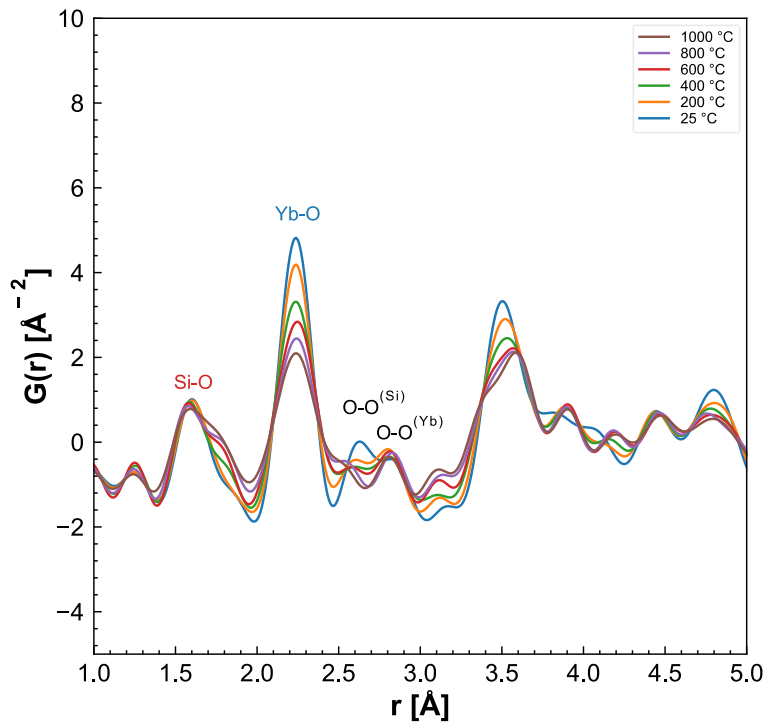


Figure 5.13: Neutron PDF of ytterbium disilicate from room temperature to 1000 °C after the resonance reduction.

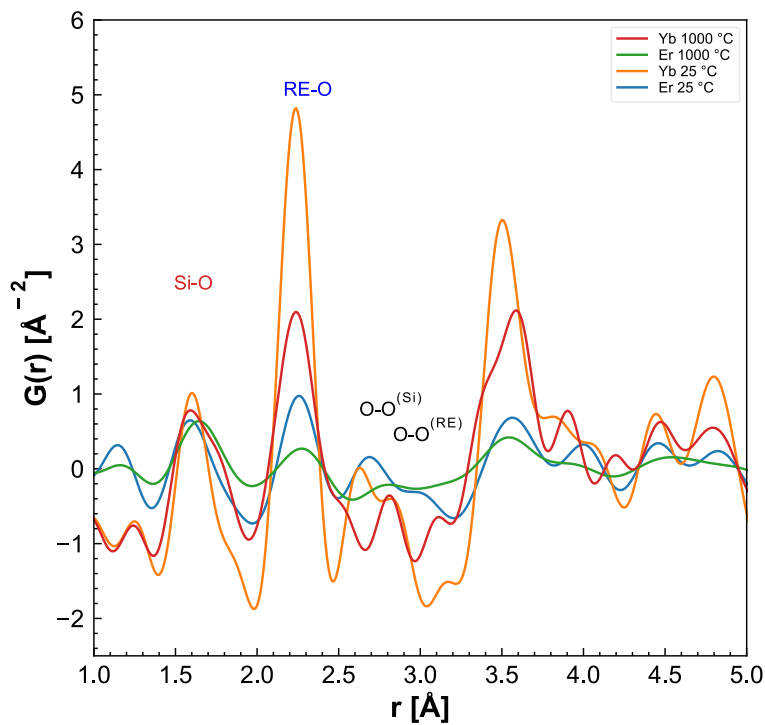


Figure 5.14: Neutron PDF of ytterbium and erbium disilicate at room temperature and at 1000 °C.

The PDF data was fit using PDF-GUI software.^{101–108} Given that refinement of X-ray diffraction data led to the conclusion that both ytterbium disilicate and erbium disilicate were monoclinic, this was used as the starting condition. The same crystallographic reference file as prior diffraction work was used. The fitting was poorer than expected for the ytterbium disilicate at room temperature. The fit from PDF-GUI, shown in **Figure 5.15**, poorly fits the Si-O peak at approximately 1.6 Å, and does not satisfactorily capture the Yb-O or O-O peaks at approximately 2.2 Å and 2.8 Å respectively. The residual weight for the triclinic fit is 14.5%, while the residual weight for the monoclinic fit is 17.1%. The poor monoclinic fitting continues beyond the room temperature data for ytterbium. After seeking the help from and collaborating with an expert in PDF fitting, the next course of action was to fit the ytterbium disilicate in parts and to attempt using a triclinic reference file for the material. The *x*-axis in PDF corresponds to interatomic distance, therefore by fitting in parts one can more easily determine if there are local distortions that only occur up to a specific distance. This type of segmentation of the fit is called “Boxcar” fitting and has been used previously to identify differences in local and long range crystallographic order.^{109,110} The triclinic structure of ytterbium disilicate is rarely reported and is explored in **Chapter 6** of this thesis. In fact, ytterbium disilicate is a state-of-the-art material as an EBC due to its wide acceptance as only being stable in the monoclinic structure. The only other mention of the triclinic phase of ytterbium disilicate has been in crystallization studies on sol-gel or plasma sprayed ytterbium disilicate.^{32,111–113} The X-ray and neutron diffraction of the sample confirm that the material is a phase pure monoclinic crystal, but Bragg diffraction provides only long range crystallographic information. The ytterbium disilicate neutron PDF data was fit using the triclinic phase with greater success than the monoclinic phase, shown in **Figure 5.16**. The fit is not perfect, in fact beyond an *r* value of approximately 3.2 Å the fit seems to be offset along the *y*-axis. After discussion with collaborators, this offset is due to how the neutron data was collected from banks of different detectors and then stitched together and is possibly an artificial offset not representative of the data that would otherwise be fit properly. The triclinic fit is valid up to about 5.2 Å, indicating that there are local distortions in dimensions less than those of the unit cell that result in the lattice resembling a triclinic crystal structure more so than the monoclinic structure. Triclinic and monoclinic fits were attempted for ytterbium disilicate at every temperature at which data was collected, showing that ytterbium disilicate has a triclinic distortion across the entire temperature range. The fits for the temperature dependent data are shown in **Figures 5.17** and **5.18**. Additionally, the Q_{\max} was varied to determine if the characteristic features of the triclinic distortion that are not captured by the monoclinic fit are real and not resonance ripples introduced by the Fourier transform. These ripples are a part of every PDF and can be clearly seen in **Figure 5.15** below approximately 1.2 Å. These ripples can interfere with the analysis of the fit and data by introducing shoulders to peaks that are not real. This is of concern given that a major distinction between the monoclinic and triclinic fits of ytterbium disilicate is the Si-O peak at 1.6 Å that has a shoulder on the

high r value side. The PDFs were generated with incrementally increasing Q_{\max} values, by increments of one, to see how any features would shift and to fit once again using triclinic and monoclinic structures. As shown in **Figure 5.19**, the changes in Q_{\max} do alter some of the features when compared to the original data at a Q_{\max} of 24 \AA^{-1} . The fits proved impossible for either triclinic or monoclinic at the Q_{\max} of 26 \AA^{-1} . However, all other Q_{\max} values produced data that was fit better by the triclinic phase than the monoclinic phase in the short-range. At the very least, the Q_{\max} of 24 \AA^{-1} was within the range of values to produce PDF data of the best possible quality given experimental constraints.

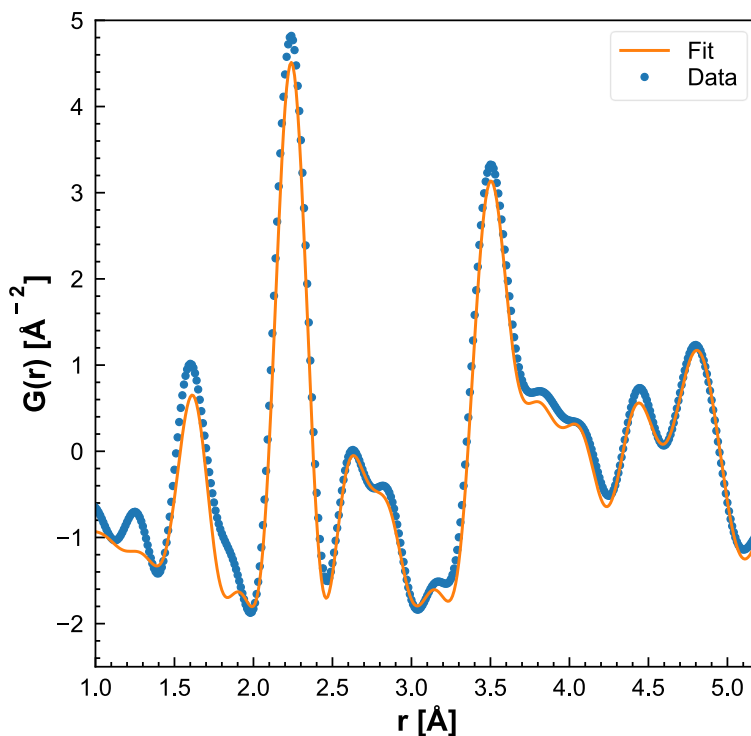


Figure 5.15: Monoclinic fit of room temperature neutron PDF data for ytterbium disilicate.

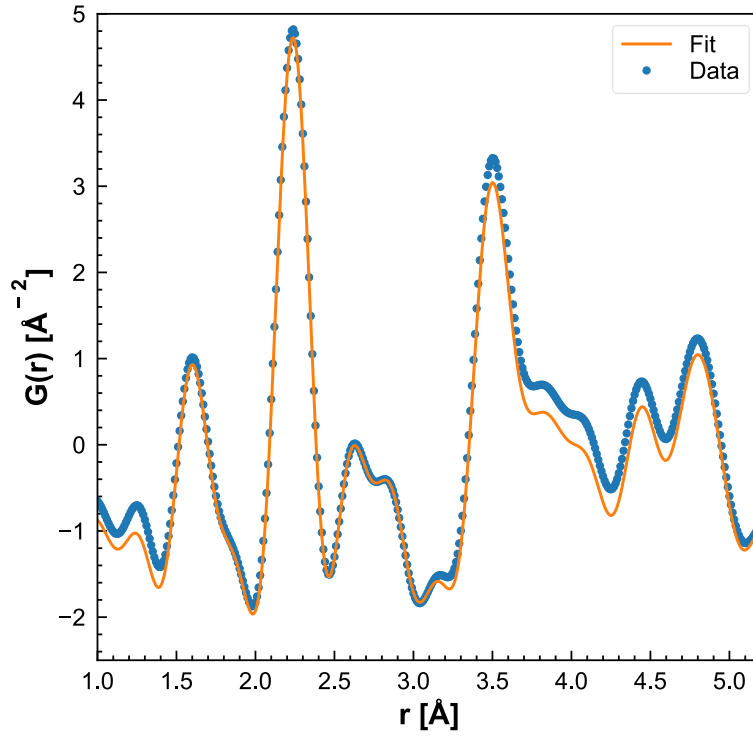


Figure 5.16: Triclinic fit of room temperature neutron PDF data for ytterbium disilicate.

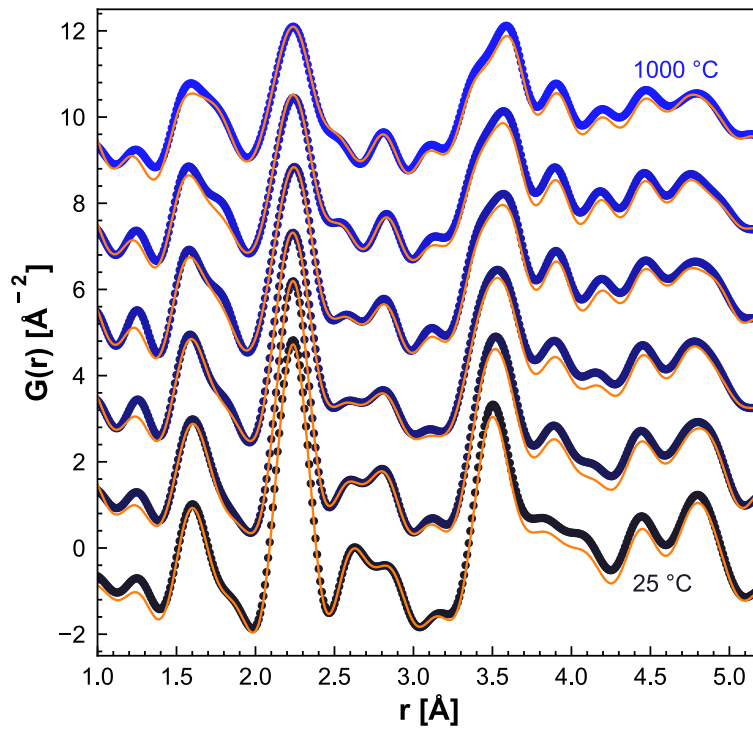


Figure 5.17: Triclinic fits to neutron PDF data from room temperature to 1000 °C for ytterbium disilicate.

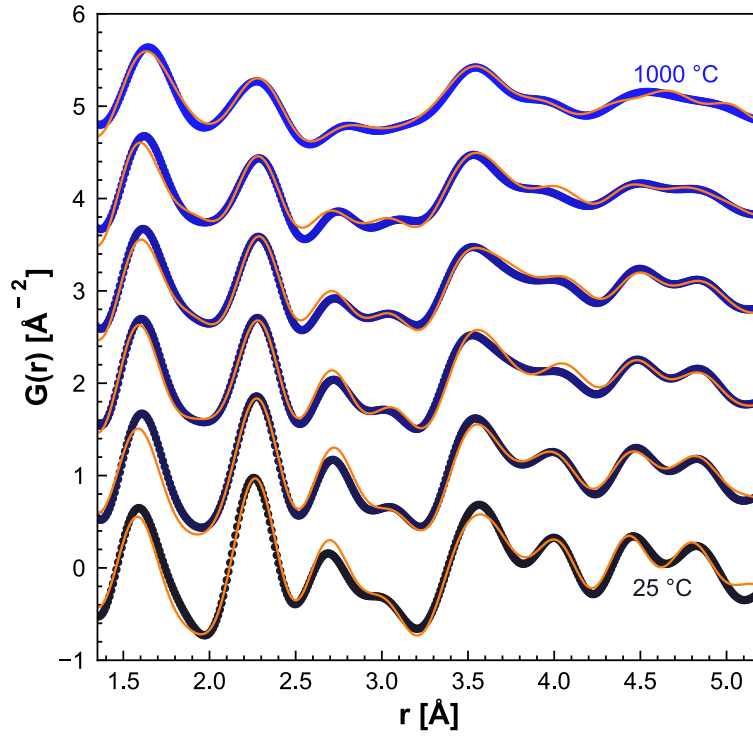


Figure 5.18: Monoclinic fits to neutron PDF data from room temperature to 1000 °C for erbium disilicate.

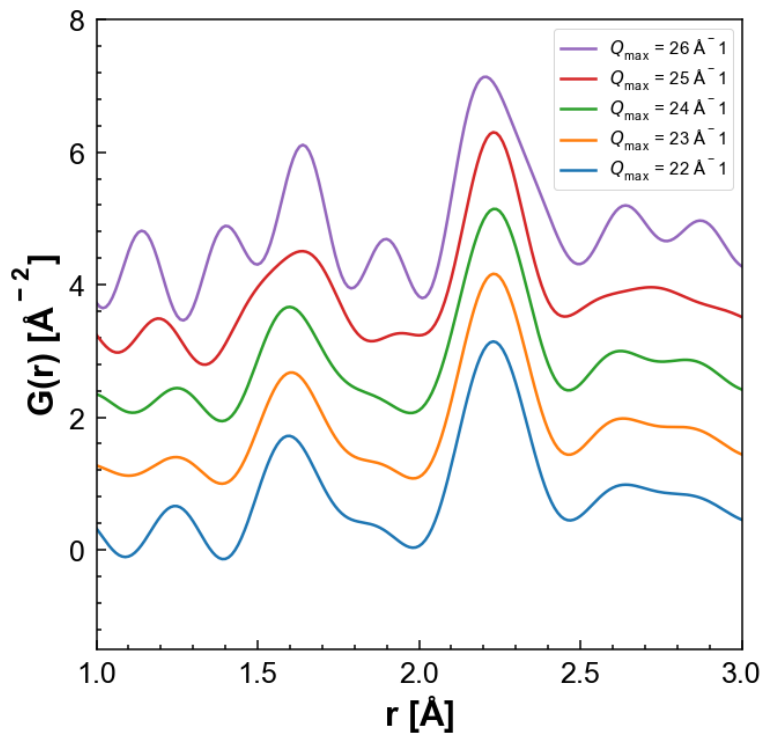


Figure 5.19: Comparison of neutron PDF data for ytterbium disilicate at different Q_{\max} values. Data has been offset for clarity.

The same fitting procedures were performed for erbium disilicate, where the triclinic and monoclinic structures were used separately to fit the data from room temperature to 1000 °C. Unlike for ytterbium, the erbium disilicate PDF data was only able to be fit using the monoclinic structure across the entire temperature range. The intensity of the erbium disilicate PDFs is much lower than for ytterbium, making fitting more difficult. Regardless of the lower counting statistics in the erbium PDFs, a triclinic fit was poor even at room temperature where fitting would be the easiest owing to better signal-to-noise ratios. The monoclinic and triclinic fits at room temperature are shown in **Figures 5.20** and **5.21** respectively. These figures indicate that the local structure of erbium disilicate matches the long-range structure measured by Bragg diffraction. The neutron diffraction patterns were fit to the monoclinic structure for ytterbium and erbium disilicate with a residual weight of 2-3%, and the fits are shown in **Figure 5.22**. These differences in local distortions are hypothesized to be the reason for the rare earth cation dependent CTE anisotropy discovered in **Chapter 4**. A triclinic local distortion allows the ytterbium disilicate lattice to expand with more degrees of freedom than the monoclinic local structure of erbium disilicate. These additional degrees of freedom may, in turn, lead to the beta angle U-shape that is characteristic of samples that exhibit rotation of thermal expansion principal axes upon heating.

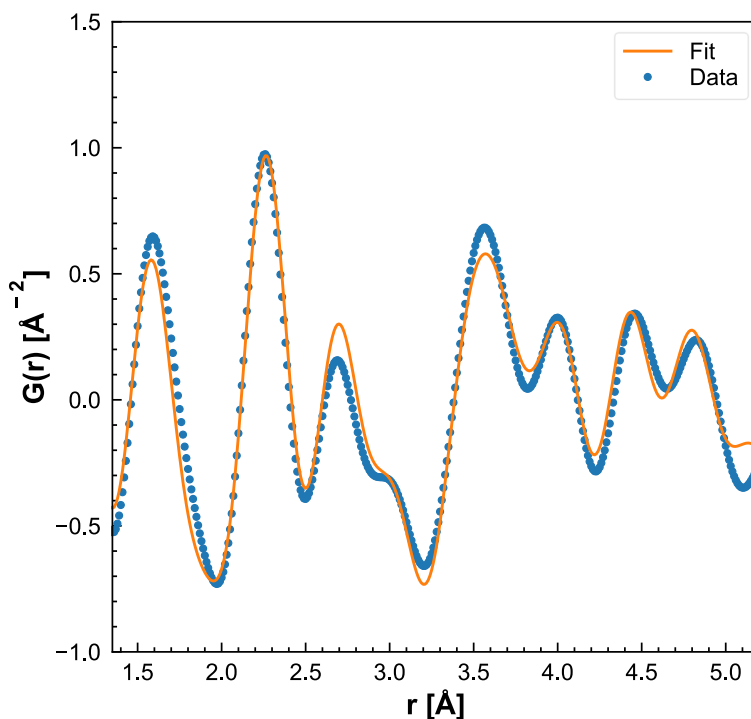


Figure 5.20: Monoclinic fit of room temperature neutron PDF data for erbium disilicate.

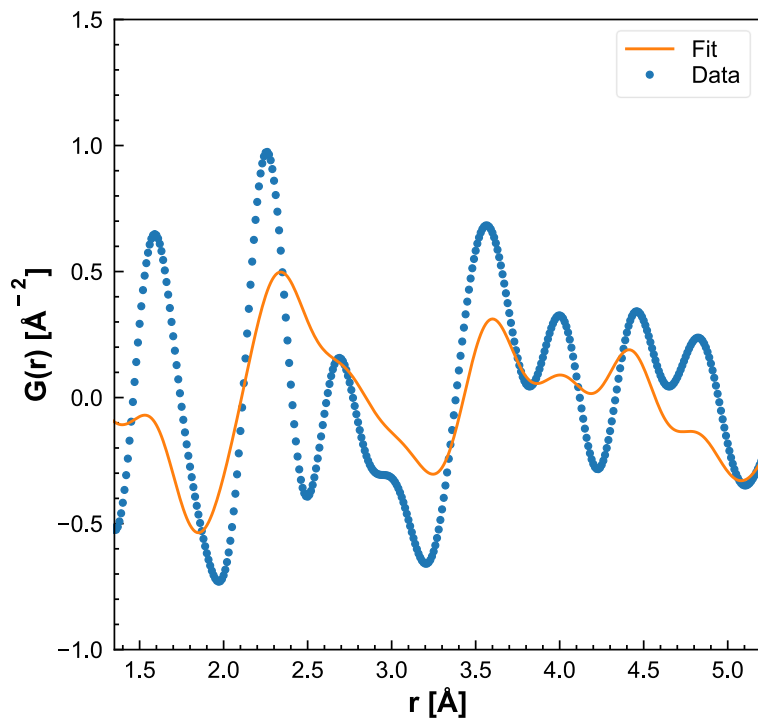


Figure 5.21: Triclinic fit of room temperature neutron PDF data for erbium disilicate.

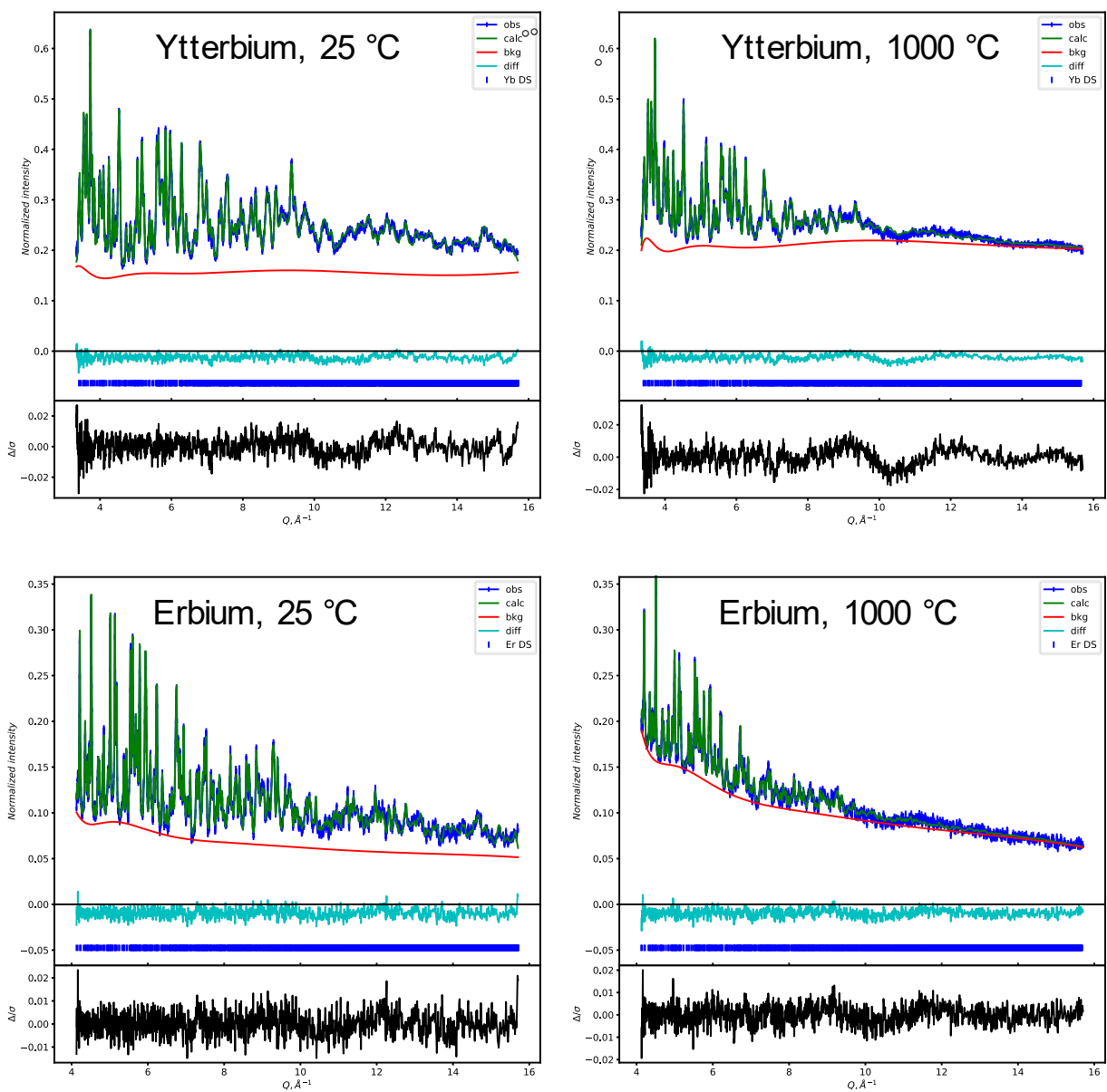


Figure 5.22: Rietveld refinements of ytterbium and erbium disilicate neutron diffraction patterns. The refinements confirm that the samples are monoclinic in the long range.

The fit structures of the two REDS were shown to be qualitatively and quantitatively distinct and are hypothesized to be the reason for the CTE anisotropy discussed in the previous chapter. Taking a step further, the fit structures' lattice parameters determined from the PDF data were input into a principal axis calculation and visualization software called PASCAL.¹¹⁴ This software takes input lattice parameters at the different temperatures and calculates the changes in principal axes and volume. PASCAL calculated the information given in **Tables 5.1** and **5.2**, where the linear coefficient of thermal expansion for the three

principal axes are given (X_1 , X_2 , and X_3) for ytterbium and erbium disilicate. Additionally, the directions of the principal axes for the two REDS were produced from PASCAL and are shown in **Tables 5.3** and **5.4**. The data produced by PASCAL showed that the local structure, sub one unit cell, has a different expansion behavior than the bulk. The local structure for both materials is calculated to be contracting, denoted by the negative signs in **Tables 5.1** and **5.2**. The expansion of the principal axes is not the same for ytterbium and erbium disilicate. For ytterbium disilicate, the X_1 and X_2 principal axes have a negative linear CTE, but in erbium the X_1 and X_3 axes have a negative linear CTE. This indicates that the local structure has different preferred expansion directions, which then affect the long-range expansion of the REDS. The reason for the difference in principal axes expansion behavior is hypothesized to be due to f -orbital electron screening of the d -orbitals. The f -orbitals are considered to not participate in bonding, but due to the contraction they may screen the d -orbitals from the nucleus. This means that the differences in the number of f -electrons between ytterbium and erbium may be indirectly contributing to local differences in bonding and structure through screening of the d -orbitals, leading to the provided differences in CTE anisotropic behavior.

Table 5.1: Linear CTE values of the three principal axes for ytterbium disilicate calculated by PASCAL.

Axes	Linear CTE ($\times 10^{-6} \text{ }^\circ\text{C}^{-1}$)
X_1	-95.2371
X_2	-28.9114
X_3	19.8151

Table 5.2: Linear CTE values of the three principal axes for erbium disilicate calculated by PASCAL.

Axes	Linear CTE ($\times 10^{-6} \text{ }^\circ\text{C}^{-1}$)
X_1	-26.3028
X_2	15.2576
X_3	-81.1069

Table 5.3: Eigenvector components of the principal axes for ytterbium disilicate calculated by PASCAL.

T (°C)	X_1			X_2			X_3		
	a	b	c	a	b	c	a	b	c
200.0	0.9306	0.225	0.2889	-0.4433	0.8613	0.2481	0.4294	0.6929	-0.5792
400.0	0.9358	0.206	0.2861	-0.4029	0.8877	0.2227	0.4793	0.6316	-0.6094
600.0	0.9477	0.1678	0.2714	-0.3447	0.9158	0.2061	-0.5121	-0.5698	0.6427
800.0	0.947	0.1693	0.2729	-0.3419	0.9182	0.2	-0.5209	-0.5569	0.6469
1000.0	0.9468	0.1697	0.2733	-0.3428	0.9178	0.2003	-0.5209	-0.5579	0.6461

Table 5.4: Eigenvector components of the principal axes for erbium disilicate calculated by PASCAL.

T (°C)	X_1			X_2			X_3		
	a	b	c	a	b	c	a	b	c
200.0	0.0	1.0	-0.0	-0.5694	-0.0	0.8221	0.5664	0.0	0.8241
400.0	0.0	1.0	0.0	-0.4728	-0.0	0.8812	0.6309	-0.0	0.7758
600.0	-0.0	1.0	-0.0	0.9913	0.0	0.132	0.0791	0.0	0.9969
800.0	-0.0	1.0	-0.0	0.9934	0.0	0.1147	0.0873	0.0	0.9962
1000.0	-0.0	1.0	-0.0	0.9998	0.0	0.0189	0.1313	0.0	0.9913

5.7 Conclusions

The anisotropic CTE behavior arises from local distortions on the scale of sub one unit cell dimensions due to the rare earth cation present in solid solution. These distortions were characterized by *in situ* neutron scattering measurements and subsequent generation of PDFs to elucidate how interatomic distances change from room temperature to 1000 °C. It is hypothesized that *f*-orbital electrons screen the *d*-orbitals, therefore indirectly contributing to bonding and affecting the polyhedral dimensions within the REDS lattice along preferred crystallographic directions. The long-range order of ytterbium disilicate has been widely accepted as monoclinic, but this chapter shows that the short-range order is triclinic while the long-range order shown by Bragg diffraction is monoclinic. The triclinic distortions allow for greater degrees of freedom for the lattice during expansion, resulting in greater CTE anisotropy than in the locally monoclinic structure.

5.8 Acknowledgments

The work presented in this chapter would not have been possible without the collaboration of others. Professor Prasanna Balachandran at the University of Virginia computationally derived the Raman spectra and phonon dispersions discussed throughout the chapter. Additionally, conversations with Professor Balachandran aided in understanding Raman, FTIR, and UV-Vis results and how they connect with the structure of the REDSs. Professor Thomas Beechem at Purdue University was instrumental in helping the author identify the resonant Raman peaks and their significance in differentiating the erbium disilicate spectra from the other REDSs. Professor Michelle Dolgos at the University of Calgary taught the author how to perform Rietveld refinements as well as participated greatly in discussing the neutron PDF fits, originally suggesting that the triclinic phase be used. Dr. Matthew Tucker at Oak Ridge National Laboratory aided in the proposal writing and experimental design of the experiments at the SNS NOMAD beamline. At the beamline, Dr. Tucker trained the users on instrument operation and data collection practices. In subsequent months, Dr. Tucker would provide valuable insights into the data analysis and performed the resonance reduction required for successful PDF fitting.

Chapter 6 Phase Purity and Evolution in Sol-Gel Derived Single Component and Multi-Component Rare Earth Disilicates

The contents of this chapter have been published in the Journal of the American Ceramic Society, doi: [10.1111/jace.19672](https://doi.org/10.1111/jace.19672), with the following authors:

Alejandro Salanova,¹ Elizabeth J. Opila,¹ and Jon F. Ihlefeld²

¹Department of Materials Science and Engineering, University of Virginia, Charlottesville, Virginia 22904 USA

²Charles L. Brown Department of Electrical and Computer Engineering, University of Virginia, Charlottesville, Virginia 22904 USA

The body of this chapter has been adapted to include supplemental information and figures, where appropriate.

6.1 Motivation

The phase purity of REDSs made via sol-gel was a concern during initial attempts, and eventually a >93 % phase pure final material was used in experiments detailed in the previous chapter as the weight fraction of the disilicate phase was sufficient for XRD analysis. Prior literature insufficiently describes the processes of sol-gel procedures and only gives readers a view of the results. In this work, the sol-gel procedure is examined more closely to determine important variables that prevented the production of a phase pure final material. Additionally, phase evolution behavior of the amorphous sol-gel products is studied to elucidate crystallization temperatures and phase transitions unseen in previous studies on already crystalline materials.

6.2 Abstract

Rare earth disilicates are a focus of study for use as environmental barrier coatings in gas-turbine engines. These coatings require thermomechanical and thermochemical stability at elevated temperatures and properties can be tailored through the use of multi-component rare earth disilicates. Producing rare earth disilicates via sol-gel is documented in literature, but there are differing procedures with varying phase

purities. This work establishes trends that dictate the effects of water content, pH, and heat treatment conditions that determine the final phase purity of Yb, Er, Lu, Sc, and Y disilicate powders made via sol-gel. The phase(s) of the powders were identified and quantified using X-ray diffraction to extract weight fractions. *In situ* X-ray diffraction during heating from room temperature to 1200 °C was used to observe the crystallization and phase evolution of the sol-gel-based powders, allowing for the identification of a rarely reported low temperature triclinic phase in ytterbium-, erbium-, and lutetium-based disilicate sol-gels that forms prior to transformation into a monoclinic phase. *Ex situ* X-ray diffraction allowed for the phase identification of sol-gels processed at 1400 °C. These experiments demonstrated that phase-pure disilicates could be formed under conditions with no intentional water additions, a target pH of 2, and long heat treatment times at high temperatures (e.g. 1400 °C). These conditions remain valid for not only single cation rare earth disilicates of Yb, Er, Lu, Sc, and Y, but also a multi-component disilicate containing equimolar concentrations of all of these cations.

6.3 Introduction

Thermal and environmental barrier coatings (T/EBCs) are required for protecting silicon carbide-based ceramic matrix composites (CMCs) from deleterious reactions at elevated temperatures in gas turbine combustion environments.^{4,5,7,8,10,11,13,15,17-19} To adequately protect the underlying CMC, the T/EBC must possess a low coefficient of thermal expansion (CTE) mismatch, phase stability through the application temperature range, a high melting temperature, and reduced silica activity relative to phase pure silica.¹⁵ One viable candidate material system possessing these criteria for T/EBC applications is the rare earth disilicate (REDS). Despite their promise, REDS can still undergo reactions with water vapor and transform into monosilicates or oxides with distinct properties not always beneficial in T/EBCs. The thermomechanical and thermochemical properties of REDS can be tailored and improved through the inclusion of additional rare earth cations to produce a multicomponent REDS.^{22,35,78}

Increased numbers of rare earth cations past a single cation all the way up to high entropy compositions have also been used to modify the macroscopic properties of solids such as thermal expansion and thermal conductivity.^{22,35,78,115} For multi-component compositions, rare earth disilicates benefit from the large number of available rare earths (the lanthanides as well as scandium and yttrium) that can be incorporated. The choice of which cations are to be included will influence the final material polymorphs due to differences in ionic radii, as reported by Felsche.^{27,88} From the many possible compositions/polymorphs to use in applications, the monoclinic phase (sometimes referred to as the Type-C or β phase) that consists of the smallest cations (i.e. Sc, Lu, and Yb) with the $C 2/m$ space group is the most viable for T/EBC purposes. The $C 2/m$ phase has a compatible CTE with respect to SiC and has been reported to have no polymorphic transformations upon heating.^{23,27,35}

The literature contains many different synthesis techniques for REDS, but one of the most common is the sol-gel method given the many years of foundational work in the synthesis of silicates via sol-gel processes.^{35,43,52–58} Typically, a rare earth nitrate and tetraethyl orthosilicate (TEOS) are used as precursors dissolved in an alcohol-containing solution at different pH levels. The resulting powders vary in phase purity from single-phase disilicates to a phase mixture containing the monosilicate phase (e.g. RE₂SiO₅) where the residual SiO₂ may be present as a tertiary amorphous phase. Several prior works understated the presence of the secondary phases due to the extremely low intensity of peaks in X-ray diffraction analysis while others attempted to remove the secondary monosilicate phase by adding excess TEOS to react out any silica deficient monosilicate phase.^{35,52–57} The presence of excess silica is deleterious to the performance of a T/EBC, however, given that silica has a melting point several hundred degrees lower than the REDS and a high reactivity with water vapor in combustion environments, requiring its removal before use.²⁹ When REDS-based T/EBCs see real-world use, they are typically applied through plasma spray deposition. The highly energetic process frequently results in an amorphous coating that upon crystallization can contain varying quantities of mono- and disilicates. As such, knowledge of the progression of phase formation from amorphous-to-crystalline is desired.

TEOS is a metal alkoxide, which typically reacts readily with water. This reaction is known as hydrolysis since a hydroxyl ion becomes attached to the metal atom.^{44,51} The reactions for partial and complete hydrolysis of TEOS are shown in **Equations 6.1** and **6.2**, respectively.



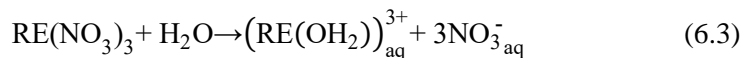
In these reactions, *R* represents an ethyl group. Understanding the reactions that occur during the REDS sol-gel process can allow for tailoring weight fractions of the various phases of rare-earth silicates or producing a phase pure REDS. Hydrolysis of TEOS is catalyzed by the presence of H⁺ and OH⁻, with a minimum in reaction rate in the pH range of 4-7. The rate of the hydrolysis reaction increases with the concentration of H⁺ and OH⁻ species, meaning that pushing pH to high or low extremes promotes the conversion of TEOS to silica.^{44,51} Sol-gel synthesis of REDS has also resulted in previously un-observed phases. For example, Zhao *et al.*³² reported that a triclinic phase crystallized in Yb disilicate that had otherwise not been seen in literature. This triclinic phase is not present in published phase diagrams or in Felsche's previous reports on the polymorphs of REDS. Other rare earth cations do have well reported monoclinic and triclinic polymorphs, such as erbium and yttrium disilicate.^{27,53} According to Felsche,²⁷ the triclinic and monoclinic phases of erbium disilicate have the following cell parameters: *a* = 6.583 Å, *b* = 6.609 Å, *c* = 12.000 Å, *α* = 94.50°, *β* = 90.57°, *γ* = 91.79° for the triclinic phase, and *a* = 6.841 Å,

$b = 9.135 \text{ \AA}$, $c = 4.694 \text{ \AA}$, $\beta = 101.70^\circ$ for the monoclinic phase and differing molar volumes for the two phases. The presence of this triclinic phase may complicate the phase stability of the T/EBCs required for thermomechanical stability via phase transformations during the initial heating and crystallization of the plasma-spray deposited coating or even during heating and cooling cycles in normal use.^{27,29} The present study focuses on the processing parameters that control the resulting phase of single component and a multicomponent REDS made via sol-gel with a focus on the parameters that enable preparation of phase pure REDS. In addition, the phase evolution of these REDS from the xerogel to the final crystalline product is studied during heating via *in situ* X-ray diffraction (XRD).

6.4 Experimental Methods

6.4.1 Sol-Gel Synthesis

Yb, Er, Lu, Sc, Y, and a multicomponent (containing all five cations listed) REDS were synthesized via a sol-gel method with a procedure that was modified from previous work and is depicted via a flowchart in **Figure 6.1**.³⁵ Rare earth nitrates (99.9% purity, Alfa Aesar) and TEOS (98% purity, Acros Organics) precursors were mixed into a 100 mL reaction solution where the nitrates were weighed and then the corresponding volume of TEOS required was calculated based on molecular weight and density. The volume of TEOS corresponded to a 1:1 molar ratio to the rare earth cations present. Typical conditions used 2.4×10^{-3} moles of the rare earth nitrate and TEOS in the 100 mL solution. The water content of the rare earth nitrates was measured via thermogravimetric analysis (Netzsch STA-449 F1). The water content was accounted for in the composition calculation. The rare earth nitrates and TEOS were dissolved in a reaction solution to dissociate ions and induce the hydrolysis reactions described in **Equations 6.1** and **6.2**. The rare earth nitrate ion dissolution is described by **Equation 6.3**.



The reaction solution contained anhydrous ethanol and de-ionized water. The ratio of the two solvents was varied to determine the effects of water content on phase formation. The pH was then modified as either hydrochloric acid or ammonium hydroxide were added dropwise via a syringe until a desired pH was reached as measured by a pH meter (Fisher Scientific Accumet AE150 pH Benchtop Meter). The reaction solution was stirred until no visible precursor remained, after which the solution was placed on a hot plate that was set to 60 °C without stirring. The dissociated rare earth ions and silica containing organics are presumed to be homogeneously distributed through the mixture. The rare earth ions will form an aqueous rare earth oxide, while the TEOS is hydrolyzed to produce silica.⁵³ The aqueous silica and rare earth oxide form a linked network of precipitates as the reaction solution is evaporated during heating. The solution was left to gel, which took varying amounts of time depending on water content (1-3 days with higher water

content taking longer). Once the gel formed, it was transferred to a platinum crucible and dried in a box furnace (Thermo Scientific Thermolyne) at 550 °C for 24 hours in static ambient air to form a xerogel. The resulting xerogel was crushed in a Diamonite mortar and pestle until a fine powder remained. The powder was returned to a platinum crucible and exposed to a 1400 °C static ambient air environment for 18 hours in a box furnace (Rapid Temperature Furnace, CM, Inc.) to form the crystalline product. For the multicomponent REDS, the same procedure was followed using equimolar quantities of each rare earth cation added as nitrate precursors, and the appropriate molar quantity of TEOS was added to ensure a RE:Si ratio of one. The first rare earth cation selected for synthesis was Yb, followed by Er, Y, Lu, Sc, and a multicomponent mixture of all five cations. The fraction of water was varied, ranging from 0, 10, 50, and 90 mL of water out of the total 100 mL reaction solution.

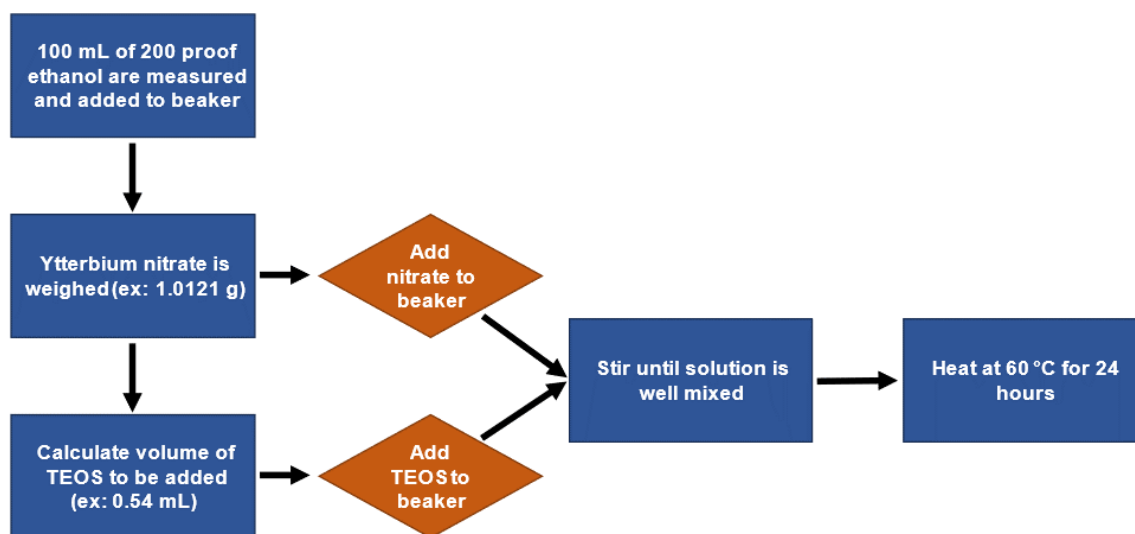


Figure 6.1: Experimental flowchart showing a synthesis procedure of a Yb disilicate sol-gel with the mass and volume for the nitrate and TEOS respectively.

6.4.2 Diffraction Experiments

Two sets of diffraction experiments were performed using XRD: *ex situ* (i.e. after heating the powder in a furnace) and *in situ* (i.e. performing XRD while heating the powder). The reason for both was due to temperature limitations in the *in situ* heating furnace. The purpose of the *in situ* heating XRD experiments was to observe the crystallization behavior and phase evolution as the temperature increased. The *in situ* work had an upper limit of 1200 °C. The *ex situ* experiments measured the room temperature diffraction patterns of the powders after they were heated in a furnace to 1400 °C. The *ex situ* diffraction experiments were performed with a Malvern Panalytical X'pert X-ray diffractometer (Cu K α X-ray wavelength of 1.54 Å) to identify and quantify the phase fraction of the REDS powders. A Bragg-Brentano geometry and

X'celerator detector were used to perform powder diffraction experiments and the powder was constantly rotated using a spinner stage during the measurement. Once the *ex situ* XRD experiments identified solvent parameters that resulted in a phase pure REDS after 1400 °C furnace heat treatment, the *in situ* experiments were conducted. The *in situ* experiments involved the same synthesis procedure as previously described but the process was stopped after the 550 °C box furnace step. After the 550 °C xerogel product was ground into a powder, *in situ* hot stage XRD was performed using a Malvern Panalytical Empyrean X-ray diffractometer (Cu K α X-ray wavelength of 1.54 Å) in a Bragg-Brentano geometry, an Anton Parr HTK1200N hot stage, and GaliPIX3D detector. The temperature was ramped at a rate of 10 °C/min stopping at 50-degree intervals between 50 °C and 1200 °C for approximately 15-minute holds to perform XRD scans over a 10 to 90° 2θ range.

6.4.3 Phase Identification

The collected diffraction patterns were analyzed using GSAS-II software to quantify weight fractions of the observed phases.⁶² The phases for the rare earth disilicate, monosilicate, and oxide were imported from crystallography information files (*.CIF) collected from the ICSD database.^{76,77,116} The residual weight percent (R_{wp}) for every refinement of the weight fraction was in the range of 9-13% for all experiments in this manuscript. Phase identification for hot stage data was performed using HighScore Plus (Malvern Panalytical) software after the patterns were collected.

6.5 Results and Discussion

6.5.1 Effect of Water Content and pH on Phase Formation

Figure 6.2 shows the XRD patterns for all the pH of 2 Yb REDS sol-gels. The XRD patterns for the other pH values are provided in **Figures 6.3** and **6.4**. **Table 6.1** shows the phase weight percentage results of the Yb solvent dependence experiments after heat treatment of the powders at 1400 °C, where the numbers given correspond to the disilicate monoclinic phase (space group $C 2/m$). The percentages given in parentheses correspond to the weight percent of monosilicate phase (MS), if there is a MS present. If the balance does not equal 100%, then the percentage is completed by the presence of ytterbium oxide. Starting with the effect of water content for fixed pH ranges, the following observations were made: The solutions containing the most quantities of water did not produce single-phase REDS, instead two or more phases were identified, typically the desired disilicate and the undesired monosilicate, regardless of pH. This is evident in **Figure 6.2** where for a pH of 2 and no intentional water additions, a phase pure disilicate was prepared. However, for the same pH of 2 with the 90% H₂O in the solution, the derived powder had >85 wt.% monosilicate phase. Similar trends were observed for the pH of 10 where the no intentional water content had >97 wt.% disilicate phase, but the 90% water content was primarily monosilicate. The trends

also held for intermediate pH values. These are described as “Unaltered” pH in **Table 6.1**. The “Unaltered” category had pH values in the range of 4 up to approximately 6, with the lowest values corresponding to the lowest quantities of water. The exact values are given in supplemental materials **Figure 6.4**. The pH meter read a value of 4 when measuring the solution with 0% water (all anhydrous ethanol). Here, low water content (0% and 10%) derived powders primarily comprised disilicate phases. However, increasing the water content to 50% and 90% led to no observable disilicate peaks in XRD and mixtures of monosilicate and rare earth oxides were observed. The only other condition that led to rare earth oxide formation was 90% water and a pH of 2. In observing the trends of phases present for fixed water content and varied pH (i.e. vertical columns on Table 1), it was generally observed the low pH and high pH solutions led to the highest disilicate phase fractions. Using high pH (pH = 10) or low pH (pH = 2) resulted in higher disilicate fractions over those syntheses in which solution pH was not intentionally controlled. The largest content of disilicate phase formation over the broadest range of water content was observed for the low pH condition, followed by the high pH condition. It is hypothesized that solutions at pH of 2 undergo a faster hydrolysis reaction than in the unaltered solutions. The solutions require more H⁺ to increase the hydrolysis reaction rate, therefore increasing reaction rate with lower pH values and free sufficient silica from TEOS to produce the disilicate. While at or just below neutral pH values, the unaltered solutions have a comparatively slow rate hydrolysis reaction.

Table 6.1: Weight percentages of the *C 2/m* monoclinic phase in crystallized Yb₂Si₂O₇ sol-gels. Values in parentheses indicate the weight percentage of Yb₂SiO₅ monosilicate phase. In cases where the total does not equal 100%, the balance is completed by ytterbium oxide. The “Unaltered” row indicates that only solvent and the RE and Si precursors were added to solution, but no acid or base was added to adjust pH.

Yb Disilicate Weight Fraction				
pH	0% H ₂ O	10% H ₂ O	50% H ₂ O	90% H ₂ O
2	100%	98.7% (1.3% MS)	94.4% (5.6% MS)	10% (85.7% MS)
Unaltered	88.4% (11.6% MS)	98.7% (1.3% MS)	~0% (81.3% MS)	~0% (61.3% MS)
10	97.5% (2.5% MS)	96.7% (3.3% MS)	75.6% (24.4% MS)	25.3% (74.7% MS)

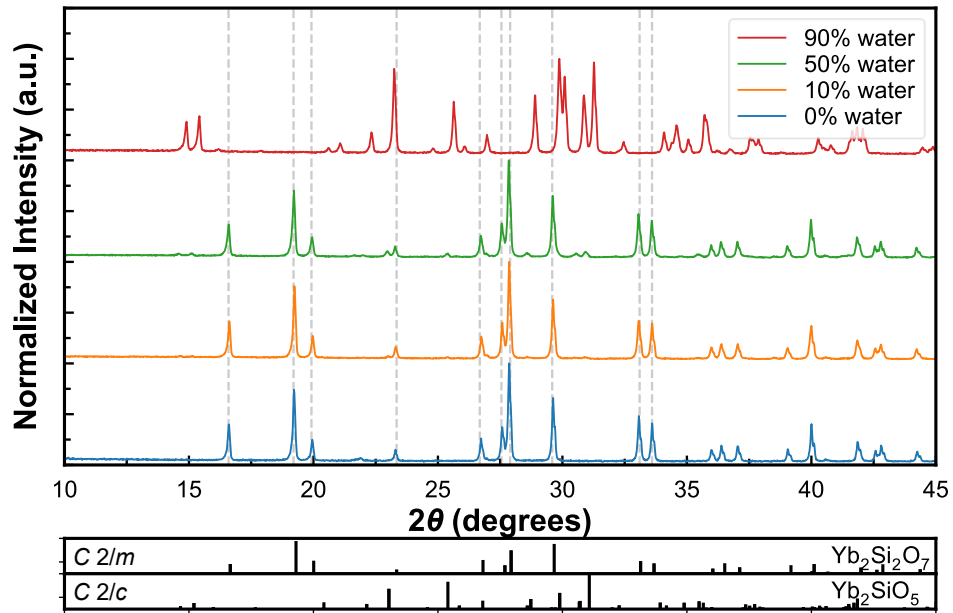


Figure 6.2: XRD patterns of Yb silicate sol-gels made with varying water contents with a pH of 2. The dashed vertical lines correspond to the $C 2/m$ Yb₂Si₂O₇ phase. The degree of phase purity increases as water content decreases, with 90% water content being predominantly the Yb₂SiO₅ phase.

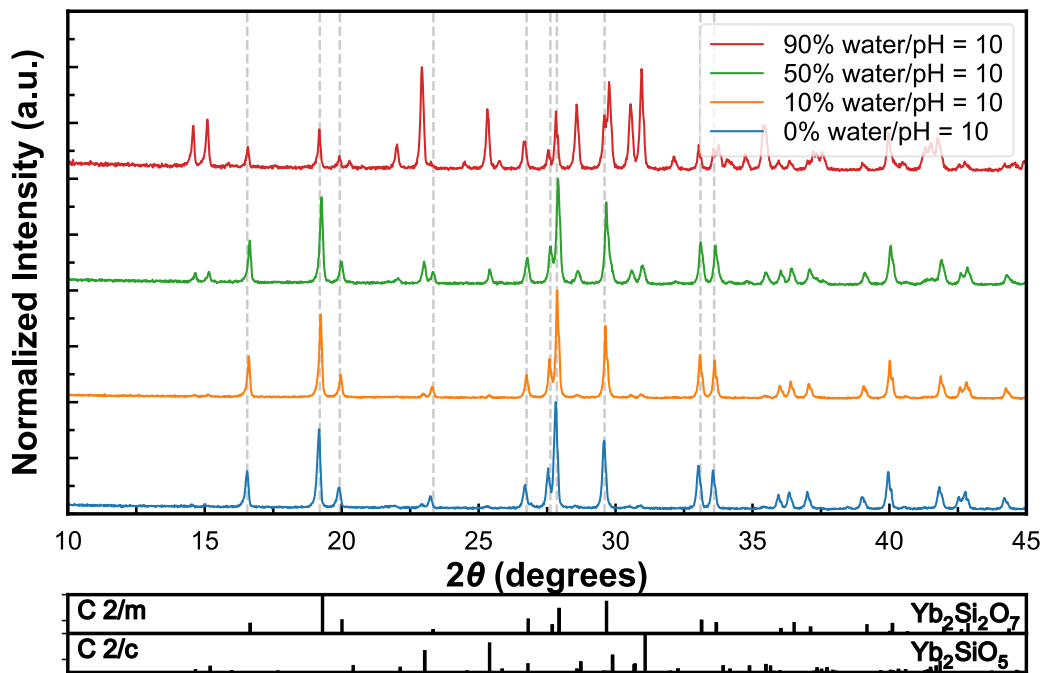


Figure 6.3: XRD patterns of ytterbium disilicate sol-gels at with varying water concentrations. The pH was uncontrolled and is recorded.

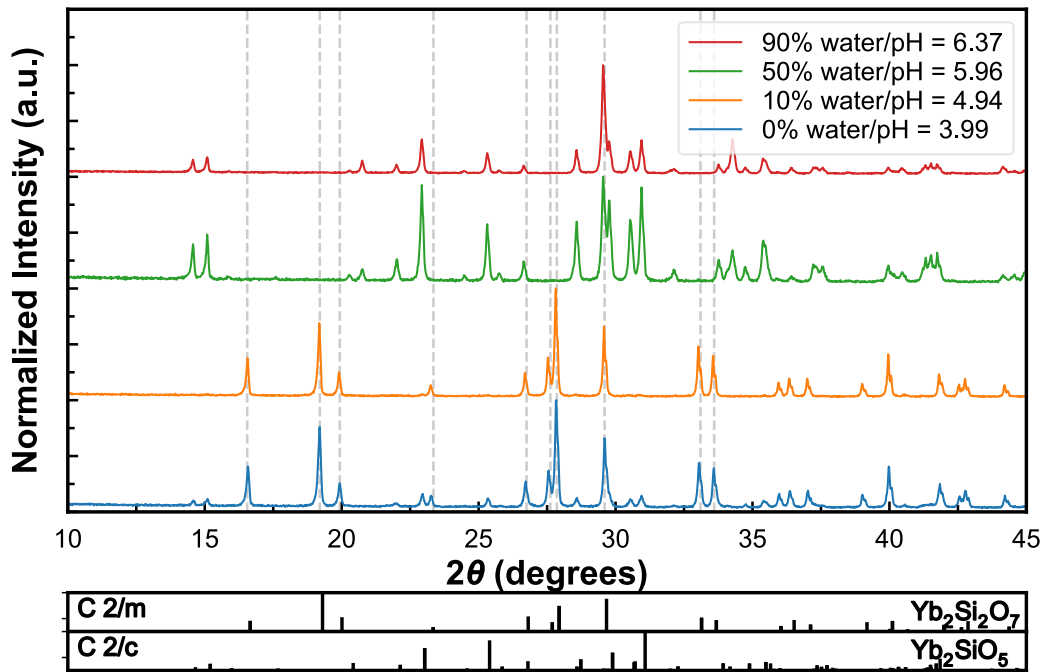


Figure 6.4: XRD patterns of ytterbium disilicate sol-gels at pH of 10 with varying water concentrations.

From these data, the observed trend is that little to no water and low pH in the reaction solution is required to achieve a phase pure disilicate. These results may seem contradictory to the reaction provided in **Equation 6.1**, with water being necessary for the hydrolysis of TEOS to occur. However, the water in the TEOS hydrolysis reaction can come from two sources: the rare earth nitrates that are hygroscopic and are sourced as rare earth nitrate hydrates, and the other source is humidity in the ambient. The Yb-nitrate hydrate used in this study contained an average of 3.3- H_2O molecules per Yb atom as determined from thermogravimetric analysis. This corresponds to 3.3 H_2O per silicon atom in solution as Yb and Si were mixed in a 1:1 ratio. Typical relative humidity levels in the laboratory were 48.4% for a typical temperature 21.7 °C. Additionally, the hydrolysis reaction of TEOS has been reported to be catalyzed by acids and bases, leading to the hypothesis that the final phase purity is controlled by the hydrolysis reaction of TEOS and not the rare earth nitrate.^{46,51,117,118} The catalysis of the hydrolysis reaction due to an acid or base is attributed to nucleophilic substitution reactions. There are many differing proposed exact reactions or mechanisms for both the acidic and basic regimes.^{44,51,117,118}

Following the results of the Yb sol-gel experiments, the behavior of other individual rare earth silicates was assessed, starting with Er. Observing phase formation for different rare earths under the same pH and water content conditions allowed a test of the hypothesis that the TEOS hydrolysis reaction is the rate limiting or controlling factor. Additionally, this knowledge of the pH and water dependence of phase formation was required for the eventual synthesis of a multi-component ceramic that would utilize multiple

rare earth nitrates in solution to all react with TEOS. The XRD patterns for erbium disilicate are provided in the supplemental materials **Figures 6.5** and **6.6**. **Table 6.2** shows the weight percentages of the disilicate *C 2/m* phase in the 1400 °C crystallized erbium silicate sol-gels. Similar to the ytterbium silicates, conditions of low water content and low pH result in greater phase purity. Only Er₂Si₂O₇ was observed for no intentional water additions and a pH of 2, which is the same behavior as observed for Yb₂Si₂O₇. The trend differs, however, from Yb in the pH = 10 series. In this case, the highest fractions of disilicate were observed for the 10 and 50% H₂O conditions rather than the no intentional water condition. The mechanisms driving this are unclear since the Er-nitrate was found to have 5.0 H₂O per Er, which is higher than the Yb nitrate. Given this initial water content, it may have been expected that the 0% water condition should have behaved similar to the 10% and 50% conditions.

Table 6.2: Weight percentages of the *C 2/m* monoclinic phase in crystallized Er₂Si₂O₇ sol-gels. Values in parentheses indicate the weight percentage of monosilicate phase. In cases where the total does not equal 100%, the balance is completed by erbium oxide.

Er Disilicate Weight Fraction				
pH	0% H ₂ O	10% H ₂ O	50% H ₂ O	90% H ₂ O
2	100%	98.7% (1.3% MS)	94.4% (5.6% MS)	84.5% (15.5% MS)
10	88.0% (12.0% MS)	97.2% (2.8% MS)	93.8% (6.2% MS)	19.6% (80.4% MS)

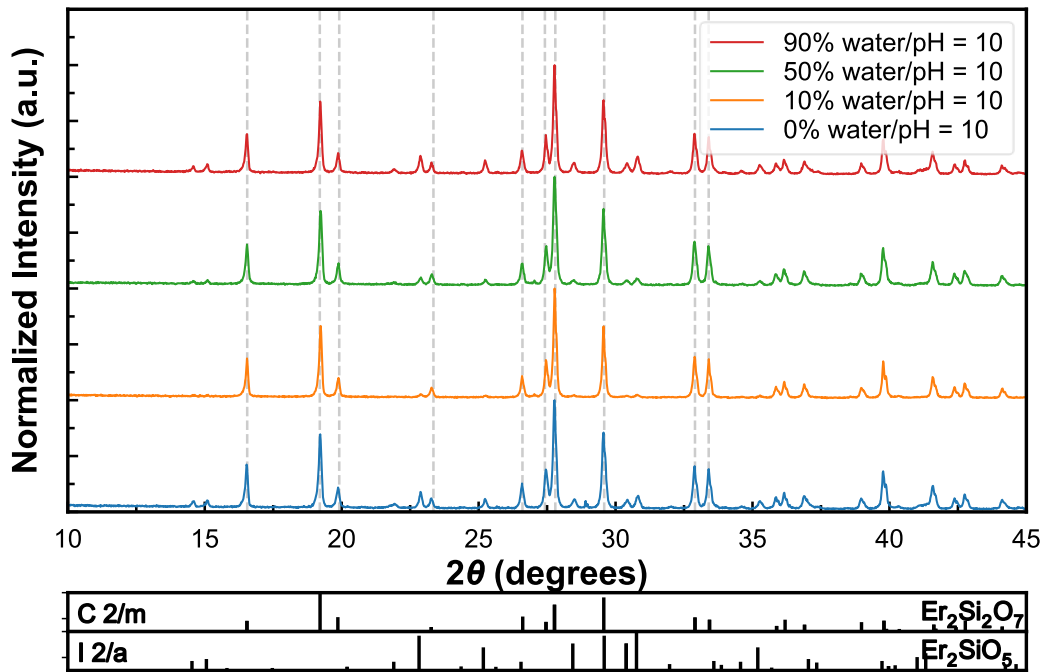


Figure 6.5: XRD patterns of erbium disilicate sol-gels at pH of 10 with varying water concentrations.

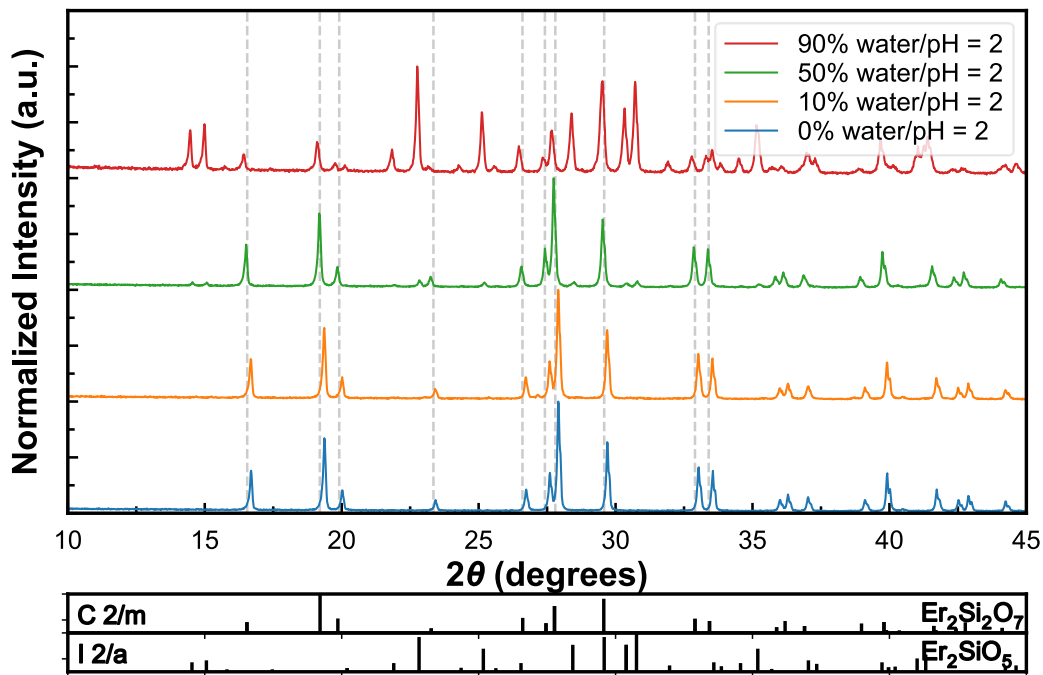


Figure 6.6: XRD patterns of erbium disilicate sol-gels at pH of 2 with varying water concentrations.

Regardless of the differences between Yb and Er silicate sol-gels at the high pH conditions, the maximum phase purity is again observed for a 0% intentional water addition and a pH of 2, suggesting that

the Er nitrate provides sufficient water to drive the hydrolysis reaction of TEOS under acidic conditions. The water content of the other nitrates used was measured via thermogravimetric analysis (TGA) to be as follows: Lu-nitrate had approximately 3.6 H₂O, Sc-nitrate had approximately 9.5 H₂O, and Y-nitrate had approximately 6.0 H₂O. The trends in Yb and Er disilicate sol-gel synthesis were then tested for the Sc, Lu, and Y cations, replicating the 0% added water and target pH of 2. The XRD patterns of the 1400 °C crystallized powders are shown in **Figure 6.7**. Some differences were noted in the final phase purity of the REDS relative to the Yb and Er sol-gels. Yttrium had a monosilicate secondary phase, lutetium had a silica (cristobalite) secondary phase, and scandium had a scandium oxide secondary phase. More specifically, the disilicate phase in the Y sol-gel was 95.0 wt.%, with a 5.0% weight fraction of the monosilicate phase. The Sc sol-gel had a disilicate weight fraction of 97.8% and a 2.2% weight fraction of a secondary scandium oxide phase.

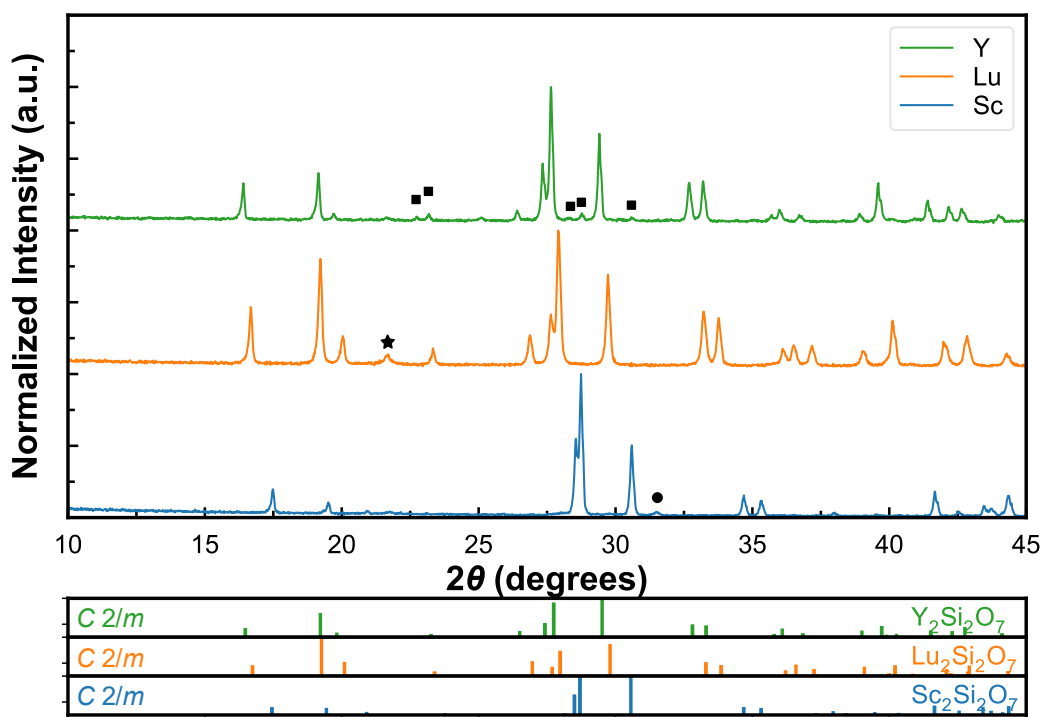


Figure 6.7: XRD patterns of Sc, Lu, and Y silicate sol-gels made with 0% water added and a pH of 2. All three are predominantly the *C 2/m* phase but do have secondary phases indicated by black squares, stars, and circles for the monosilicates, silica, and oxide phases, respectively.

The selection of Sc, Lu, Yb, Er, and Y for study as single cation REDS provided the basis for the mixing of all five cations in equimolar concentrations to produce a multicomponent REDS under the same synthesis conditions. These five cations can crystallize in the *C 2/m* phase as single cation REDS, with high or complete phase purity. Yttrium disilicate is known to have multiple polymorphs that are dependent on

temperature,²⁷ but under the specific steps outlined in this work as a single component, Y disilicate stabilizes in the $C 2/m$ phase. The next steps were to determine if the same procedure remained valid for producing phase-pure multicomponent REDS. Once again, the parameters of 0% water added and a pH of 2 were used to produce a gel that was crystallized by heating to 1400 °C and characterized via XRD. **Figure 6.8** shows the pattern of $(\text{Sc}_{0.2} \text{Lu}_{0.2} \text{Yb}_{0.2} \text{Er}_{0.2} \text{Y}_{0.2})_2\text{Si}_2\text{O}_7$ with the disilicate $C 2/m$ peaks indexed via vertical gray dashed lines. The multicomponent REDS produced shows phase purity similar to Yb and Er sol-gel-derived powders, where no monosilicate or oxide phases are observed as secondary phases. There is a peak corresponding to cristobalite that appears at around 22 degrees in 2θ . This indicates that the rare earth nitrates most likely absorbed water prior to the synthesis procedure, resulting in their molecular weights to differ, causing the RE:Si ratio to deviate from 1:1 and the starting solution to be silica rich. Regardless of the presence of silica, the synthesis procedures outlined here with an 18 hour 1400 °C thermal treatment illustrate the effect of water content and pH on the reaction rate of TEOS, with lower water concentration and low pH being ideal. Excessive amounts of water likely drive the TEOS hydrolysis to occur too quickly and result in SiO_2 segregating leading to monosilicate formation. Importantly, this low water, low pH process is shown to produce many single and a multi-component REDS with near phase purity.

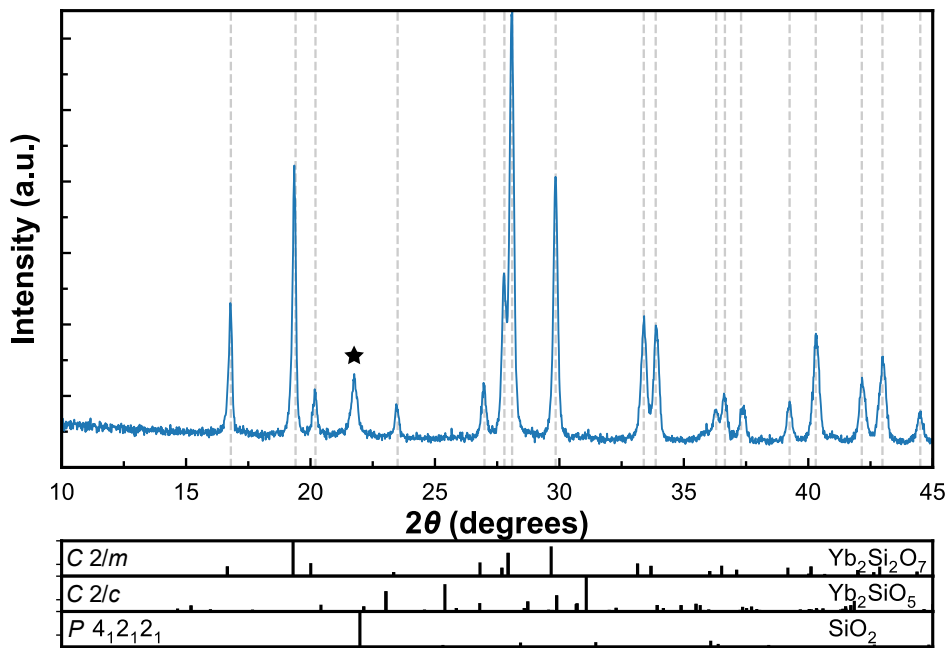


Figure 6.8: XRD pattern of a five component REDS. The $C 2/m$ phase has been indexed via vertical dashed lines. The XRD pattern shows no secondary monosilicate phase and a silica peak at approximately 22° in 2θ , marked by a star symbol.

6.5.2 Crystallization and Phase Evolution of Xerogel

Yb disilicate is widely reported to be stable in the $C 2/m$ monoclinic phase, but prior work by Zhao *et al.* identified a lower temperature triclinic phase before the REDS crystallized into the monoclinic phase.³² Besides their work, the triclinic phase was observed in two works by Garcia *et al.*^{111,112} The samples in these works were not derived from sol-gel processes, but were prepared via an air-plasma sprayed process. As the triclinic phase has been observed in materials processed by vastly different approaches, it is supportive that its formation is intrinsic to the crystallization process for ytterbium disilicate. Seminal works and phase diagrams for these materials typically only show data above 1400 °C.²⁹ To fill the knowledge gap of phase evolution and to determine if similar triclinic phases form in other REDS, *in situ* hot stage XRD was used to observe the crystallization and potential phase transformations of sol-gel derived REDS. The following samples were characterized during heating *in situ* with XRD: $\text{Yb}_2\text{Si}_2\text{O}_7$, $\text{Er}_2\text{Si}_2\text{O}_7$, $\text{Y}_2\text{Si}_2\text{O}_7$, $\text{Sc}_2\text{Si}_2\text{O}_7$, and $(\text{Sc}_{0.2}\text{Lu}_{0.2}\text{Yb}_{0.2}\text{Er}_{0.2}\text{Y}_{0.2})_2\text{Si}_2\text{O}_7$. The synthesis methods described above that produced a single-phase REDS for each rare earth were utilized to produce xerogels that were then heat treated at 550 °C and ground into fine powders for the *in situ* heating XRD experiments. **Figure 6.9** shows the XRD patterns of a Yb sol-gel ramped from room temperature to 1200 °C in a hot-stage XRD. The monoclinic peaks corresponding to the $C 2/m$ phase are indexed with vertical dashed lines to illustrate phase presence.^{45,76,77,119,120} The patterns show the initial crystallization of a triclinic phase that occurs between 950 and 1000 °C. The triclinic phase transitions into the $C 2/m$ phase as temperature increases. The *in situ* study is limited by the instrument's maximum temperature of 1200 °C, but the *ex situ* experiments shown previously for the same sol-gel indicates that phase purity is also dependent on heat treatment temperature and time.

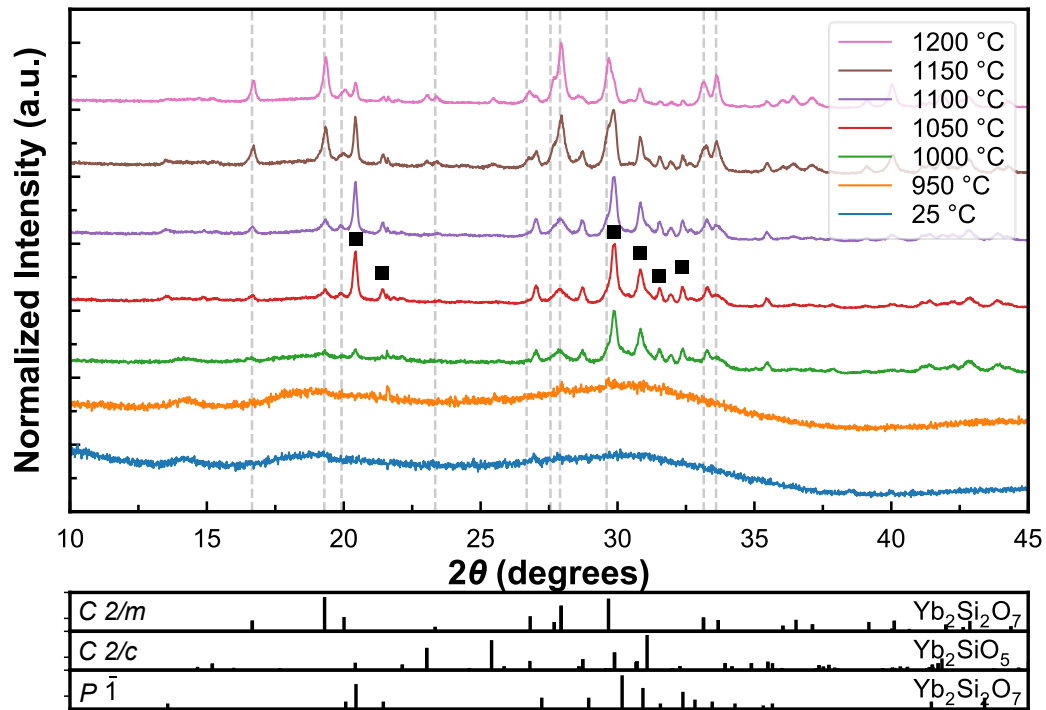


Figure 6.9: Diffraction patterns of *in situ* hot-stage XRD for a Yb silicate sol-gel. A triclinic phase nucleates at 1000 °C and is eventually replaced by the *C 2/m* monosilicate phase. The triclinic phase is indexed above the 1050 °C pattern by black squares.

Subsequent REDS diffraction patterns are shown in **Figures 6.10-6.13**, showing intermediary phase compositions throughout the heating profile that differ from the *ex situ* work for each of Er, Y, and Lu disilicates, respectively. Er and Y silicate XRD patterns in **Figures 6.10** and **6.11**, respectively, show the same triclinic to monoclinic phase transition as Yb, which is expected as these phases have been reported by Felsche.²⁷ While the triclinic phase is prevalent during crystallization, it does not appear in the *ex situ* patterns of Yb, Er, and Y silicates that were heat treated at 1400 °C. The temperature of the triclinic to monoclinic disilicate phase transition is expected to increase with larger RE ionic radius as given by the phase boundaries described in Felsche’s work.²⁷ This increase in crystallization temperature is noticeable during the heating in **Figures 6.9** and **6.10**, where the triclinic ytterbium disilicate phase crystallizes at a lower temperature than for erbium disilicate. The heat treatment temperature of the REDS holds great importance as do the synthesis parameters discussed in the previous sections. Given the maximum temperature limitations of the hot-stage, the *in situ* work could not reach the temperatures possible in the *ex situ* experiments, but it is hypothesized that the weight fraction of the monoclinic disilicate phase increases with temperature and time at temperature. The XRD patterns for Sc and Lu sol-gels shown in **Figures 6.12** and **6.13**, respectively, do not have the same polymorph transition from the triclinic to the

monoclinic phase. Instead, the Lu sol-gel only has the monosilicate and monoclinic disilicate phases. The weight fraction of the monosilicate phase decreases as temperature increases, which matches the *ex situ* results shown previously in **Figure 6.7** where $\text{Lu}_2\text{Si}_2\text{O}_7$ is the only phase. A similar trend is seen in the Sc sol-gel where instead of a triclinic phase or even the monosilicate phase, there are two phases: the disilicate and scandium oxide. The Sc oxide weight fraction is prevalent at lower temperatures but begins to disappear with rising temperatures, again matching **Figure 6.7**.

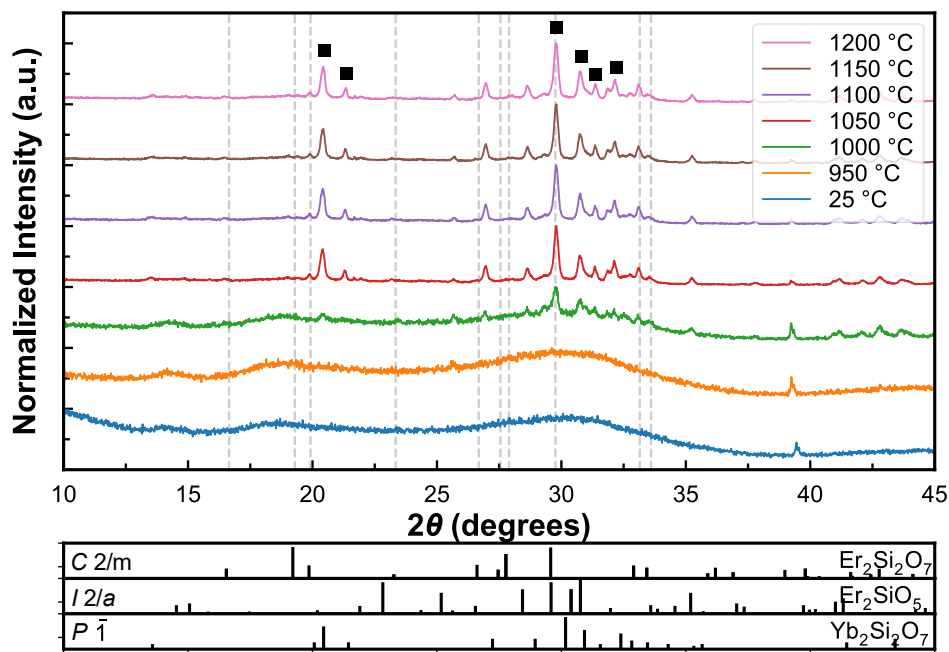


Figure 6.10: Hot-stage XRD of Er silicate sol-gel. The vertical dashed lines correspond to the $C 2/m$ phase that are seen *ex situ* and are absent in the given patterns. The predominant polymorph is the triclinic phase where the pattern for the triclinic $P \bar{1}$ phase of Yb disilicate is given as a reference for general peak location in black below the plot and with black squares above the 1200 °C pattern.

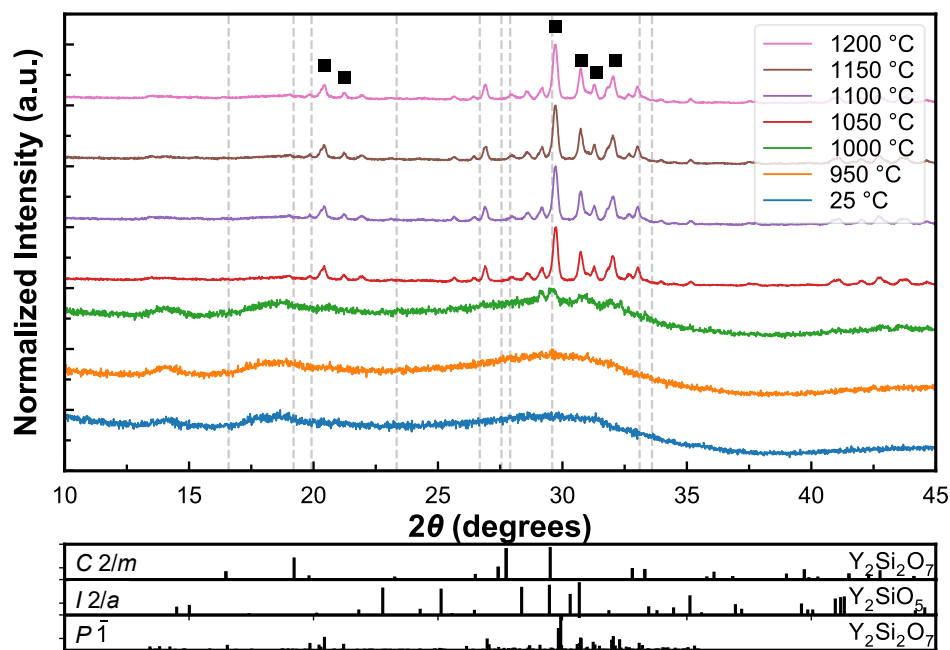


Figure 6.11: Hot-stage XRD of a Y silicate sol-gel. The vertical dashed lines correspond to the $C 2/m$ phase that is seen *ex situ* and is absent in the given patterns. The peaks corresponding to the triclinic phase have been indexed by black squares above the 1200 °C pattern.

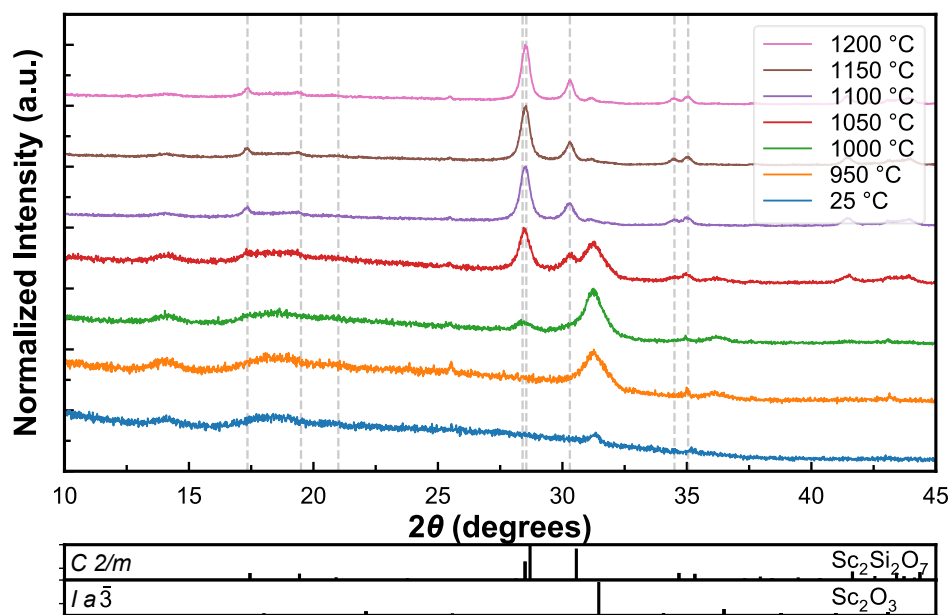


Figure 6.12: Hot-stage XRD of a Sc silicate sol-gel. The vertical dashed lines correspond to the $C 2/m$ phase seen *ex situ*. No triclinic or monosilicate was detected during crystallization. Instead, scandium oxide nucleates and decreases in weight fraction as temperature rises.

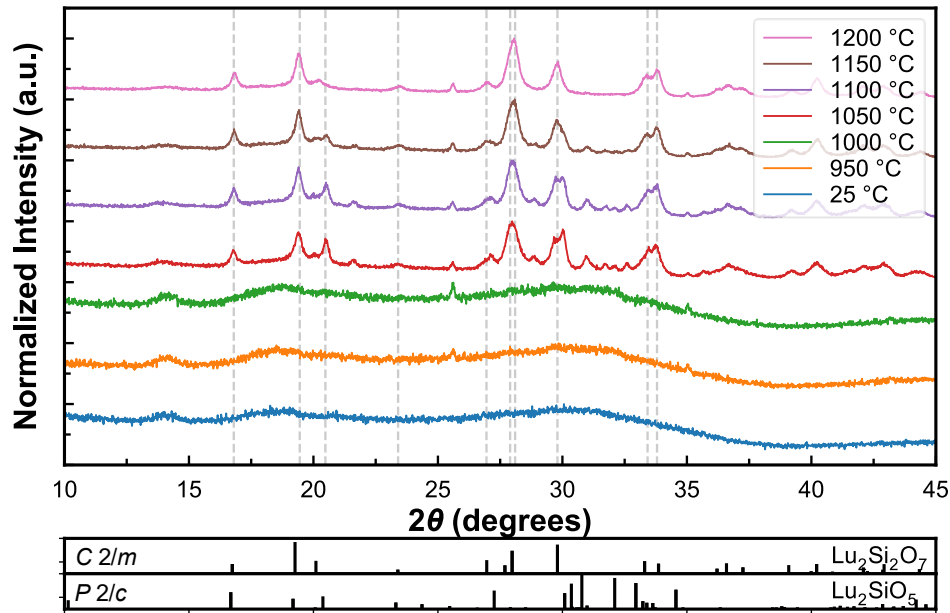


Figure 6.13: Hot-stage XRD of a Lu silicate sol-gel. The vertical dashed lines correspond to the $C 2/m$ phase that was seen in *ex situ* experiments. A monosilicate phase is visible and decreases in weight fraction as temperature increases.

The XRD patterns of $(\text{Sc}_{0.2}\text{Lu}_{0.2}\text{Yb}_{0.2}\text{Er}_{0.2}\text{Y}_{0.2})_2\text{Si}_2\text{O}_7$ a multi-component REDS, during crystallization is shown in **Figure 6.14**. The presence of the disilicate, $C 2/m$ phase, is indicated by the vertical gray dashed lines. As illustrated, the $C 2/m$ phase is the predominant phase in the crystalline material. Secondary phases, such as the triclinic phase of the disilicate as well as the monosilicate, are present during crystallization that do not appear in *ex situ* XRD of the same material in **Figure 6.8**. The presence of the triclinic phase is small but is most evident when inspecting the broad peak shape at approximately 30° in 2θ that is rounded due to the presence of both the triclinic and monoclinic phases. As temperature increases, this peak sharpens as the triclinic phase fraction decreases. At above 20° in 2θ , a peak corresponding to the triclinic phase can also be seen at 1050°C . This peak decreases in intensity, indicating again the phase transformation. The presence of alumina is visible in the peaks at approximately 26° and 36° in 2θ , originating from the alumina sample holder. These results indicate the importance of high heat treatment temperatures and long heat treatment times to enable the complete evolution of the disilicate phase to produce a phase pure final material.

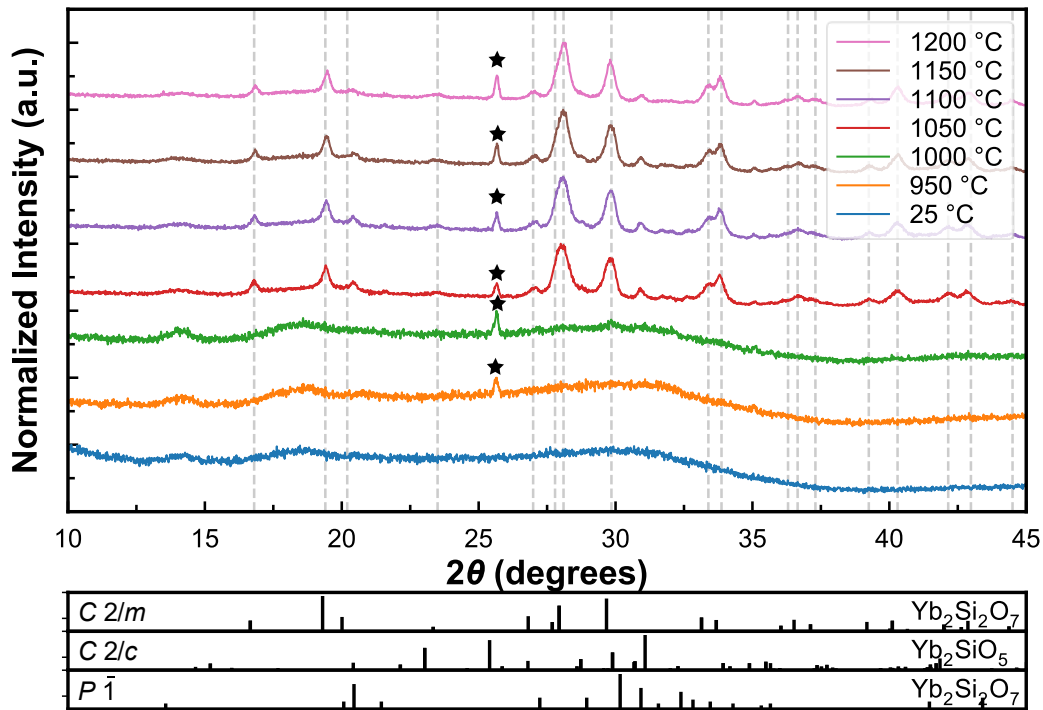


Figure 6.14: *In situ* XRD of the multi-component REDS with the following composition: (Sc, Lu, Yb, Er, Y)₂Si₂O₇. Reference patterns for Yb disilicate polymorphs and Yb monosilicate are given below, and vertical dashed lines indicate the approximate location of *C 2/m* peaks. A star is used to mark an alumina sample holder peak.

To gain insight into the progression of the triclinic to monoclinic phase transformation during crystallization, additional *ex situ* crystallization studies were performed on the Yb disilicate. **Figure 6.15** shows the *ex situ* crystallization of Yb disilicate sol-gels at 4 different heat treatment durations at 1000 °C. The vertical dashed lines indicate the locations of the monoclinic disilicate phase. The triclinic phase nucleates first and eventually converts into the monoclinic phase as time and temperature increase. The weight fraction of the triclinic phase for the 1, 3, 10, and 24 hour heat treatments are 96.9%, 91.5%, 62.4%, and 46.0%, respectively, suggesting a slow transformation from the triclinic to monoclinic phase. The most intense monoclinic disilicate peak, at approximately 28° in 2θ as seen in **Figure 6.8**, results in a broad peak shape in the lowest heat treatment times. The peak sharpens as heat treatment time increases and indicates the contrast in nucleation and growth behavior of the monoclinic and triclinic phases. The broad peaks are due to small crystallites that then grow at longer time and temperature.

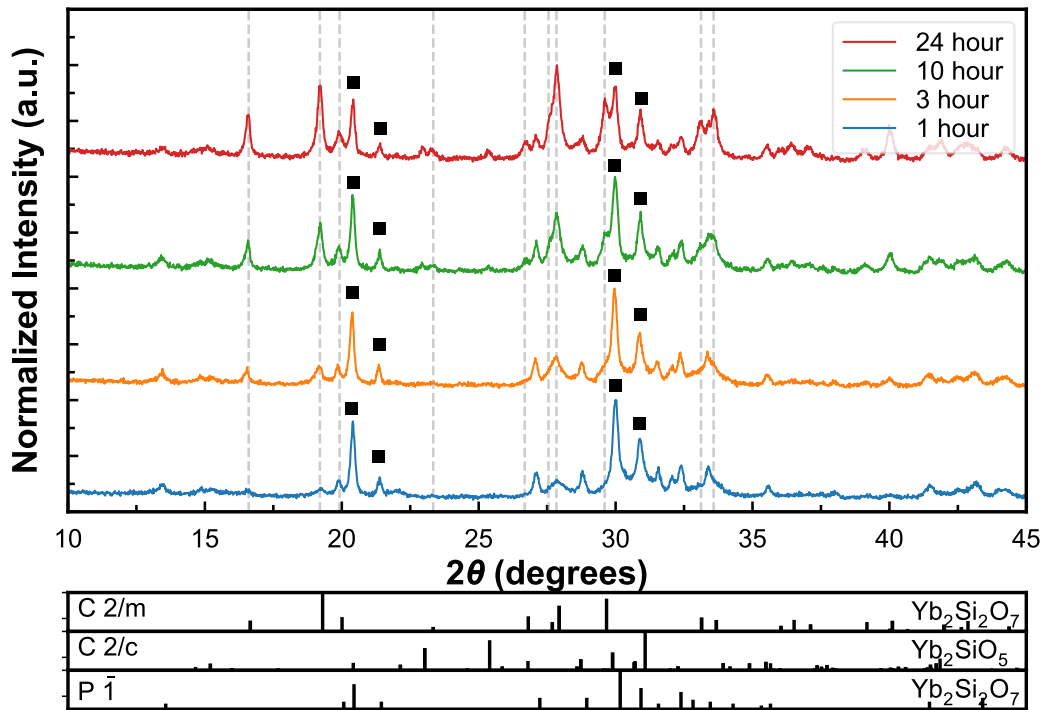


Figure 6.15: XRD patterns for Yb disilicate sol-gel derived powders heat treated at 1000 °C for 1, 3, 10, and 24 hours. The dashed vertical line indicate the peak positions of the monoclinic disilicate phase. The black squares indicates the triclinic peaks.

The triclinic phase may present a design challenge for implementation of REDS as T/EBCs due to the phase transition from triclinic to monoclinic with initial heating. This phase transformation could potentially be deleterious because of thermomechanical instability of the coating. To illustrate this potential challenge, the unit cell volumes of the triclinic and monoclinic structures of the disilicates were normalized by the formula units (f.u.) per unit cell volume. The molar volume of monoclinic $\text{Er}_2\text{Si}_2\text{O}_7$ phase being $143.65 \text{ \AA}^3/\text{f.u.}$ and the triclinic $\text{Er}_2\text{Si}_2\text{O}_7$ phase is only $130.08 \text{ \AA}^3/\text{f.u.}$ suggesting an expansion of 10.4% upon transforming from the triclinic to the monoclinic phase.²⁷ Garcia *et al.* report the molar volumes of the two polymorphs of $\text{Yb}_2\text{Si}_2\text{O}_7$ as 78.29 and 85.52 cm^3 for the triclinic and monoclinic phase respectively. The transformation into the monoclinic phase results in a 9.24% volume expansion.¹¹² This substantial difference will lead to thermal expansion stresses as the phase transformation occurs with a large expansion between the triclinic and monoclinic phases.

6.6 Conclusion

This work outlines conditions that can be used to prepare REDS powders with high phase purity. The use of little to no water, low pH, and high crystallization temperatures resulted in higher phase purity for

the desired disilicate phase for single cation and multicomponent REDS. The synthesis of single rare earth cation and multi-component REDS via sol-gel requires control of the TEOS hydrolysis reaction to produce an intended final phase mixture. Too fast of hydrolysis driven by excess water likely leads to the segregation of SiO₂, which prevents the atomic scale mixing necessary to realize RE₂Si₂O₇ as the first crystallization product. The use of *in situ* and *ex situ* XRD to study crystallization showed the importance of processing temperature and phase evolution that occurs as the temperature is increased. An intermediate triclinic phase seen in the crystallization of Yb, Er, and Y disilicates has been confirmed and can be a potential hazard to thermomechanical stability within a REDS T/EBC. Several other REDS had secondary phases (monosilicates, silica, and oxide) appear and subsequently disappear during crystallization and the origin of these phases likely was related to water content and/or non-stoichiometric batching due to water adsorbed on the rare earth nitrate precursors. Understanding the sol-gel processing criteria and crystallization behavior allows production of more consistent phase pure REDS, informs the synthesis of producing mixed phase powders with desired ratios, and outlines the amorphous to crystalline transition that REDS may see as T/EBCs in application.

6.7 Acknowledgements

This work was supported by the U.S. National Science Foundation's (NSF) Designing Materials to Revolution and Engineer our Future (DMREF) program under award number 1921973. Utilization of the Panalytical Empyrean, X'pert, and Anton Parr Hot-Stage instruments within UVA's Nanoscale Materials Characterization Facility (NMCF) was fundamental to this work.

Chapter 7 Conclusions

The application of REDSs as EBC materials requires consideration into the processing and thermo-mechanical properties of these coatings. This thesis focused on the fundamental science that governs the synthesis and high temperature behavior of REDS through the study of CTE anisotropy and sol-gel reaction chemistry. The major conclusions of this work are listed below:

- Multi-component REDS follow a rule of mixtures, enabling the stabilization of RE cations into atypical phases. This behavior was observed through the stabilization of a multi-component REDS containing dysprosium into the $C 2/m$ monoclinic phase. The phase was confirmed with hot stage XRD as stable to 1200 °C, despite a single component dysprosium disilicate forming the triclinic phase with no monoclinic polymorph.
- The CTE can be tailored depending on RE cation composition, improving or harming the CTE mismatch with the underlying CMC. The linear CTE and the second-rank CTE tensor were calculated for the REDS, showing that the CTE can be tailored by the RE cations present. These changes in CTE based on composition can improve or worsen the thermal stresses between the EBC and underlying CMC material.
- The CTE is anisotropic, and this anisotropy is dependent on the RE cation(s). The CTE anisotropy is described by a rotation in principal axes or change in eigenvectors. The principal axis rotation for ytterbium disilicate was approximately 47° while for erbium disilicate it was only 3°. The rotation was present for all ytterbium containing multi-component REDS and several other REDS exhibited this rotation as single component REDS (yttrium and lutetium disilicate).
- The cation dependent CTE principal axes were investigated by a number of methods, with neutron PDF concluding that there are local distortions of the lattice that do not match the long range diffraction data. The neutron PDF showed that the ytterbium disilicate sample has triclinic local distortions at less than 6 Å length scales, which is below the unit cell dimensions. The erbium disilicate sample does not have triclinic local distortions, instead the local structure is monoclinic. The triclinic distortion allows for greater degrees of freedom for the local ytterbium lattice to deform as temperature increases, resulting in the anisotropic CTE behavior observed.
- The sol-gel synthesis of REDS is commonly used in literature but is rarely consistent in procedure or final phase purity. This work developed a methodology for understanding and consistently synthesizing phase pure REDS materials through sol-gel synthesis. The sol-gel process is sensitive to water and pH, where very small quantities of water adsorbed onto the hygroscopic RE nitrate precursors and a pH at or below 2 is enough to advance the hydrolysis reaction and promote single

phase purity. Additionally, special care must be taken to measure the amount of water absorbed by the nitrate precursor to properly maintain a 1:1 Si:RE ratio.

- Production of amorphous REDS material allowed for *in situ* X-ray crystallization studies that observed the phase evolution analogous to what is seen in application as the plasma coated layers of the EBC crystallization. Ytterbium disilicate is typically considered to only be stable in the $C 2/m$ phase, but this work observed the crystallization of a triclinic phase that was then converted to the expected $C 2/m$ as temperature increased. The triclinic phase crystallized from amorphous material after the sample reached 1000 °C but disappeared at approximately 1200 °C. The phase transition is irreversible, not being present on cooling or subsequent re-heating. The transient triclinic phase has implications regarding the thermal stresses of ytterbium disilicate as an EBC materials as the triclinic to monoclinic phase transition has a volume expansion of 9.2%.

Chapter 8 Future Work

8.1 Recommendations on Future Research

8.1.1 Other REDS Compositions

The REs investigated in this work are only a subset of all possibilities. The cations remaining that are of interest are holmium, gadolinium, thulium as well as more work on dysprosium and lutetium as either single cation or multi-component REDSs. Understanding the limits of the average ionic radius effect described in **Chapter 4** with larger cations and distinct compositions is of interest. Specifically, it is of interest to understand what the greatest difference between ionic radius can be before phase separation. Additionally, the thermal expansion behaviors are unknown for these multi-component systems. A four component system of the following composition: $(\text{Lu,Yb,Er,Gd})_2\text{Si}_2\text{O}_7$, should produce the monoclinic $C 2/m$ phase according to the average ionic radius being less than 0.9 \AA . The phase stability and thermal expansion should be investigated if the final phase is as predicted. Additions of scandium in solid solution should also allow for the stabilization of gadolinium if the difference in ionic radius is not too great. Additionally, thulium disilicate is of interest since it is the cation between erbium and ytterbium. Thulium could serve as a valuable data point in the comparison between erbium and ytterbium as well as the effects of f-orbital electrons on the properties of REDS.

8.1.2 Non-equimolar Rare-Earth Concentrations

The equimolar compositions were maintained for multi-component compositions due to the prevalent definition of HE alloys consisting of minimum five equimolar constituent species homogeneously mixed in solid solution.³⁹ There is ample processing space where these RE cation ratios are varied to further expand on stability ranges. For example, the $(\text{Yb,Nd})_2\text{Si}_2\text{O}_7$ composition made in Chapter 3 produced a two phase mixture when equimolar due to the large difference in ionic radius between the two REs, but by decreasing the concentration of neodymium the final product may result in a single phase material. Much of this is inspired by the work done by Mackenzie Ridley^{22,41} and this would be a continuation using the advantages of the sol-gel method to make small batches of different combinations with relative ease. The cations that currently garner the most curiosity would be neodymium, gadolinium, and dysprosium since all are too large to stabilize in the monoclinic $C 2/m$ phase as single component REDSs. Scandium is also of interest due to its very small size relative to all other REs.

8.1.3 Beamline Experiments above 1000 °C

An important experimental parameter that was limited in synchrotron experiments was the maximum temperature for *in situ* XRD. Finding and applying for time at beamlines such as 6-ID-D at the Advanced Photon Source at Argonne National Laboratory could allow for building the same tensor derived

anisotropic CTE model at temperatures above 1000 °C. Given the high temperature applications for REDS as T/EBCs, increasing the experimental temperature would better inform how the thermomechanical stresses evolve during operation and if phase transformations are present in multicomponent REDS phase pure in current temperature ranges. A benefit of the lower temperature range is that the experiment and equipment allowed for small temperature steps of about 2 °C between each scan at the APS, while for higher temperatures it's typical that temperatures steps are about 50-100 °C. This loss in temperature resolution means that the temperatures at which CTE behavior and phase transformations occur will be less exact.

8.1.4 Stress Calculations and Elastic Modulus

The CTE is better described as the temperature dependent strain, meaning as temperature increases, stresses develop due to the changes in dimensions. A second rank stress tensor can be calculated from the CTE tensor and the elastic modulus. A major obstacle in this work is determining the elastic modulus tensor, which is a fourth rank tensor. The elastic modulus tensor has eighty-one coefficients but can be reduced to thirty-six since the stress and strain tensors are both symmetric second rank tensors. The tensor can be further simplified through symmetry, given below for a monoclinic crystal⁶⁴:

$$\begin{pmatrix} s_{11} & s_{12} & s_{13} & 0 & s_{15} & 0 \\ s_{12} & s_{22} & s_{23} & 0 & s_{25} & 0 \\ s_{13} & s_{23} & s_{33} & 0 & s_{35} & 0 \\ 0 & 0 & 0 & s_{44} & 0 & s_{46} \\ s_{15} & s_{25} & s_{35} & 0 & s_{55} & 0 \\ 0 & 0 & 0 & s_{46} & 0 & s_{66} \end{pmatrix} \quad (8.1)$$

The fourth rank tensor simplifies from eighty-one terms to twenty total terms (thirteen unique terms due to equivalent values). Acquiring the elastic modulus tensor experimentally can be done by forming a single crystal of material. Acoustic pulses are applied at different orientations and their propagation is measured to obtain coefficients. The elastic modulus can then be calculated for a polycrystalline material using the Voigt-Reuss-Hill method, where the elastic constants are given below⁶⁴:

$$E_R = 15/[5(s_{11}+s_{22}+s_{33}) + 2(s_{12}+s_{13}+s_{23}) + (s_{44}+s_{55}+s_{66})] \quad (8.2)$$

$$G_R = 15/[4(s_{11}+s_{22}+s_{33}) - 4(s_{12}+s_{13}+s_{23}) + 3(s_{44}+s_{55}+s_{66})] \quad (8.3)$$

$$\nu_R = (E_R/2G_R) - 1 \quad (8.4)$$

Performing this experimentally is most likely too difficult to perform in a reasonable amount of time, and computational collaboration would most likely be the more straightforward approach to calculating the elastic modulus tensor. Once the elastic modulus tensor is acquired, the stress tensor can be

calculated and used to model the anisotropic stresses in the REDSs. The understanding of the stress states in the crystal can be applied to how specific grain orientation may lead to material failure and if certain RE compositions can improve the stress state.

Chapter 9 Appendix

9.1 Supplemental Information

9.1.1 GSAS-II Sequential Rietveld Refinement of Hot Stage Data

The following procedure serves as a general procedure for the refinement performed. This cannot be comprehensive in all cases since each refinement requires different refined parameters and understanding of the base material.

1. Import the phase(s) of your material as *.CIF files.
2. Import the first data file, typically the room temperature scan. Only import a single file.
3. Assign instrument parameters acquired via a standard (CeO₂ in this case, but usually LaB₆ in in-lab scenarios). If you don't have a standard, press cancel, then a new dialogue box appears. Select the built-in defaults such as Cu K-alpha data.
4. Go to the data tree and select **background**. Make sure the refinement flag is checked and set the number of coefficients anywhere from 6-9. The higher the value, the more likely you are to begin fitting noise.
5. Go to **calculate** at the top and click "**Refine**". Inspect the background's fit and repeat steps 4 and 5 if needed.
6. Click on the phase you imported previously and under the "**General**" tab check the "Refine unit cell" box.
7. **Refine**
8. Back in the data tree with our data file, go to sample parameters and check the **sample displacement** box. (If this doesn't appear, make sure you have the correct diffractometer type selected). This is only applicable for reflection geometry experiments.
9. **Refine**
10. Remember to save your project very regularly.
11. For single phase skip to step 15. If you have multiple phase (> 5 wt.% each) then the phase fraction should also be refined. In the "**Data**" tab of the phases, check the "**Phase fraction**" box for every phase.
12. One now needs to make sure that all the phase fractions add up to 100%. Go to the data tree and select "**Constraints**". Go to the "**Histogram/Phase**" tab. In the top toolbar, click "**Edit Constr.**" And then "**Add constraint equation**".
13. A box will appear and in the "**Filter**" search box type in the word "**scale**". Click on "**0:0:Scale**" since this is the first phase of the first data file. Hit OK. Then select "**all:0:Scale**" which is all phases for the first data file. Hit OK.

14. Refine

15. Return to the phase and click on the “**Data**” tab. Change the “**Preferred orientation model**” to “**Spherical harmonics**”, set the “**Harmonic order**” to **6**, and check the refine box. You can change the harmonic order but be careful not to go too high for the same reasons given in step 4. This refines texture, changing peak intensity ratios.

16. Refine

17. Now for refining peak broadening. Under the “**Data**” tab, check the “**microstrain**” box. Be aware of extremely large values or negatives. The default value is 1000. (The microstrain model can be changed from isotropic in certain cases, such as for a monoclinic crystal it can be set to uniaxial and the “Unique axis, HKL:” can be set to 0 1 0”).

18. Refine

19. Uncheck “**microstrain**” and check “**size(μm)**”. This is crystallite size and is strongly correlated with microstrain. Be aware of large or small values. GSAS-II will only display values $10 > x > 0.001$, but the calculated value can be orders of magnitude different. The default value is 1.

20. Refine

21. If the microstrain and crystallite size both refined to reasonable values, you can attempt refining them together or continue cycling between the two separately.

22. The following steps correspond to a sequential refinement. If you are not doing a sequential refinement then go to “**Controls**”, change “**Max cycles**” to **10**, and **refine** again. You could end here, but if you want to refine atomic positions, u parameters, and site occupancy, skip to step 33.

23. Uncheck all refined parameters that were checked except for Background. Don’t forget to uncheck the “**Refine unit cell**” box in the general tab for your phases.

24. In the “**Data**” tab under phases, check all the boxes under “**Hydrostatic/elastic strain**”. They will have different labels for different crystal structures, such as **D11**, **D22**, **D33**, and **D13** for a monoclinic crystal. This is how we calculate unit cell parameters sequentially.

25. Import all the data you wish to refine sequentially, excluding the data already imported.

26. Assign the same instrument parameters as before.

27. Go to “**Controls**” and change “**Max cycles**” to **10**. Press the “**Select datasets**” button and select all your files. Then check the “**Copy results to next Histogram**” box. This takes the refined parameters of the current file to the next, which allows for big changes in parameters to not result in a failed refinement or convergence.

28. Select the first data file in the data tree that we have been refining already. Click on the “**Commands**” tab in the top toolbar and then select “**Copy params**”. Copy the parameters to all the data files.
29. Go to each of your phases and, with the “**Data**” tab selected, go to the “**Edit Phase**” option in the toolbar. Select “**Copy data**” and copy the phase data for every data file. Repeat each phase.
30. Now the only parameters being refined are background and lattice parameters through hydrostatic strain. **Refine** (The refine option most likely says “Sequential refine” now).
31. One will have sequential results below all their data files that show all the parameters. This is a very useful tool for quickly seeing trends and determining if any parameters are outside of acceptable bounds.
32. Repeat steps 8-21 but this time do so for the first data file and click on the “**copy flags**” option. This option is available by hovering over options in your toolbar on the top like we did when copying data. Do not copy params or data again, only flags!
33. It is possible to refine atomic positions, u parameters, and site occupancy. Go to the phase you want to refine and then navigate to the “**Atoms**” tab. Here is essentially the .CIF files that were imported. If unwanted changes are made, go to “**Edit Atoms**” on top, “**Reimport Atoms**”, select .CIF file, and reselect the .CIF file you used initially to restore the values to their originals.
34. In the “**Atoms**” tab you can double click individual boxes in the “**refine**” column to cause a dropdown to appear. In that dropdown you can select what to refine. An alternative is to double click the “**refine**” column and select the parameters from there. One can refine individually or several parameters at once.
35. It is advised to start with atomic coordinates (X), then thermal parameters (U), and if necessary, end with site fractions (F). Refine these parameters starting with the element with the highest Z, and then add the next heaviest element. Lighter elements may not produce valid values to x-rays lack of sensitivity to them.

9.1.2 Extra Thermal Expansion Ellipsoids

The thermal expansion tensors were calculated for more than just the compositions given in previous chapters. REDSs containing, Lu, Y, Sc, and a two component (Lu,Er) were made. The data for the single component REDS was acquired at the Advanced Photon Source at Argonne National Laboratory, beamline 11-ID-C. The data for the two component REDS was acquired with in-lab instrumentation using the Empyrean and Anton Parr hot Stage described in **Chapter 4**. A reminder that blue corresponds to the coldest temperature at which measurements were taken (room temperature), and red is the hottest

measurement temperature (1000 °C for synchrotron and 1200 °C for in-lab instrumentation). **Figure 9.1** shows the 2D ellipsoid of Lu disilicate in the (010) plane. Unlike almost every other ellipsoid, there seems to be a smaller ellipsoid along the c axis that shrinks as temperature increases. There is a rotation of 13° in the direction of maximum and minimum CTE observed for Lu. **Figure 9.2** shows the 2D ellipsoid of Y disilicate in the (010) plane. There is a rotation of approximately 15° in the direction of maximum and minimum CTE observed for Lu. **Figure 9.3** shows the 2D ellipsoid of Sc disilicate in the (010) plane. There is a rotation of approximately 0.7° in the direction of maximum and minimum CTE observed for Sc. **Figure 9.4** shows the 2D ellipsoid of $(\text{Lu}_{0.5}\text{Er}_{0.5})_2\text{Si}_2\text{O}_7$ disilicate in the (010) plane. There is a rotation of approximately 9° in the direction of maximum and minimum CTE observed for $(\text{Lu}_{0.5}\text{Er}_{0.5})_2\text{Si}_2\text{O}_7$.

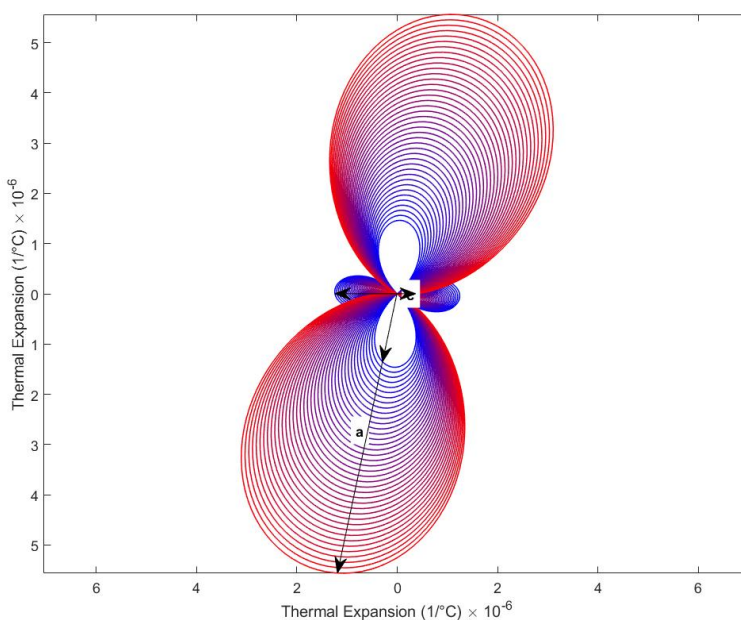


Figure 9.1: 2-D polar plots showing the change in the magnitude of CTE along crystallographic directions in the (010) plane from room temperature to 1000 °C for Lu disilicate. The color gradient represents the temperature, with blue being the lowest temperature and red being the highest.

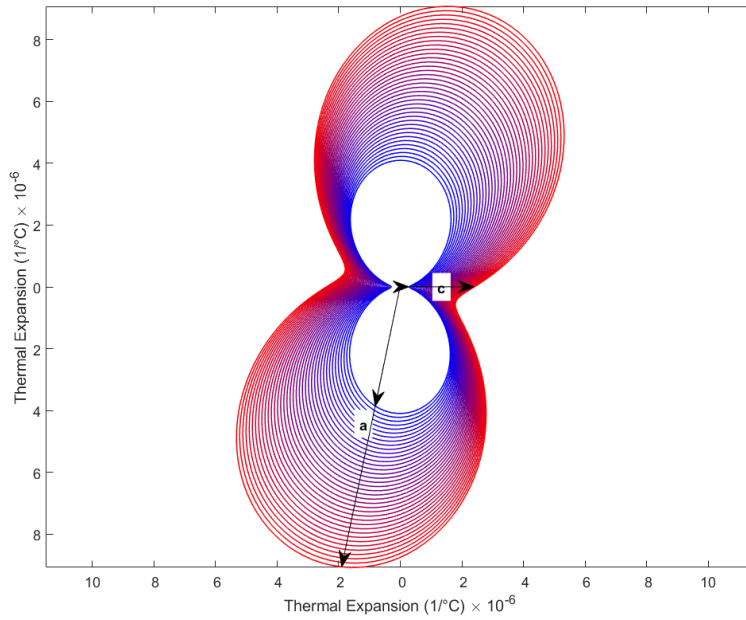


Figure 9.2: 2-D polar plots showing the change in the magnitude of CTE along crystallographic directions in the (010) plane from room temperature to 1000 °C for Y disilicate. The color gradient represents the temperature, with blue being the lowest temperature and red being the highest.

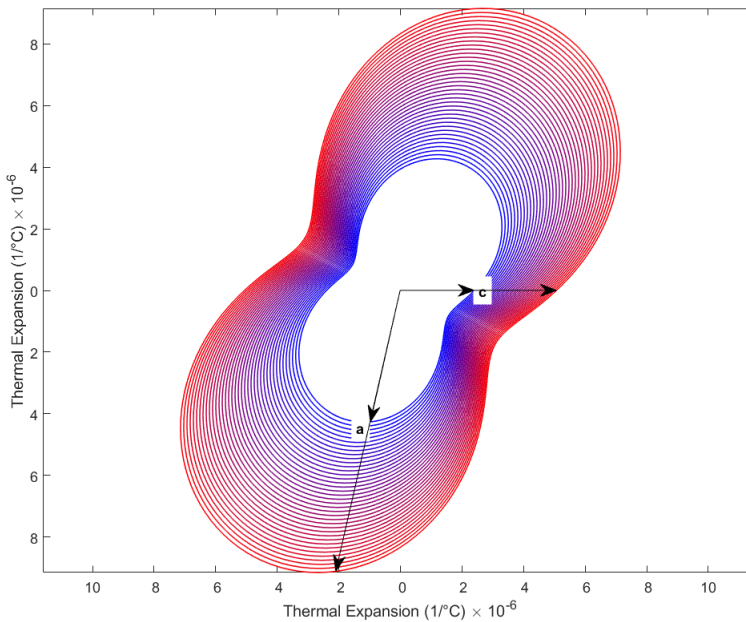


Figure 9.3: 2-D polar plots showing the change in the magnitude of CTE along crystallographic directions in the (010) plane from room temperature to 1000 °C for Sc disilicate. The color gradient represents the temperature, with blue being the lowest temperature and red being the highest.

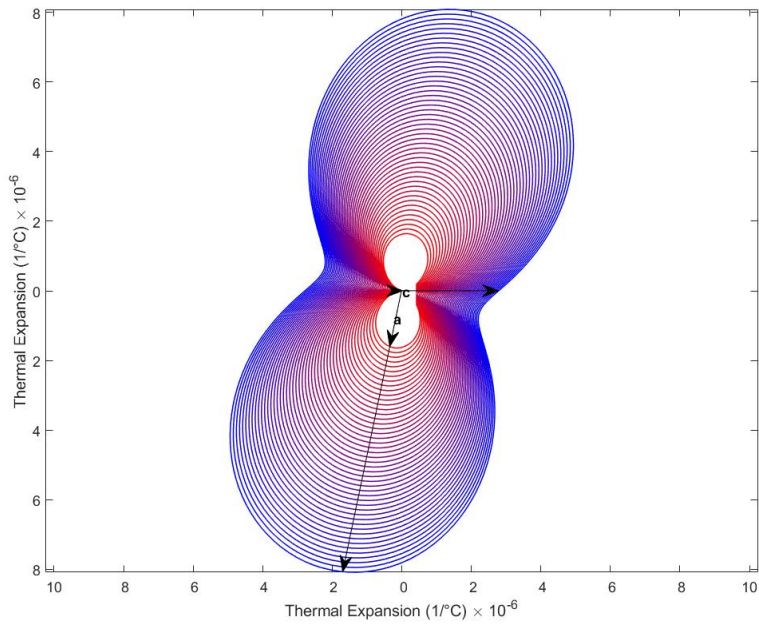


Figure 9.4: 2-D polar plots showing the change in the magnitude of CTE along crystallographic directions in the (010) plane from room temperature to 1000 °C for $(\text{Lu}_{0.5}\text{Er}_{0.5})_2\text{Si}_2\text{O}_7$. The color gradient represents the temperature, with blue being the lowest temperature and red being the highest.

9.1.3 Negative Thermal Expansion

The ellipsoids shown in the previous section show a cross section of a more complete 3D representation. A 3D representation the entirety of the CTE behavior and in the case of the figures below, indicate crystallographic directions in which the crystal has a negative CTE. **Figure 9.5** illustrates the 3D evolution of CTE for $(\text{Lu}_{0.5}\text{Er}_{0.5})_2\text{Si}_2\text{O}_7$. The orange/yellow coloring shown corresponds to negative thermal expansion, while blue is positive expansion. The y-axis shown in the plot is nearly in-line with the unknit cell's *b*-axis, meaning $(\text{Lu}_{0.5}\text{Er}_{0.5})_2\text{Si}_2\text{O}_7$ contracts along the *b*-axis at high enough temperatures (above 1000 °C).

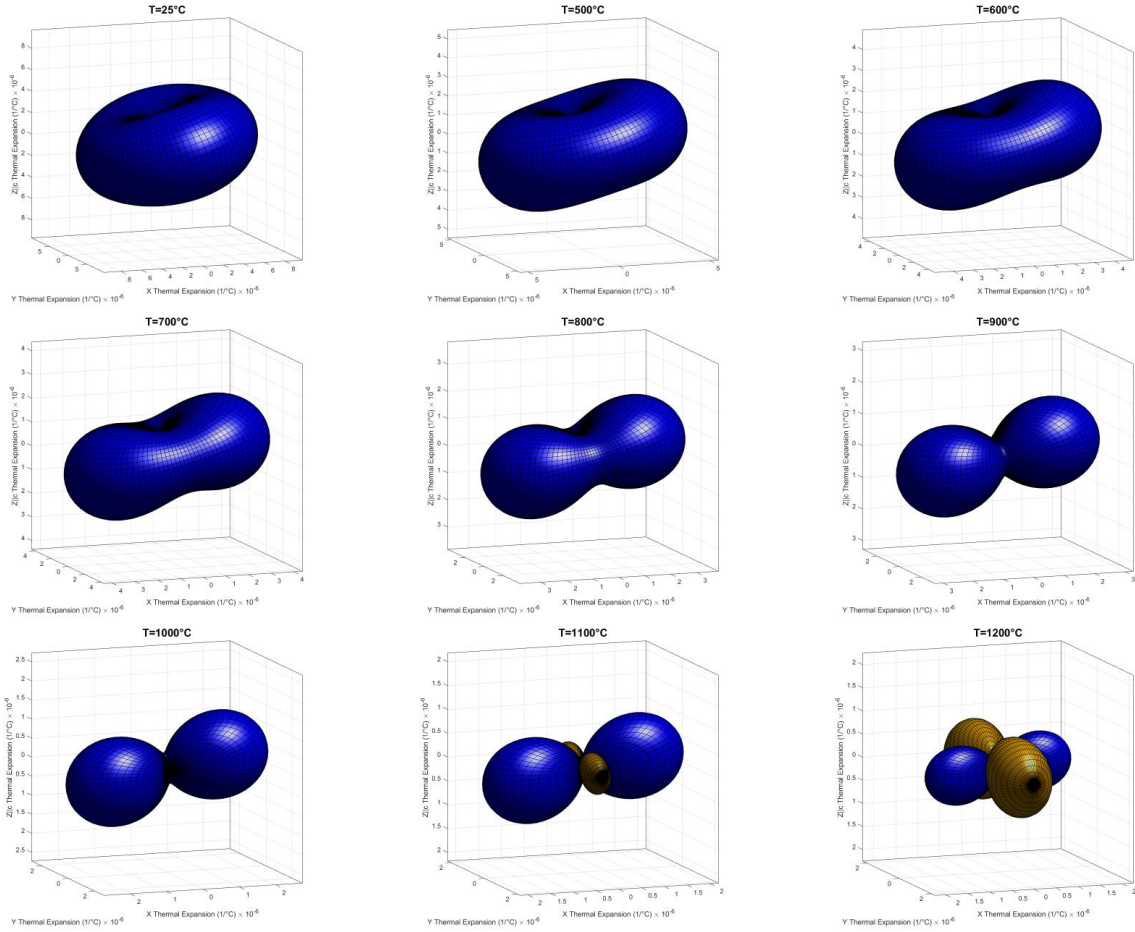


Figure 9.5: 3D representations of the coefficient of thermal expansion (CTE) tensors for $(\text{Lu}_{0.5}\text{Er}_{0.5})_2\text{Si}_2\text{O}_7$ at different temperatures. The CTE along the y-axis becomes negative above 1000 °C.

9.1.4 CTEAS Tensor Data

Table 9.1: Tensor data determined by CTEAS program for Yb disilicate data gathered at beamline 11-ID-C at APS. The numbers in parenthesis correspond to the non-zero coefficient.

TEMP	CTE(11)	CTE(13)	CTE(22)	CTE(31)	CTE(33)
25	3.64E-06	6.60E-07	3.28E-06	6.60E-07	2.43E-06
50	3.69E-06	6.17E-07	3.31E-06	6.17E-07	2.47E-06
75	3.75E-06	5.73E-07	3.33E-06	5.73E-07	2.50E-06
100	3.80E-06	5.29E-07	3.36E-06	5.29E-07	2.53E-06
125	3.85E-06	4.86E-07	3.38E-06	4.86E-07	2.57E-06
150	3.91E-06	4.42E-07	3.41E-06	4.42E-07	2.60E-06
175	3.96E-06	3.98E-07	3.43E-06	3.98E-07	2.63E-06

200	4.02E-06	3.55E-07	3.46E-06	3.55E-07	2.66E-06
225	4.07E-06	3.11E-07	3.48E-06	3.11E-07	2.70E-06
250	4.12E-06	2.67E-07	3.51E-06	2.67E-07	2.73E-06
275	4.18E-06	2.24E-07	3.53E-06	2.24E-07	2.76E-06
300	4.23E-06	1.80E-07	3.56E-06	1.80E-07	2.80E-06
325	4.28E-06	1.36E-07	3.58E-06	1.36E-07	2.83E-06
350	4.34E-06	9.26E-08	3.61E-06	9.26E-08	2.86E-06
375	4.39E-06	4.89E-08	3.63E-06	4.89E-08	2.90E-06
400	4.45E-06	5.21E-09	3.66E-06	5.21E-09	2.93E-06
425	4.50E-06	-3.85E-08	3.68E-06	-3.85E-08	2.96E-06
450	4.55E-06	-8.22E-08	3.71E-06	-8.22E-08	2.99E-06
475	4.61E-06	-1.26E-07	3.73E-06	-1.26E-07	3.03E-06
500	4.66E-06	-1.70E-07	3.76E-06	-1.70E-07	3.06E-06
525	4.71E-06	-2.13E-07	3.78E-06	-2.13E-07	3.09E-06
550	4.77E-06	-2.57E-07	3.81E-06	-2.57E-07	3.13E-06
575	4.82E-06	-3.01E-07	3.83E-06	-3.01E-07	3.16E-06
600	4.88E-06	-3.44E-07	3.86E-06	-3.44E-07	3.19E-06
625	4.93E-06	-3.88E-07	3.88E-06	-3.88E-07	3.23E-06
650	4.98E-06	-4.32E-07	3.91E-06	-4.32E-07	3.26E-06
675	5.04E-06	-4.76E-07	3.93E-06	-4.76E-07	3.29E-06
700	5.09E-06	-5.19E-07	3.96E-06	-5.19E-07	3.32E-06
725	5.14E-06	-5.63E-07	3.98E-06	-5.63E-07	3.36E-06
750	5.20E-06	-6.07E-07	4.01E-06	-6.07E-07	3.39E-06
775	5.25E-06	-6.51E-07	4.03E-06	-6.51E-07	3.42E-06
800	5.31E-06	-6.94E-07	4.06E-06	-6.94E-07	3.46E-06
825	5.36E-06	-7.38E-07	4.08E-06	-7.38E-07	3.49E-06
850	5.41E-06	-7.82E-07	4.11E-06	-7.82E-07	3.52E-06
875	5.47E-06	-8.26E-07	4.13E-06	-8.26E-07	3.56E-06
900	5.52E-06	-8.69E-07	4.16E-06	-8.69E-07	3.59E-06
925	5.58E-06	-9.13E-07	4.18E-06	-9.13E-07	3.62E-06
950	5.63E-06	-9.57E-07	4.21E-06	-9.57E-07	3.65E-06
975	5.68E-06	-1.00E-06	4.23E-06	-1.00E-06	3.69E-06
1000	5.74E-06	-1.04E-06	4.26E-06	-1.04E-06	3.72E-06

Table 9.2: Eigen values and angles determined by CTEAS program for Yb disilicate data gathered at beamline 11-ID-C at APS.

TEMP	EIG1	EIG2	EIG3	EIG1ANGLE	EIG2ANGLE	EIG3ANGLE
25	3.93E-06	3.28E-06	2.14E-06	160	90	110
50	3.95E-06	3.31E-06	2.21E-06	161	90	109
75	3.97E-06	3.33E-06	2.28E-06	162	90	108
100	3.99E-06	3.36E-06	2.34E-06	164	90	106
125	4.02E-06	3.38E-06	2.40E-06	165	90	105
150	4.04E-06	3.41E-06	2.46E-06	167	90	103
175	4.07E-06	3.43E-06	2.52E-06	168	90	102
200	4.10E-06	3.46E-06	2.58E-06	170	90	100
225	4.14E-06	3.48E-06	2.63E-06	172	90	98.5
250	4.17E-06	3.51E-06	2.68E-06	173	90	96.8
275	4.21E-06	3.53E-06	2.73E-06	175	90	95.1
300	4.25E-06	3.56E-06	2.77E-06	177	90	93.3
325	4.30E-06	3.58E-06	2.82E-06	178	90	91.6
350	4.34E-06	3.61E-06	2.86E-06	180	90	89.9
375	4.39E-06	3.63E-06	2.89E-06	178	90	88.2
400	4.45E-06	3.66E-06	2.93E-06	176	90	86.5
425	4.50E-06	3.68E-06	2.96E-06	175	90	84.9
450	4.56E-06	3.71E-06	2.99E-06	173	90	83.3
475	4.62E-06	3.73E-06	3.02E-06	172	90	81.8
500	4.68E-06	3.76E-06	3.04E-06	170	90	80.3
525	4.74E-06	3.78E-06	3.07E-06	169	90	78.9
550	4.81E-06	3.81E-06	3.09E-06	168	90	77.6
575	4.87E-06	3.83E-06	3.11E-06	166	90	76.4
600	4.94E-06	3.86E-06	3.12E-06	165	90	75.2
625	5.01E-06	3.88E-06	3.14E-06	164	90	74.1
650	5.09E-06	3.91E-06	3.16E-06	163	90	73
675	5.16E-06	3.93E-06	3.17E-06	162	90	72
700	5.23E-06	3.96E-06	3.18E-06	161	90	71.1
725	5.31E-06	3.98E-06	3.19E-06	160	90	70.2
750	5.38E-06	4.01E-06	3.21E-06	159	90	69.4

775	5.46E-06	4.03E-06	3.22E-06	159	90	68.6
800	5.54E-06	4.06E-06	3.22E-06	158	90	67.9
825	5.62E-06	4.08E-06	3.23E-06	157	90	67.2
850	5.70E-06	4.11E-06	3.24E-06	157	90	66.6
875	5.77E-06	4.13E-06	3.25E-06	156	90	65.9
900	5.85E-06	4.16E-06	3.25E-06	155	90	65.4
925	5.94E-06	4.18E-06	3.26E-06	155	90	64.8
950	6.02E-06	4.21E-06	3.27E-06	154	90	64.3
975	6.10E-06	4.23E-06	3.27E-06	154	90	63.8
1000	6.18E-06	4.26E-06	3.28E-06	153	90	63.4

Table 9.3: Tensor data determined by CTEAS program for Er disilicate data gathered at beamline 11-ID-C at APS. The numbers in parenthesis correspond to the non-zero coefficient.

TEMP	CTE(11)	CTE(13)	CTE(22)	CTE(31)	CTE(33)
25	3.74E-06	-2.87E-07	3.68E-06	-2.87E-07	8.46E-07
50	3.79E-06	-3.01E-07	3.69E-06	-3.01E-07	8.85E-07
75	3.85E-06	-3.15E-07	3.71E-06	-3.15E-07	9.25E-07
100	3.90E-06	-3.29E-07	3.72E-06	-3.29E-07	9.64E-07
125	3.95E-06	-3.43E-07	3.73E-06	-3.43E-07	1.00E-06
150	4.00E-06	-3.56E-07	3.74E-06	-3.56E-07	1.04E-06
175	4.05E-06	-3.70E-07	3.75E-06	-3.70E-07	1.08E-06
200	4.11E-06	-3.84E-07	3.76E-06	-3.84E-07	1.12E-06
225	4.16E-06	-3.98E-07	3.77E-06	-3.98E-07	1.16E-06
250	4.21E-06	-4.12E-07	3.78E-06	-4.12E-07	1.20E-06
275	4.26E-06	-4.26E-07	3.80E-06	-4.26E-07	1.24E-06
300	4.31E-06	-4.40E-07	3.81E-06	-4.40E-07	1.28E-06
325	4.37E-06	-4.54E-07	3.82E-06	-4.54E-07	1.32E-06
350	4.42E-06	-4.68E-07	3.83E-06	-4.68E-07	1.36E-06
375	4.47E-06	-4.82E-07	3.84E-06	-4.82E-07	1.40E-06
400	4.52E-06	-4.96E-07	3.85E-06	-4.96E-07	1.43E-06
425	4.58E-06	-5.10E-07	3.86E-06	-5.10E-07	1.47E-06
450	4.63E-06	-5.24E-07	3.88E-06	-5.24E-07	1.51E-06
475	4.68E-06	-5.38E-07	3.89E-06	-5.38E-07	1.55E-06

500	4.73E-06	-5.52E-07	3.90E-06	-5.52E-07	1.59E-06
525	4.78E-06	-5.66E-07	3.91E-06	-5.66E-07	1.63E-06
550	4.84E-06	-5.80E-07	3.92E-06	-5.80E-07	1.67E-06
575	4.89E-06	-5.94E-07	3.93E-06	-5.94E-07	1.71E-06
600	4.94E-06	-6.08E-07	3.94E-06	-6.08E-07	1.75E-06
625	4.99E-06	-6.22E-07	3.95E-06	-6.22E-07	1.79E-06
650	5.04E-06	-6.36E-07	3.97E-06	-6.36E-07	1.83E-06
675	5.10E-06	-6.50E-07	3.98E-06	-6.50E-07	1.87E-06
700	5.15E-06	-6.64E-07	3.99E-06	-6.64E-07	1.91E-06
725	5.20E-06	-6.78E-07	4.00E-06	-6.78E-07	1.94E-06
750	5.25E-06	-6.92E-07	4.01E-06	-6.92E-07	1.98E-06
775	5.30E-06	-7.06E-07	4.02E-06	-7.06E-07	2.02E-06
800	5.36E-06	-7.20E-07	4.03E-06	-7.20E-07	2.06E-06
825	5.41E-06	-7.34E-07	4.05E-06	-7.34E-07	2.10E-06
850	5.46E-06	-7.48E-07	4.06E-06	-7.48E-07	2.14E-06
875	5.51E-06	-7.62E-07	4.07E-06	-7.62E-07	2.18E-06
900	5.56E-06	-7.76E-07	4.08E-06	-7.76E-07	2.22E-06
925	5.62E-06	-7.90E-07	4.09E-06	-7.90E-07	2.26E-06
950	5.67E-06	-8.04E-07	4.10E-06	-8.04E-07	2.30E-06
975	5.72E-06	-8.18E-07	4.11E-06	-8.18E-07	2.34E-06
1000	5.77E-06	-8.32E-07	4.12E-06	-8.32E-07	2.38E-06

Table 9.4: Eigen values and angles determined by CTEAS program for Er disilicate data gathered at beamline 11-ID-C at APS.

TEMP	EIG1	EIG2	EIG3	EIG1ANGLE	EIG2ANGLE	EIG3ANGLE
25	3.77E-06	3.68E-06	8.18E-07	9.32E+00	90	8.07E+01
50	3.83E-06	3.69E-06	8.55E-07	9.55E+00	90	8.04E+01
75	3.88E-06	3.71E-06	8.91E-07	9.78E+00	90	8.02E+01
100	3.94E-06	3.72E-06	9.27E-07	1.00E+01	90	8.00E+01
125	3.99E-06	3.73E-06	9.64E-07	1.02E+01	90	7.98E+01
150	4.05E-06	3.74E-06	1.00E-06	1.05E+01	90	7.95E+01
175	4.10E-06	3.75E-06	1.04E-06	1.07E+01	90	7.93E+01
200	4.16E-06	3.76E-06	1.07E-06	1.09E+01	90	7.91E+01

225	4.21E-06	3.77E-06	1.11E-06	1.11E+01	90	7.89E+01
250	4.27E-06	3.78E-06	1.14E-06	1.13E+01	90	7.87E+01
275	4.32E-06	3.80E-06	1.18E-06	1.15E+01	90	7.85E+01
300	4.38E-06	3.81E-06	1.21E-06	1.17E+01	90	7.83E+01
325	4.43E-06	3.82E-06	1.25E-06	1.20E+01	90	7.80E+01
350	4.49E-06	3.83E-06	1.29E-06	1.22E+01	90	7.78E+01
375	4.54E-06	3.84E-06	1.32E-06	1.24E+01	90	7.76E+01
400	4.60E-06	3.85E-06	1.36E-06	1.25E+01	90	7.75E+01
425	4.66E-06	3.86E-06	1.39E-06	1.27E+01	90	7.73E+01
450	4.71E-06	3.88E-06	1.43E-06	1.29E+01	90	7.71E+01
475	4.77E-06	3.89E-06	1.46E-06	1.31E+01	90	7.69E+01
500	4.83E-06	3.90E-06	1.50E-06	1.33E+01	90	7.67E+01
525	4.88E-06	3.91E-06	1.53E-06	1.35E+01	90	7.65E+01
550	4.94E-06	3.92E-06	1.57E-06	1.37E+01	90	7.63E+01
575	4.99E-06	3.93E-06	1.60E-06	1.39E+01	90	7.61E+01
600	5.05E-06	3.94E-06	1.64E-06	1.40E+01	90	7.60E+01
625	5.11E-06	3.95E-06	1.67E-06	1.42E+01	90	7.58E+01
650	5.16E-06	3.97E-06	1.71E-06	1.44E+01	90	7.56E+01
675	5.22E-06	3.98E-06	1.74E-06	1.45E+01	90	7.55E+01
700	5.28E-06	3.99E-06	1.77E-06	1.47E+01	90	7.53E+01
725	5.33E-06	4.00E-06	1.81E-06	1.49E+01	90	7.51E+01
750	5.39E-06	4.01E-06	1.84E-06	1.50E+01	90	7.50E+01
775	5.45E-06	4.02E-06	1.88E-06	1.52E+01	90	7.48E+01
800	5.51E-06	4.03E-06	1.91E-06	1.54E+01	90	7.46E+01
825	5.56E-06	4.05E-06	1.95E-06	1.55E+01	90	7.45E+01
850	5.62E-06	4.06E-06	1.98E-06	1.57E+01	90	7.43E+01
875	5.68E-06	4.07E-06	2.01E-06	1.58E+01	90	7.42E+01
900	5.74E-06	4.08E-06	2.05E-06	1.60E+01	90	7.40E+01
925	5.79E-06	4.09E-06	2.08E-06	1.61E+01	90	7.39E+01
950	5.85E-06	4.10E-06	2.12E-06	1.63E+01	90	7.37E+01
975	5.91E-06	4.11E-06	2.15E-06	1.64E+01	90	7.36E+01
1000	5.96E-06	4.12E-06	2.18E-06	1.66E+01	90	7.34E+01

Table 9.5: Tensor data determined by CTEAS program for Y disilicate data gathered at beamline 11-ID-C at APS. The numbers in parenthesis correspond to the non-zero coefficient.

TEMP	CTE(11)	CTE(13)	CTE(22)	CTE(31)	CTE(33)
25	4.10E-06	-2.10E-08	2.99E-06	-2.10E-08	2.89E-07
50	4.22E-06	-7.20E-08	3.07E-06	-7.20E-08	3.46E-07
75	4.35E-06	-1.23E-07	3.16E-06	-1.23E-07	4.03E-07
100	4.47E-06	-1.74E-07	3.24E-06	-1.74E-07	4.60E-07
125	4.60E-06	-2.25E-07	3.32E-06	-2.25E-07	5.17E-07
150	4.73E-06	-2.76E-07	3.41E-06	-2.76E-07	5.74E-07
175	4.85E-06	-3.27E-07	3.49E-06	-3.27E-07	6.31E-07
200	4.98E-06	-3.79E-07	3.57E-06	-3.79E-07	6.88E-07
225	5.10E-06	-4.30E-07	3.66E-06	-4.30E-07	7.45E-07
250	5.23E-06	-4.81E-07	3.74E-06	-4.81E-07	8.02E-07
275	5.35E-06	-5.32E-07	3.82E-06	-5.32E-07	8.59E-07
300	5.48E-06	-5.83E-07	3.91E-06	-5.83E-07	9.16E-07
325	5.61E-06	-6.35E-07	3.99E-06	-6.35E-07	9.73E-07
350	5.73E-06	-6.86E-07	4.08E-06	-6.86E-07	1.03E-06
375	5.86E-06	-7.37E-07	4.16E-06	-7.37E-07	1.09E-06
400	5.98E-06	-7.88E-07	4.24E-06	-7.88E-07	1.14E-06
425	6.11E-06	-8.40E-07	4.33E-06	-8.40E-07	1.20E-06
450	6.23E-06	-8.91E-07	4.41E-06	-8.91E-07	1.26E-06
475	6.36E-06	-9.43E-07	4.49E-06	-9.43E-07	1.32E-06
500	6.49E-06	-9.94E-07	4.58E-06	-9.94E-07	1.37E-06
525	6.61E-06	-1.05E-06	4.66E-06	-1.05E-06	1.43E-06
550	6.74E-06	-1.10E-06	4.74E-06	-1.10E-06	1.49E-06
575	6.86E-06	-1.15E-06	4.83E-06	-1.15E-06	1.54E-06
600	6.99E-06	-1.20E-06	4.91E-06	-1.20E-06	1.60E-06
625	7.12E-06	-1.25E-06	4.99E-06	-1.25E-06	1.66E-06
650	7.24E-06	-1.30E-06	5.08E-06	-1.30E-06	1.72E-06
675	7.37E-06	-1.35E-06	5.16E-06	-1.35E-06	1.77E-06
700	7.49E-06	-1.41E-06	5.25E-06	-1.41E-06	1.83E-06
725	7.62E-06	-1.46E-06	5.33E-06	-1.46E-06	1.89E-06
750	7.75E-06	-1.51E-06	5.41E-06	-1.51E-06	1.95E-06

775	7.87E-06	-1.56E-06	5.50E-06	-1.56E-06	2.00E-06
800	8.00E-06	-1.61E-06	5.58E-06	-1.61E-06	2.06E-06
825	8.13E-06	-1.66E-06	5.66E-06	-1.66E-06	2.12E-06
850	8.25E-06	-1.72E-06	5.75E-06	-1.72E-06	2.18E-06
875	8.38E-06	-1.77E-06	5.83E-06	-1.77E-06	2.23E-06
900	8.50E-06	-1.82E-06	5.91E-06	-1.82E-06	2.29E-06
925	8.63E-06	-1.87E-06	6.00E-06	-1.87E-06	2.35E-06
950	8.76E-06	-1.92E-06	6.08E-06	-1.92E-06	2.41E-06

Table 9.6: Eigen values and angles determined by CTEAS program for Y disilicate data gathered at beamline 11-ID-C at APS.

TEMP	EIG1	EIG2	EIG3	EIG1ANGLE	EIG2ANGLE	EIG3ANGLE
25	4.10E-06	2.99E-06	2.88E-07	1.76E+02	90	9.39E+01
50	4.22E-06	3.07E-06	3.44E-07	1.75E+02	90	9.46E+01
75	4.35E-06	3.16E-06	3.99E-07	1.75E+02	90	9.54E+01
100	4.48E-06	3.24E-06	4.52E-07	1.74E+02	90	9.60E+01
125	4.61E-06	3.32E-06	5.04E-07	1.73E+02	90	9.67E+01
150	4.74E-06	3.41E-06	5.55E-07	1.73E+02	90	9.73E+01
175	4.88E-06	3.49E-06	6.06E-07	1.72E+02	90	9.80E+01
200	5.01E-06	3.57E-06	6.55E-07	1.71E+02	90	9.86E+01
225	5.14E-06	3.66E-06	7.03E-07	1.71E+02	90	9.91E+01
250	5.28E-06	3.74E-06	7.50E-07	1.70E+02	90	9.97E+01
275	5.42E-06	3.82E-06	7.97E-07	1.70E+02	90	1.00E+02
300	5.55E-06	3.91E-06	8.43E-07	1.69E+02	90	1.01E+02
325	5.69E-06	3.99E-06	8.88E-07	1.69E+02	90	1.01E+02
350	5.83E-06	4.08E-06	9.32E-07	1.68E+02	90	1.02E+02
375	5.97E-06	4.16E-06	9.76E-07	1.68E+02	90	1.02E+02
400	6.11E-06	4.24E-06	1.02E-06	1.67E+02	90	1.03E+02
425	6.25E-06	4.33E-06	1.06E-06	1.67E+02	90	1.03E+02
450	6.39E-06	4.41E-06	1.10E-06	1.67E+02	90	1.03E+02
475	6.53E-06	4.49E-06	1.15E-06	1.66E+02	90	1.04E+02
500	6.67E-06	4.58E-06	1.19E-06	1.66E+02	90	1.04E+02
525	6.82E-06	4.66E-06	1.23E-06	1.66E+02	90	1.04E+02

550	6.96E-06	4.74E-06	1.27E-06	1.65E+02	90	1.05E+02
575	7.10E-06	4.83E-06	1.31E-06	1.65E+02	90	1.05E+02
600	7.25E-06	4.91E-06	1.35E-06	1.65E+02	90	1.05E+02
625	7.39E-06	4.99E-06	1.39E-06	1.64E+02	90	1.06E+02
650	7.53E-06	5.08E-06	1.42E-06	1.64E+02	90	1.06E+02
675	7.68E-06	5.16E-06	1.46E-06	1.64E+02	90	1.06E+02
700	7.82E-06	5.25E-06	1.50E-06	1.63E+02	90	1.07E+02
725	7.97E-06	5.33E-06	1.54E-06	1.63E+02	90	1.07E+02
750	8.12E-06	5.41E-06	1.58E-06	1.63E+02	90	1.07E+02
775	8.26E-06	5.50E-06	1.61E-06	1.63E+02	90	1.07E+02
800	8.41E-06	5.58E-06	1.65E-06	1.62E+02	90	1.08E+02
825	8.56E-06	5.66E-06	1.69E-06	1.62E+02	90	1.08E+02
850	8.70E-06	5.75E-06	1.72E-06	1.62E+02	90	1.08E+02
875	8.85E-06	5.83E-06	1.76E-06	1.62E+02	90	1.08E+02
900	9.00E-06	5.91E-06	1.80E-06	1.62E+02	90	1.08E+02
925	9.15E-06	6.00E-06	1.83E-06	1.61E+02	90	1.09E+02
950	9.29E-06	6.08E-06	1.87E-06	1.61E+02	90	1.09E+02

Table 9.7: Tensor data determined by CTEAS program for Lu disilicate data gathered at beamline 11-ID-C at APS. The numbers in parenthesis correspond to the non-zero coefficient.

TEMP	CTE(11)	CTE(13)	CTE(22)	CTE(31)	CTE(33)
25	1.46E-06	-1.15E-07	1.15E-06	-1.15E-07	-1.24E-06
50	1.56E-06	-1.52E-07	1.20E-06	-1.52E-07	-1.20E-06
75	1.65E-06	-1.90E-07	1.25E-06	-1.90E-07	-1.16E-06
100	1.75E-06	-2.27E-07	1.30E-06	-2.27E-07	-1.12E-06
125	1.85E-06	-2.64E-07	1.35E-06	-2.64E-07	-1.08E-06
150	1.94E-06	-3.02E-07	1.40E-06	-3.02E-07	-1.03E-06
175	2.04E-06	-3.39E-07	1.45E-06	-3.39E-07	-9.94E-07
200	2.14E-06	-3.77E-07	1.50E-06	-3.77E-07	-9.52E-07
225	2.24E-06	-4.14E-07	1.55E-06	-4.14E-07	-9.11E-07
250	2.33E-06	-4.51E-07	1.60E-06	-4.51E-07	-8.70E-07
275	2.43E-06	-4.89E-07	1.65E-06	-4.89E-07	-8.28E-07
300	2.53E-06	-5.26E-07	1.70E-06	-5.26E-07	-7.87E-07

325	2.62E-06	-5.64E-07	1.75E-06	-5.64E-07	-7.46E-07
350	2.72E-06	-6.01E-07	1.80E-06	-6.01E-07	-7.04E-07
375	2.82E-06	-6.39E-07	1.85E-06	-6.39E-07	-6.63E-07
400	2.92E-06	-6.76E-07	1.90E-06	-6.76E-07	-6.22E-07
425	3.01E-06	-7.13E-07	1.95E-06	-7.13E-07	-5.80E-07
450	3.11E-06	-7.51E-07	2.00E-06	-7.51E-07	-5.39E-07
475	3.21E-06	-7.88E-07	2.05E-06	-7.88E-07	-4.97E-07
500	3.30E-06	-8.26E-07	2.10E-06	-8.26E-07	-4.56E-07
525	3.40E-06	-8.63E-07	2.15E-06	-8.63E-07	-4.15E-07
550	3.50E-06	-9.01E-07	2.20E-06	-9.01E-07	-3.73E-07
575	3.60E-06	-9.38E-07	2.25E-06	-9.38E-07	-3.32E-07
600	3.69E-06	-9.76E-07	2.30E-06	-9.76E-07	-2.90E-07
625	3.79E-06	-1.01E-06	2.35E-06	-1.01E-06	-2.49E-07
650	3.89E-06	-1.05E-06	2.40E-06	-1.05E-06	-2.07E-07
675	3.99E-06	-1.09E-06	2.45E-06	-1.09E-06	-1.66E-07
700	4.08E-06	-1.13E-06	2.50E-06	-1.13E-06	-1.24E-07
725	4.18E-06	-1.16E-06	2.55E-06	-1.16E-06	-8.27E-08
750	4.28E-06	-1.20E-06	2.60E-06	-1.20E-06	-4.12E-08
775	4.38E-06	-1.24E-06	2.65E-06	-1.24E-06	3.02E-10
800	4.47E-06	-1.28E-06	2.70E-06	-1.28E-06	4.18E-08
825	4.57E-06	-1.31E-06	2.75E-06	-1.31E-06	8.34E-08
850	4.67E-06	-1.35E-06	2.81E-06	-1.35E-06	1.25E-07
875	4.77E-06	-1.39E-06	2.86E-06	-1.39E-06	1.66E-07
900	4.86E-06	-1.43E-06	2.91E-06	-1.43E-06	2.08E-07
925	4.96E-06	-1.47E-06	2.96E-06	-1.47E-06	2.50E-07
950	5.06E-06	-1.50E-06	3.01E-06	-1.50E-06	2.91E-07
975	5.16E-06	-1.54E-06	3.06E-06	-1.54E-06	3.33E-07
1000	5.25E-06	-1.58E-06	3.11E-06	-1.58E-06	3.74E-07

Table 9.8: Eigen values and angles determined by CTEAS program for Lu disilicate data gathered at beamline 11-ID-C at APS.

TEMP	EIG1	EIG2	EIG3	EIG1ANGLE	EIG2ANGLE	EIG3ANGLE
25	1.46E-06	1.15E-06	-1.25E-06	1.73E+02	90	9.65E+01
50	1.56E-06	1.20E-06	-1.21E-06	1.73E+02	90	9.72E+01
75	1.67E-06	1.25E-06	-1.17E-06	1.72E+02	90	9.79E+01
100	1.77E-06	1.30E-06	-1.14E-06	1.71E+02	90	9.86E+01
125	1.87E-06	1.35E-06	-1.10E-06	1.71E+02	90	9.92E+01
150	1.97E-06	1.40E-06	-1.07E-06	1.70E+02	90	9.98E+01
175	2.08E-06	1.45E-06	-1.03E-06	1.70E+02	90	1.00E+02
200	2.18E-06	1.50E-06	-9.98E-07	1.69E+02	90	1.01E+02
225	2.29E-06	1.55E-06	-9.65E-07	1.69E+02	90	1.01E+02
250	2.40E-06	1.60E-06	-9.32E-07	1.68E+02	90	1.02E+02
275	2.50E-06	1.65E-06	-9.00E-07	1.68E+02	90	1.02E+02
300	2.61E-06	1.70E-06	-8.69E-07	1.67E+02	90	1.03E+02
325	2.72E-06	1.75E-06	-8.37E-07	1.67E+02	90	1.03E+02
350	2.82E-06	1.80E-06	-8.07E-07	1.66E+02	90	1.04E+02
375	2.93E-06	1.85E-06	-7.76E-07	1.66E+02	90	1.04E+02
400	3.04E-06	1.90E-06	-7.46E-07	1.66E+02	90	1.04E+02
425	3.15E-06	1.95E-06	-7.17E-07	1.65E+02	90	1.05E+02
450	3.26E-06	2.00E-06	-6.87E-07	1.65E+02	90	1.05E+02
475	3.37E-06	2.05E-06	-6.58E-07	1.64E+02	90	1.06E+02
500	3.48E-06	2.10E-06	-6.29E-07	1.64E+02	90	1.06E+02
525	3.59E-06	2.15E-06	-6.01E-07	1.64E+02	90	1.06E+02
550	3.70E-06	2.20E-06	-5.72E-07	1.64E+02	90	1.06E+02
575	3.81E-06	2.25E-06	-5.44E-07	1.63E+02	90	1.07E+02
600	3.92E-06	2.30E-06	-5.16E-07	1.63E+02	90	1.07E+02
625	4.03E-06	2.35E-06	-4.89E-07	1.63E+02	90	1.07E+02
650	4.14E-06	2.40E-06	-4.61E-07	1.62E+02	90	1.08E+02
675	4.25E-06	2.45E-06	-4.34E-07	1.62E+02	90	1.08E+02
700	4.37E-06	2.50E-06	-4.07E-07	1.62E+02	90	1.08E+02
725	4.48E-06	2.55E-06	-3.80E-07	1.62E+02	90	1.08E+02
750	4.59E-06	2.60E-06	-3.53E-07	1.62E+02	90	1.08E+02

775	4.70E-06	2.65E-06	-3.26E-07	1.61E+02	90	1.09E+02
800	4.81E-06	2.70E-06	-3.00E-07	1.61E+02	90	1.09E+02
825	4.93E-06	2.75E-06	-2.73E-07	1.61E+02	90	1.09E+02
850	5.04E-06	2.81E-06	-2.47E-07	1.61E+02	90	1.09E+02
875	5.15E-06	2.86E-06	-2.21E-07	1.61E+02	90	1.09E+02
900	5.27E-06	2.91E-06	-1.95E-07	1.60E+02	90	1.10E+02
925	5.38E-06	2.96E-06	-1.69E-07	1.60E+02	90	1.10E+02
950	5.49E-06	3.01E-06	-1.43E-07	1.60E+02	90	1.10E+02
975	5.61E-06	3.06E-06	-1.18E-07	1.60E+02	90	1.10E+02
1000	5.72E-06	3.11E-06	-9.20E-08	1.60E+02	90	1.10E+02

Table 9.9: Tensor data determined by CTEAS program for Sc disilicate data gathered at beamline 11-ID-C at APS. The numbers in parenthesis correspond to the non-zero coefficient.

TEMP	CTE(11)	CTE(13)	CTE(22)	CTE(31)	CTE(33)
25	3.94E-06	-1.17E-06	4.62E-06	-1.17E-06	2.40E-06
50	4.06E-06	-1.22E-06	4.66E-06	-1.22E-06	2.47E-06
75	4.18E-06	-1.26E-06	4.70E-06	-1.26E-06	2.54E-06
100	4.30E-06	-1.30E-06	4.74E-06	-1.30E-06	2.62E-06
125	4.42E-06	-1.34E-06	4.77E-06	-1.34E-06	2.69E-06
150	4.54E-06	-1.38E-06	4.81E-06	-1.38E-06	2.76E-06
175	4.65E-06	-1.42E-06	4.85E-06	-1.42E-06	2.83E-06
200	4.77E-06	-1.46E-06	4.89E-06	-1.46E-06	2.90E-06
225	4.89E-06	-1.51E-06	4.92E-06	-1.51E-06	2.97E-06
250	5.01E-06	-1.55E-06	4.96E-06	-1.55E-06	3.05E-06
275	5.13E-06	-1.59E-06	5.00E-06	-1.59E-06	3.12E-06
300	5.25E-06	-1.63E-06	5.04E-06	-1.63E-06	3.19E-06
325	5.37E-06	-1.67E-06	5.07E-06	-1.67E-06	3.26E-06
350	5.49E-06	-1.71E-06	5.11E-06	-1.71E-06	3.33E-06
375	5.60E-06	-1.75E-06	5.15E-06	-1.75E-06	3.41E-06
400	5.72E-06	-1.80E-06	5.19E-06	-1.80E-06	3.48E-06
425	5.84E-06	-1.84E-06	5.22E-06	-1.84E-06	3.55E-06
450	5.96E-06	-1.88E-06	5.26E-06	-1.88E-06	3.62E-06
475	6.08E-06	-1.92E-06	5.30E-06	-1.92E-06	3.70E-06

500	6.20E-06	-1.96E-06	5.34E-06	-1.96E-06	3.77E-06
525	6.32E-06	-2.00E-06	5.37E-06	-2.00E-06	3.84E-06
550	6.44E-06	-2.04E-06	5.41E-06	-2.04E-06	3.91E-06
575	6.55E-06	-2.09E-06	5.45E-06	-2.09E-06	3.98E-06
600	6.67E-06	-2.13E-06	5.49E-06	-2.13E-06	4.06E-06
625	6.79E-06	-2.17E-06	5.52E-06	-2.17E-06	4.13E-06
650	6.91E-06	-2.21E-06	5.56E-06	-2.21E-06	4.20E-06
675	7.03E-06	-2.25E-06	5.60E-06	-2.25E-06	4.27E-06
700	7.15E-06	-2.29E-06	5.64E-06	-2.29E-06	4.34E-06
725	7.27E-06	-2.33E-06	5.67E-06	-2.33E-06	4.42E-06
750	7.39E-06	-2.38E-06	5.71E-06	-2.38E-06	4.49E-06
775	7.51E-06	-2.42E-06	5.75E-06	-2.42E-06	4.56E-06
800	7.62E-06	-2.46E-06	5.79E-06	-2.46E-06	4.63E-06
825	7.74E-06	-2.50E-06	5.82E-06	-2.50E-06	4.71E-06
850	7.86E-06	-2.54E-06	5.86E-06	-2.54E-06	4.78E-06
875	7.98E-06	-2.58E-06	5.90E-06	-2.58E-06	4.85E-06
900	8.10E-06	-2.63E-06	5.94E-06	-2.63E-06	4.92E-06
925	8.22E-06	-2.67E-06	5.97E-06	-2.67E-06	5.00E-06
950	8.34E-06	-2.71E-06	6.01E-06	-2.71E-06	5.07E-06

Table 9.10: Eigen values and angles determined by CTEAS program for Sc disilicate data gathered at beamline 11-ID-C at APS.

TEMP	EIG1	EIG2	EIG3	EIG1ANGLE	EIG2ANGLE	EIG3ANGLE
25	4.62E-06	4.58E-06	1.77E-06	90	1.47E+02	1.23E+02
50	4.66E-06	4.72E-06	1.81E-06	90	1.47E+02	1.24E+02
75	4.70E-06	4.86E-06	1.86E-06	90	1.46E+02	1.24E+02
100	4.74E-06	5.00E-06	1.91E-06	90	1.46E+02	1.24E+02
125	4.77E-06	5.15E-06	1.96E-06	90	1.46E+02	1.24E+02
150	4.81E-06	5.29E-06	2.01E-06	90	1.46E+02	1.24E+02
175	4.85E-06	5.43E-06	2.05E-06	90	1.46E+02	1.24E+02
200	4.89E-06	5.57E-06	2.10E-06	90	1.46E+02	1.24E+02
225	4.92E-06	5.72E-06	2.15E-06	90	1.46E+02	1.24E+02
250	4.96E-06	5.86E-06	2.20E-06	90	1.46E+02	1.24E+02
275	5.00E-06	6.00E-06	2.24E-06	90	1.46E+02	1.24E+02

300	5.04E-06	6.15E-06	2.29E-06	90	1.46E+02	1.24E+02
325	5.07E-06	6.29E-06	2.34E-06	90	1.46E+02	1.24E+02
350	5.11E-06	6.43E-06	2.39E-06	90	1.46E+02	1.24E+02
375	5.15E-06	6.57E-06	2.44E-06	90	1.46E+02	1.24E+02
400	5.19E-06	6.72E-06	2.48E-06	90	1.46E+02	1.24E+02
425	5.22E-06	6.86E-06	2.53E-06	90	1.46E+02	1.24E+02
450	5.26E-06	7.00E-06	2.58E-06	90	1.46E+02	1.24E+02
475	5.30E-06	7.15E-06	2.63E-06	90	1.46E+02	1.24E+02
500	5.34E-06	7.29E-06	2.68E-06	90	1.46E+02	1.24E+02
525	5.37E-06	7.43E-06	2.72E-06	90	1.46E+02	1.24E+02
550	5.41E-06	7.58E-06	2.77E-06	90	1.46E+02	1.24E+02
575	5.45E-06	7.72E-06	2.82E-06	90	1.46E+02	1.24E+02
600	5.49E-06	7.86E-06	2.87E-06	90	1.46E+02	1.24E+02
625	5.52E-06	8.01E-06	2.92E-06	90	1.46E+02	1.24E+02
650	5.56E-06	8.15E-06	2.96E-06	90	1.46E+02	1.24E+02
675	5.60E-06	8.29E-06	3.01E-06	90	1.46E+02	1.24E+02
700	5.64E-06	8.43E-06	3.06E-06	90	1.46E+02	1.24E+02
725	5.67E-06	8.58E-06	3.11E-06	90	1.46E+02	1.24E+02
750	5.71E-06	8.72E-06	3.15E-06	90	1.46E+02	1.24E+02
775	5.75E-06	8.86E-06	3.20E-06	90	1.46E+02	1.24E+02
800	5.79E-06	9.01E-06	3.25E-06	90	1.46E+02	1.24E+02
825	5.82E-06	9.15E-06	3.30E-06	90	1.46E+02	1.24E+02
850	5.86E-06	9.29E-06	3.35E-06	90	1.46E+02	1.24E+02
875	5.90E-06	9.44E-06	3.39E-06	90	1.46E+02	1.24E+02
900	5.94E-06	9.58E-06	3.44E-06	90	1.46E+02	1.24E+02
925	5.97E-06	9.72E-06	3.49E-06	90	1.46E+02	1.24E+02
950	6.01E-06	9.87E-06	3.54E-06	90	1.46E+02	1.24E+02

Table 9.11: Tensor data determined by CTEAS program for (Yb,Er) disilicate data gathered at beamline 11-ID-C at APS. The numbers in parenthesis correspond to the non-zero coefficient.

TEMP	CTE(11)	CTE(13)	CTE(22)	CTE(31)	CTE(33)
25	3.41E-06	2.80E-07	2.97E-06	2.80E-07	1.86E-06
50	3.50E-06	2.41E-07	3.03E-06	2.41E-07	1.91E-06
75	3.59E-06	2.03E-07	3.09E-06	2.03E-07	1.96E-06
100	3.68E-06	1.65E-07	3.14E-06	1.65E-07	2.02E-06
125	3.77E-06	1.27E-07	3.20E-06	1.27E-07	2.07E-06
150	3.86E-06	8.90E-08	3.25E-06	8.90E-08	2.12E-06
175	3.95E-06	5.09E-08	3.31E-06	5.09E-08	2.18E-06
200	4.04E-06	1.28E-08	3.37E-06	1.28E-08	2.23E-06
225	4.13E-06	-2.53E-08	3.42E-06	-2.53E-08	2.28E-06
250	4.22E-06	-6.35E-08	3.48E-06	-6.35E-08	2.34E-06
275	4.31E-06	-1.02E-07	3.54E-06	-1.02E-07	2.39E-06
300	4.40E-06	-1.40E-07	3.59E-06	-1.40E-07	2.44E-06
325	4.49E-06	-1.78E-07	3.65E-06	-1.78E-07	2.49E-06
350	4.58E-06	-2.16E-07	3.71E-06	-2.16E-07	2.55E-06
375	4.67E-06	-2.54E-07	3.76E-06	-2.54E-07	2.60E-06
400	4.76E-06	-2.92E-07	3.82E-06	-2.92E-07	2.65E-06
425	4.85E-06	-3.30E-07	3.87E-06	-3.30E-07	2.71E-06
450	4.95E-06	-3.69E-07	3.93E-06	-3.69E-07	2.76E-06
475	5.04E-06	-4.07E-07	3.99E-06	-4.07E-07	2.81E-06
500	5.13E-06	-4.45E-07	4.04E-06	-4.45E-07	2.86E-06
525	5.22E-06	-4.83E-07	4.10E-06	-4.83E-07	2.92E-06
550	5.31E-06	-5.21E-07	4.16E-06	-5.21E-07	2.97E-06
575	5.40E-06	-5.60E-07	4.21E-06	-5.60E-07	3.02E-06
600	5.49E-06	-5.98E-07	4.27E-06	-5.98E-07	3.08E-06
625	5.58E-06	-6.36E-07	4.32E-06	-6.36E-07	3.13E-06
650	5.67E-06	-6.74E-07	4.38E-06	-6.74E-07	3.18E-06
675	5.76E-06	-7.12E-07	4.44E-06	-7.12E-07	3.24E-06
700	5.85E-06	-7.51E-07	4.49E-06	-7.51E-07	3.29E-06
725	5.94E-06	-7.89E-07	4.55E-06	-7.89E-07	3.34E-06
750	6.03E-06	-8.27E-07	4.61E-06	-8.27E-07	3.39E-06

775	6.12E-06	-8.65E-07	4.66E-06	-8.65E-07	3.45E-06
800	6.21E-06	-9.04E-07	4.72E-06	-9.04E-07	3.50E-06
825	6.31E-06	-9.42E-07	4.78E-06	-9.42E-07	3.55E-06
850	6.40E-06	-9.80E-07	4.83E-06	-9.80E-07	3.61E-06
875	6.49E-06	-1.02E-06	4.89E-06	-1.02E-06	3.66E-06
900	6.58E-06	-1.06E-06	4.94E-06	-1.06E-06	3.71E-06
925	6.67E-06	-1.09E-06	5.00E-06	-1.09E-06	3.77E-06
950	6.76E-06	-1.13E-06	5.06E-06	-1.13E-06	3.82E-06
975	6.85E-06	-1.17E-06	5.11E-06	-1.17E-06	3.87E-06
1000	6.94E-06	-1.21E-06	5.17E-06	-1.21E-06	3.93E-06

Table 9.12: Eigen values and angles determined by CTEAS program for (Yb,Er) disilicate data gathered at beamline 11-ID-C at APS.

TEMP	EIG1	EIG2	EIG3	EIG1ANGLE	EIG2ANGLE	EIG3ANGLE
25	3.45E-06	2.97E-06	1.81E-06	173.75	90	96.25
50	3.53E-06	3.03E-06	1.88E-06	175.21	90	94.79
75	3.61E-06	3.09E-06	1.94E-06	176.65	90	93.35
100	3.69E-06	3.14E-06	2.00E-06	178.05	90	91.95
125	3.78E-06	3.20E-06	2.06E-06	179.42	90	90.58
150	3.86E-06	3.25E-06	2.12E-06	179.25	90	89.25
175	3.95E-06	3.31E-06	2.17E-06	177.96	90	87.96
200	4.04E-06	3.37E-06	2.23E-06	176.72	90	86.72
225	4.13E-06	3.42E-06	2.28E-06	175.54	90	85.54
250	4.22E-06	3.48E-06	2.33E-06	174.4	90	84.4
275	4.32E-06	3.54E-06	2.38E-06	173.31	90	83.31
300	4.41E-06	3.59E-06	2.43E-06	172.27	90	82.27
325	4.51E-06	3.65E-06	2.48E-06	171.28	90	81.28
350	4.61E-06	3.71E-06	2.52E-06	170.34	90	80.34
375	4.70E-06	3.76E-06	2.57E-06	169.45	90	79.45
400	4.80E-06	3.82E-06	2.61E-06	168.6	90	78.6
425	4.90E-06	3.87E-06	2.66E-06	167.8	90	77.8
450	5.01E-06	3.93E-06	2.70E-06	167.03	90	77.03
475	5.11E-06	3.99E-06	2.74E-06	166.31	90	76.31

500	5.21E-06	4.04E-06	2.78E-06	165.62	90	75.62
525	5.31E-06	4.10E-06	2.82E-06	164.96	90	74.96
550	5.42E-06	4.16E-06	2.86E-06	164.34	90	74.34
575	5.52E-06	4.21E-06	2.90E-06	163.75	90	73.75
600	5.63E-06	4.27E-06	2.94E-06	163.19	90	73.19
625	5.74E-06	4.32E-06	2.97E-06	162.66	90	72.66
650	5.84E-06	4.38E-06	3.01E-06	162.16	90	72.16
675	5.95E-06	4.44E-06	3.05E-06	161.67	90	71.67
700	6.06E-06	4.49E-06	3.08E-06	161.22	90	71.22
725	6.16E-06	4.55E-06	3.12E-06	160.78	90	70.78
750	6.27E-06	4.61E-06	3.16E-06	160.36	90	70.36
775	6.38E-06	4.66E-06	3.19E-06	159.97	90	69.97
800	6.49E-06	4.72E-06	3.23E-06	159.59	90	69.59
825	6.60E-06	4.78E-06	3.26E-06	159.23	90	69.23
850	6.71E-06	4.83E-06	3.30E-06	158.88	90	68.88
875	6.82E-06	4.89E-06	3.33E-06	158.55	90	68.55
900	6.92E-06	4.94E-06	3.37E-06	158.23	90	68.23
925	7.03E-06	5.00E-06	3.40E-06	157.93	90	67.93
950	7.14E-06	5.06E-06	3.43E-06	157.64	90	67.64
975	7.25E-06	5.11E-06	3.47E-06	157.36	90	67.36
1000	7.37E-06	5.17E-06	3.50E-06	157.1	90	67.1

Table 9.13: Tensor data determined by CTEAS program for (Yb,Er,Y) disilicate data gathered at beamline 11-ID-C at APS. The numbers in parenthesis correspond to the non-zero coefficient.

TEMP	CTE(11)	CTE(13)	CTE(22)	CTE(31)	CTE(33)
25	3.43E-06	2.66E-07	2.78E-06	2.66E-07	1.45E-06
50	3.53E-06	2.22E-07	2.85E-06	2.22E-07	1.49E-06
75	3.64E-06	1.78E-07	2.92E-06	1.78E-07	1.53E-06
100	3.74E-06	1.35E-07	2.98E-06	1.35E-07	1.57E-06
125	3.84E-06	9.12E-08	3.05E-06	9.12E-08	1.60E-06
150	3.94E-06	4.76E-08	3.12E-06	4.76E-08	1.64E-06
175	4.04E-06	3.95E-09	3.19E-06	3.95E-09	1.68E-06
200	4.14E-06	-3.97E-08	3.25E-06	-3.97E-08	1.71E-06

225	4.24E-06	-8.33E-08	3.32E-06	-8.33E-08	1.75E-06
250	4.34E-06	-1.27E-07	3.39E-06	-1.27E-07	1.79E-06
275	4.44E-06	-1.71E-07	3.46E-06	-1.71E-07	1.83E-06
300	4.54E-06	-2.14E-07	3.52E-06	-2.14E-07	1.86E-06
325	4.64E-06	-2.58E-07	3.59E-06	-2.58E-07	1.90E-06
350	4.74E-06	-3.02E-07	3.66E-06	-3.02E-07	1.94E-06
375	4.84E-06	-3.45E-07	3.72E-06	-3.45E-07	1.97E-06
400	4.94E-06	-3.89E-07	3.79E-06	-3.89E-07	2.01E-06
425	5.04E-06	-4.33E-07	3.86E-06	-4.33E-07	2.05E-06
450	5.14E-06	-4.76E-07	3.93E-06	-4.76E-07	2.09E-06
475	5.25E-06	-5.20E-07	3.99E-06	-5.20E-07	2.12E-06
500	5.35E-06	-5.64E-07	4.06E-06	-5.64E-07	2.16E-06
525	5.45E-06	-6.08E-07	4.13E-06	-6.08E-07	2.20E-06
550	5.55E-06	-6.51E-07	4.20E-06	-6.51E-07	2.23E-06
575	5.65E-06	-6.95E-07	4.26E-06	-6.95E-07	2.27E-06
600	5.75E-06	-7.39E-07	4.33E-06	-7.39E-07	2.31E-06
625	5.85E-06	-7.83E-07	4.40E-06	-7.83E-07	2.35E-06
650	5.95E-06	-8.26E-07	4.46E-06	-8.26E-07	2.38E-06
675	6.05E-06	-8.70E-07	4.53E-06	-8.70E-07	2.42E-06
700	6.15E-06	-9.14E-07	4.60E-06	-9.14E-07	2.46E-06
725	6.25E-06	-9.58E-07	4.67E-06	-9.58E-07	2.50E-06
750	6.35E-06	-1.00E-06	4.73E-06	-1.00E-06	2.53E-06
775	6.45E-06	-1.05E-06	4.80E-06	-1.05E-06	2.57E-06
800	6.55E-06	-1.09E-06	4.87E-06	-1.09E-06	2.61E-06
825	6.65E-06	-1.13E-06	4.94E-06	-1.13E-06	2.64E-06
850	6.76E-06	-1.18E-06	5.00E-06	-1.18E-06	2.68E-06
875	6.86E-06	-1.22E-06	5.07E-06	-1.22E-06	2.72E-06
900	6.96E-06	-1.26E-06	5.14E-06	-1.26E-06	2.76E-06
925	7.06E-06	-1.31E-06	5.21E-06	-1.31E-06	2.79E-06
950	7.16E-06	-1.35E-06	5.27E-06	-1.35E-06	2.83E-06
975	7.26E-06	-1.40E-06	5.34E-06	-1.40E-06	2.87E-06
1000	7.36E-06	-1.44E-06	5.41E-06	-1.44E-06	2.91E-06

Table 9.14: Eigen values and angles determined by CTEAS program for (Yb,Er,Y) disilicate data gathered at beamline 11-ID-C at APS.

TEMP	EIG1	EIG2	EIG3	EIG1ANGLE	EIG2ANGLE	EIG3ANGLE
25	3.47E-06	2.78E-06	1.42E-06	176.15	90	93.85
50	3.56E-06	2.85E-06	1.47E-06	177.53	90	92.47
75	3.65E-06	2.92E-06	1.51E-06	178.85	90	91.15
100	3.74E-06	2.98E-06	1.56E-06	179.89	90	89.89
125	3.84E-06	3.05E-06	1.60E-06	178.68	90	88.68
150	3.94E-06	3.12E-06	1.64E-06	177.53	90	87.53
175	4.04E-06	3.19E-06	1.68E-06	176.44	90	86.44
200	4.14E-06	3.25E-06	1.71E-06	175.41	90	85.41
225	4.24E-06	3.32E-06	1.75E-06	174.44	90	84.44
250	4.35E-06	3.39E-06	1.78E-06	173.51	90	83.51
275	4.45E-06	3.46E-06	1.81E-06	172.64	90	82.64
300	4.56E-06	3.52E-06	1.85E-06	171.82	90	81.82
325	4.67E-06	3.59E-06	1.88E-06	171.04	90	81.04
350	4.77E-06	3.66E-06	1.91E-06	170.3	90	80.3
375	4.88E-06	3.72E-06	1.93E-06	169.61	90	79.61
400	4.99E-06	3.79E-06	1.96E-06	168.95	90	78.95
425	5.11E-06	3.86E-06	1.99E-06	168.33	90	78.33
450	5.22E-06	3.93E-06	2.01E-06	167.74	90	77.74
475	5.33E-06	3.99E-06	2.04E-06	167.18	90	77.18
500	5.44E-06	4.06E-06	2.06E-06	166.65	90	76.65
525	5.56E-06	4.13E-06	2.09E-06	166.15	90	76.15
550	5.67E-06	4.20E-06	2.11E-06	165.68	90	75.68
575	5.79E-06	4.26E-06	2.13E-06	165.23	90	75.23
600	5.90E-06	4.33E-06	2.16E-06	164.8	90	74.8
625	6.02E-06	4.40E-06	2.18E-06	164.39	90	74.39
650	6.13E-06	4.46E-06	2.20E-06	164	90	74
675	6.25E-06	4.53E-06	2.22E-06	163.63	90	73.63
700	6.37E-06	4.60E-06	2.24E-06	163.28	90	73.28
725	6.48E-06	4.67E-06	2.27E-06	162.95	90	72.95
750	6.60E-06	4.73E-06	2.29E-06	162.63	90	72.63

775	6.72E-06	4.80E-06	2.31E-06	162.32	90	72.32
800	6.83E-06	4.87E-06	2.33E-06	162.03	90	72.03
825	6.95E-06	4.94E-06	2.35E-06	161.75	90	71.75
850	7.07E-06	5.00E-06	2.37E-06	161.49	90	71.49
875	7.19E-06	5.07E-06	2.39E-06	161.23	90	71.23
900	7.31E-06	5.14E-06	2.41E-06	160.99	90	70.99
925	7.43E-06	5.21E-06	2.42E-06	160.75	90	70.75
950	7.55E-06	5.27E-06	2.44E-06	160.53	90	70.53
975	7.67E-06	5.34E-06	2.46E-06	160.31	90	70.31
1000	7.79E-06	5.41E-06	2.48E-06	160.11	90	70.11

Table 9.15: Tensor data determined by CTEAS program for (Yb,Er,Y,Dy) disilicate data gathered at beamline 11-ID-C at APS. The numbers in parenthesis correspond to the non-zero coefficient.

TEMP	CTE(11)	CTE(13)	CTE(22)	CTE(31)	CTE(33)
25	2.43E-06	3.36E-07	2.32E-06	3.36E-07	9.21E-07
50	2.56E-06	2.93E-07	2.39E-06	2.93E-07	9.79E-07
75	2.68E-06	2.51E-07	2.47E-06	2.51E-07	1.04E-06
100	2.81E-06	2.09E-07	2.55E-06	2.09E-07	1.09E-06
125	2.94E-06	1.67E-07	2.63E-06	1.67E-07	1.15E-06
150	3.07E-06	1.25E-07	2.70E-06	1.25E-07	1.21E-06
175	3.19E-06	8.25E-08	2.78E-06	8.25E-08	1.27E-06
200	3.32E-06	4.03E-08	2.86E-06	4.03E-08	1.32E-06
225	3.45E-06	-1.95E-09	2.94E-06	-1.95E-09	1.38E-06
250	3.58E-06	-4.42E-08	3.01E-06	-4.42E-08	1.44E-06
275	3.71E-06	-8.64E-08	3.09E-06	-8.64E-08	1.50E-06
300	3.83E-06	-1.29E-07	3.17E-06	-1.29E-07	1.55E-06
325	3.96E-06	-1.71E-07	3.25E-06	-1.71E-07	1.61E-06
350	4.09E-06	-2.13E-07	3.32E-06	-2.13E-07	1.67E-06
375	4.22E-06	-2.55E-07	3.40E-06	-2.55E-07	1.73E-06
400	4.34E-06	-2.98E-07	3.48E-06	-2.98E-07	1.78E-06
425	4.47E-06	-3.40E-07	3.56E-06	-3.40E-07	1.84E-06
450	4.60E-06	-3.82E-07	3.63E-06	-3.82E-07	1.90E-06
475	4.73E-06	-4.24E-07	3.71E-06	-4.24E-07	1.96E-06

500	4.85E-06	-4.67E-07	3.79E-06	-4.67E-07	2.01E-06
525	4.98E-06	-5.09E-07	3.87E-06	-5.09E-07	2.07E-06
550	5.11E-06	-5.51E-07	3.94E-06	-5.51E-07	2.13E-06
575	5.24E-06	-5.94E-07	4.02E-06	-5.94E-07	2.19E-06
600	5.37E-06	-6.36E-07	4.10E-06	-6.36E-07	2.24E-06
625	5.49E-06	-6.78E-07	4.18E-06	-6.78E-07	2.30E-06
650	5.62E-06	-7.20E-07	4.25E-06	-7.20E-07	2.36E-06
675	5.75E-06	-7.63E-07	4.33E-06	-7.63E-07	2.42E-06
700	5.88E-06	-8.05E-07	4.41E-06	-8.05E-07	2.48E-06
725	6.01E-06	-8.48E-07	4.49E-06	-8.48E-07	2.53E-06
750	6.13E-06	-8.90E-07	4.56E-06	-8.90E-07	2.59E-06
775	6.26E-06	-9.32E-07	4.64E-06	-9.32E-07	2.65E-06
800	6.39E-06	-9.75E-07	4.72E-06	-9.75E-07	2.71E-06
825	6.52E-06	-1.02E-06	4.80E-06	-1.02E-06	2.76E-06
850	6.64E-06	-1.06E-06	4.87E-06	-1.06E-06	2.82E-06
875	6.77E-06	-1.10E-06	4.95E-06	-1.10E-06	2.88E-06
900	6.90E-06	-1.14E-06	5.03E-06	-1.14E-06	2.94E-06
925	7.03E-06	-1.19E-06	5.11E-06	-1.19E-06	2.99E-06
950	7.16E-06	-1.23E-06	5.19E-06	-1.23E-06	3.05E-06
975	7.28E-06	-1.27E-06	5.26E-06	-1.27E-06	3.11E-06
1000	7.41E-06	-1.31E-06	5.34E-06	-1.31E-06	3.17E-06

Table 9.16: Eigen values and angles determined by CTEAS program for (Yb,Er,Y,Dy) disilicate data gathered at beamline 11-ID-C at APS.

TEMP	EIG1	EIG2	EIG3	EIG1ANGLE	EIG2ANGLE	EIG3ANGLE
25	2.50E-06	2.32E-06	8.50E-07	171.6	90	98.4
50	2.61E-06	2.39E-06	9.26E-07	173.4	90	96.6
75	2.72E-06	2.47E-06	9.99E-07	175.12	90	94.88
100	2.84E-06	2.55E-06	1.07E-06	176.76	90	93.24
125	2.95E-06	2.63E-06	1.14E-06	178.31	90	91.69
150	3.08E-06	2.70E-06	1.20E-06	179.78	90	90.22
175	3.20E-06	2.78E-06	1.26E-06	178.85	90	88.85
200	3.32E-06	2.86E-06	1.32E-06	177.56	90	87.56

225	3.45E-06	2.94E-06	1.38E-06	176.35	90	86.35
250	3.58E-06	3.01E-06	1.44E-06	175.23	90	85.23
275	3.71E-06	3.09E-06	1.49E-06	174.17	90	84.17
300	3.84E-06	3.17E-06	1.55E-06	173.19	90	83.19
325	3.97E-06	3.25E-06	1.60E-06	172.28	90	82.28
350	4.11E-06	3.32E-06	1.65E-06	171.42	90	81.42
375	4.24E-06	3.40E-06	1.70E-06	170.63	90	80.63
400	4.38E-06	3.48E-06	1.75E-06	169.88	90	79.88
425	4.51E-06	3.56E-06	1.80E-06	169.18	90	79.18
450	4.65E-06	3.63E-06	1.85E-06	168.53	90	78.53
475	4.79E-06	3.71E-06	1.89E-06	167.92	90	77.92
500	4.93E-06	3.79E-06	1.94E-06	167.35	90	77.35
525	5.07E-06	3.87E-06	1.99E-06	166.81	90	76.81
550	5.21E-06	3.94E-06	2.03E-06	166.3	90	76.3
575	5.35E-06	4.02E-06	2.08E-06	165.83	90	75.83
600	5.49E-06	4.10E-06	2.12E-06	165.38	90	75.38
625	5.63E-06	4.18E-06	2.16E-06	164.96	90	74.96
650	5.77E-06	4.25E-06	2.21E-06	164.56	90	74.56
675	5.92E-06	4.33E-06	2.25E-06	164.18	90	74.18
700	6.06E-06	4.41E-06	2.29E-06	163.82	90	73.82
725	6.20E-06	4.49E-06	2.34E-06	163.48	90	73.48
750	6.34E-06	4.56E-06	2.38E-06	163.16	90	73.16
775	6.49E-06	4.64E-06	2.42E-06	162.86	90	72.86
800	6.63E-06	4.72E-06	2.46E-06	162.57	90	72.57
825	6.77E-06	4.80E-06	2.51E-06	162.29	90	72.29
850	6.92E-06	4.87E-06	2.55E-06	162.03	90	72.03
875	7.06E-06	4.95E-06	2.59E-06	161.78	90	71.78
900	7.21E-06	5.03E-06	2.63E-06	161.55	90	71.55
925	7.35E-06	5.11E-06	2.67E-06	161.32	90	71.32
950	7.50E-06	5.19E-06	2.71E-06	161.1	90	71.1
975	7.64E-06	5.26E-06	2.75E-06	160.9	90	70.9
1000	7.79E-06	5.34E-06	2.79E-06	160.7	90	70.7

Table 9.17: Tensor data determined by CTEAS program for (Lu,Yb,Er,Y,Dy) disilicate data gathered at beamline 11-ID-C at APS. The numbers in parenthesis correspond to the non-zero coefficient.

TEMP	CTE(11)	CTE(13)	CTE(22)	CTE(31)	CTE(33)
25	3.09E-06	1.94E-07	2.78E-06	1.94E-07	1.17E-06
50	3.20E-06	1.55E-07	2.84E-06	1.55E-07	1.22E-06
75	3.30E-06	1.15E-07	2.91E-06	1.15E-07	1.27E-06
100	3.41E-06	7.49E-08	2.97E-06	7.49E-08	1.32E-06
125	3.51E-06	3.51E-08	3.04E-06	3.51E-08	1.37E-06
150	3.62E-06	-4.74E-09	3.10E-06	-4.74E-09	1.41E-06
175	3.72E-06	-4.46E-08	3.16E-06	-4.46E-08	1.46E-06
200	3.83E-06	-8.44E-08	3.23E-06	-8.44E-08	1.51E-06
225	3.93E-06	-1.24E-07	3.29E-06	-1.24E-07	1.56E-06
250	4.03E-06	-1.64E-07	3.36E-06	-1.64E-07	1.60E-06
275	4.14E-06	-2.04E-07	3.42E-06	-2.04E-07	1.65E-06
300	4.24E-06	-2.44E-07	3.49E-06	-2.44E-07	1.70E-06
325	4.35E-06	-2.84E-07	3.55E-06	-2.84E-07	1.75E-06
350	4.45E-06	-3.24E-07	3.62E-06	-3.24E-07	1.80E-06
375	4.56E-06	-3.63E-07	3.68E-06	-3.63E-07	1.84E-06
400	4.66E-06	-4.03E-07	3.74E-06	-4.03E-07	1.89E-06
425	4.77E-06	-4.43E-07	3.81E-06	-4.43E-07	1.94E-06
450	4.87E-06	-4.83E-07	3.87E-06	-4.83E-07	1.99E-06
475	4.98E-06	-5.23E-07	3.94E-06	-5.23E-07	2.03E-06
500	5.08E-06	-5.63E-07	4.00E-06	-5.63E-07	2.08E-06
525	5.19E-06	-6.03E-07	4.07E-06	-6.03E-07	2.13E-06
550	5.29E-06	-6.43E-07	4.13E-06	-6.43E-07	2.18E-06
575	5.40E-06	-6.83E-07	4.19E-06	-6.83E-07	2.23E-06
600	5.50E-06	-7.23E-07	4.26E-06	-7.23E-07	2.27E-06
625	5.61E-06	-7.63E-07	4.32E-06	-7.63E-07	2.32E-06
650	5.71E-06	-8.03E-07	4.39E-06	-8.03E-07	2.37E-06
675	5.81E-06	-8.43E-07	4.45E-06	-8.43E-07	2.42E-06
700	5.92E-06	-8.83E-07	4.52E-06	-8.83E-07	2.47E-06
725	6.02E-06	-9.23E-07	4.58E-06	-9.23E-07	2.51E-06
750	6.13E-06	-9.63E-07	4.65E-06	-9.63E-07	2.56E-06

775	6.23E-06	-1.00E-06	4.71E-06	-1.00E-06	2.61E-06
800	6.34E-06	-1.04E-06	4.77E-06	-1.04E-06	2.66E-06
825	6.44E-06	-1.08E-06	4.84E-06	-1.08E-06	2.71E-06
850	6.55E-06	-1.12E-06	4.90E-06	-1.12E-06	2.75E-06
875	6.65E-06	-1.16E-06	4.97E-06	-1.16E-06	2.80E-06
900	6.76E-06	-1.20E-06	5.03E-06	-1.20E-06	2.85E-06
925	6.86E-06	-1.24E-06	5.10E-06	-1.24E-06	2.90E-06
950	6.97E-06	-1.28E-06	5.16E-06	-1.28E-06	2.95E-06
975	7.07E-06	-1.32E-06	5.22E-06	-1.32E-06	2.99E-06
1000	7.18E-06	-1.36E-06	5.29E-06	-1.36E-06	3.04E-06

Table 9.18: Eigen values and angles determined by CTEAS program for (Lu,Yb,Er,Y,Dy) disilicate data gathered at beamline 11-ID-C at APS.

TEMP	EIG1	EIG2	EIG3	EIG1ANGLE	EIG2ANGLE	EIG3ANGLE
25	3.11E-06	2.78E-06	1.15E-06	2.08	90	87.92
50	3.21E-06	2.84E-06	1.21E-06	0.8	90	89.2
75	3.31E-06	2.91E-06	1.26E-06	0.43	90	90.43
100	3.41E-06	2.97E-06	1.32E-06	1.59	90	91.59
125	3.51E-06	3.04E-06	1.36E-06	2.71	90	92.71
150	3.62E-06	3.10E-06	1.41E-06	3.76	90	93.76
175	3.72E-06	3.16E-06	1.46E-06	4.77	90	94.77
200	3.83E-06	3.23E-06	1.51E-06	5.72	90	95.72
225	3.94E-06	3.29E-06	1.55E-06	6.62	90	96.62
250	4.05E-06	3.36E-06	1.59E-06	7.48	90	97.48
275	4.16E-06	3.42E-06	1.64E-06	8.29	90	98.29
300	4.27E-06	3.49E-06	1.68E-06	9.05	90	99.05
325	4.38E-06	3.55E-06	1.72E-06	9.77	90	99.77
350	4.49E-06	3.62E-06	1.76E-06	10.46	90	100.46
375	4.61E-06	3.68E-06	1.80E-06	11.11	90	101.11
400	4.72E-06	3.74E-06	1.83E-06	11.72	90	101.72
425	4.84E-06	3.81E-06	1.87E-06	12.31	90	102.31
450	4.95E-06	3.87E-06	1.91E-06	12.86	90	102.86
475	5.07E-06	3.94E-06	1.94E-06	13.38	90	103.38

500	5.18E-06	4.00E-06	1.98E-06	13.88	90	103.88
525	5.30E-06	4.07E-06	2.02E-06	14.35	90	104.35
550	5.42E-06	4.13E-06	2.05E-06	14.8	90	104.8
575	5.54E-06	4.19E-06	2.09E-06	15.23	90	105.23
600	5.65E-06	4.26E-06	2.12E-06	15.63	90	105.63
625	5.77E-06	4.32E-06	2.15E-06	16.02	90	106.02
650	5.89E-06	4.39E-06	2.19E-06	16.39	90	106.39
675	6.01E-06	4.45E-06	2.22E-06	16.74	90	106.74
700	6.13E-06	4.52E-06	2.25E-06	17.08	90	107.08
725	6.25E-06	4.58E-06	2.29E-06	17.4	90	107.4
750	6.37E-06	4.65E-06	2.32E-06	17.7	90	107.7
775	6.49E-06	4.71E-06	2.35E-06	18	90	108
800	6.61E-06	4.77E-06	2.38E-06	18.28	90	108.28
825	6.73E-06	4.84E-06	2.41E-06	18.54	90	108.54
850	6.86E-06	4.90E-06	2.45E-06	18.8	90	108.8
875	6.98E-06	4.97E-06	2.48E-06	19.05	90	109.05
900	7.10E-06	5.03E-06	2.51E-06	19.28	90	109.28
925	7.22E-06	5.10E-06	2.54E-06	19.51	90	109.51
950	7.34E-06	5.16E-06	2.57E-06	19.73	90	109.73
975	7.46E-06	5.22E-06	2.60E-06	19.94	90	109.94
1000	7.59E-06	5.29E-06	2.63E-06	20.14	90	110.14

9.2 Abbreviations, Acronyms, etc.

BTU – British thermal unit. One BTU is equal to approximately 1055.06 Joules.

Quads – One Quad is equal to one quadrillion BTU.

T/EBCs – Thermal/Environmental barrier coatings. These coatings serve to protect against high temperatures and/or reactions with the environment.

CMCs - Ceramic matrix composite. The current material of choice for gas-turbine engine components made typically from SiC.

SiC – The chemical formula for Silicon Carbide, an alloy of silicon and carbon.

CVD – Chemical vapor deposition.

CVI – Chemical vapor infiltration.

PIP – Precursor infiltration and pyrolysis.

RMI – Reactive melt infiltration.

BSAS – A Barium oxide, Strontium oxide, aluminum oxide, and silicon oxide mixture used for T/EBC applications.

RE – Rare-earth, including all the lanthanides as well as scandium (Sc) and yttrium (Y).

CTE – Coefficient of thermal expansion.

REDS – Rare-earth disilicate.

CMAS (calcium-magnesium alumino-silicate)

HEA – High entropy alloy

HEC – High entropy ceramic

HE – High entropy

TEOS – Tetraethyl Orthosilicate

UV-Vis - Ultraviolet-visible spectroscopy

FTIR - Fourier Transform Infrared Spectroscopy

PLD – Pulsed laser deposition

EDTA - Ethylenediaminetetraacetic acid

Chapter 10 References

1. Langston, L. S. Powering Ahead. *Mech. Eng.* **133**, 30–33 (2011).
2. Alibrandi, W. Forecast International: Forecast International Predicts Tremendous World Growth for Gas Turbines Over Next 15 Years. *Forecast International*
<https://www.forecastinternational.com/press/release.cfm?article=13049#.V3JTCr6dK1e>.
3. Lawrence Livermore National Laboratory (LLNL). Energy, Water, and Carbon Informatics.
<https://flowcharts.llnl.gov/>.
4. Padture, N. P. Advanced structural ceramics in aerospace propulsion. *Nat. Mater.* **15**, 804–809 (2016).
5. Lee, K. N., Fox, D. S. & Bansal, N. P. Rare earth silicate environmental barrier coatings for SiC/SiC composites and Si₃N₄ ceramics. *J. Eur. Ceram. Soc.* **25**, 1705–1715 (2005).
6. Clarke, D. R. & Phillpot, S. R. Thermal barrier coating materials. *Mater. Today* **8**, 22–29 (2005).
7. Padture, N. P. Environmental degradation of high-temperature protective coatings for ceramic-matrix composites in gas-turbine engines. *Npj Mater. Degrad.* **3**, 11 (2019).
8. Lee, K. N. *et al.* Upper Temperature Limit of Environmental Barrier Coatings Based on Mullite and BSAS. *J. Am. Ceram. Soc.* **86**, 1299–1306 (2003).
9. Han, J., Wang, Y., Liu, R. & Wan, F. Theoretical and experimental investigation of Xenotime-type rare earth phosphate REPO₄, (RE = Lu, Yb, Er, Y and Sc) for potential environmental barrier coating applications. *Sci. Rep.* **10**, 13681 (2020).
10. Xu, Y., Hu, X., Xu, F. & Li, K. Rare earth silicate environmental barrier coatings: Present status and prospective. *Ceram. Int.* **43**, 5847–5855 (2017).
11. Cao, X. Q., Vassen, R. & Stoeber, D. Ceramic materials for thermal barrier coatings. *J. Eur. Ceram. Soc.* **24**, 1–10 (2004).
12. Zok, F. W. Ceramic-matrix composites enable revolutionary gains in turbine engine efficiency. *Am Ceram Soc Bull* **95**, 22–8 (2016).
13. Spitsberg, I. & Steibel, J. Thermal and environmental barrier coatings for SiC/SiC CMCs in aircraft engine applications. *Int. J. Appl. Ceram. Technol.* **1**, 291–301 (2004).
14. Greil, P. Polymer derived engineering ceramics. *Adv. Eng. Mater.* **2**, 339–348 (2000).
15. Opila, E. J., Smialek, J. L., Robinson, R. C., Fox, D. S. & Jacobson, N. S. SiC recession caused by SiO₂ scale volatility under combustion conditions: II, thermodynamics and gaseous-diffusion model. *J. Am. Ceram. Soc.* **82**, 1826–1834 (1999).
16. Opila, E. J. & Hann Jr, R. E. Paralineer oxidation of CVD SiC in water vapor. *J. Am. Ceram. Soc.* **80**, 197–205 (1997).

17. Robertson, A. L., Solá, F., Zhu, D., Salem, J. & White, K. W. Microscale fracture mechanisms of HfO₂-Si environmental barrier coatings. *J. Eur. Ceram. Soc.* **39**, 2409–2418 (2019).
18. Harder, B. J. Oxidation performance of Si-HfO₂ environmental barrier coating bond coats deposited via plasma spray-physical vapor deposition. *Surf. Coat. Technol.* **384**, 125311 (2020).
19. Anton, R., Leisner, V., Watermeyer, P., Engstler, M. & Schulz, U. Hafnia-doped silicon bond coats manufactured by PVD for SiC/SiC CMCs. *Acta Mater.* **183**, 471–483 (2020).
20. Heimann, R. B. *Plasma-Spray Coating: Principles and Applications*. (John Wiley & Sons, 2008).
21. Ridley, M. & Opila, E. Thermochemical stability and microstructural evolution of Yb₂Si₂O₇ in high-velocity high-temperature water vapor. *J. Eur. Ceram. Soc.* **41**, 3141–3149 (2021).
22. Ridley, M., Gaskins, J., Hopkins, P. & Opila, E. Tailoring thermal properties of multi-component rare earth monosilicates. *Acta Mater.* **195**, 698–707 (2020).
23. Boakye, E. E., Mogilevsky, P., Hay, R. S. & Cinibulk, M. K. Rare-Earth Disilicates As Oxidation-Resistant Fiber Coatings for Silicon Carbide Ceramic-Matrix Composites: Oxide, Oxidation Resistant Coating for SiC/SiC Composite. *J. Am. Ceram. Soc.* **94**, 1716–1724 (2011).
24. Hu, X. *et al.* Thermal properties and Calcium-Magnesium-Alumina-Silicate (CMAS) resistance of LuPO₄ as environmental barrier coatings. *J. Eur. Ceram. Soc.* **40**, 1471–1477 (2020).
25. Wang, F., Guo, L., Wang, C. & Ye, F. Calcium-magnesium-alumina-silicate (CMAS) resistance characteristics of LnPO₄ (Ln = Nd, Sm, Gd) thermal barrier oxides. *J. Eur. Ceram. Soc.* **37**, 289–296 (2017).
26. Lee, K. N., Eldridge, J. I. & Robinson, R. C. Residual stresses and their effects on the durability of environmental barrier coatings for SiC ceramics. *J. Am. Ceram. Soc.* **88**, 3483–3488 (2005).
27. Felsche, J. Polymorphism and crystal data of the rare-earth disilicates of type RE₂Si₂O₇. *J. Common Met.* **21**, 1–14 (1970).
28. Shannon, R. D. Revised effective ionic radii and systematic studies of interatomic distances in halides and chalcogenides. *Acta Crystallogr. Sect. A* **32**, 751–767 (1976).
29. Toropov, N. A. & Bondar, I. A. Silicates of the Rare Earth Elements. IV. New Silicates in the Lanthanum Oxide–Silica System. *Izv Akad Nauk SSSR Ser Khim* **5**, 739–44 (1961).
30. Toropov, A. & Bondar, I. A. *Izv. Akad. Nauk. SSSR, Ser. Khim.; Bull. Acad. Sci. USSR. Div Chem SciEngl Tansl* **4**, 502–8 (1961).
31. Zagumennyi, A. I., Zavartsev, Y. D. & Kutovoi, S. A. Scintillation substances (variants). (2006).
32. Zhao, C., Wang, F., Sun, Y. & Zhou, Y. Synthesis and characterization of β-Yb₂Si₂O₇ powders. *Ceram. Int.* **39**, 5805–5811 (2013).
33. Fernández-Carrión, A. J., Allix, M. & Becerro, A. I. Thermal expansion of rare-earth pyrosilicates. *J. Am. Ceram. Soc.* **96**, 2298–2305 (2013).

34. Dolan, M. D. *et al.* Structures and anisotropic thermal expansion of the α , β , γ , and δ polymorphs of $\text{Y}_2\text{Si}_2\text{O}_7$. *Powder Diffr.* **23**, 20–25 (2008).
35. Salanova, A., Brummel, I. A., Yakovenko, A. A., Opila, E. J. & Ihlefeld, J. F. Phase stability and tensorial thermal expansion properties of single to high-entropy rare-earth disilicates. *J. Am. Ceram. Soc.* **106**, 3228–3238 (2023).
36. Rohrer, G. S. *Structure and Bonding in Crystalline Materials*. (Cambridge University Press, 2001).
37. Nye, J. F. *Physical Properties of Crystals: Their Representation by Tensors and Matrices*. (Oxford university press, 1985).
38. Rost, C. M. *et al.* Entropy-stabilized oxides. *Nat. Commun.* **6**, 8485 (2015).
39. Miracle, D. B. & Senkov, O. N. A critical review of high entropy alloys and related concepts. *Acta Mater.* **122**, 448–511 (2017).
40. Yeh, J.-W. *et al.* Nanostructured high-entropy alloys with multiple principal elements: novel alloy design concepts and outcomes. *Adv. Eng. Mater.* **6**, 299–303 (2004).
41. Ridley, M. & Opila, E. Variable thermochemical stability of $\text{RE}_2\text{Si}_2\text{O}_7$ (RE = Sc, Nd, Er, Yb, or Lu) in high-temperature high-velocity steam. *J. Am. Ceram. Soc.* **105**, 1330–1342 (2022).
42. Galunin, E., Alba, M. D. & Vidal, M. Stability of Rare-Earth Disilicates: Ionic Radius Effect. *J. Am. Ceram. Soc.* **94**, 1568–1574 (2011).
43. Hench, L. L. & West, J. K. The sol-gel process. *Chem. Rev.* **90**, 33–72 (1990).
44. Brinker, C. J. Hydrolysis and condensation of silicates: Effects on structure. *J. Non-Cryst. Solids* **100**, 31–50 (1988).
45. Müller-Bunz, H. & Schleid, T. Über die Oxidsilicate $\text{M}_2\text{O} [\text{SiO}_4]$ der schweren Lanthanoide (M=Dy–Lu) im A-Typ. *Z. Für Anorg. Allg. Chem.* **625**, 613–618 (1999).
46. Rahaman, M. N. *Ceramic Processing*. (CRC Press, 2017). doi:10.1201/9781315157160.
47. Ebelmen, J. J. *Recherches Sur Les Combinaisons Des Acides Borique et Silicique Avec Les Ethers*. (1846).
48. Graham, T. On the properties of silicic acid and other analogous colloidal substances. *J. Chem. Soc.* **17**, 318–327 (1864).
49. Iler, R. K. *The Colloid Chemistry of Silica and Silicates*. vol. 80 (LWW, 1955).
50. Stöber, W., Fink, A. & Bohn, E. Controlled growth of monodisperse silica spheres in the micron size range. *J. Colloid Interface Sci.* **26**, 62–69 (1968).
51. Brinker, C. J. & Scherer, G. W. *Sol-Gel Science: The Physics and Chemistry of Sol-Gel Processing*. (Academic press, 2013).

52. Li, Y., You, B., Zhao, W., Zhang, W. & Yin, M. Synthesis and Luminescent Properties of Nano-scale $Y_2Si_2O_7:Re^{3+}$ (Re=Eu, Tb) Phosphors via Sol-Gel Method. *Chin. J. Chem. Phys.* **21**, 376–380 (2008).
53. Parmentier, J. *et al.* Phase Transformations in Gel-Derived and Mixed-Powder-Derived Yttrium Disilicate, $Y_2Si_2O_7$, by X-Ray Diffraction and ^{29}Si MAS NMR. *J. Solid State Chem.* **149**, 16–20 (2000).
54. Boonstra, A. H. & Bernards, T. N. M. The dependence of the gelation time on the hydrolysis time in a two-step SiO_2 sol-gel process. *J. Non-Cryst. Solids* **105**, 207–213 (1988).
55. Jayaseelan, D. D., Ueno, S., Ohji, T. & Kanzaki, S. Sol-gel synthesis and coating of nanocrystalline $Lu_2Si_2O_7$ on Si_3N_4 substrate. *Mater. Chem. Phys.* **84**, 192–195 (2004).
56. Hreniak, D. *et al.* Luminescence properties of Tb-doped yttrium disilicate prepared by the sol-gel method. *J. Sol-Gel Sci. Technol.* **32**, 195–200 (2004).
57. Jothinathan, E., Vanmeensel, K., Vleugels, J. & Van der Biest, O. Powder synthesis, processing and characterization of lanthanum silicates for SOFC application. *J. Alloys Compd.* **495**, 552–555 (2010).
58. Feldhoff, A., Arnold, M., Martynczuk, J., Gesing, Th. M. & Wang, H. The sol-gel synthesis of perovskites by an EDTA/citrate complexing method involves nanoscale solid state reactions. *Solid State Sci.* **10**, 689–701 (2008).
59. Bragg, W. H. & Bragg, W. L. The reflection of X-rays by crystals. *Proc. R. Soc. Lond. Ser. Contain. Pap. Math. Phys. Character* **88**, 428–438 (1913).
60. Laue, M. Eine quantitative Prüfung der Theorie für die Interferenzerscheinungen bei Röntgenstrahlen. *Ann. Phys.* **346**, 989–1002 (1913).
61. Rietveld, H. M. A profile refinement method for nuclear and magnetic structures. *J. Appl. Crystallogr.* **2**, 65–71 (1969).
62. Toby, B. H. & Von Dreele, R. B. GSAS-II: the genesis of a modern open-source all purpose crystallography software package. *J. Appl. Crystallogr.* **46**, 544–549 (2013).
63. Jones, Z. a., Sarin, P., Haggerty, R. P. & Kriven, W. M. CTEAS: a graphical-user-interface-based program to determine thermal expansion from high-temperature X-ray diffraction. *J. Appl. Crystallogr.* **46**, 550–553 (2013).
64. Newnham, R. E. *Properties of Materials: Anisotropy, Symmetry, Structure.* (Oxford university press, 2005).
65. Küppers, H. Thermal expansion. (2006).
66. Belousov, R. I. & Filatov, S. K. Algorithm for calculating the thermal expansion tensor and constructing the thermal expansion diagram for crystals. *Glass Phys. Chem.* **33**, 271–275 (2007).

67. Nakamoto, K. *Infrared and Raman Spectra of Inorganic and Coordination Compounds, Part B: Applications in Coordination, Organometallic, and Bioinorganic Chemistry*. (John Wiley & Sons, 2009).
68. Jubu, P. R., Yam, F. K., Igba, V. M. & Beh, K. P. Tauc-plot scale and extrapolation effect on bandgap estimation from UV–vis–NIR data—a case study of β -Ga₂O₃. *J. Solid State Chem.* **290**, 121576 (2020).
69. Makuła, P., Pacia, M. & Macyk, W. How To Correctly Determine the Band Gap Energy of Modified Semiconductor Photocatalysts Based on UV–Vis Spectra. *J. Phys. Chem. Lett.* **9**, 6814–6817 (2018).
70. Tauc, J., Grigorovici, R. & Vancu, A. Optical properties and electronic structure of amorphous germanium. *Phys. Status Solidi B* **15**, 627–637 (1966).
71. Danks, A. E., Hall, S. R. & Schnepf, Z. The evolution of ‘sol–gel’ chemistry as a technique for materials synthesis. *Mater. Horiz.* **3**, 91–112 (2016).
72. Sun, K. & Lee, W.-H. Sol-gel preparation of rare-earth silicate glasses. *J. Non-Cryst. Solids* **92**, 145–152 (1987).
73. Li, Y. & Almeida, R. M. Elimination of porosity in heavily rare-earth doped sol–gel derived silicate glass films. *J. Sol-Gel Sci. Technol.* **61**, 332–339 (2012).
74. Lebedeva, Yu. E., Popovich, N. V., Orlova, L. A. & Chainikova, A. S. Sol-Gel Synthesis of Functionally Different Materials in the System Y₂O₃–Al₂O₃–SiO₂. *Glass Ceram.* **71**, 400–404 (2015).
75. Pechini, M. P. Method of preparing lead and alkaline earth titanates and niobates and coating method using the same to form a capacitor. (1967).
76. Smolin, Y. I. & Shepelev, Y. F. The crystal structures of the rare earth pyrosilicates. *Acta Crystallogr. B* **26**, 484–492 (1970).
77. Smolin, Y. I. Crystal structure of ytterbium oxyorthosilicate Yb₂SiO₅. *Sov. Phys. Crystallogr. USSR* **14**, 854 (1970).
78. Braun, J. L. *et al.* Charge-induced disorder controls the thermal conductivity of entropy-stabilized oxides. *Adv. Mater.* **30**, 1805004 (2018).
79. Dong, Y. *et al.* High-entropy environmental barrier coating for the ceramic matrix composites. *J. Eur. Ceram. Soc.* **39**, 2574–2579 (2019).
80. Zhang, Y. *et al.* Microstructures and properties of high-entropy alloys. *Prog. Mater. Sci.* **61**, 1–93 (2014).
81. Aparicio, M. & Durán, A. Yttrium silicate coatings for oxidation protection of carbon–silicon carbide composites. *J. Am. Ceram. Soc.* **83**, 1351–1355 (2000).
82. Klemm, H. Silicon nitride for high-temperature applications. *J. Am. Ceram. Soc.* **93**, 1501–1522 (2010).

83. Fukuda, K. & Matsubara, H. Thermal Expansion of δ -Yttrium Disilicate. *J. Am. Ceram. Soc.* **87**, 89–92 (2004).
84. Sun, Z., Zhou, Y., Wang, J. & Li, M. Thermal properties and thermal shock resistance of γ - $\text{Y}_2\text{Si}_2\text{O}_7$. *J. Am. Ceram. Soc.* **91**, 2623–2629 (2008).
85. Ueno, S., Jayaseelan, D. D., Kita, H., Ohji, T. & Lin, H. T. Comparison of water vapor corrosion behaviors of $\text{Ln}_2\text{Si}_2\text{O}_7$ (Ln= Yb and Lu) and ASiO_4 (A= Ti, Zr and Hf) EBC's. in *Key Engineering Materials* vol. 317 557–560 (Trans Tech Publ, 2006).
86. Chen, H., Gao, Y., Liu, Y. & Luo, H. Hydrothermal synthesis of ytterbium silicate nanoparticles. *Inorg. Chem.* **49**, 1942–1946 (2010).
87. Tang, X., Gao, Y., Chen, H. & Luo, H. Hydrothermal synthesis of lutetium disilicate nanoparticles. *J. Solid State Chem.* **188**, 38–43 (2012).
88. Shannon, R. D. Revised effective ionic radii and systematic studies of interatomic distances in halides and chalcogenides. *Acta Crystallogr. A* **32**, 751–767 (1976).
89. Nørlund Christensen, A. Investigation by the use of profile refinement of neutron powder diffraction data of the geometry of the $[\text{Si}_2\text{O}_7]^{6-}$ ions in the high temperature phases of rare earth disilicates prepared from the melt in crucible-free synthesis. *Z. Für Krist.-Cryst. Mater.* **209**, 7–13 (1994).
90. Salanova, A., Brummel, I. A., Yakovenko, A. A., Opila, B. J. & Ihlefeld, J. F. Lattice Parameters and CTE Tensor Components of Rare Earth Disilicates. University of Virginia Dataverse <https://doi.org/10.18130/V3/XI7QGF> (2022).
91. Kettle, S. F. A. & Smith, A. J. The stereochemistry of metal complexes as an indication of f-orbital participation in the metal–ligand bonding. *J Chem Soc A* **0**, 688–692 (1967).
92. Figgis, B. N. & Hitchman, M. A. *Ligand Field Theory and Its Applications*. vol. N/A (Wiley-VCH Verlag GmbH & Co. KGaA, Germany, 1999).
93. Tucker, M. G., Dove, M. T. & Keen, D. A. Direct measurement of the thermal expansion of the Si-O bond by neutron total scattering. *J. Phys. Condens. Matter* **12**, L425 (2000).
94. Tucker, M. G., Squires, M. P., Dove, M. T. & Keen, D. A. Dynamic structural disorder in cristobalite: neutron total scattering measurement and reverse Monte Carlo modelling. *J. Phys. Condens. Matter* **13**, 403 (2001).
95. Tucker, M. G., Keen, D. A. & Dove, M. T. A detailed structural characterization of quartz on heating through the α - β phase transition. *Mineral. Mag.* **65**, 489–507 (2001).
96. Dove, M. T. *et al.* Crystal structure of the high-pressure monoclinic phase-II of cristobalite, SiO_2 . *Mineral. Mag.* **64**, 569–576 (2000).
97. Keen, D. A., Tucker, M. G. & Dove, M. T. Reverse Monte Carlo modelling of crystalline disorder. *J. Phys. Condens. Matter* **17**, S15 (2005).

98. Wells, S. A., Dove, M. T. & Tucker, M. G. Finding best-fit polyhedral rotations with geometric algebra. *J. Phys. Condens. Matter* **14**, 4567 (2002).
99. Wells, S. A., Dove, M. T., Tucker, M. G. & Trachenko, K. Real-space rigid-unit-mode analysis of dynamic disorder in quartz, cristobalite and amorphous silica. *J. Phys. Condens. Matter* **14**, 4645 (2002).
100. Lucas, T. Pair distribution function studies of inorganic materials under extreme conditions. (University of Birmingham, 2013).
101. Liu, C.-H. *et al.* sasPDF: pair distribution function analysis of nanoparticle assemblies from small-angle-scattering data. Preprint at <https://doi.org/10.48550/arXiv.1910.08186> (2020).
102. Juhás, P., Louwen, J. N., Eijck, L. van, Vogt, E. T. C. & Billinge, S. J. L. PDFgetN3: atomic pair distribution functions from neutron powder diffraction data using ad hoc corrections. *J. Appl. Crystallogr.* **51**, 1492–1497 (2018).
103. Shi, C. xINTERPDF: a graphical user interface for analyzing intermolecular pair distribution functions of organic compounds from X-ray total scattering data. *J. Appl. Crystallogr.* **51**, 1498–1499 (2018).
104. Juhás, P., Farrow, C., Yang, X., Knox, K. & Billinge, S. Complex modeling: a strategy and software program for combining multiple information sources to solve ill posed structure and nanostructure inverse problems. *Acta Crystallogr. Sect. Found. Adv.* **71**, 562–568 (2015).
105. Granlund, L., Billinge, S. J. L. & Duxbury, P. M. Algorithm for systematic peak extraction from atomic pair distribution functions. *Acta Crystallogr. Sect. Found. Adv.* **71**, 392–409 (2015).
106. Juhás, P., Davis, T., Farrow, C. L. & Billinge, S. J. L. PDFgetX3: a rapid and highly automatable program for processing powder diffraction data into total scattering pair distribution functions. *J. Appl. Crystallogr.* **46**, 560–566 (2013).
107. Farrow, C. L. *et al.* PDFfit2 and PDFgui: computer programs for studying nanostructure in crystals. *J. Phys. Condens. Matter* **19**, 335219 (2007).
108. Proffen, T. & Billinge, S. J. L. PDFFIT, a program for full profile structural refinement of the atomic pair distribution function. *J. Appl. Crystallogr.* **32**, 572–575 (1999).
109. Usher, T.-M. *et al.* Local and average structures of BaTiO₃-Bi(Zn_{1/2}Ti_{1/2})O₃. *J. Appl. Phys.* **120**, 184102 (2016).
110. Hou, D., Zhao, C., Paterson, A. R., Li, S. & Jones, J. L. Local structures of perovskite dielectrics and ferroelectrics via pair distribution function analyses. *J. Eur. Ceram. Soc.* **38**, 971–987 (2018).
111. Garcia, E., Sotelo-Mazon, O., Poblano-Salas, C. A., Trapaga, G. & Sampath, S. Characterization of Yb₂Si₂O₇-Yb₂SiO₅ composite environmental barrier coatings resultant from in situ plasma spray processing. *Ceram. Int.* **46**, 21328–21335 (2020).

112. Garcia, E. *et al.* Crystallization behavior of air-plasma-sprayed ytterbium-silicate-based environmental barrier coatings. *J. Eur. Ceram. Soc.* **41**, 3696–3705 (2021).
113. Salanova, A., Opila, E. J. & Ihlefeld, J. F. Phase purity and evolution in sol–gel derived single component and multicomponent rare-earth disilicates. *J. Am. Ceram. Soc.* **107**, 3687–3700 (2024).
114. Cliffe, M. J. & Goodwin, A. L. PASCAL: a principal axis strain calculator for thermal expansion and compressibility determination. *J. Appl. Crystallogr.* **45**, 1321–1329 (2012).
115. Kotsonis, G. N. *et al.* High-entropy oxides: Harnessing crystalline disorder for emergent functionality. *J. Am. Ceram. Soc.* **106**, 5587–5611 (2023).
116. Saiki, A., Ishizawa, N., Mizutani, N. & Kato, M. Structural change of C-rare earth sesquioxides of Yb₂O₃ and Er₂O₃ as a function of temperature. *J. Ceram. Soc. Jpn.* **93**, 649–654 (1985).
117. Voronkov, M. G., Yuzhelevskii, Y. A. & Mileshevich, V. P. The siloxane bond and its influence on the structure and physical properties of organosilicon compounds. *Russ. Chem. Rev.* **44**, 355 (1975).
118. McNeil, K. J., DiCaprio, J. A., Walsh, D. A. & Pratt, R. F. Kinetics and mechanism of hydrolysis of a silicate triester, tris(2-methoxyethoxy)phenylsilane. *J. Am. Chem. Soc.* **102**, 1859–1865 (1980).
119. Soetebier, F. & Umland, W. Crystal structure of lutetium disilicate, Lu₂Si₂O₇. *Z. Für Krist.-New Cryst. Struct.* **217**, 22–22 (2002).
120. Smolin, Y. I., Shepelev, Y. F. & Titov, A. P. Refinement of crystal-structure of thortveitite Sc₂Si₂O₇. *Kristallografiya* vol. 17 857–858 (1972).